



HAL
open science

Fluid-solid interaction in a non-convex granular media : application to rotating drums and packed bed reactors

Andriarimina Rakotonirina

► **To cite this version:**

Andriarimina Rakotonirina. Fluid-solid interaction in a non-convex granular media : application to rotating drums and packed bed reactors. Chemical engineering. Université de Lyon, 2016. English. NNT : 2016LYSEN047 . tel-01483571

HAL Id: tel-01483571

<https://theses.hal.science/tel-01483571>

Submitted on 6 Mar 2017

HAL is a multi-disciplinary open access archive for the deposit and dissemination of scientific research documents, whether they are published or not. The documents may come from teaching and research institutions in France or abroad, or from public or private research centers.

L'archive ouverte pluridisciplinaire **HAL**, est destinée au dépôt et à la diffusion de documents scientifiques de niveau recherche, publiés ou non, émanant des établissements d'enseignement et de recherche français ou étrangers, des laboratoires publics ou privés.



Numéro National de Thèse: 2016LYSEN047

THÈSE de DOCTORAT DE L'UNIVERSITÉ DE LYON

opérée par

l'École Normale Supérieure de Lyon

École Doctorale N° 206

École Doctorale de Chimie de Lyon

Spécialité de Doctorat: Mécanique des fluides pour les procédés

Discipline: Chimie

Soutenue publiquement le 01 Décembre 2016,

par

Andriarimina Daniel RAKOTONIRINA

FLUID-SOLID INTERACTION IN A NON-CONVEX GRANULAR MEDIA: APPLICATION TO ROTATING DRUMS AND PACKED BED REACTORS

INTÉRACTION FLUIDE-SOLIDE EN MILIEUX GRANULAIRES DE PARTICULES
NON-CONVEXES: APPLICATION AUX TAMBOURS TOURANTS ET RÉACTEURS À LIT
FIXE

Devant le jury composé de :

Prof.	C. MÜLLER	Eidgenössische Technische Hochschule Zürich	Rapporteur
Prof.	N. DEEN	Technische Universiteit Eindhoven	Rapporteur
Dr.	F. RADJAÏ	Directeur de Recherche CNRS, LMGC Montpellier	Examineur
Prof.	C. DELENNE	Université de Montpellier, Hydrosiences Montpellier	Examineur
Dr.	J.-Y. DELENNE	Directeur de Recherche INRA, IATE Montpellier	Examineur
Prof.	A. WACHS	University of British Columbia	Directeur
Dr.	M. ROLLAND	IFP Energies nouvelles	Encadrant
Dr.	A. HAMMOUTI	IFP Energies nouvelles	Encadrant

REMERCIEMENTS

CES quelques lignes sont dédiées à toutes les personnes formidables et admirables que j'ai eu l'occasion de rencontrer durant ces dix dernières années d'études sans qui ce manuscrit de thèse n'aurait jamais existé. Cette thèse n'aurait pas été la même sans celles que j'ai cotoyées pendant ces trois dernières années. Certes, ces quelques lignes sont bien assez maigres mais comportent toute ma sincérité.

Je voudrais tout d'abord exprimer mes plus profonds remerciements à Anthony Wachs et Matthieu Rolland qui m'ont guidé tout au long de cette aventure. Parfois le chemin a été long, éprouvant, escarpé mais l'arrivée à destination fait toujours oublier toutes les difficultés. A Anthony, le *chef*, pour sa patience, sa passion qu'il a su transmettre à ses étudiants. Il a été d'un support inconditionnel, a su m'apprendre à repousser mes limites. Aujourd'hui, je suis très fier de dire que je ne regrette pas d'avoir choisi de faire cette thèse avec lui. A Matthieu, pour sa patience, ses conseils bien avisés et surtout son aide, ô combien précieuse, pour l'aboutissement de cette thèse. Merci de m'avoir fait découvrir le monde de l'industrie, tes conseils resteront à jamais dans mes pratiques dans ma future carrière, enfin si j'en oublie pas quelques uns. Messieurs, vos encadrement étaient, pour moi, ce dont j'avais rêvé d'avoir pour une thèse.

Je tiens aussi à remercier Neils Deen et Christoph Müller d'avoir accepté de rapporter mes travaux de thèse et de m'avoir aidé à améliorer mes connaissances dans le domaine. Mes remerciements vont aussi aux membres du jury Farhag Radjaï, Jean-Yves Delenne, Carole Delenne qui m'ont honoré de leur présence.

Je tiens à ne surtout pas oublier l'encadrement de Abdelkader Hammouti durant la dernière année de ma thèse qui m'a été d'une aide très précieuse. Je remercie aussi Jean-Yves Delenne pour toutes les discussions qu'on a pu avoir durant ma thèse. Elles ont permis d'améliorer ma compréhension de la mécanique des milieux granulaires.

Je remercie également Véronique Henriot de m'avoir accueilli au sein du département de mécanique des fluides d'IFP Energies nouvelles mais également Thierry Bécue de m'avoir permis de rester après la soutenance de ma mi-thèse.

Je remercie tout particulièrement tous les membres de l'équipe PeliGRIFF, à savoir Kad, le *nouveau chef*, pour ses conseils, son aide très précieuse qui va au-delà du cadre du travail et surtout pour son amitié (Kad a été comme un grand frère), Guillaume, Jean-Lou pour les derniers gros calculs, Florian, Amir, Mostafa. Je tiens à remercier Amir mon premier co-bureau de m'avoir supporté surtout toutes sortes de musiques qu'il a pu entendre à travers mon casque, pour les nombreuses fois qu'il m'avait offert son aide surtout au-delà du cadre du travail. Merci à Flo, qui nous a rejoint en 2014, qui a certainement trouvé l'idée de m'offrir un off-road en 4x4 comme cadeau. Et Mostafa, notre petit dernier, qui nous a appris plein d'expressions souvent à plier de rire. Celle qui m'a le plus marqué est: "la fin de thèse est comme un feu rouge, on ne s'arrête pas au dernier moment mais on se prépare à s'arrêter depuis une bonne distance".

Ici, je tiens à remercier Rim pour son bon humeur partout où on va, Haïfa, Ferdaous, Yoldes (comme une maman), Mafalda pour toutes ces sorties et tous ces repas qui m'ont aidé à me déconnecter, de temps en temps, de mes travaux de thèse.

Je remercie aussi les formidables collègues thésards membres de l'ADIFP que j'ai eu la chance de rencontrer.

Je remercie également tous les membres de la direction mécanique appliquée d'IFPEN de m'avoir permis de connaître une bonne ambiance de travail. Manu, comment oublier les cours du bord du Rhône, merci pour tout chef! Arnaud, Sophie, Alice, Alex pour le covoiturage, Fabien, Fabrice, Martin, Ian, Michael, Vincent, Didier, Timothée, Christian, les 2 Philippe, Philippe merci pour tous ces plats africains qui m'ont tant fait rappeler mon pays, Jean-Pierre, Francis le beau-gosse, Fred, Guillaume, Véro, Cyril pour le sport et les discussions scientifiques, Malika, Myriam, Pierre-Antoine, le nouveau thésard et ancien stagiaire, d'avoir partagé notre bureau. Je tiens aussi à remercier Françoise pour son aide et sa disponibilité pour toutes les tâches administratives.

Mes remerciements vont également à toutes les personnes que j'ai pu rencontrer à Madagascar pour avoir rendu mes études possibles. Par ordre chronologique, Ridha de m'avoir donné la possibilité de travailler pour lui afin que je puisse économiser pour réaliser mon rêve. Je tiens à exprimer ma profonde et éternelle gratitude à la famille Razafintsalama & Lugan de m'avoir donné l'opportunité de poursuivre mes études en France, sans vous tout cela n'aurait juste été qu'un rêve, les mots ne seront jamais assez pour vous remercier. Je remercie également Rina, Randza et surtout Andalinda pour leur participation dans l'accomplissement de ce rêve. Je tiens aussi à remercier les amis qui sont devenus un peu comme une famille dans un pays qui est très loin du mien. Ils ont fait de mon séjour en France, surtout à Toulouse, agréable. A savoir, Anicet, Mahery, Zo, Yves, Mario, Andalinda, Randza et Lalaina.

Je tiens à remercier également ma famille (mes parents, mes frères (Aina, Mamy) et ma soeur (Enoka)) qui m'a été d'un soutien infaillible et incontournable. Cette famille qui m'a donné le courage de me lever quand j'étais à terre, cette famille qui me donne et me donnera toujours cette rage de vaincre. On est parti de très très loin mais je vous ai dit que j'allais y arriver et maintenant j'y suis. Je tiens à remercier aussi mes meilleurs amis de Madagascar Mihaja, Tantely, Jacky, Nirina et Sitraka qui m'ont toujours soutenu malgré la distance et qui m'ont toujours porté dans leurs cœurs.

Je conclurai en remerciant de tout cœur Betelhem pour ces années de bonheur passées à mes côtés, pour son soutien inconditionnel durant toute cette thèse. Les mots me manqueront toujours pour t'exprimer ma gratitude.

À ma famille,
À Betlehem,

CONTENTS

CONTENTS	vii
ABSTRACT	xv
RÉSUMÉ	xvii
1 GRANULAR MEDIA AND ITS APPLICATIONS	1
1 INTRODUCTION TO GRANULAR MEDIA	2
2 ROTATING DRUMS	4
3 HETEROGENEOUS CATALYST SHAPE	5
3.1 Industrial context	5
3.2 Shape and apparent catalytic activity	7
3.3 Pressure drop and Void fraction	7
3.4 Summary on catalyst shape optimization: Need for predictive tools	9
4 SCOPE OF THE THESIS	9
2 GRANULAR FLOW SIMULATION: A LITERATURE REVIEW	13
1 LABORATORY SCALE EXPERIMENTS OF DRY GRANULAR FLOW	14
2 GRANULAR MEDIA MODELLING	15
2.1 Hard sphere approach	15
2.2 Soft-particle and Discrete Element Method (DEM)	15
2.3 Non-Smooth Contact Dynamics (NSCD)	16
2.4 Hybrid soft and hard sphere collision	16
2.5 Continuum Mechanics Methods (CMM)	16
2.6 Other approaches	17
3 CONTACT DETECTION ALGORITHM	17
4 DISCRETE ELEMENT METHOD WITH COMPLEX PARTICLE SHAPES	17
4.1 Importance of particle shape	18
4.2 Brief review of particle shape in literature	18
5 SYNTHESIS	22
3 NON-CONVEX GRANULAR MEDIA MODELLING WITH GRAINS_{3D}	25
1 INTRODUCTION	26
2 NEW GLUED CONVEX METHOD	27
2.1 Equations of motion	28
2.2 Strategy	29
2.3 Mass properties	29
2.4 Time integration	30
2.5 GJK-based contact detection	31
2.6 Contact force and torque	32

3	VALIDATION TESTS	36
3.1	Methodology	36
3.2	Normal cylinder-wall impact	36
4	RESULTS	41
4.1	Packing porosity	41
4.2	Rotating drum	45
5	CONCLUSION AND DISCUSSION	52
4	OPTIMIZING PARTICLE SHAPE IN FIXED BEDS: SIMULATION OF VOID FRACTION WITH POLY-LOBED PARTICLES	55
1	INTRODUCTION	56
2	METHODS AND MATERIAL	57
2.1	DEM with non-convex particles	57
2.2	Simulation principle	58
2.3	Void fraction analysis	58
2.4	Cases description	59
3	SIMULATIONS WITH RANDOM INSERTION AND DATA ANALYSIS	60
3.1	Repeating the packing	61
3.2	Effect of insertion window size	61
3.3	Overall uncertainty	62
4	RESULTS	63
4.1	Bi-periodic container	63
4.2	Cylindrical container	64
5	DISCUSSION	65
5.1	Effect of domain size in bi-periodic directions?	66
5.2	Remark on the effect of container size	66
6	CONCLUSION	67
5	GRAINS3D: A MASSIVELY PARALLEL 3D DEM CODE	69
1	INTRODUCTION	70
2	NUMERICAL MODEL	71
3	DOMAIN DECOMPOSITION PARALLEL STRATEGY	72
4	COMPUTATIONAL PERFORMANCE	77
4.1	Assessing memory management on multi-core node architecture	77
4.2	Granular slumping	85
4.3	Coupling with a fluid in an Euler/Lagrange framework, application to fluidized beds	91
5	DISCUSSION AND PERSPECTIVES	97
6	PARTICLE-RESOLVED SIMULATION: STATE OF THE ART	101
1	BODY CONFORMAL MESH METHOD	103
1.1	Arbitrary-Lagrangian-Eulerian (ALE)	103
1.2	Deforming-Spatial-Domain/Stabilized Space-Time (DSD/SST)	103
2	FIXED MESH METHODS	104
2.1	Lattice-Boltzmann Method (LBM)	104
2.2	Immersed Boundary Method (IBM)	105
2.3	Distributed Lagrange Multiplier / Fictitious Domain (DLM/FD)	105
3	ADAPTIVE MESH REFINEMENT (AMR)	106
4	CONCLUSION	107

7	NON-CONVEX PARTICLES WITH PELIGRIFF AND PRESSURE DROP IN FIXED BED REACTORS	III
1	INTRODUCTION	II2
2	A DLM/FD METHOD FOR PRS OF PARTICULATE FLOWS WITH NON-CONVEX PARTICLES	II3
3	NUMERICAL MODEL	II4
3.1	Introduction to PeliGRIFF	II4
3.2	Governing equations for the fluid flow solver	II4
3.3	Time discretization scheme	II5
3.4	Colocation Points on non-convex particles	II6
4	ACCURACY OF THE COMPUTED SOLUTIONS	II8
4.1	Methodology	II8
4.2	Flow past a single poly-lobed particle in a tri-periodic domain	II9
4.3	Flow past a small packed bed of poly-lobed particles	123
5	PRESSURE DROP THROUGH PACKED BEDS OF POLY-LOBED PARTICLES	124
5.1	A quick review of single phase pressure drop in fixed beds	124
5.2	Method	127
5.3	Results	128
6	CONCLUSION AND PERSPECTIVES	134
8	CONCLUSION AND PERSPECTIVES	137
	BIBLIOGRAPHY	143

TABLE DES MATIÈRES

1	LES MILIEUX GRANULAIRES ET LEURS APPLICATIONS	1
1	INTRODUCTION SUR LES MILIEUX GRANULAIRES	2
2	LES TAMBOURS TOURNANTS	4
3	FORME DE GRAINS DE CATALYSEUR POUR LA CATALYSE HÉTÉROGÈNE	5
3.1	Contexte industriel	5
3.2	Forme et activité catalytique	7
3.3	Perte de charge et taux de vide	7
3.4	Résumé sur l'optimisation des formes de catalyseur : besoin d'outils prédictifs	9
4	PORTÉE DE LA THÈSE	9
2	SIMULATION NUMÉRIQUE D'ÉCOULEMENT GRANULAIRE : UNE REVUE DE LA LITTÉRATURE	13
1	ÉCOULEMENTS GRANULAIRES SECS À L'ÉCHELLE DU LABORATOIRE	14
2	MODÉLISATION DES MILIEUX GRANULAIRES	15
2.1	L'approche sphère molle	15
2.2	Particule molle et méthode des éléments discrets	15
2.3	Non-Smooth Contact Dynamics (NSCD)	16
2.4	Modèle hybride : sphère molle et sphère rigide	16
2.5	Méthode de la mécanique des milieux continus	16
2.6	Autres approches	17
3	ALGORITHME DE DÉTECTION DE CONTACT	17
4	PARTICULES DE FORME COMPLEXE AVEC LA MÉTHODE DES ÉLÉMENTS DISCRETS	17
4.1	Importance de la forme des particules	18
4.2	Les formes de particules dans la littérature	18
5	SYNTHÈSE	22
3	MODÉLISATION DES MILIEUX GRANULAIRES AVEC GRAINS _{3D}	25
1	INTRODUCTION	26
2	LA NOUVELLE MÉTHODE DES CONVEXES COLLÉS	27
2.1	Équation du mouvement	28
2.2	Stratégie	29
2.3	Les propriétés massiques	29
2.4	Intégration temporelle	30
2.5	Détection de contact GJK	31
2.6	Force de contact et moment	32
3	VALIDATION	36
3.1	Méthodologie	36
3.2	Impact cylindre-parois	36
4	RÉSULTATS	41
4.1	Porosité	41

4.2	Tambour tourant	45
5	CONCLUSION ET DISCUSSION	52
4	OPTIMISATION DES FORMES DES PARTICULES : SIMULATION DU TAUX DE VIDE AVEC DES PARTICULES POLY-LOBÉES	55
1	INTRODUCTION	56
2	MÉTHODES ET MATÉRIELS	57
2.1	DEM avec des particules non-convexes	57
2.2	Principe de simulation	58
2.3	Analyse du taux de vide	58
2.4	Description des cas	59
3	SIMULATIONS AVEC INSERTION ALÉATOIRE ET ANALYSE DE DONNÉES	60
3.1	Répétition du chargement	61
3.2	Effet de la fenêtre d'insertion	61
3.3	Incertitude globale	62
4	RÉSULTATS	63
4.1	Récipient bi-périodique	63
4.2	Récipient cylindrique	64
5	DISCUSSION	65
5.1	Effet de la taille du domaine dans les directions bi-périodiques ?	66
5.2	Remarque sur l'effet de la taille du récipient	66
6	CONCLUSION	67
5	GRAINS3D : UN CODE DEM MASSIVEMENT PARALLÈLE	69
1	INTRODUCTION	70
2	MODÈLE NUMÉRIQUE	71
3	STRATÉGIE DE DÉCOMPOSITION DE DOMAINE	72
4	PERFORMANCE NUMÉRIQUE	77
4.1	Évaluation de la gestion de mémoire sur une architecture à nœuds multi-cœurs	77
4.2	Effondrement granulaire	85
4.3	Couplage avec du fluide dans une approche Euler/Lagrange, application aux lits fluidisés	91
5	DISCUSSION ET PERSPECTIVES	97
6	SIMULATION NUMÉRIQUE DIRECTE : ÉTAT DE L'ART	101
1	MAILLAGE ADAPTATIF	103
1.1	Arbitrary-Lagrangian-Eulerian (ALE)	103
1.2	Deforming-Spatial-Domain/Stabilized Space-Time (DSD/SST)	103
2	MAILLAGE FIXE	104
2.1	Méthode de Boltzmann sur réseau	104
2.2	Méthode des frontières immergées	105
2.3	Méthode des multiplicateurs de Lagrange distribués / Domain fictif	105
3	RAFFINEMENT DE MAILLAGE ADAPTATIF	106
4	CONCLUSION	107
7	PARTICULES NON-CONVEXES AVEC PELIGRIFF ET PERTE DE CHARGE DANS LES RÉACTEURS À LITS FIXES	III
1	INTRODUCTION	112

2	UNE MÉTHODE DLM/FD POUR LA RÉOLUTION DES ÉCOULEMENTS FLUIDE- PARTICULES AVEC DES PARTICULES NON-CONVEXES	113
3	MODÈLE NUMÉRIQUE	114
3.1	Introduction à PeliGRIFF	114
3.2	Les équations gouvernant le solveur fluide	114
3.3	Schéma de discretisation temporelle	115
3.4	Points de collocation sur des particules non-convexes	116
4	PRÉCISION DES SOLUTIONS CALCULÉES	118
4.1	Méthodologie	118
4.2	Écoulement autour d'une particule multi-lobée isolée dans un domaine tri- périodique	119
4.3	Écoulement au travers d'un lit fixe de particules multi-lobées	123
5	PERTE DE CHARGE AU TRAVERS DES LITS FIXES DE PARTICULES MULTI-LOBÉES	124
5.1	Brève revue sur la perte de charge monophasique au travers d'un lit fixe	124
5.2	Méthode	127
5.3	Résultats	128
6	CONCLUSION ET PERSPECTIVES	134
8	CONCLUSION ET PERSPECTIVES	140

ABSTRACT

Non convex granular media are involved in many industrial processes as, e.g., particle calcination/drying in rotating drums or solid catalyst particles in chemical reactors. In the case of optimizing the shape of catalysts, the experimental discrimination of new shapes based on packing density and pressure drop proved to be difficult due to the limited control of size distribution and loading procedure. There is therefore a strong interest in developing numerical tools to predict the dynamics of granular media made of particles of arbitrary shape and to simulate the flow of a fluid (either liquid or gas) around these particles. Non-convex particles are even more challenging than convex particles due to the potential multiplicity of contact points between two solid bodies. In this work, we implement new numerical strategies in our home made high-fidelity parallel numerical tools: Grains3D for granular dynamics of solid particles and PeliGRIFF for reactive fluid/solid flows. The first part of this work consists in extending the modelling capabilities of Grains3D from convex to non-convex particles based on the decomposition of a non-convex shape into a set of convex particles. We validate our numerical model with existing analytical solutions and experimental data on a rotating drum filled with *2D cross* particle shapes. We also use Grains3D to study the loading of semi-periodic small size reactors with trilobed and quadralobed particles. The second part of this work consists in extending the modelling capabilities of PeliGRIFF to handle poly-lobed (and hence non-convex) particles. Our Particle Resolved Simulation (PRS) method is based on a Distributed Lagrange Multiplier / Fictitious Domain (DLM/FD) formulation combined with a Finite Volume / Staggered Grid (FV/SG) discretization scheme. Due to the lack of analytical solutions and experimental data, we assess the accuracy of our PRS method by examining the space convergence of the computed solution in assorted flow configurations such as the flow through a periodic array of poly-lobed particles and the flow in a small size packed bed reactor. Our simulation results are overall consistent with previous experimental work.

Keywords: Non-convex Particles, Discrete Element Method, Granular Mechanics, Direct Numerical Simulation, Rotating Drums, Fixed Beds, Porous Media, High Performance Computing

RÉSUMÉ

Cette thèse porte sur l'étude numérique des écoulements fluide-particules rencontrés dans l'industrie. Ces travaux se situent dans le cadre de la compréhension des phénomènes qui se déroulent dans des tambours tournants et réacteurs à lit fixe en présence de particules de forme non convexe. En effet, la forme des particules influence de manière importante la dynamique de ces milieux. A cet effet, nous nous sommes servis de la plateforme numérique parallèle Grans3D pour la dynamique des milieux granulaires et PeliGRIFF pour les écoulements multiphasiques. Dans la première partie de cette thèse, nous avons développé une nouvelle stratégie numérique qui permet de prendre en compte des particules de forme arbitrairement non convexe dans le solveur Grains3D. Elle consiste à décomposer une forme non convexe en plusieurs formes convexes quelconques. Nous avons nommé cette méthode "glued-convex". Le modèle a été validé avec succès sur des résultats théoriques et expérimentaux de tambours tournants en présence de particules en forme de croix. Nous avons aussi utilisé le modèle pour simuler le chargement de réacteurs à lits fixes puis des lois de corrélation sur les taux de vide ont été déduites de nos résultats numériques. Dans ces travaux, nous avons aussi testé les performances parallèles de nos outils sur des simulations numériques à grande échelle de divers systèmes de particules convexes. La deuxième partie de cette thèse a été consacrée à l'extension du solveur PeliGRIFF à pouvoir prendre en compte la présence de particules multilobées (non convexes) dans des écoulements monophasiques. Une approche du type Simulation Numérique Directe, basée sur les Multiplicateurs de Lagrange Distribués / Domaine Fictif (DLM/FD), a alors été adoptée pour résoudre l'écoulement autour des particules. Une série d'études de convergence spatiale a été faite basée sur diverses configurations et divers régimes. Enfin, ces outils ont été utilisés pour simuler des écoulements au travers de lits fixes de particules de forme multi-lobée dans le but d'étudier l'influence de la forme des particules sur l'hydrodynamique dans ces lits. Les résultats ont montré une consistance avec les résultats expérimentaux disponibles dans la littérature.

Mots clés: Particule non convexe, Mécanique des Milieux Granulaires, Simulation Numérique Directe, Tambours Tournants, Lits Fixes, Milieux Poreux, Calcul Haute Performance

GRANULAR MEDIA AND ITS APPLICATIONS



CONTENTS

1	INTRODUCTION TO GRANULAR MEDIA	2
2	ROTATING DRUMS	4
3	HETEROGENEOUS CATALYST SHAPE	5
3.1	Industrial context	5
3.2	Shape and apparent catalytic activity	7
3.3	Pressure drop and Void fraction	7
3.4	Summary on catalyst shape optimization: Need for predictive tools	9
4	SCOPE OF THE THESIS	9

“Un corps est liquide lorsqu’il est divisé en plusieurs petites parties qui se meuvent séparément les unes des autres en plusieurs façons différentes, et qu’il est dur lorsque toutes ses parties s’entre-touchent, sans être en action pour s’éloigner l’une de l’autre”.

Descartes (1852)

I INTRODUCTION TO GRANULAR MEDIA

The idea of [Descartes \(1852\)](#) can be extended to granular media such that a granular media might be a particular state of matter usually defined between liquid and solid. It behaves like a liquid because it flows, can fill a container and can take its shape. Unlike liquids, a non horizontal free surface can be stable. It also behaves like a solid since it can resist to compression and slightly to shear stress (or deviatoric stress). However, a solid can resist to traction, whereas a granular media can not.






Ultra-fine powder	Super-fine powder	Granular powder	Granular solid	Broken solid
				
[0.1; 1] μm	[1.0; 10] μm	[10; 100] μm	[0.1; 3] mm	> 3 mm
Powders			Granular materials	

Table 1.1 – Particle classification and examples. Credit: [Brown and Richards \(1970\)](#)

Since a granular media is a collection of particles, it is essential to introduce the concept and the definition of the particle size classification, particle shape, roughness, etc (TAB. 1.1).

The sorted categories of particles are encountered in many applications such as in civil engineering, food processing, pharmaceuticals, foundry, geophysics, astrophysics, oil and gas, energy, etc. Thus, each field of applications has its own specific vocabulary for the classification of the shape and size.

In the field of civil engineering, the cement industry appears to be one of the largest users of granular materials. In fact, cement is obtained by mixing limestone (80%) and clay (40%) at high temperature. There is also the concrete manufacturing industry which plays a significant role in terms of granular materials usage. For instance, Lafarge, a French multinational company, which is the world leader in the production of cement, construction aggregates and concrete has 166 plants in the world and a capacity of 225 Mt/year.



Figure 1.1 – Cement plant



Figure 1.2 – Inside a cement mill

After water, granular materials are the second most used resources on Earth ([Duran \(1999\)](#)). One of the main issues encountered in the field of food processing is the storage prob-

lem and the discharge of containers. FIG. 1.4 illustrates the particular problem of segregation in the discharge of containers. Generally, segregation occurs when a flowing granular media made of various particle sizes is disturbed leading to a rearrangement of particles. It appears often while vibrating a container during a pouring or a discharge procedure.



Figure 1.3 – Hopper discharge



Figure 1.4 – Segregation inside a hopper near the exit hole

Granular materials are also seen in nature such as sand on the beach, in the desert (10% of Earth surface), in rivers, on continental shelves and abyssal plains, on hills, etc. There are various phenomena which are related to the presence of sand, for instance the displacement of sand dunes in the desert, river bed erosion, submarine avalanche, etc.

Nature can put on display dreadful and devastating phenomena such as snow avalanches (FIG. 1.5) and landslides (FIG. 1.6).



Figure 1.5 – Typical powder snow avalanche.



Figure 1.6 – Landslide burying a six-lane motorway in Taiwan.

Technically, an avalanche is an amount of snow sliding down a mountainside while landslide is the movement of rock, shallow debris or earth down a slope. In particular, *powder snow avalanche* (FIG. 1.5) is known as an extremely violent avalanche. The typical mass of an avalanche can easily exceed 10 Gt and its velocity can reach 300 km/h . This type of avalanche holds a large amount of snow grains in the surrounding turbulent fluid. This phenomenon is usually close to a dust storm in arid and semi-arid regions (FIG. 1.7) where particles are suspended in the fluid. Another example is *pyroclastic flows* known as *pyroclastic density currents* which come from volcano eruptions (FIG. 1.8) and where hot gas of about 1000° C is mixed with rocks with a current velocity up to 700 km/h . The boulders moving in pyroclastic flows have very high kinetic energy so that they can flatten trees and destroy a whole building which comes across their path. The hot gases are extremely lethal since they can spontaneously incinerate living organisms.



Figure 1.7 – A dust storm passing over Onslow in Australia.



Figure 1.8 – Pyroclastic flow flowing into the Tar River in North Carolina.

Granular media are also found in the field of astrophysics. For example, the rings of Saturn (FIG. 1.9) which are a massive collection of granular materials that infinitely collide while rotating around the planet. Another example is the granular materials found in Mars which are investigated during Mars exploration by NASA's Mars rover Curiosity. In FIG. 1.10, the rover cuts a wheel scuff mark into a wind-formed ripple at the "Rocknest" site to examine the particle-size distribution of the material forming the ripple.

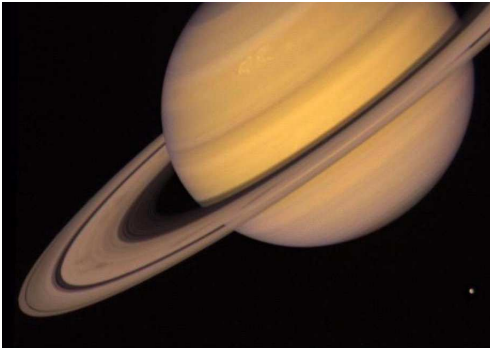


Figure 1.9 – Rings of Saturn.



Figure 1.10 – NASA's Mars rover Curiosity. Credit: NASA/JPL-Caltech.

All of these phenomena involving granular media are still challenging to describe especially at a very large scale, where the overall dynamics is controlled by the scale of an individual particle. Hence, scientist and engineers set up small-scale laboratory experimentations in order to have an insight in the physics involved in the study of granular dynamics. In addition, numerical simulations play an important role as enhanced physical models implemented in modern parallel codes lead to increasingly accurate numerical models able to examine large scale granular flows.

2 ROTATING DRUMS

Granular media flow is of utmost interest in many other industries. Rotating furnaces are widely used in treatment of solids like drying, torrefaction, pyrolysis, calcination, impregnation, chemical treatment ... In all these cases, it is highly preferable that the granular media is mixed so as to control residence time and to prevent that the solid stays too long near or far from the walls (or the injection points). The rotating drum is an experimental device that is widely used to study the dynamics of granular media. The reproducibility of experiments are

quite satisfactory and the system is continuously fed. One of the advantages of the set-up is that experiments can be reproduced in short period of time. Hence, it offers the possibility of performing a large amount of experiments on many flow regimes. The rotating drum is also often chosen to study environmental flows such as pyroclastic flows or avalanches. Granular flow regimes are known to be impacted by particle shapes. For this purpose, many authors studied the influence of particle shape on the dynamics of granular media, among others [Favier et al. \(1999\)](#), [Höhner et al. \(2013; 2014\)](#), [Lu et al. \(2014\)](#). However, the numerical simulations are performed on limited amount of particle shapes.

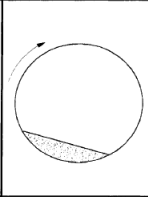
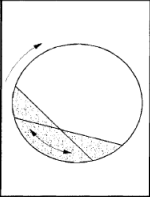

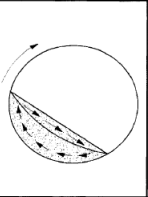
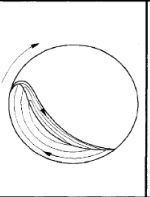
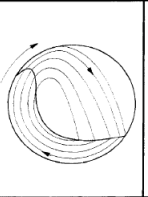
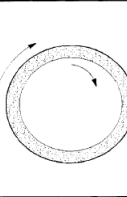
Slipping motion		Cascading ("tumbling") motion			Cataracting motion	
Sliding	Surging	Slumping	Rolling	Cascading	Cataracting	Centrifuging
						
Slipping		Mixing			Crushing	Centrifuging

Figure 1.11 – Different regimes found in rotating drum. Credits: [Mellmann \(2001\)](#).

Many flow regimes can appear as a function of the rotation rate. [Mellmann \(2001\)](#) proposed mathematical models to predict the transitions between the different forms of transverse motion of a free-flowing bed material in a rotating drum. These regimes are widely referred to in the literature and are summarized in FIG. 1.11.

The Froude number Fr is usually the key factor of the characterization of the regime transitions in rotating drums. Nonetheless, this dimensionless number is often subjected to modification to account for the height of the bed of granular media, the particle diameter to the drum diameter aspect ratio (d_p/D_d) or the material properties of particles and of the drum.

3 HETEROGENEOUS CATALYST SHAPE

3.1 Industrial context

Catalytic reactions and reactors have numerous applications such as production of chemicals bulk, petroleum refining, fine chemical pharmaceuticals, biomass conversion, etc. Most catalytic refining and petrochemical reactions are operated in fixed bed reactors. In these reactors, catalyst pellets are randomly stacked in a large cylindrical vessel and reactants, usually gas and liquid, flow through the bed to react inside the catalyst pellets. Catalyst pellets are designed to be porous so that the reacting fluid can penetrate the particle to reach the reactive phase (noble metals, metal sulphides, etc.) coated onto them. Main interest of heterogeneous catalysis is that the surface area available for reaction is very large (typically 20 – 200 m^2/g per pellet). Catalyst particles are typically [0.2; 5] mm in size and can be spherical, cylindrical or can have more complex shapes (FIGS. 1.12 and 1.13). Catalyst shape is chosen in order to optimize the reactor performance.

Performance, in the point of view of the refiner, is a compromise between catalyst lifetime and cost, reactor yield, mechanical strength and operating costs. A higher catalyst activity is generally preferable as it allows to operate either at lower temperature or in more severe conditions (higher flow-rate or more difficult feedstock). A better activity can be achieved by in-



(a) Example of spherical catalyst particles. Credits: Falmouth Products Inc., Falmouth, MA.



(b) Example of catalyst particles developed at IFPEN.

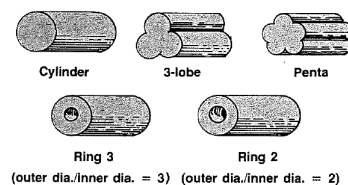
Figure 1.12 – Example of catalyst pellets.

creasing the amount of active phase which generally results in a more expensive catalyst. In the case of mass transfer limitations, it can be interesting to increase the pellet surface to volume ratio: the higher external area ensures a better accessibility to the inner volume of the pellet. A higher surface to volume ratio can be achieved in reducing pellet size or changing the pellet shape. Pressure drop in the fixed bed should be minimum to reduce the gas compression costs, especially on the hydrogen feed. This is achieved using large pellets and high voidage packing. Catalyst lifetime is limited by several mechanisms: bed plugging, catalyst leaching (part of the active phase is taken out with products), catalyst ageing (active phase changes in time and is less active), catalyst coking (formations of deposits in the particle reduced access to active sites), etc. Changing catalyst shape is a way to manage bed plugging. Mechanical strength depend on the pellet support material, its inner porosity and of course on the pellet shape. A low mechanical strength leads to a higher risk of pellet breakage which results in high pressure drop. If fines are produced during pellet breakage, they can even plug the bed. In summary, shape change in a convenient way to optimize catalyst performance.

Catalyst production method has an impact on its costs. Extrusion of the pellets (FIG. 1.13b) is quite cheap and allows to modify the shape by changing the die. Therefore, an important effort is dedicated to the extrudate shapes and consists in finding the most optimised ones.



(a) Common shapes used in industrial applications.



(b) Extrudate catalyst pellets. Credit: Cooper et al. (1986).

Figure 1.13 – Various shape of catalyst pellets.

From a chemical engineering perspective, optimizing a catalyst shape means finding a shape minimizing pressure drop while maximizing the chemical conversion rate of the catalyst.

3.2 Shape and apparent catalytic activity

Inside the particle, mass transfer limitations may prevent all catalytic sites to exhibit full performances: if reactant diffusion is slow compared to reactant consumption, it is possible that reactant concentration at the center may be significantly lower than at catalyst pellet surface. Using the classical Thiele approach (Thiele (1939)), chemical engineers can estimate the loss of activity due to mass transfer limitation. Catalyst efficiency is defined as the ratio of the activity of the particle to the activity of the particle if the concentration was uniform. For a reaction of order n , this can be written :

$$\eta = \frac{\iiint_{\mathbf{V}} K_i C^m dv}{\iiint_{\mathbf{V}} K_i C_0^m dv} \quad (1.1)$$

The analytical solutions of this equation are based on the dimensionless number known as Thiele Modulus. It compares the consumption by the reaction and the diffusion phenomena. If it is larger than 1 then the reaction is mass transfer limited.

$$\Phi_L = L_p \left(\frac{K_i C^{m-1}}{D_{eff}} \right)^{0.5} \quad (1.2)$$

Φ_L denotes the Thiele modulus, L_p a characteristic particle dimension, K_i the intrinsic reaction rate constant, C the concentration of reactant, n the reaction order and D_{eff} the effective diffusivity.

Exact derivation of efficiency as a function of the Thiele modulus exists for semi-infinite plate, sphere and infinite cylinder (FIG. 1.14).

For example:

- (i) For plate: $\eta = \tanh \Phi_L / \Phi_L$
- (ii) For sphere: $\eta = (3\Phi_L \coth 3\Phi_L - 1) / 3\Phi_L^2$
- (iii) For cylinder: $\eta = I_1(2\Phi_L) / \Phi_L I_0(2\Phi_L)$

where $I_n(x)$ is the Bessel function of order n .

For these derivations, the Thiele modulus does not depend on shape if it is rewritten using $L_p = V_p / S_p$, as proposed by Aris (1957).

For a given Thiele modulus, it may appear that shape has little effect of the efficiency (FIG. 1.14). Nevertheless, for $\Phi_L \sim 1$, which is a frequent case, changing shape can improve efficiency by a few percent, which is significant for industrial purposes. In fact, shape optimisation is mostly about changing the Thiele Modulus by changing the characteristic dimension of the particle L_p .

In order to improve efficiency, it is interesting to lower the Thiele modulus, hence increasing the ratio V_p / S_p . Hence, this leads to the development of poly-lobed extrudates.

3.3 Pressure drop and Void fraction

Before industrialising a new shape of catalyst, it should be known how the shape will affect pressure drop and the amount of catalyst that can be loaded in a reactor.

A large number of correlations has been proposed in literature. They are based whether on empirical data or on numerical models. Among others, Cooper et al. (1986) proposed a

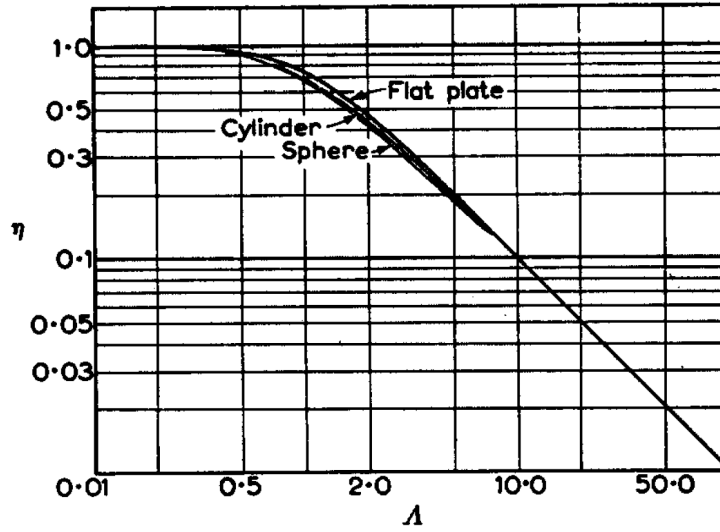


Figure 1.14 – Effectiveness factor for various shapes. X-axis : Thiele modulus, Y-axis : efficiency. Credit: [Aris \(1957\)](#).

model which is based on the correlations of [Midoux et al. \(1976\)](#). The model is written in the following from:

$$\Delta P_{LG} = f_1(\mathbf{X}) \cdot \Delta P_L = f_2(\mathbf{X}) \cdot \Delta P_G \quad (1.3)$$

where $\mathbf{X} = \sqrt{\frac{\Delta P_G}{\Delta P_L}}$ and ΔP_{LG} denotes the two-phase pressure drop per unit length. ΔP_G and ΔP_L denote respectively the pressure drop of gas and liquid if they exist and assumed to flow alone. If the pressure drop of a single phase flow is known, then the gas-liquid pressure drop can be computed with sufficient accuracy. Being able to predict single phase pressure drop is thus sufficient in the context of shape optimization.

The correlation of single phase pressure drop in packed bed of [Ergun and Orning \(1949\)](#) and [Ergun \(1952\)](#) is widely used in the chemical sectors. They suggested to predict the pressure drop through a packed bed as the sum of a viscous term (friction on particle surface) and an inertia term (change in direction, expansion, contraction).

$$\frac{\Delta P}{H} = 150 \frac{\mu(1-\varepsilon)^2}{\varepsilon^3} \frac{u}{d_p^2} + 1.75 \frac{\rho_f(1-\varepsilon)}{\varepsilon^3} \frac{u^2}{d_p} \quad (1.4)$$

where ε , μ , U , d_p , H and ρ_f denote respectively bed void fraction, fluid dynamic viscosity, particle diameter, height of the bed and fluid density. The numerical constants (150 and 1.75) are fitted to match experimental data points and depend on the particle shape.

The correlation EQ. 1.4 exhibits a very strong dependency on void fraction. So far, there is yet no way to analytically predict the void fraction of a packed bed for an arbitrary (new) particle shape. Experiments are necessary and they are not so easy to perform. A first problem is that particles have random dimensions: for extrudates, the diameter is almost constant but the length can vary a lot in an uncontrolled manner. Length distribution variations may influence experimental results. A second issue is that a good accuracy of the void fraction is required to be able to discriminate shapes. Reaching high accuracy requires the use of large vessels, and repetition of experiments which is seldom performed on prototype shapes produced in small amounts. A third issue is that the bed void fraction depends on the loading procedure and it is very likely that some procedures designed for a specific shape may lead to very different results on others (for example: cylinders subjected to vibration tend to align vertically, which is

of course not observed on spheres). Thus, void fraction measurements in these beds are quite time consuming.

The pressure drop correlation uses a “particle diameter”, whose definition is not straightforward for non spherical particles. Several approaches have been suggested that try to estimate an “equivalent diameter” based on shape factors (Cooper et al. (1986)):

$$d_e = \frac{1}{\phi_s} \left(6 \cdot \frac{V_p}{S_p} \right) \quad (1.5)$$

where ϕ_s is the shape factor (surface area of a sphere of equal volume/surface area of the particle), V_p and S_p denotes respectively the volume and the surface of the particle. Interestingly, this expression resembles the characteristic length recommended by Aris Aris (1957) to compute the Thiele modulus.

It can be seen in FIG. 1.15 that the pressure drop is quite dependent on particle shape and volume to surface ratio. So far correlations to estimate pressure drop of new particles shapes are failing to be predictive enough due to a lack of knowledge of the void fraction as well as scarce and scattered of experimental data (Nemec and Levec (2005)).

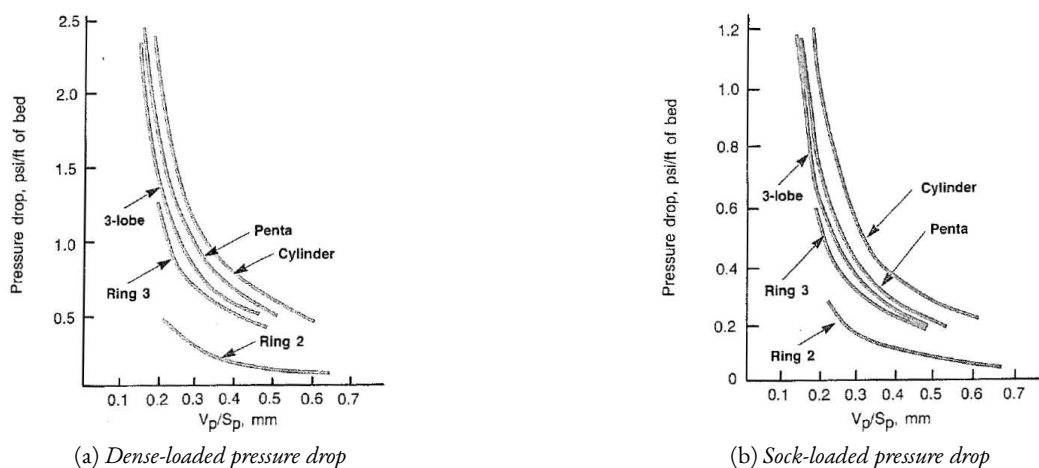


Figure 1.15 – Dependency of pressure drop on loading technique and particle shape. Credit: Cooper et al. (1986).

3.4 Summary on catalyst shape optimization: Need for predictive tools

Changing particle shapes can be quite interesting to increase particle efficiency through increasing the surface to volume ratio. Efficiency wise, shape selection can be performed using simulation tools. On the opposite side, the pressure drop estimation requires experiments that are time consuming and ill-adapted to screen a large number of candidate shapes. New numerical tools are welcome to ease particle shape evaluation.

4 SCOPE OF THE THESIS

This Ph.D. thesis is a multi-disciplinary work in the framework of a collaboration between two departments at IFP Energies nouvelles:

- Fluid Mechanics Department,
- Process Experimentation Department,

INRA Montpellier and the CNRS laboratory of Mechanics and Civil Engineering at Montpellier.

The overall objective of this work is twofold :

- to develop numerical tools:
 - Extension of the modelling capabilities of Grains3D (a massively parallel Discrete Element Method code for granular dynamics) to treat non-convex particles based on a decomposition of a non-convex particle into a set of convex ones
 - Extension of the modelling the capabilities of PeliGRIFF (a massively parallel Direct Numerical Simulation code) to handle non-convex particles in the coupling the dispersed granular phase with the flow solver using a Distributed Lagrange Multiplier / Fictitious Domain (DLM/FD) formulation
- to use these enhanced of the tools to improve physical comprehension of:
 - Silo discharge
 - Dam breaking
 - Fluidization
 - Simulation of 2D- and 3D- cross particles in a rotating drum
 - Assessing the effect of catalyst shape on fixed bed void fraction
 - Assessing the effect of catalyst shape on pressure drop

This work has been or will be presented for publication in 4 papers that will be used as the back bone of this thesis manuscript which is organized as follows:

- Chapter 2: Granular flow simulation: A literature review
- Chapter 3: Non-convex granular media modelling with Grains3D (paper 1)
- Chapter 4: Optimizing particle shape in fixed beds: simulation of void fraction with poly-lobed particles (paper 2)
- Chapter 5: Grains3D: a massively parallel 3D DEM code (paper 3)
- Chapter 6: A literature review on Particle-Resolved Simulation
- Chapter 7: Non-convex particles with PeliGRIFF and pressure drop in fixed bed reactors (paper 4)
- Chapter 8: Conclusion and perspectives

RÉSUMÉ

Ce chapitre introduit les contextes scientifique et technique des milieux granulaires ainsi que leurs différentes applications. En particulier, les tambours tournants et les réacteurs à lit fixe. Dans la première application, un intérêt particulier est porté sur la dynamique des milieux granulaires dans les tambours tournants en vue d'étudier l'impact de la forme des particules celle-ci. Pour ce qui est de la deuxième application, la prise en compte de nouvelles formes de grains de catalyseur permet d'augmenter leur efficacité en augmentant le rapport surface-volume. Grâce aux simulations numériques, il est alors possible de tester plusieurs formes de particules et de calculer les pertes de charge au travers des lits de catalyseurs formés par ceux issus des sélections.

Les principaux objectifs de cette thèse sont organisés en deux volets:

- Développement d'outils numériques:
 - Extension du code Grains3D (code "Discrete Element Method" massivement parallèle pour la dynamique des milieux granulaires) pour pouvoir traiter des particules de formes non-convexes. Le modèle est basé sur la décomposition de la forme non-convexe en plusieurs formes convexes quelconques.
 - Extension du module Simulation Numérique Directe du code PeliGRIFF pour le couplage entre la phase dispersée (particules non-convexes) et le solveur des équation de Navier-Stokes en utilisant la formulation Multiplicateur de Lagrange / Domaine Fictif ("Distributed Lagrange Multipliers / Fictitious Domain").
- Utilisation des modèles implémentés pour des études physiques, telles que:
 - Vidange de silo
 - Effondrement de colonne de particules
 - Fluidisation
 - Dynamique des particules en forme de croix dans des tambours tournants
 - Effet de forme des catalyseurs sur le taux de vide dans des lits fixes
 - Effet de forme des catalyseurs sur la perte de charge au travers des lits fixes

Ces travaux de thèse ont donné lieu à quatre articles soumis ou encore à soumettre qui serviront de bases pour ce manuscrit:

- Chapitre 2: Simulation numérique d'écoulement granulaire: une revue de la littérature
- Chapitre 3: Modélisation des milieux granulaires avec Grains3D (article 1)
- Chapitre 4: Optimisation des formes des particules: simulation du taux de vide avec des particules poly-lobées (article 2)
- Chapitre 5: Grains3D: Un code DEM massivement parallèle (article 3)
- Chapitre 6: Simulation Numérique Directe: état de l'art
- Chapitre 7: Particules non-convexes avec PeliGRIFF et perte de charge dans les réacteurs à lit fixe (article 4)
- Chapitre 8: Conclusion et Perspectives

GRANULAR FLOW SIMULATION: A LITERATURE REVIEW

2

CONTENTS

1	LABORATORY SCALE EXPERIMENTS OF DRY GRANULAR FLOW	14
2	GRANULAR MEDIA MODELLING	15
2.1	Hard sphere approach	15
2.2	Soft-particle and Discrete Element Method (DEM)	15
2.3	Non-Smooth Contact Dynamics (NSCD)	16
2.4	Hybrid soft and hard sphere collision	16
2.5	Continuum Mechanics Methods (CMM)	16
2.6	Other approaches	17
3	CONTACT DETECTION ALGORITHM	17
4	DISCRETE ELEMENT METHOD WITH COMPLEX PARTICLE SHAPES	17
4.1	Importance of particle shape	18
4.2	Brief review of particle shape in literature	18
5	SYNTHESIS	22

I LABORATORY SCALE EXPERIMENTS OF DRY GRANULAR FLOW

Numerical simulations are meaningless without experimental validations. These validations allow scientists to gain confidence in their numerical tools. Therefore, numerical models can then later be used to produce more accurate predictions.

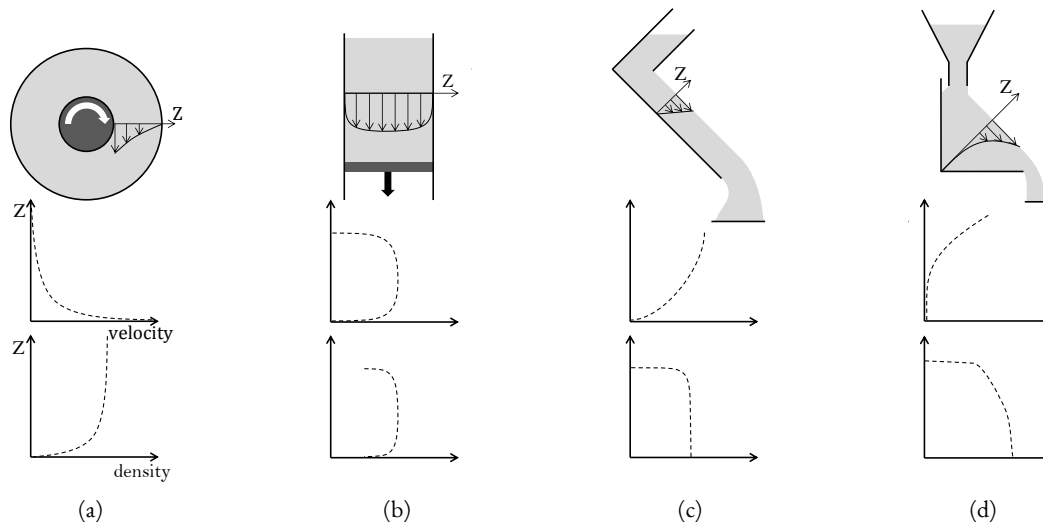


Figure 2.1 – Sketch of dense granular flows in experimental studies (Pouliquen and Chevoir (2002)). (a) Shear cell, (b) Vertical chute, (c) Inclined surface, (d) Heap formation.

Many dry granular flow configurations can be studied at the laboratory scale. Configurations presented in FIG. 2.1 are among the most studied ones. The shear cell configuration (FIG. 2.1a) is a classical case where an imposed strain rate in the form of a relative motion is applied to a collection of particles between two walls which can be either those of coaxial cylinders (Miller et al. (1996), Schöllmann (1999)), or those of parallel planes (Babic et al. (1990), Aharonov and Sparks (1999)). This type of configuration is useful in the investigation of the effect of continuous shear stress on granular materials. FIG. 2.1b shows a gravity-driven flow confined between two vertical planes or in a cylinder (Nedderman and Laohakul (1980), Nedderman and Laohakul (1980), Denniston and Li (1999)) controlled by a horizontal plan or disk with a vertical, steady and uniform motion. Since hopper discharge is a matter of interest in many fields, this configuration offers the opportunity to gain a better comprehension of phenomena which are involved in industrial facilities as e.g. mining. Flows on inclined planes (Hanes and Walton (2000), Silbert et al. (2001)) in FIG. 2.1c are common for the study of geophysical phenomena such as landslides or avalanches. This experimental set up gives a representation of how granular materials are accelerated by an inclined surface (e.g. down a hill). FIG. 2.1d exhibits a flow on a pile (Khakhar et al. (2001), Andreotti and Douady (2001)) where the slope is promoted by the flow rate which is the unique control parameter of the system.

Hypothesis 2.1 In the following sections, the study of a granular media is carried out under the following assumptions:

- attraction forces are neglected (e.g. electrostatic, capillary, van der Waals, etc.)
- particles are most of the time in contact, a packing of granular material can be considered as porous medium

2 GRANULAR MEDIA MODELLING

Far from being understood, granular media is a simple system of large number of particles of various shapes, sizes and materials (Umbanhowar (1997)). The motion of the system can be described by the classical Newton's laws of motion which are the foundation of classical Mechanics. The nature of contact depends on the type of materials and geometrical properties of particles and defines the behaviour of the granular media which can be simulated by various methods.

2.1 Hard sphere approach

Elastic collision essentially governs the hard sphere model. The state of the particles after a collision is described by the conservation of momentum (translational and angular). The collision is only reduced to the interpretation of the total kinetic energy which is converted to potential energy associated with a repulsive force between two bodies and converted back again to kinetic energy. The following hypothesis are adopted in this approach:

- Contact occurs at a single point only
- Collisions are supposed to be binary and quasi-instantaneous
- Multiple collisions are defined as a succession of binary collisions

During a collision, the energy is conserved in the elastic deformation associated to normal and tangential displacements of the contact point, then dissipated in these directions.

Before a contact, for given velocities, only three coefficients are needed to evaluate the post-collisional velocities (Herrmann and Luding (1998)):

- The coefficient of normal restitution which defines the incomplete restitution of the normal component of the relative velocity.
- The coefficient of friction which relates the tangential force to the normal force (Coulomb's law)
- The coefficient of maximum tangential restitution which delimits the restitution of tangential velocity of the contact point.

2.2 Soft-particle and Discrete Element Method (DEM)

"Soft-particle" is usually referred to the deformation of the particle during contact. In reality, this method allows a small overlap of particles during the contact. Whilst particles remain geometrically rigid, the deformation is considered in the formulation of force models. The duration of contact is finite and multiple contact may occur simultaneously.

Discrete Element Method, sometimes called Distinct Element Method has been developed over the past 30+ years. Cundall and Strack (1979) historically designed DEM for industrial process simulations of very small systems. The numerical model dealt with granular assemblies made of discs and spherical particles.

Following this work, numerous authors in different scientific communities were interested in modelling systems up to 1000 particles in two dimensions using idealised particles. Later on, DEM models have been improved in a way that complex three dimensional geometries can be treated. As the computing power increases, large scale simulations started to show an important potential. In their study, Walther and Sbalzarini (2009) presented a large-scale computation of 122 million particles using High Performance Computing to simulate a sand avalanche.

Thanks to High Performance Computing, the realism of granular simulation has been drastically improved. Therefore, large scale industrial applications can be treated such as oil and gas refining or geophysical flows. With the increase of computing power, researchers are

now able to simulate multiphase flow systems. For instance, particulate flows which are systems of particles filled with fluid in their surrounding interstices. This type of system can be simulated by coupling a Computational Fluid Dynamics code and a Discrete Element Method code (e.g. [Tsuji et al. \(1993\)](#) and [Wachs \(2011\)](#)).

Most of DEM simulations are performed using spherical particles. Nevertheless, real particles have irregular or complex shape. Spherical particles are usually used because of the easiness of its characterization. In fact, its radius is all that is needed to describe it. The contact detection is simple, it satisfies $\|G_1 G_2\| - r_1 - r_2 \leq 0$, where G and r denote respectively the centres of gravity and the radii of particle 1 and particle 2. The contact model is defined as a single point whereas for complex particles it can be several surfaces, lines or points. As a consequence, the mechanical behaviour of granular materials can be modified ([Nouguier-Lehon et al. \(2003\)](#), [Szarf et al. \(2009\)](#), [Flemmer et al. \(1993\)](#), [Escudie et al. \(2006\)](#)).

The accuracy of computations is improved by introducing a variety of contact detection algorithms for various particle shapes.

2.3 Non-Smooth Contact Dynamics (NSCD)

The Non-Smooth Contact Dynamics also called Contact Dynamics was originally resulting from the mathematical formulation of non-smooth dynamics developed by [Moreau \(1977; 1994\)](#), [Jean and Pratt \(1985\)](#), [Jean \(1995; 1999\)](#). It is also a Discrete Element Method ([Radjai and Richefeu \(2009\)](#)) dedicated for numerical simulations of granular materials. Unlike the traditional DEM soft-sphere model, the NSCD method does not use numerical schemes to resolve the small time and length scales involved in particle-particle interactions. The effects of small scales are incorporated in contact laws with a non-smooth formulation described at larger scales.

This method has been successfully applied to numerous problems, among other the works of [Radjai et al. \(1996; 1998\)](#), [Radjai and Roux \(2002\)](#), [McNamara and Herrmann \(2004\)](#), [Azéma et al. \(2007\)](#).

2.4 Hybrid soft and hard sphere collision

[Buist et al. \(2016\)](#) introduced the hybrid soft and hard sphere model. It is a novel and efficient approach to compute collisions in particulate flow systems. It takes the advantages of both the hard sphere collision model and the soft sphere model. In fact, the hard sphere model is used for binary collisions, whereas the soft sphere model is required for multi-body contacts. The hybrid model has the ability of discarding the numerical integration of the contact for all pairs of binary interactions. Hence, the model allows the use of large time step which decreases the computing time.

2.5 Continuum Mechanics Methods (CMM)

The distinctive feature of this model is that it uses an Eulerian approach for the granular behaviour ([Tüzün et al. \(1982\)](#), [Polderman et al. \(1987\)](#), [Jenike \(1987\)](#), [Drescher \(1992\)](#) and [Dziugys and Peters \(2001\)](#)). The set of continuum equations (continuum mechanics) can be used to describe the motion of granular media. In this framework, a granular media can be described as a viscoplastic “granular fluid”, a “granular gas” ([Campbell \(1990\)](#)) or a viscoelastic-plastic soil.

The equations of fluid mechanics are involved in this model. If the motion of the granular flow is rapid enough, predicting the system behaviour leads to the solution of a turbulent two-phase flow. In that case, the model becomes less accurate and very complex. Thus, this

method is suitable for particular processes only (Barker (1994)) and its results can differ from experimental data by an order of magnitude (Džiugys and Peters (2001)).

2.6 Other approaches

Other approaches exist in the literature such as:

- Geometrically steepest descent method which has been studied by Jullien and Meakin (1987)
- Quasi-static approach (Borja and Wren (1995))
- Shinbrot's model which combines CMM and DEM models (Umbanhowar (1997))

3 CONTACT DETECTION ALGORITHM

The contact resolution is very important, particularly in the investigation of multi-body system evolution over time. This has a significant number of applications such as computer graphic, computer animation, especially in 3D computer games (Palmer and Grimsdale (1995)), robotics (Gilbert and Foo (1990)) and military applications.

For large number of objects the contact detection is a major computational obstacle. In fact, the process of contact detection is divided in two phases: the neighbour search phase and the contact resolution phase. Thus, numerous authors investigated algorithms for particulate simulations (Iwai et al. (1999), Gilbert et al. (1988), Feng and Owen (2004) and King (2008)) in order to increase the accuracy of contact detection and decrease its computational cost.

4 DISCRETE ELEMENT METHOD WITH COMPLEX PARTICLE SHAPES

Granular dynamics are described in terms of Newton's laws of motion which are physical laws that laid the foundation of classical Mechanics (Newton (1687)). They are summarized as follows:

NEWTON'S LAWS OF MOTION

- **FIRST LAW:** Every body perseveres in its state of rest, or of uniform motion in a right line, unless it is compelled to change that state by forces impressed thereon
- **SECOND LAW:** The alteration of motion is ever proportional to the motive force impressed; and is made in the direction of the right line in which that force is impressed
- **THIRD LAW:** To every action there is always opposed an equal reaction: or the mutual actions of two bodies upon each other are always equal, and directed to contrary parts

Modelling difficulties arise from the consideration of particle shapes which can range from a very simple shape such as sphere in 3D or disk in 2D to very complex shapes. In fact, a continuously increasing number of studies is dedicated to non-spherical particles. In addition, contact detection requires robust and fast algorithms in order to save computing cost. Thanks

to High Performance Computing, Discrete Element Method allows the computation of large systems relevant of industrial applications such as oil and gas refining processes which are the main scope of this thesis.

4.1 Importance of particle shape

DEM simulations can provide both macroscopic and microscopic measurements in granular media, but the shape representation of particles is still a challenging aspect. Therefore, handling non-spherical particle shape in DEM simulations is not straightforward. Contact detection algorithm are very rarely valid for any shapes. Many authors designed advanced strategies to compute contacts between various types of shape but most of these strategies are only suitable for a single specific shape such as cubes (Fraige et al. (2008)), ellipsoids (Džiugys and Peters (2001)). Super-quadrics offer a first level of versatility as many shape can be approached by varying coefficients in the generalised quadric equation (Cleary (2010)).

Traditionally, particles shape is approximated by a sphere in 3D and a disc in 2D. The shape plays a significant role in Discrete Element Method simulations since neither a sphere nor a disc approximation can always reproduce the real behaviour of granular assemblies. The major differences between real and approximated particle shapes are: resistance to shear stress and failure, volume of revolution, realistic void fraction and energy partition.

Intuitively, it is easy to figure out how the force is oriented when two circular particles collide. In fact, the normal force is directed along the line of both centres and no torque is generated. Whereas for non-circular particles, if the normal force is not directed toward the centre of mass, a torque is generated (see FIG. 2.2).

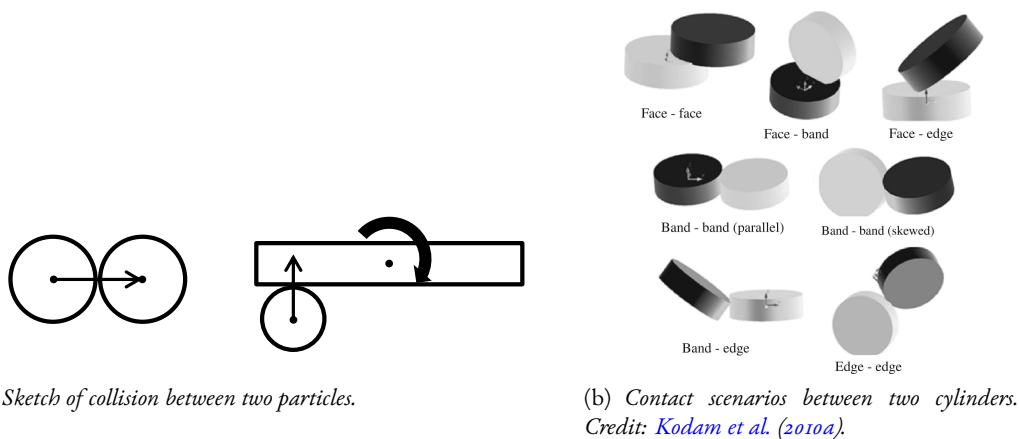


Figure 2.2 – Decomposition of trilobal and quadralobal particle shapes into convex shapes. View of the cross sections.

4.2 Brief review of particle shape in literature

Ellipse/Ellipsoid

One of the simplest representation of non-spherical shape is an ellipsoid in 3D and ellipse in 2D. The algebraic and parametric form of an ellipsoid is expressed as follows:

$$\left(\frac{x}{a}\right)^2 + \left(\frac{y}{b}\right)^2 + \left(\frac{z}{c}\right)^2 = 1 \quad (2.1)$$

$$x = a \cos \theta \cos \vartheta, \quad y = b \cos \theta \sin \vartheta, \quad z = c \sin \theta \quad (2.2)$$

Where x, y, z are the coordinates in the fixed-body reference system, whereas a, b, c are the half length of the principal axes of the shape, $\theta \in [-\pi/2; \pi/2]$ and $\vartheta \in [-\pi; \pi]$ are the parametric representation of the particle.

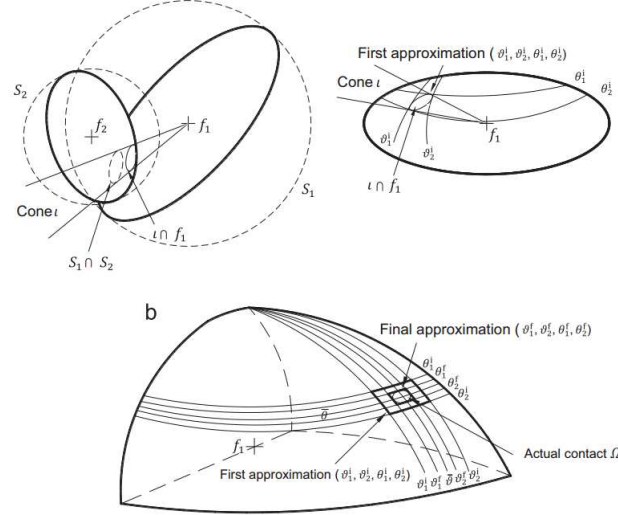


Figure 2.3 – Contact approximation between two ellipsoids using a curvilinear region defined by pairs of θ - and ϑ -curves: (a) first approximation and (b) final approximation. Credit: Lu et al. (2015) (adapted from Rothenburg and Bathurst (1991)).

The contact detection algorithm relies on the determination of the intersection point between two ellipses in 2D (Rothenburg and Bathurst (1991)) and two ellipsoids in 3D (Oudafel and Rothenburg (1999)). The contact resolution procedure in 3D is illustrated in FIG. 2.3.

Super-quadrics

The so-called *super-quadric* equation allows the representation of both convex and non-convex shapes and was suggested by Barr (1981) and later on adopted in Discrete Element Method by Williams and Pentland (1992). The algebraic and the parametric forms are expressed as:

$$f(x, y, z) = \left(\left(\frac{x}{a} \right)^{\frac{2}{\varepsilon_2}} + \left(\frac{y}{b} \right)^{\frac{2}{\varepsilon_2}} \right)^{\frac{\varepsilon_2}{\varepsilon_1}} + \left(\frac{z}{c} \right)^{\frac{2}{\varepsilon_1}} - 1 \quad (2.3)$$

$$x = a(\sin \theta)^{\varepsilon_1}(\cos \vartheta)^{\varepsilon_2}, \quad y = b(\sin \theta)^{\varepsilon_1}(\sin \vartheta)^{\varepsilon_2}, \quad z = c(\cos \vartheta)^{\varepsilon_1} \quad (2.4)$$

where a, b, c denote the half length of the principal axes of the shape, and ε_1 and ε_2 are the parameters which control the “blockiness” of the particle. ε_1 controls the blockiness of the cross-sectional planes yOz and yOz , whereas ε_2 controls that of the cross-sectional plane in xOy . When $\varepsilon_1 = \varepsilon_2 = 1$ the equation of the super-quadric EQ. 2.3 is equal to that of the ellipsoids (EQ. 2.1). $\theta \in [-\pi/2; \pi/2]$ and $\vartheta \in [-\pi; \pi]$ are the parametric representations of both super-quadric and ellipsoid.

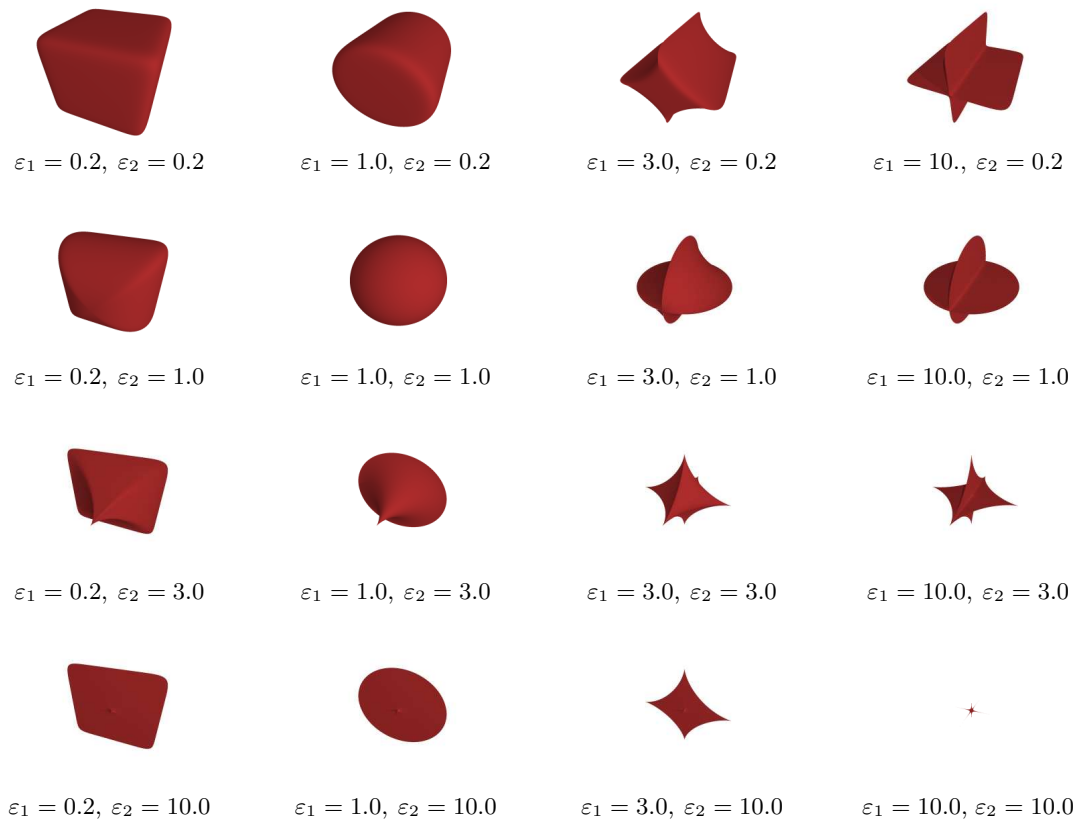


Figure 2.4 – Examples of 3D super-quadrics. Credit: [Lu et al. \(2015\)](#).

Polygons and Polyhedrons

Since ellipsoidal and super-quadric shapes do not always represent all particles found in nature and industry, many authors oriented their research in the exploration of polygonal and polyhedral shapes (e.g. [Hart et al. \(1988\)](#) and [Lee et al. \(2009\)](#)). While new shapes are designed, new corresponding contact algorithms are required. Polygons in 2D and polyhedra in 3D are such shapes that ellipsoids can not represent and super-quadrics can only but asymptotically. For instance, the contact detection algorithm is quite straightforward in 2D. In fact, the contact detection algorithm relies on the number of edges of the polygon. The computational cost scales with $N_i \times N_j$ where N_i and N_j are the numbers of vertices of the colliding particles i and j .

In 3D, the contact resolution can be very complex. In fact, the contact detection algorithm requires some complex combinations of elements such as vertex-vertex, vertex-edge, vertex-face, edge-edge, edge-face and face-face. The computational efficiency of the contact detection algorithms of polygonal/polyhedral particles is improved by introducing the so-called "Common Plane" algorithm developed by [Cundall \(1988\)](#).

Definition 2.1 *A common is a plane that, in some sense, bisects the space between the two contacting particles.* [Cundall \(1988\)](#)

[G. Nezami et al. \(2006\)](#) demonstrated the uniqueness of the Common Plane for any couple of two convex particles and the perpendicularity of the contact normal to the CP.

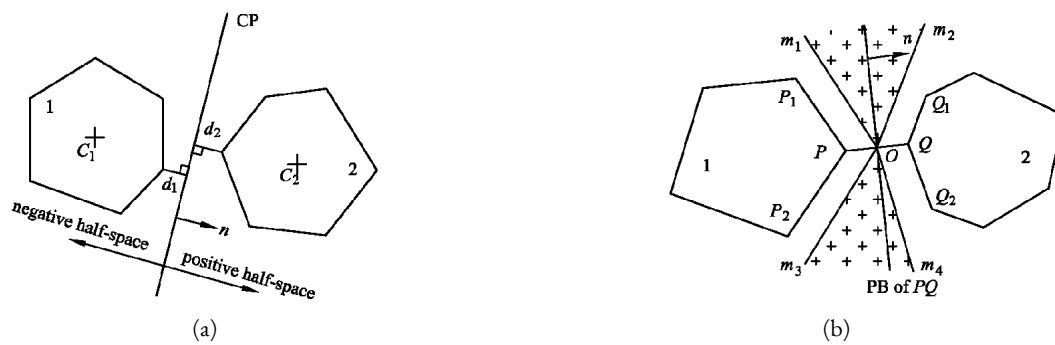
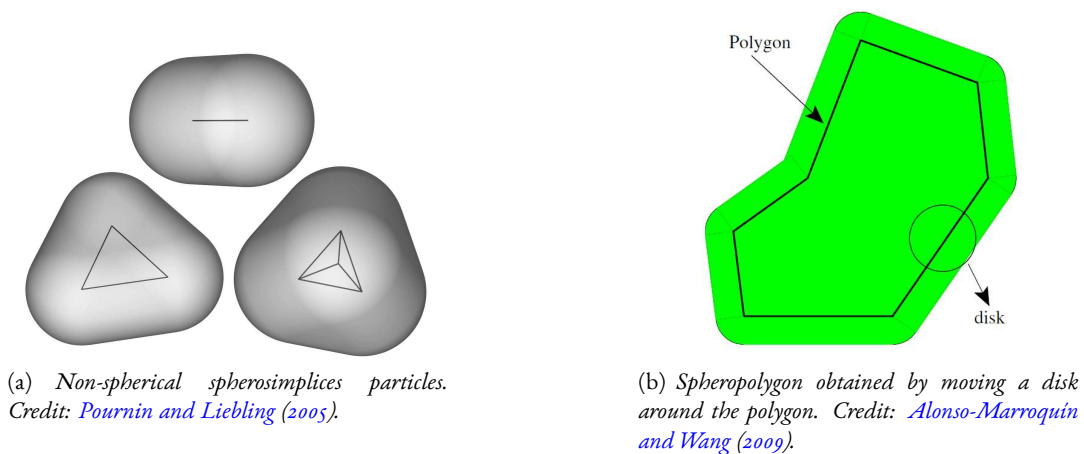


Figure 2.5 – Illustration of the common plane technique between two colliding polygons. (a) Definition of the common plane, (b) Five probable planes for the common plane all pass through the mid-point O of the linear section PQ (P and Q are the “closest vertices” of polygon 1 and 2). They are the plane which is perpendicular to the linear section PQ , and the planes that are parallel to the polygon edge PP_1 , PP_2 , QQ_1 and QQ_2 where P_1 and P_2 are the vertices of particle 1 next to P and Q_2 and Q_1 are the vertices of particle 2 next to Q . Credit: [Lu et al. \(2015\)](#) (adapted from [Nezami et al. \(2004\)](#)).

Spherosimplices

The modelling of non-spherical particles using the so-called “*spherosimplices*” has received a particular interest over the last decade (e.g. [Pournin and Liebling \(2005\)](#) and [Alonso-Marroquín and Wang \(2009\)](#)). A *spherosimplices*-shaped particle is a combination of a skeleton (e.g. a point, a linear segment, a polygon or a polyhedron) and a disk or a sphere (e.g. FIG. 2.6)



(a) Non-spherical *spherosimplices* particles. Credit: [Pournin and Liebling \(2005\)](#).

(b) Spheropolygon obtained by moving a disk around the polygon. Credit: [Alonso-Marroquín and Wang \(2009\)](#).

Figure 2.6 – Various *spherosimplices* particle shapes.

Composite particles made of multiple spheres

Particles composed of multiple spheres are often called “*glued spheres*” (FIG. 2.7) in the literature, referring to the fact that spherical particles are glued together to build the composite shape. This method is quite popular in the DEM community (e.g. [Nolan and Kavanagh \(1995\)](#), [Kruggel-Emden et al. \(2008\)](#)).

One of the advantages of this method is its ability to reproduce a given shape with a loose approximation by “gluing” many spherical particles together. Therefore, a fast and robust contact detection algorithm for spheres can be applied to the particle. Nonetheless, a very

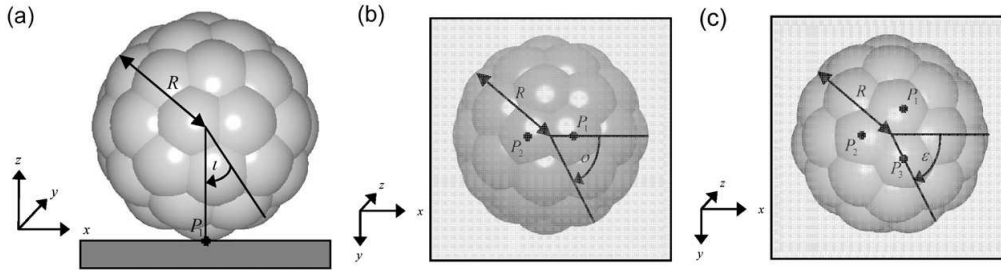


Figure 2.7 – Multi-sphere particle impacting a flat wall. (a) single contact, (b) double contact and (c) a triple contact. Credit: Kruggel-Emden et al. (2008).

large number of spheres has to be glued to reach a high definition of surface smoothness which increases the computational cost of the method.

The particularity of this method is that, if required, the primary spheres can also overlap with each other. Such a built particle is governed by rigid-body motion so that the relative positions of the components do not change during collisions. The forces and torques acting on primary spheres are summed relatively to the centre of mass of the composite particle and are subsequently used to calculate its trajectories (Favier et al. (1999)).

5 SYNTHESIS

Since almost any non-convex particle can be decomposed into a set of arbitrary convex particles, none of the previous strategies is suitable for the goal of this study. In fact, the closest method would be the *glued spheres* method but regardless of the computation cost. Another option would be the use of *super-quadrics* but the range of parameters of their equation does not allow the access of the targeted shapes of this study. The other methods do not fall in line with the scope of the present study. Based on these observations, it is concluded that the best strategy and suitable for modelling granular media of non-convex particles, at least at the current state of the granular code Grains3D, is the decomposition of a non-convex particle into a set of arbitrary convex bodies. The model is called “*glued convex*” and is introduced in the next chapter.

RÉSUMÉ

Ce chapitre comprend une revue détaillée de la littérature sur la modélisation des milieux granulaires de particules de formes complexes. Différentes approches sont alors exposées ainsi que la complexité de la détection de contacts entre deux objets. En premier lieu, le modèle de sphère dure est présenté avec ses avantages et ses inconvénients. En second lieu, la combinaison modèle de sphère molle et méthode des éléments discrets (DEM) qui est couramment utilisée dans la littérature. Ensuite, le modèle “Non-Smooth Contact Dynamics (NSCD)” et le modèle hybride sphère molle et sphère dure. Et enfin, quelques modèles qui sont moins utilisés que ceux cités précédemment tels que la méthode des milieux continus ou l’approche quasi-statique ou encore le modèle de Shinbrot.

La détection de contact est un problème à part entière car elle est souvent dépendante de la forme étudiée. En effet, pour certaines formes de particules, le contact peut se résoudre analytiquement tandis que pour d’autres formes elle nécessite des algorithmes puissants. Dans ce chapitre, quelques formes courantes sont introduites avec les méthodes de résolution des contacts associées.

Cette revue de littérature a permis de mettre en évidence que les modèles existants dans la littérature sont inadéquats pour les problèmes qui font l’objet de cette thèse. D’où la proposition du nouveau modèle nommé *glued convex* (“convexes collés”).

NON-CONVEX GRANULAR MEDIA MODELLING WITH GRAINS₃D

3

CONTENTS

1	INTRODUCTION	26
2	NEW GLUED CONVEX METHOD	27
2.1	Equations of motion	28
2.2	Strategy	29
2.3	Mass properties	29
2.4	Time integration	30
2.5	GJK-based contact detection	31
2.6	Contact force and torque	32
3	VALIDATION TESTS	36
3.1	Methodology	36
3.2	Normal cylinder-wall impact	36
4	RESULTS	41
4.1	Packing porosity	41
4.2	Rotating drum	45
5	CONCLUSION AND DISCUSSION	52

This chapter has been submitted for publication in *Powder Technology*:

A. D. Rakotonirina, A. Wachs, J.-Y. Delenne, F. Radjai. Grains₃D, a flexible DEM approach for particles of arbitrary convex shape - Part III: extension to non-convex particles.

In this paper, the “*glued convex*” method is presented to model non-convex particle shape with validation cases. Then we used the model to explore the effect of particle shapes on packing porosity and on flow regimes in rotating drum with 2D- and 3D-crosses.

ABSTRACT

Large-scale simulation using the Discrete Element Method (DEM) is a matter of interest as it allows to improve our understanding of the flow dynamics of granular flows involved in many industrial processes and the environment flows. In industry, it leads to an improved design and an overall optimisation of the corresponding equipment and process. Most of DEM simulations in the literature have been performed using spherical particles. Very few studies dealt with non-spherical particles, even less with non-convex ones. Even spherical or convex bodies do not always represent the real shape of certain particles. In fact, more complex shaped particles are found in many industrial applications as, e.g., catalytic pellets in chemical reactors. Their shape influences markedly the behaviour of these systems. The aim of this study is to go one step further into the understanding of the flow dynamics of granular media made of non-convex particles. Our strategy is based on decomposing a non-convex shaped particle into a set of convex bodies, called elementary components. The novel method is called “glued convex” method, as an extension of the popular “glued spheres” method. At the level of elementary components of a “glued convex” particle, we employ the same contact detection strategy based on a Gilbert-Johnson-Keerthi algorithm and a linked-cell spatial sorting that accelerates the resolution of the contact. The new “glued convex” model is implemented as an extension of our in-house high fidelity code Grains3D that already supplies accurate solutions for arbitrary convex particles. The extension to non-convex particles are illustrated on the filling of catalytic reactors and the flow dynamics in a rotating drum.

1 INTRODUCTION

Discrete Element Method was originally designed to handle spherical particles. The method is now able to deal with more complex particle shapes (Cundall (1988), Hart et al. (1988), Wachs et al. (2012)). Thanks to its conceptual simplicity this method is widely used in granular media modelling. Its computational implementation is very straightforward for spheres but is quite difficult for complex particle shapes. Many approaches have been investigated since the late 80's, among them the works of Cundall (1988) and Hart et al. (1988). They studied a system composed of polyhedral blocks and used a robust and rapid technique (Common Plane technique) to detect and to categorise contacts between two polyhedral blocks. Later on, many authors worked on the extension of DEM to non-spherical particles. For example, Munjiza et al. (2009) constructed a poly-ellipsoid particle by “gluing” ellipsoids together. One of the most famous extensions of DEM is the “glued spheres” model in which a complex shape is approximated by “gluing” spherical particles. For instance, Nolan and Kavanagh (1995) used this approximation to study the random close packings of cylindrical-, bean- and nail-shaped particles. They found good agreement between their simulations and experimental data. Song et al. (2006) used this approach to study the contact criteria for tablet-flat surface and tablet-tablet contact. At first sight, this method seems to be well adapted to any shape. Nonetheless, the higher the number of spheres is the less efficient the computation becomes as Song et al. (2006) demonstrated. Li et al. (2004) modelled sphero-disc particles to study the flow behaviour, the arching and discharging in a hopper. Another extension of Discrete Element Method to polygonal shaped particles was suggested by Hart et al. (1988), Feng and Owen (2004) and polyhedral shaped particles (Fraige et al. (2008), Lee et al. (2009)). These new features enabled research groups to address several problems in the field of geophysics (Hentz et al. (2004), Jing (1998), Camborde et al. (2000)).

Available strategies in the literature to handle complex shapes were already reviewed in de-

tail in [Wachs et al. \(2012\)](#). We simply give here again a short overview. [Williams and O'Connor \(1995\)](#) introduced the Discrete Function Representation of a particle shape to address contact resolution. DPR is applicable to convex geometries and to a restricted set of concave geometries. [Williams and Pentland \(1992\)](#) explored the critical influence of particle shape on granular dynamics and suggested super-quadric particles for geophysical applications. This method allows the design of particles with rounded edges such as ellipsoid, blocks, or tablets by introducing a continuous function ($f(x, y, z) = (x/a)^m + (y/b)^m + (z/c)^m - 1 = 0$) that defines the geometry of the object. The weakness of this method relies on the handling of contact detection. In fact, the more the edge angularity increases the more the discretisation needs points to discretise $f(x, y, z)$. Therefore, computational cost of the contact detection increases with edge (or shape) angularity. A probability-based contact algorithm is presented in the work of [Jin et al. \(2011\)](#): contacts between non-spherical particles are translated into those between spherical particles with probability. [Alonso-Marroquín and Wang \(2009\)](#) presented a method to simulate two-dimensional granular materials with spheropolygon shaped particles. The particle shape is represented by the classical concept of a Minkowski sum ([Bekker and Roerdink \(2001\)](#)), which permits the representation of complex shapes without the need to define the object as a composite of spherical or convex particles. Hence, this approach has proven to be much better than the glued spheres method. The modelling of non-spherical particles using the so-called “spherosimplices” has received a particular interest over the last decade ([Alonso-Marroquín and Wang \(2009\)](#), [Pournin and Liebling \(2005\)](#)). A *spherosimplex*-shaped particle is combination of a skeleton (e.g. a point, a linear segment, a polygon or a polyhedron) and a disk or a sphere.

Contact resolution is a core component of DEM simulations. A proper contact resolution ensures accurate DEM computed solutions. The Gilbert-Johnson-Keerthi (GJK) algorithm ([Bergen \(1999\)](#), [Gilbert et al. \(1988\)](#)) is a good candidate for this particular problem and well suited for arbitrary convex shaped particles. This algorithm was first introduced by [Petit et al. \(2001\)](#) and later generalized by [Wachs et al. \(2012\)](#) to study the effect of non-spherical particle shape in granular flows. The GJK algorithm is an iterative approach to compute the euclidean minimal distance between two convex objects. The GJK reduces the problem of finding the minimal distance between two convex bodies to finding the minimal distance between their Minkowski difference and the origin ([Gilbert et al. \(1988\)](#)).

Beyond the problem of contact detection, modelling difficulties related to multiple contact handling for complex shaped particles also require to be addressed. In the existing literature on this problem, [Abbaspour-Fard \(2004\)](#) pointed out the validity of a multi-sphere model in various phenomena such as sliding, dropping and conveying, while [Kruggel-Emden et al. \(2008\)](#) studied the macroscopic collision properties of the glued sphere model and compared them to experimental results. In their study, the total contact force of a multi-sphere particle impacting a flat wall is treated by computing the mean of the forces at each contact point. Later on [Höhner et al. \(2011\)](#) pointed out that this method is not accurate enough. They showed that there is a non-negligible effect of the particle shape approximation (artificial roughness created by gluing spheres) on the force temporal evolution in normal and tangential directions.

2 NEW GLUED CONVEX METHOD

The aim of this study is to introduce a novel variant of Discrete Element Method able to deal with non-convex particle shapes and to use it to simulate the flow dynamics of granular media. The strategy is based on decomposing a non-convex particle, called the composite, into a set of convex bodies, called elementary components. This approach, called “glued con-

vex”, is inspired by the glued spheres method introduced by [Nolan and Kavanagh \(1995\)](#). Our glued convex method is implemented in our in-house granular solver Grains3D ([Wachs et al. \(2012\)](#)). This enable us to use existing methods, models and algorithms already implemented in Grains3D such as time integration of equations of motion, quaternions for body rotation, linked-cell spatial sorting and the Gilbert-Johnson-Keerthi algorithm for collision detection ([Gilbert et al. \(1988\)](#), [Gilbert and Foo \(1990\)](#)). In particular, the GJK algorithm is applied to elementary components. A contact between a glued convex particle, i.e., a composite, and another glued convex particle, i.e., another composite is detected if at least one elementary component of the former contacts with one elementary component of the latter.

A two dimensional illustration is presented in [FIG. 3.1](#).

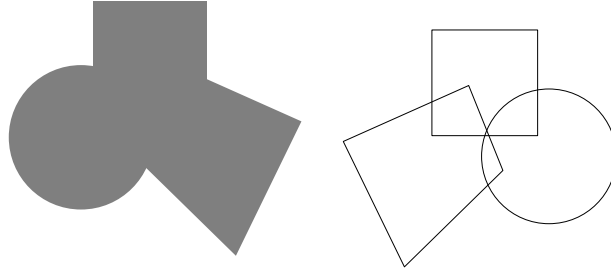


Figure 3.1 – 2D illustration of the decomposition of a non-convex particle into a set of elementary convex components.

2.1 Equations of motion

The dynamics of a granular material made of (non-convex) particles is entirely governed by Newton’s law ([Newton \(1687\)](#)). Assuming that N bodies make up the granular system is made of N particles, the complete set of equations which governs the flow dynamics is:

$$M_i \frac{d\mathbf{U}_i}{dt} = \mathbf{F}_i \quad (3.1)$$

$$\mathbf{J}_i \frac{d\boldsymbol{\omega}_i}{dt} + \boldsymbol{\omega}_i \wedge \mathbf{J}_i \boldsymbol{\omega}_i = \mathbf{M}_i \quad (3.2)$$

$$\frac{d\mathbf{x}_i}{dt} = \mathbf{U}_i \quad (3.3)$$

$$\frac{d\boldsymbol{\theta}_i}{dt} = \boldsymbol{\omega}_i \quad (3.4)$$

where M_i , \mathbf{J}_i , \mathbf{x}_i and $\boldsymbol{\theta}_i$ denote the mass, moment of inertia tensor, position of the centre of mass and angular position of particle i , $i \in [0, N - 1]$. The translational velocity vector \mathbf{U}_i and the angular velocity vector $\boldsymbol{\omega}_i$ of the centre of mass are involved in the decomposition of the velocity vector as $\mathbf{v}_i = \mathbf{U}_i + \boldsymbol{\omega}_i \wedge \mathbf{R}_i$, where \mathbf{R}_i denotes the position vector with respect to the centre of mass of a particle i . \mathbf{F}_i and \mathbf{M}_i stand for the sum of all forces and torques applied on particle i . They are defined as follow:

$$\mathbf{F}_i = M_i \mathbf{g} + \sum_{j=0, j \neq i}^{N-1} \mathbf{F}_{ij} \quad (3.5)$$

$$\mathbf{M}_i = \sum_{j=0, j \neq i}^{N-1} \mathbf{R}_j \wedge \mathbf{F}_{ij} \quad (3.6)$$

\mathbf{R}_j denotes a vector which points from the centre of mass of the particle i to the contact point with particle j . It is assumed that all particles are subjected to gravity and contact forces only.

2.2 Strategy

It is important to show the strategy adopted in the present work which allows the computation of granular flow made of non-convex particles. Our strategy is based on the following general steps:

- Apply the Newton's second law on a non-convex particle
- Compute the translational and angular velocities of its centre of mass
- Compute the position and angular positions of its centre of mass
- Derive the positions and velocities of each convex component from that of the composite particle taking into account their relative positions
- Due to the decomposition of a non-convex body into a set of convex particles, the contact forces are computed at the level of the elementary particles

Considering two reference frames \mathcal{R} and \mathcal{R}' , where \mathcal{R} is that of the space-fixed coordinates system which does not depend on the particle configuration and \mathcal{R}' is that of the particle and fixed at its centre of mass, these steps are summarized in the following set of equations after the computation of momentum equations EQ. 3.1 and EQ. 3.2:

- Setting the centre of mass \mathbf{r}_i of the convex component i according to the reference frame \mathcal{R} .
- Evaluating the centre of mass of the non-convex object \mathbf{r}_g and deriving the position of the component i according to the reference frame \mathcal{R}' as $\mathbf{r}'_i = \mathbf{r}_i - \mathbf{r}_g$
- Computing the rotation matrix derived from the convex elementary particles:

$$\mathcal{M}_i = \mathcal{M} \cdot \mathcal{M}_i^0 \quad (3.7)$$

\mathcal{M}_i is the matrix of rotation of the convex component i , \mathcal{M} is that of the composite particle and \mathcal{M}_i^0 is the initial matrix of rotation of the component i .

- Translating the component i using a displacement vector \mathbf{d}_i defined as:

$$\mathbf{d}_i = (\mathcal{M} \cdot \mathbf{r}'_i) - \mathbf{r}_i \quad (3.8)$$

- Computing the velocity

$$\mathbf{U}_i = \mathbf{U} + \boldsymbol{\omega} \wedge (\mathcal{M} \cdot \mathbf{r}'_i) \quad (3.9)$$

$$\boldsymbol{\omega}_i = \boldsymbol{\omega} \quad (3.10)$$

where \mathbf{U} and $\boldsymbol{\omega}$ denote respectively the translational and rotational velocities of the non-convex particle.

2.3 Mass properties

One of the challenges encountered with a non-convex particle shape is the computation of its mass properties (volume, centre of mass and components of moment of inertia tensor). In fact, the numerical integration of the volume sums involves the use of Boolean Algebra with

solids since our non-convex particles are made of arbitrary convex shaped components which can overlap each other. This requires either to rely on an appropriate library such as the Computational Geometry Algorithms Library (Doe (2009)) or to implement an algorithm which provides an accurate approximation of the various volume sums corresponding to the particle mass properties. The latter option is used since it has a good compromise between accuracy and low complexity. Inspired by Monte-Carlo algorithms and the work of Alonso-Marroquín and Wang (2009), we carry out a numerical integration based on a pixelated particle. For the volume approximation, it consist in:

- defining a box which circumscribes the shape (FIG. 3.2),
- uniformly discretising the box in the three directions,
- finding if the points \mathbf{X}_i , centre of the cells are either inside or outside the shape,
- summing up the volumes of all the cells that are found inside the shape to get the approximated volume.

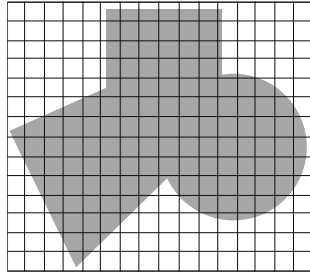


Figure 3.2 – Discretisation strategy illustrated in 2D.

The centre of mass is then defined as follow:

$$\mathbf{X}_g = \frac{1}{V} \sum_{i=0}^N \mathbf{X}_i v_i \quad (3.11)$$

where \mathbf{X}_g denotes the vector position of the centre of mass, V is the approximated volume of the non-convex object, \mathbf{X}_i is the centre of the cell i and v_i its volume. Using the same approximation method it is easy to compute the components of the moment of inertia tensor which can be expressed as follows:

$$J_{k,l} = \sum_{i=0}^N f_{kl}(\mathbf{X}_i) v_i \quad \text{for } k, l = 1, 2, 3 \quad (3.12)$$

FIG. 3.3 shows clearly the grid convergence of the algorithm applied to the calculation of the volume of a sphere, a cylinder and two overlapping cylinders. The approximated volume and the relative error between the two volumes is plotted as a function of the number of discretisation points per direction. The error decreases in a relatively monotone way as the number of discretisation points per direction increases.

In this study, all the DEM simulations of glued convex shaped particles are performed with at least 500 grid points per direction to ensure correct results on the approximation of mass properties.

2.4 Time integration

Džugys and Peters (2001) carried out a full survey on the most popular integration schemes used in DEM simulations. This survey revealed that at least a second-order accurate in time

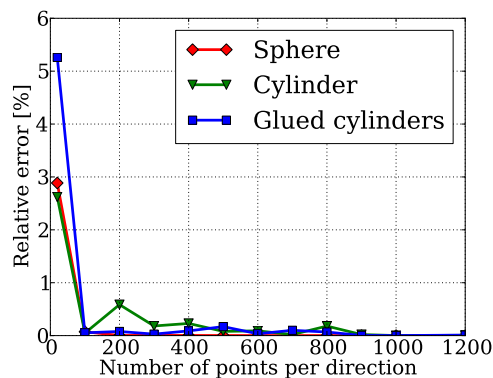


Figure 3.3 – Convergence of the relative error on the volume of a sphere, a cylinder and a glued convex made of two overlapping cylinders.

scheme is required to properly predict the time evolution of the granular system. Our study uses the same DEM code as the one used by [Wachs et al. \(2012\)](#). Hence, the time integration is performed with a second-order leap-frog Verlet scheme ([Langston et al. \(1994; 1995\)](#)):

$$\begin{aligned} \mathbf{U} \left(t + \frac{\Delta t}{2} \right) &= \mathbf{U} \left(t - \frac{\Delta t}{2} \right) + \frac{\mathbf{F}(t)}{M} \Delta t \\ \mathbf{x}(t + \Delta t) &= \mathbf{x}(t) + \mathbf{U} \left(t + \frac{\Delta t}{2} \right) \Delta t \end{aligned} \quad (3.13)$$

2.5 GJK-based contact detection

[Gilbert et al. \(1988\)](#) introduced the Gilbert-Johnson-Keerthi algorithm to compute the distance between two convex polyhedra. In 1990, the algorithm was improved by [Gilbert and Foo \(1990\)](#) to deal with general convex objects. Since each elementary component of a non-convex particle is a convex object, the Gilbert-Johnson-Keerthi algorithm can be applied to each elementary component to detect a potential collision with any other elementary component of a neighbouring non-convex particle. For further details on the use of Gilbert-Johnson-Keerthi algorithm for arbitrary convex shaped particles, the interested reader is referred to the work of [Wachs et al. \(2012\)](#).

By means of linked-cell spatial sorting ([Grest et al. \(1989\)](#)) for proximity detection, our GJK-based collision detection strategy can be summarized as follows:

- Use linked-cells to find pairs of particles (P_i, P_j) that potentially interact,
- For each pair that potentially interact, apply the Gilbert-Johnson-Keerthi distance algorithm to compute the minimal distance between all pairs (E_k, E_l) of elementary components where E_k is an elementary component of particle P_i and E_l is an elementary component of particle P_j . The computing time of contact detection between two non-convex particles scales as $N_i \times N_j$ where N_i and N_j are the number of elementary components of particle P_i and particle P_j , respectively.
- the pairs (E_k, E_l) in contact contribute to the total contact force and torque ([Wachs et al. \(2012\)](#)).

As pointed out in [Wachs et al. \(2012\)](#), the GJK algorithm applied right away to convex shapes is helpful to tell whether two convex shapes touch or not (if they do touch, the minimal distance between them is 0) but does not supply information on the contact features as contact point, overlap distance and unit normal vector at the point of contact. To access to

this information, we suggest in [Wachs et al. \(2012\)](#) a 3-step procedure. This 3-step procedure for contact resolution is illustrated in [FIG. 3.4](#) and summarized below as follows:

- Apply an homothety \mathcal{H} to the pairs of convex elementary components ($E_k = A, E_l = B$) to slightly shrink them (by a thickness r_A and r_B respectively), such they do not overlap ([Wachs et al. \(2012\)](#)),
- Compute the minimal distance between the two shrunk objects A and B ,
- Based on the information provided by the GJK algorithm, reconstruct the contact features as:

$$\delta = d(\mathcal{H}_A(A), \mathcal{H}_B(B)) - C_{\mathcal{H}_A(A)} - C_{\mathcal{H}_B(B)} \quad (3.14)$$

$$C = \frac{C_A + C_B}{2} \quad (3.15)$$

$$\mathbf{n}_C = \frac{C_B - C_A}{\|C_B - C_A\|} \quad (3.16)$$

where δ is the overlap distance, C the contact point and \mathbf{n}_C the unit normal vector.

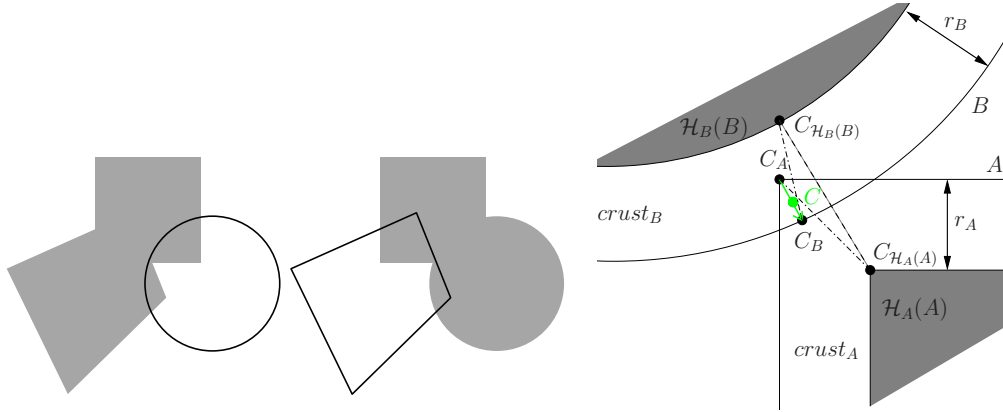


Figure 3.4 – Contact handling scenario between non-convex particles.

Contact is assumed to occur if $\delta \leq 0$. For more detail about our contact detection resolution method, the interested reader is referred to [Wachs et al. \(2012\)](#).

2.6 Contact force and torque

The total contact force between two non-convex composite particles is calculating as a mean contact force over all their contact points. In other words, the total contact force is the sum of all forces resulting from contacts between two elementary components of the two non-convex composite particles divided by the total number of contact points. Same applies to the total torque where we pay a particular attention of using the right leverages (leverage calculated with respect to the centre of mass of the non-convex composite particle, not the center of mass of the elementary component).

[Džiugys and Peters \(2001\)](#) reviewed the most popular contact force models in the literature. In this work, we follow [Wachs et al. \(2012\)](#) and employ a simple contact force model in which The total collision force \mathbf{F}_{ij} between two particles i and j acting on the contact surface is:

$$\mathbf{F}_{ij} = \mathbf{F}_{ij,el} + \mathbf{F}_{ij,dn} + \mathbf{F}_{ij,t} \quad (3.17)$$

The three components contributed to the total force have the following meaning and expression:

- The normal Hookean elastic restoring force reads:

$$\mathbf{F}_{ij,el} = k_n \delta_{ij} \mathbf{n}_c \quad (3.18)$$

where k_n is a spring stiffness constant. In theory, k_n can be related to material properties and contact geometry, but in DEM simulations it is essentially a numerical parameter that controls the amount of overlap between particles. δ_{ij} denotes the overlap distance between particles i and j and \mathbf{n}_c the unit normal vector at the contact point.

- The normal dissipative (viscous-like) force reads:

$$\begin{aligned} \mathbf{F}_{ij,dn} &= -2\gamma_n m_{ij} \mathbf{U}_{rn} \\ \text{where } m_{ij} &= \frac{M_i M_j}{M_i + M_j} \end{aligned} \quad (3.19)$$

where γ_n is the normal dissipation coefficient and m_{ij} the reduced mass of particles i and j . \mathbf{U}_{rn} denotes the normal relative velocity between both particles.

- The tangential friction force reads as follows:

$$\mathbf{F}_{ij,t} = -\min\{\mu_c |\mathbf{F}_{el}|, |\mathbf{F}_{dt}|\} \mathbf{t}_c \quad (3.20)$$

$$\mathbf{F}_{dt} = -2\gamma_t m_{ij} \mathbf{U}_{rt} \quad (3.21)$$

\mathbf{F}_{dt} denotes the dissipative frictional contribution, γ_t the dissipative tangential friction coefficient, \mathbf{U}_{rt} the tangential relative velocity between both particles and \mathbf{t}_c the unit tangential vector at the contact surface.

DEM parameters for convex particles

Let us consider a sphere-sphere normal collision at zero gravity and a relative colliding velocity v_0 . Assuming the two spheres have the same radius R , the equation of time evolution of the penetration depth δ during the collision reads as follows:

$$\frac{d^2\delta}{dt^2} + 2\gamma_n \frac{d\delta}{dt} + \omega_0^2 \delta = 0, \quad \delta(t=0) = 0, \quad \frac{d\delta}{dt}(t=0) = v_0 \quad (3.22)$$

The starting time of contact is assumed to be $t = 0$. $\omega_0^2 = \frac{2k_n}{M}$, where M denotes the mass of each particle. Hence,

$$\delta(t) = \frac{v_0}{\sqrt{\omega_0^2 - \gamma_n^2}} e^{-\gamma_n t} \sin\left(\sqrt{\omega_0^2 - \gamma_n^2} t\right) \quad (3.23)$$

The equation EQ. 3.23 leads to the contact duration:

$$T_c = \frac{\pi}{\sqrt{\omega_0^2 - \gamma_n^2}} \quad (3.24)$$

According to Ristow (1996), for DEM simulations, the time step needs to be less than $T_c/10$ to properly integrate each contact.

The time of maximum overlap is:

$$T_{max} = \frac{1}{\sqrt{\omega_0^2 - \gamma_n^2}} \arctan\left(\frac{\sqrt{\omega_0^2 - \gamma_n^2}}{\gamma_n}\right) \quad (3.25)$$

which gives the maximum penetration depth $\delta_{max} = \delta(t = T_{max})$.

The coefficient of restitution e_n is defined as the ratio of both post-collisional and pre-collisional velocities.

$$e_n = \left| \frac{d\delta(t = T_c)}{dt} \right|_{v_0} = e^{-\gamma_n T_c} = e^{-\gamma_n \frac{\pi}{\sqrt{\omega^2 - \gamma_n^2}}} \quad (3.26)$$

If e_n is given with k_n , the damping coefficient γ_n can be deduced from EQ. 3.26:

$$\gamma_n = -\frac{\omega_0 \ln e_n}{\sqrt{\pi^2 + (\ln e_n)^2}} \quad (3.27)$$

Particle-wall and particle-particle interactions

Since particles have a non-convex shape, contacts can occur at several points. According to Kruggel-Emden et al. (2008), forces and torques acting on a composite particle and involved in the resolution of equations EQ. 3.1, EQ. 3.2, EQ. 3.3 and EQ. 3.4 can be computed as follow:

$$\mathbf{F}_i = \sum_{j=1}^M \sum_{l=1}^N (\mathbf{F}_{ijl} / a_{ijl}) \quad (3.28)$$

$$\mathbf{M}_i = \sum_{j=1}^M \sum_{l=1}^N \mathbf{R}_i \wedge \mathbf{F}_{i,t} / a_{ijl} \quad (3.29)$$

Where \mathbf{F}_{ijl} denotes the force created between objects i and j at the contact point l and a_{ijl} refers to the number of contact points during interaction.

Höhner et al. (2011) suggested to compute the forces incrementally since the number of contacts can vary during a collision. Their formulation is expressed as follows:

$$\begin{aligned} F_i^n = F_{i,el}^n + F_{i,dn}^n &= F_{i-1,el}^n + \frac{k_n}{N_i} \sum_{j=1}^{N_i} (\delta_{i,j} - \delta_{i-1,j}) \\ &+ F_{i-1,dn}^n + \frac{\gamma_n}{N_i} \sum_{j=1}^{N_i} (\dot{\delta}_{i,j} - \dot{\delta}_{i-1,j}) \end{aligned} \quad (3.30)$$

where the elastic and viscous normal contact forces are incrementally computed by calculating and dividing only the incremental force elements by the number of contact points at the iteration step i . This is done to ensure that a multiple contact can be represented as a single contact.

As emphasized in Wachs et al. (2012), setting the contact force model parameters for non-spherical particles to guarantee an accurate and proper resolution of contacts is not an easy task. Here the potential occurrence of multiple contacts between two non-convex particles renders this task even more complicated. Using the previous simple analytical model for a gravityless contact between two particles, we consider two variants below.

The first variant involves summing up the contact forces by considering a system made of parallel springs and dampers. Starting from the equation EQ. 3.22, the case of multiple contacts can be treated by assuming that the hookean elastic force and the normal dissipative force can be defined as in EQ. 3.18 and in EQ. 3.19 respectively for each contact between two elementary components. Therefore, for N contacts EQ. 3.22 becomes:

$$\frac{d^2\delta}{dt^2} + N\gamma_n \frac{d\delta}{dt} + \frac{Nk_n}{M}\delta = 0, \quad \delta(t=0) = 0, \quad \frac{d\delta}{dt}(t=0) = v_0 \quad (3.31)$$

$t = 0$ is assumed to be the initial time of contact.

EQ. 3.31 can be written as follows to have the same form as EQ. 3.22:

$$\frac{d^2\delta}{dt^2} + 2\widetilde{\gamma}_n \frac{d\delta}{dt} + \widetilde{\omega}_0^2 \delta = 0, \quad \delta(t=0) = 0, \quad \frac{d\delta}{dt}(t=0) = v_0 \quad (3.32)$$

where

$$\widetilde{\gamma}_n = \frac{N\gamma_n}{2}; \quad \widetilde{\omega}_0^2 = \frac{Nk_n}{M} \quad (3.33)$$

And the expression of the contact time becomes:

$$T_c = \frac{\pi}{\sqrt{\widetilde{\omega}_0^2}} = \frac{\pi M}{Nk_n} \quad (3.34)$$

EQ. 3.34 shows that not only the stiffness coefficient influences the time of contact but also the number of contact between elementary components. Actually, the higher the number of contact between elementary components is, the shorter the contact time is. This is a very undesirable property.

Solving equation EQ. 3.31 leads to the definition of the damping coefficient γ_n as a function of the number of contacts N and the coefficient of restitution e_n as follows:

$$\gamma_n = -\sqrt{\frac{2}{N}} \frac{\omega_0 \ln e_n}{\sqrt{\pi^2 + (\ln e_n)^2}} \quad (3.35)$$

In FIG. 3.5, we illustrate how the number of contact points modifies the damping coefficient for a given coefficient of restitution. In fact, since forces from all contacts are added up during the interaction, EQ. 3.35 corrects the excessive damping of the system.

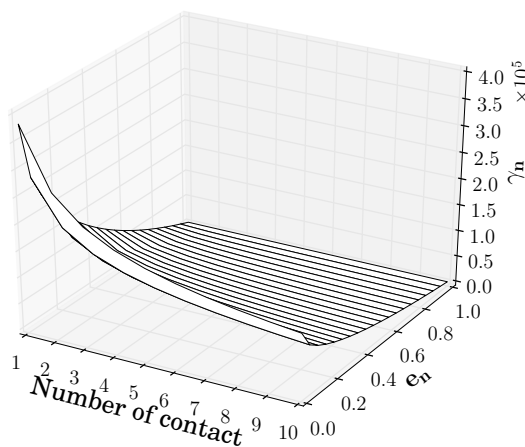


Figure 3.5 – Damping coefficient depending on the restitution coefficient e_n and the number of contact N .

Inspired by the works of Kruggel-Emden et al. (2008) and Höhner et al. (2011), the second variant to solve the multiple contact problem involves assuming that the problem can be

treated as a single contact one. In fact, we compute the elastic and dissipative normal contact forces as the sum of forces from all contact points divided by the number of contacts which occur at each time step Δt . The effect of compressing/elongating multiple springs and moving multiple dampers is modified in a way that it corresponds to a single contact dynamics.

EQ. 3.28 hence takes the following form:

$$F^n = F^{n,el} + F^{n,dn} = \frac{k_n}{N} \sum_{i=1}^N \delta_i + \frac{\gamma_n M}{N} \sum_{i=1}^N \dot{\delta}_i \quad (3.36)$$

where N denotes the number of contact points at the current time step. Compared to the work of Höhner et al. (2011), the force implemented in Grains3D is not evaluated incrementally.

From now on, the formulation of EQ. 3.31 is referred to “model A” and the formulation of EQ. 3.36 is referred to as “model B”.

3 VALIDATION TESTS

3.1 Methodology

The methodology to validate our glued convex method is rather elementary but also sufficient and well adapted. It involves running simulations with a convex shape treated as a single standard body in Grains3D and then running simulations of exactly the same flow configuration with the convex shape artificially decomposed into a set of smaller convex shapes. There is almost an infinity of possibilities. The most intuitive ones include decomposing a cube into 8 smaller cubes or decomposing a cylinder into a number of thinner cylinders. For the sake of conciseness, we have selected a single test case that also admits an analytical solution: the normal impact of a cylinder on a flat wall.

3.2 Normal cylinder-wall impact

This test case is inspired by the works of Kodam et al. (2010b) and Park (2003). It involves a cylinder impacting a flat wall in the normal direction to the wall and in a gravityless space (FIG. 3.6). The contact is also assumed frictionless. It is conceptually simple and very convenient for an accuracy assessment as it admits an analytical solution. Our goal is to compare the solutions computed with Grains3D for three representations of a cylinder to the analytical solution. These three representations are:

1. a true cylinder
2. a composite cylinder obtained by artificially slicing the true cylinder in thinner cylinders and gluing them together,
3. a glued-sphere representation of the cylinder.

The initial conditions of the test case are characterized by:

- the initial angular position θ of the cylinder with respect to the horizontal plane,
- the initial translational velocity $U = (0, 0, V_{z,g}^-)$,
- and the initial angular velocity $\omega = (0, 0, 0)$.

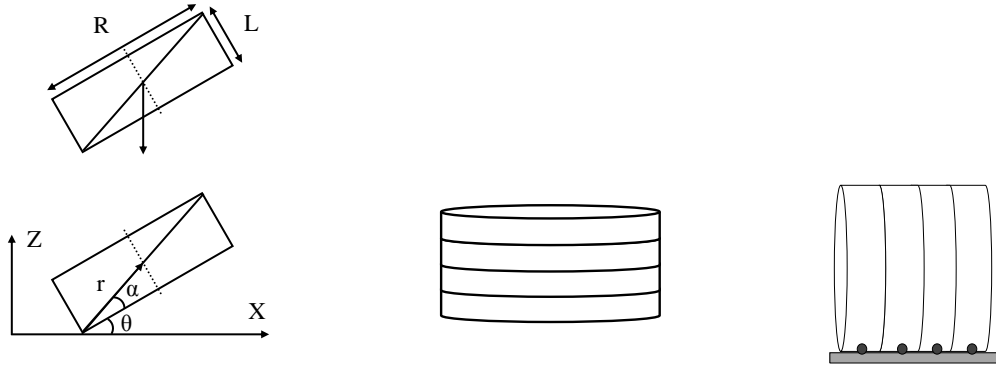
In other words, the pre-impact translational and angular velocity magnitude is set to $V_{z,g}^-$ and 0, respectively. From [Park \(2003\)](#), the post-impact angular velocity can be written as follows:

$$\omega_y^+ = \frac{MV_{z,g}^-(1 + \varepsilon)r \cos(\alpha + \theta)}{I_{yy} + Mr^2 \cos^2(\alpha + \theta)} \quad (3.37)$$

where M is the mass of the particle, $\varepsilon = -\frac{V_{z,g}^-}{V_{z,g}^+}$ is the coefficient of restitution, $V_{z,g}^-$ denotes the pre-impact velocity, α denotes the angle between the face of the cylinder and the line joining the contact point and the centre of mass, θ is the pre-impact angular position of the cylinder, I_{yy} is the moment of inertia about the y axis and $r = \sqrt{R^2 + \frac{1}{4}L^2}$ is a parameter which denotes the distance between the impact point and the centre of mass, R is the radius of the cylinder and L is the length of the cylinder (see [FIG. 3.6](#)). Similarly, the post-impact translational velocity reads as follows ([Kodam et al. \(2010b\)](#), [Park \(2003\)](#)):

$$V_{z,g}^+ = \omega_y^+ r \cos(\alpha + \theta) - \varepsilon V_{z,g}^- \quad (3.38)$$

Values of physical parameters are listed in [TAB. 3.1](#). As in [Kodam et al. \(2010b\)](#), we set $V_{z,g}^- = 1 \text{ m/s}$ and vary θ , the pre-impact angular position of the cylinder.



(a) Sketch of cylinder-wall impact. Credit: [Kodam et al. \(2010b\)](#), [Park \(2003\)](#).

(b) A cylinder decomposed into thinner cylinders.

(c) Illustration of cylinder-wall impact at 90° .

Figure 3.6 – Sketch of the cylinder-wall impact test case.

Parameter	True cylinder	Glued cylinders	Error [%]
Diameter[m]	8.0e-03	8.0e-03	0.
Length[m]	5.3e-03	5.3e-03	0.
Volume[m ³]	2.66407e-07	2.66413e-07	2.331e-03
Mass[kg]	3.1e-04	3.10007e-04	2.331e-03
Moment of inertia [kg.m ²]	1.966e-09 ^a	1.9674e-09 ^a	7.543e-02
	2.480e-09 ^b	2.4793e-09 ^b	2.626e-02
Shear modulus[GPa]	1.15	1.15	0.
Coefficient of restitution	0.85	0.85	0.

^a about central diameter, ^b about central axis.

Table 3.1 – Experimental ([Kodam et al. \(2010b\)](#)) and numerical parameters for the normal impact of a cylinder on a flat wall.

We plot in FIG. 3.7 the computed post-impact translational and angular velocities as a function of the pre-impact angular position θ , for the true cylinder and the glued cylinder (regardless of model A or model B). The agreement between these two simulations is extremely satisfactory. It reveals that the glued convex method is well implemented in our code. We also compare these two quasi-similar computed solutions to the analytical solution EQ. 3.37-EQ. 3.38. The agreement of the two computed solutions with the analytical solution is also deemed to be very good, with the largest discrepancy observed on the post-impact angular velocity at low pre-impact angular positions (FIG. 3.7b).

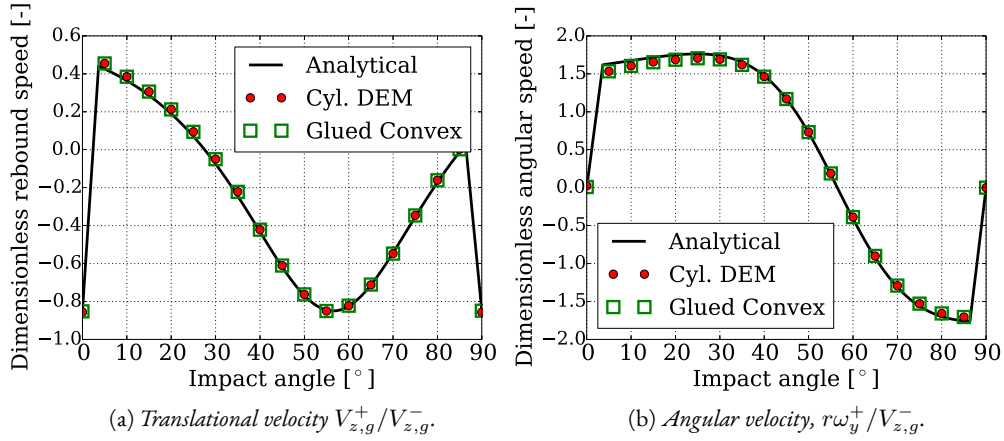


Figure 3.7 – Comparison of the dimensionless post-impact velocities.

We now investigate more deeply the differences between the two formulations to compute the total force acting on a composite particle, the so-called model A and model B. We select a particular pre-impact angular position $\theta = 90^\circ$ and plot in FIG. 3.8 the time evolution of the normal contact force exerted on the cylinder over the time of contact. As expected from the formulation of model A in which the total force is the sum of the forces exerted at each contact point, model A predicts an increasing total normal force as the number of elementary cylinders N increases (note that N is also the number of contact points for $\theta = 90^\circ$) although the magnitude of the force per elementary cylinder, i.e., per contact point, decreases. Overall, the adjustment of γ_n through EQ. 3.35 to get the expected restitution Coefficient e_n guarantees that the solution is correct, as shown in FIG. 3.7, but the main drawback of model A as predicted by EQ. 3.34 and supported by results of FIG. 3.8a is the decrease of the contact duration T_c with N . Consequently, the time step magnitude would have to be adjusted to the number of contact points in order to properly integrate a contact. This is a very undesirable property. Conversely, model B, that assumes that the total force exerted on the particle is the mean force over all contact points, provides a normal force magnitude, a contact duration as well as a maximum penetration depth independent of N , as shown in FIG. 3.8b.

Finally, we examine in the case $\theta = 90^\circ$ the effect of N on the accuracy of the computed solution. For both model A and model B and $N \leq 30$, FIG. 3.9a reveals that the error on the computed post-impact translational velocity is less than 0.5%. Model B performs remarkably better than model A with an error quasi independent of N and of the order of 0.05%. The error on the computed post-impact angular velocity plotted as a function of N in FIG. 3.9b is even more interesting. The analytical solution EQ. 3.37 predicts that the post-impact angular velocity is $\omega_y^+ = 0$. The true cylinder simulation predicts an artificial non-zero post-impact angular velocity. This is due to the assumption, violated here, that the contact is always a point while geometrically in this case it is a line. However, the GJK algorithm supplies a point,

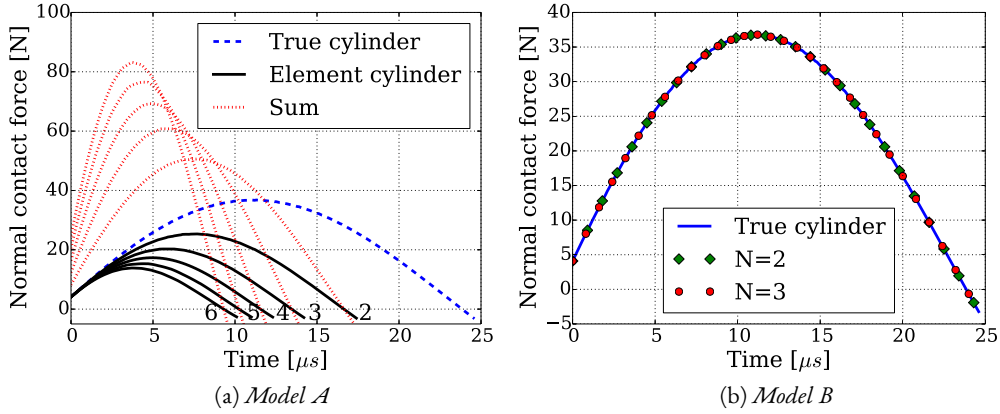


Figure 3.8 – Normal contact force evolution with time of a particle impacting a flat wall at the angle of 90° . $N = 1, \dots, i$ is the number of the components of the glued convex.

that randomly lies somewhere along that contact line and whose position is primarily determined by rounding numerical errors. This somehow flawed contact point creates an erroneous torque that makes the particle spin after contact. Interestingly, the composite cylinder simulation predicts a post-impact angular velocity ω_y^+ that tends to 0, the correct value, as N increases. This is simply a beneficial side effect of the distribution of the N contact points along the contact line. Torques from each contact point almost cancel out with each other and the total torque exerted on the particle tends to 0 as N increases. Once again, model B performs better than model A, although it is not entirely clear why. It might simply be due to rounding errors divided by N in model B.

Overall, the glued convex approach has been very satisfactorily validated in this cylinder-wall impact test case. Model B seems to perform better and is also conceptually more sensible as contact feature estimates (and in particular the duration of contact) from a single contact point configuration are still valid. To complete the validation of the model and as a side question, we run simulations with a glued sphere representation of the cylinder and evaluate how well the glued sphere approach performs in a simple impact test case.

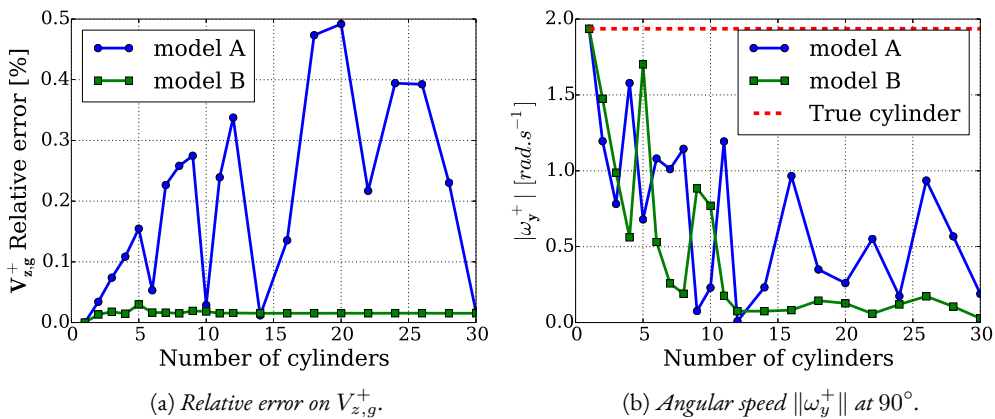


Figure 3.9 – Deviation of the velocities of a single glued cylinders DEM simulation compared to a single true cylinder DEM simulation impacting a flat wall at 90° .

We consider two composite particles made of 9 and 54 spheres, respectively, as also considered by Kodam et al. (2010b) and illustrated in FIG. 3.10. Values of physical parameters are listed in TAB. 3.2. For the mass properties, one can select those of a true cylinder or those of the glued-sphere representation. Kodam et al. (2010b) employed a mix of true cylinder (mass) and glued sphere (moment of inertia tensor) properties, although it is rather unclear what is the motivation for such a choice.

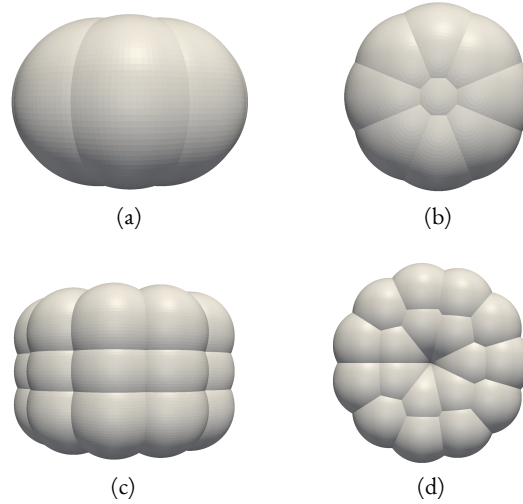


Figure 3.10 – Representations of a cylinder made of 9 glued spheres (a,b) and 54 glued spheres (c,d).

Parameter	Experiment	Glued spheres Kodam et al. (2010b)	Glued convex DEM (True parameters)
Diameter[m]	8.0e-03	8.0e-03	8.0e-03
Length[m]	5.3e-03	5.3e-03	5.3e-03
Volume[m ³]	2.664e-07	1.916e-07(9 spheres)	1.948e-07(9 spheres)
	2.664e-07	2.231e-07(54 spheres)	2.244e-07(54 spheres)
Mass[kg]	3.1e-04	3.1e-04	2.266e-04(9 spheres)
			2.611e-04(54 spheres)
Moment of inertia[kg · m ²]	1.966e-09 ^a	1.966e-09 ^a	1.320e-09 ^a (9 spheres)
	2.480e-09 ^b	2.480e-09 ^b	1.738e-09 ^b (9 spheres)
			3.281e-09 ^a (54 spheres)
			1.871e-09 ^b (54 spheres)
Shear modulus[GPa]	1.15	1.15	1.15
Coefficient of restitution	0.85	0.85	0.85

^a about central diameter, ^b about central axis

Table 3.2 – Experimental and numerical parameters for the normal impact of a cylinder modelled with glued spheres on a flat wall.

FIG. 3.11a, FIG. 3.11b, FIG. 3.11c and FIG. 3.11d show the computed solutions with 9 and 54 glued spheres. Regardless of the set of mass property parameters (true cylinder, glued spheres or a mix as in Kodam et al. (2010b)), the computed solution is qualitatively the same and does not match at all the analytical solution. For 54 glued spheres, the computed solution starts to pick up the right qualitative form but is still quantitatively markedly off. As the number of glued spheres used to represent the cylinder increases, it is however predictable that the computed solution will tend to the analytical solution. It is interesting to observe that for two particular pre-impact angular position values 0° and 90°, the glued sphere representation captures the right post-impact velocities. These two angles correspond to two particular contact

configurations in which the shape of the cylinder and specifically the artificial roundedness of the edges created by gluing spheres does not play any role. In fact, at 0° and 90° , the actual contact zone geometry is a surface and a line respectively. The homogeneous distribution of the glued spheres over the cylinder volume assures the proper computation of the normal contact force and the associated torque (that is 0). For all other pre-impact angular positions that lead to a single contact point, the error on the post-impact velocities is very significant, unless the number of glued spheres is large (probably of the order of $O(10^2 - 10^3)$), as a result of the artificial rounded edges of the glued-sphere representation of the cylinder. In general, this simple test case reveals that the glued sphere representation of a complex shape, also intuitively attractive, might provide computed solutions of very weak accuracy and should hence be used with great care, if not prohibited.

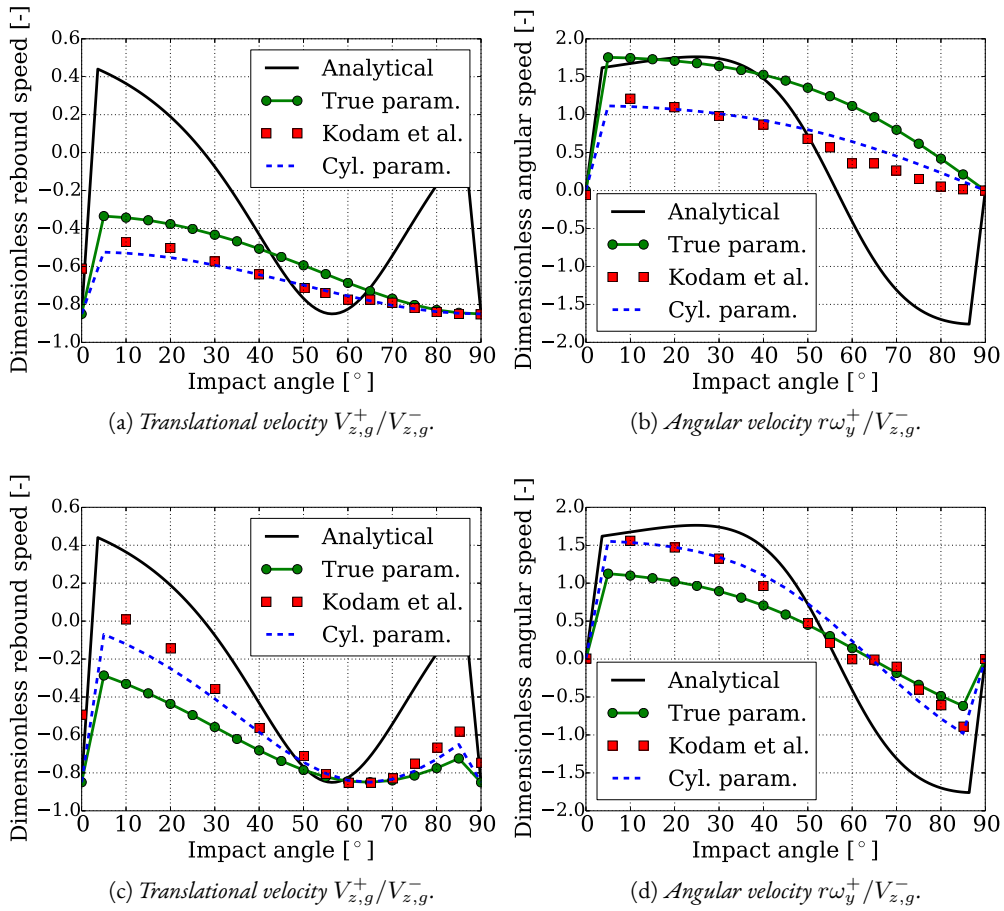


Figure 3.11 – Comparison of the dimensionless post-impact velocities of a cylinder made of 9 glued spheres (a,b) and 54 glued spheres (c,d) with the analytical solution EQ. 3.37-EQ. 3.38.

4 RESULTS

4.1 Packing porosity

Void fraction or porosity of a (static) packing of granular material is simply the measure of the ratio of the volume of empty space to the total volume of the system. Compacity corresponds to the opposite of porosity and represents the ratio of total volume of particles to total volume of the system. Compacity of convex particles packings can be estimated by computing

the Voronoï diagram of the system (Luchnikov et al. (1999)) whereas for non-convex particles the use of this method is impeded by their concavity. Consequently, another method has to be used for the characterization of compacity of random packings of non-convex particles. Here we use the same method as the one used to calculate the mass properties of a non-convex particle, i.e., we define a box embedding the packing of particles, pixelate that space with a fine cartesian constant grid size structured mesh and approximate the volume integral of the space actually occupied by particles by summing all the cells of the fine cartesian mesh whose center lies inside a particle. The method is fully parallelised as the total number of cells in this fine cartesian mesh is very often of the order of $O(10^8 - 10^9)$ to guarantee a sufficient level of accuracy.

Packings are created by inserting particles at the top of the domain. Particles settle downwards by gravity and collide with neighbouring particles and/or the bottom wall. The filling process is deemed to be complete when all particles reach a pseudo stationary state characterized by a negligible total kinetic energy of the system. We consider the two following configurations:

1. a system without lateral solid wall effects designed as a box with bi-periodic boundary conditions on the lateral (vertical) boundaries, i.e., in the horizontal directions. 1000 particles are inserted in the simulation in the following way: (i) a particle position is randomly selected in a thin parallelepiped at the top of the domain at each time t^n , (ii) a random angular position is assigned to the particle, (iii) insertion is attempted. If successful, the particle is inserted, otherwise a new random position together with a new random angular position is selected and insertion is attempted again at the next time t^{n+1} . This insertion procedure results in a moderately dense shower of particles stemming from the parallelepipedic insertion window.
2. a system with strong lateral wall effects designed as a cylindrical reactor with a circular cross-section. We select the same configuration as in our previous work Wachs et al. (2012). In Wachs et al. (2012), we examined the effect of convexity on packing porosity. Now we extend this case study to non-convexity. 250 particles are randomly inserted at the top of the domain at a flow rate of 1 particle per second until the simulation is stopped at 260 s. Lateral wall effects are deemed to be strong as the reactor diameter to particle equivalent diameter ratio is $\approx 50/8 = 6.25$, an admittedly small value.

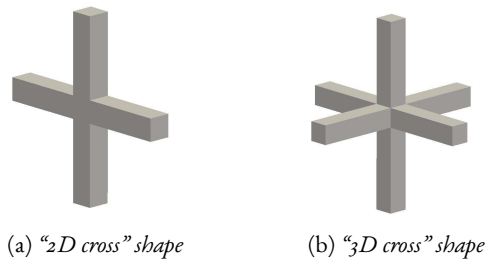


Figure 3.12 – Non-convex cross-like shapes considered in this work.

In both configurations, we consider the 4 convex shapes already examined in Wachs et al. (2012) in addition to two new non-convex cross-like shapes illustrated in FIG. 3.12. All shapes have the same volume. The two meaningful physical parameters of the contact force model are set to $e_n = 0.73$ and $\mu_c = 0.55$.

Packings of the different shapes in the wall-free bi-periodic domain are presented in FIG. 3.13. The corresponding porosities computed by our approximate numerical integration based on pixelating the space occupied by the packing of particles are shown in TAB. 3.3. Although tetrahedra already exhibit a slightly higher porosity, there is a remarkable jump of porosity between the 4 convex shapes and the 2 non-convex cross-like shapes. In fact, ε for 3D crosses is twice larger than for spheres of same volume.

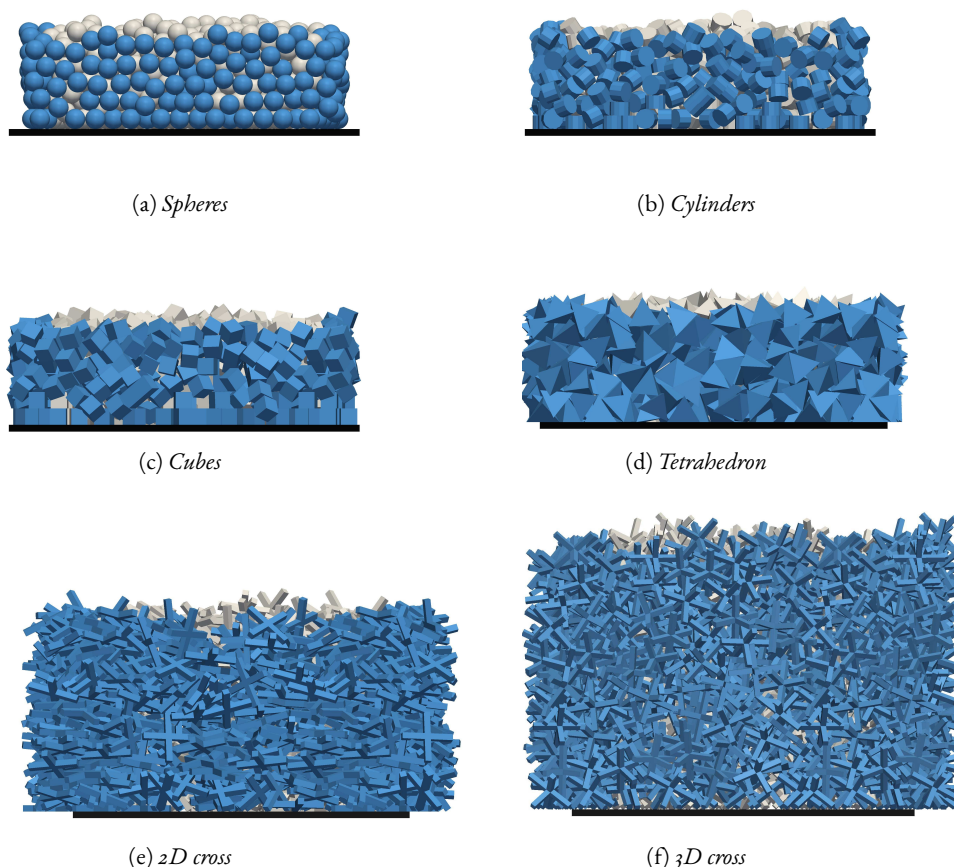


Figure 3.13 – Packings of 1000 particles of various shapes. Particles in blue are the periodic clones.

Shapes	Spheres	Cylinders	Cubes	Tetrahedron	2D cross	3D cross
ε	38.1772	38.5866	39.619	47.4582	69.4569	79.6328
Nb points*	3.2×10^7				6.4×10^7	
ε	38.1794	38.5811	39.5899	47.4586	69.4573	79.6327
Nb points*	2.56×10^8				5.12×10^8	

* Total number of cells in the structured mesh used to estimate ε

Table 3.3 – Estimation of the porosity ε [%]. The domain is discretised in the three direction.

With strong wall effects, the effect of shape on porosity ε is even more emphasised, as illustrated by FIG. 3.14. Porosity varies linearly with the height of the bed, and visually the variation of bed height as a function of shape speaks for itself. Bed height for 3D crosses (blue particles in FIG. 3.14(f)) is literally 5 times larger than that for spheres, cylinders and cubes, translating into a 5 times larger porosity. It is also 4 times larger than that for tetrahedra as well

as 2 times larger than that for 2D crosses. For 3D crosses, it is quite remarkable in FIG. 3.14(f) that ε is close to 1 close to the reactor wall in a crown of width approximately half the length of the cross beams, whereas all other shapes, even 2D crosses, are able to fill that region much better. Obviously, we have selected these 2 non-convex shapes on purpose, as they exhibit a low sphericity and promote some sort of entanglement in the packing. They are hence good candidates for high porosity packings and other unusual intricate effects in granular dynamics as we shall see in the next section. The analysis of the packing micro-structure can be easily extended e.g. by looking at the porosity radial profile, by this goes beyond the scope of the present paper. Our goal here is primarily to evaluate quantitatively packing porosity for such shapes and to shed some light on how strong the effect of shape can be, even in a very simple configuration.

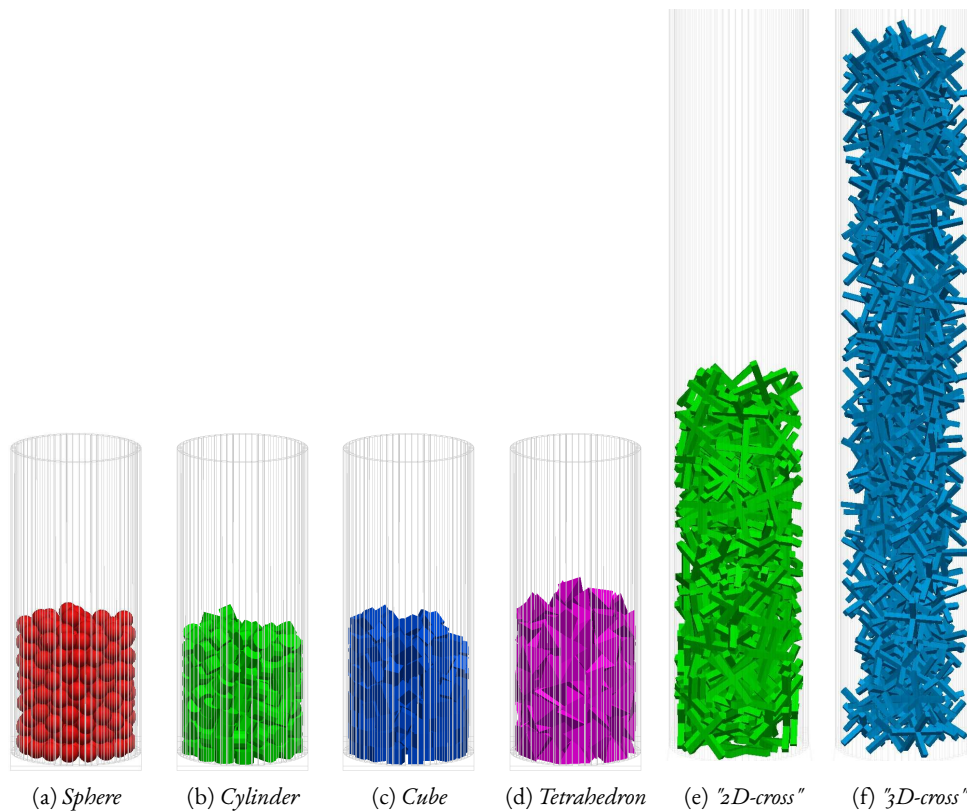


Figure 3.14 – Packing of 250 particles of 6 different shapes in a cylindrical container. Results in (a,b,c,d) are from *Wachs et al. (2012)*.

4.2 Rotating drum

Following the work of Yang et al. (2003; 2008), Wachs et al. (2012) we investigate the flow dynamics of a granular media in a rotating drum. We select the same flow configuration as in our previous work Wachs et al. (2012) and our goal is to extend results previously obtained for convex particles to non-convex particles. As in Wachs et al. (2012), the drum has a radius of $R_{drum} = 50 \text{ mm}$ and a depth of 24 mm (FIG. 3.15). A periodic boundary condition is applied along the drum axis to avoid end wall effects. The drum is loaded with mono-dispersed non-convex particles such that the region occupied by particles in the drum (regardless of porosity) corresponds to 35% of the drum volume, i.e. the pack has initially a height equal to $\approx 0.76R_{drum}$. For the non-convex shapes, we use the same 2D and 3D crosses as in Section 4.1. The new simulation results for the 2D and 3D crosses complement the existing set of results we obtained for convex particles (i.e., spheres, cylinders, cubes and regular tetrahedron) in Wachs et al. (2012). Once again, all shapes have the same volume, that corresponds here to a sphere with a radius of 1.5 mm . Values of all simulation parameters are listed in TAB. 3.4.



Figure 3.15 – Visualisation of the rotating drum.

Parameter	Value
$k_n (N \text{ m}^{-1})$	1×10^5
e_n	0.73
μ_c	0.55
$\mu_t (s^{-1})$	1×10^5
$\delta_{max} (m)$, δ_{max}/R_e	1.1403×10^{-5} , 0.007602
$T_C (s)$	4.172×10^{-5}
$\Delta t (s)$	2×10^{-6}

Table 3.4 – Contact force model parameters, estimate of contact features at $v_0 = 1 \text{ m s}^{-1}$ and time step magnitude used in rotating drum simulations.

As shown in Section 4.1 for the non-convex cross-like shapes and in Wachs et al. (2012) for tetrahedra, the total number of particles for each shape need to be adjusted such that the initial bed height is always $\approx 0.76R_{drum}$ (35% of the drum volume) due to the high variations in porosity between shapes. While the drum was loaded with 3000 spheres, cylinders and cubes, only 2600 regular tetrahedra were used in Wachs et al. (2012). Here, we fill the drum with 1500 2D crosses and 1250 3D crosses.

“3D cross” shape

FIG. 3.16 shows the internal flow structure of a system filled with 3D crosses for $\Omega \in [5; 250]$ rpm. A first sight already indicates the strong influence of the particle shape on the flow dynamics, compared to spheres and even to convex particles. Similarly to the filling process in Section 4.1, the significant differences observed all result from the ability of 3D crosses to entangle. As for other convex shapes, we observe a transition from an avalanching regime to a cataracting regime, then to a pseudo-cataracting and eventually to a centrifuging regimes as the rotation rate increases. Note that for low rotation rates, the rolling regime observed for spheres is replaced by an avalanching regime (the same was observed for convex shapes in Wachs et al. (2012)). Let us now describe qualitatively the features of each flow regime.

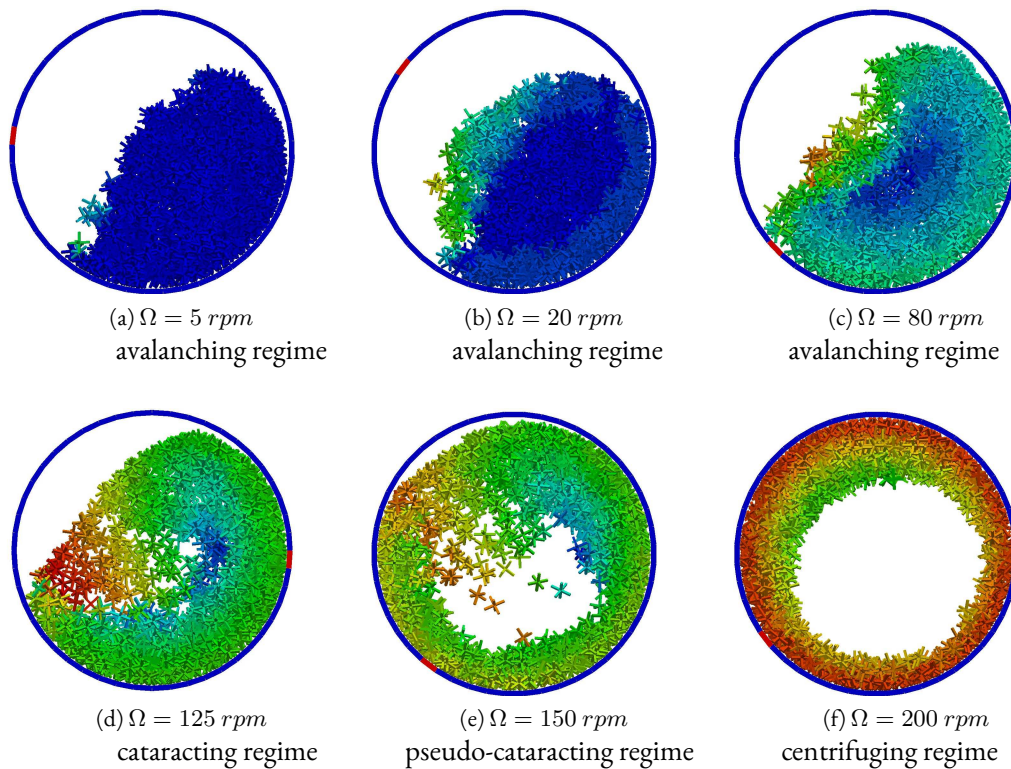


Figure 3.16 – Rotating drum filled with “3D cross” shaped particles at various rotation rates: snapshots of the pattern of particles coloured by their translational velocity magnitude (from blue (min) to red (max)).

At $\Omega = 5$ rpm, the flow regime is representative of episodic avalanches governed by the pseudo-chaotic evolution of the highly entangled micro-structure of the pack of particles. Particle rotation is strongly impeded both close to the drum wall and at the free surface. As for other shapes, particles close to the drum wall experience a rigid body motion while the major difference occurs at the free surface. Particles entanglements delay the onset of avalanching up to very high free surface angles, sometimes close to 90° . Then the pack eventually breaks and big clusters of particles detach and fall down from the top right to the bottom left of the free surface. Big cluster detachment from the rest of the pack of particles at the top right resembles to some extent the fracturing of an homogeneous solid material or a cohesive granular media. Fracturing starts at the location in the pack that shows a weakness characterized by a lower level of entanglement, i.e., a lower level of cohesion. We call this regime episodic avalanching as the frequency of occurrence of avalanches is less regular and hence tougher to define than for

convex shapes, as supported by FIG. 3.22. As the rotation rate increases to $\Omega = 20 \text{ rpm}$, big clusters of particles at the free surface disappear to give way to a thick layer of particles flowing down the free surface from the top right to the bottom left. At $\Omega = 80 \text{ rpm}$, particles gain even kinetic energy to start freeing themselves from the pack. Flow dynamics is still strongly governed by particles entanglements but the pack of particles is not as dense anymore and consequently the strength or cohesion of the pack of entangled particles is weaker. This corresponds to a transition from avalanching to cataracting, although particles at the free surface do not yet have a free-fly ballistic motion. At $\Omega = 125 \text{ rpm}$, the kinetic energy of particles at the top right of the free surface is large enough for them to almost free themselves from the pack and free fly. This flow dynamics is a typical sign of a cataracting regime (Mellmann (2001)). We would like to make a short digression of the determination of the onset of cataracting regime. As a comparison, we observe this ballistic trajectory of spherical particles in the range $150 \text{ rpm} \leq \Omega \leq 200 \text{ rpm}$, which suggests that cataracting regime starts at about 150 rpm for spheres. From FIG. 3.16, we might define the onset of cataracting regime at $\Omega = 125 \text{ rpm}$, which would hence indicate that 3D crosses exhibit a cataracting regime at lower rotation rates than spheres. At $\Omega = 125 \text{ rpm}$ the Froude number defined as $\Omega^2 R_{\text{drum}}/g$ is $\mathcal{F}r \simeq 0.87$. Looking more closely at FIG. 3.16(d), the notion of free-flight is tougher to define. Although the overall flow pattern does look like a cataracting regime, particles that detach from the top right still seem to be linked together with neighbouring particles in their pseudo free-flight in a very weak way. For spheres (see Wachs et al. (2012)-Figs(e)), it is very visible that particles flying from the top right to the bottom left of the free surface do not touch any other neighbouring particles. In other words, the transition from avalanching to cataracting is not necessarily easy to determine for 3D crosses. From $\Omega = 150 \text{ rpm}$, the cataracting regime starts to disappear and is progressively replaced by a pseudo-cataracting (or pseudo-centrifuging) regime. Ω is not high enough to already observe a fully centrifuging regime but not low enough for the cataracting regime to persist. The thin layer empty of particles at the top of the drum is a signature that the full centrifuging regime has not yet been attained. At $\Omega = 150 \text{ rpm}$, the Froude number is $\mathcal{F}r \simeq 1.25$. Finally, from $\Omega = 200 \text{ rpm}$, the fully centrifuging regime manifests, corresponding to $\mathcal{F}r \simeq 2.25$. For spheres, we determined in Wachs et al. (2012) that the transition to centrifuging regime occurs at $\Omega \simeq 220 \text{ rpm}$, i.e., for $\mathcal{F}r \simeq 2.7$. This would suggest that the transition from cataracting to centrifuging occurs at lower rotation rates for 3D crosses than for spheres. As already noticed for spheres or any other shapes, the centrifuging regime is characterized by a continuous layer of particles attached to the drum wall and rotating with the drum as a rigid body. A particular and rather fascinating feature of 3D crosses is the form of the free surface of the pack of particles undergoing a rigid body motion. While for spheres this layer has a constant thickness, it is rather irregular for 3D crosses. Actually, the entangled 3D crosses create an imprint over the early transients of the drum rotation. In other words, the free surface is determined by a competition between the strength or cohesion of the entangled pack of particles and the centrifugal force that pushes particles towards the drum wall. The free surface very rapidly adopts its final form (after a few drum rotations only) and then remains forever frozen in a rigid body rotation as shown in FIG. 3.16(f).

To illustrate how much the 3D cross-like shape hinders the rotation of a particle compared to a sphere, even without entanglements with neighbouring particles, we perform a simulation of a single particle in the drum rotating at $\Omega = 150 \text{ rpm}$ (FIG. 3.17). The resistance to rolling motion of the sphere is very low and accordingly the critical angle at which the sphere starts to roll down the drum wall very low too. 3D cross reaches much higher on the top right and their overall motion is far more chaotic. The ratio of translational to angular kinetic energy is much higher for a 3D cross than for a sphere. It would be interesting to extract this ratio in the multi-particle rotating drum simulations to shed some more light on differences in energy

conversion mechanism between sphere, convex and non-convex shapes. This is an on-going work in our group and will be the topic on a future paper.

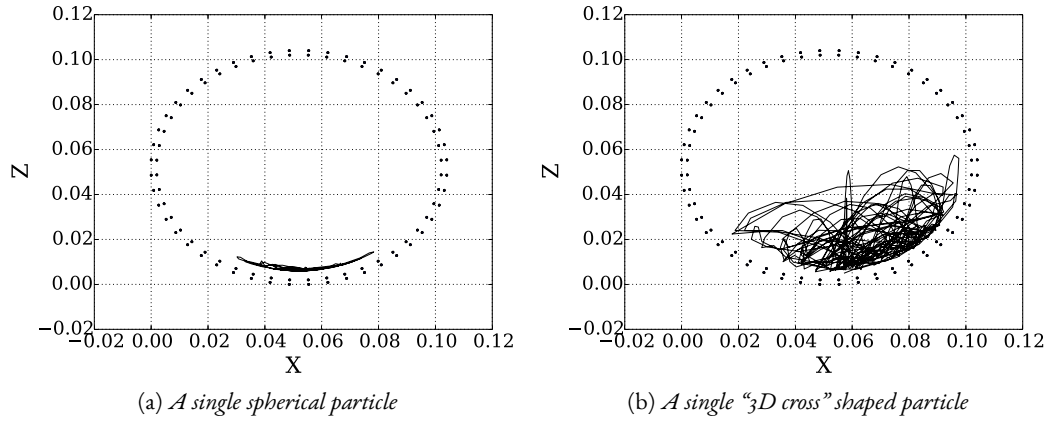


Figure 3.17 – Single particle trajectories at $\Omega = 150 \text{ rpm}$ during 10 s.

We illustrate in FIG. 3.18 the avalanching nature of the flow dynamics at low rotation rates $\Omega = 5 \text{ rpm}$ and $\Omega = 20 \text{ rpm}$. In particular at $\Omega = 5 \text{ rpm}$, we can neatly see in FIG. 3.16a(c) that the shallow layer of slumping particles at the free surface fractures in the middle into two big clusters. Another important comment concerns the determination of the dynamic angle of repose of the free surface in this avalanching regime. In fact, not only the free surface is anything but a flat surface but the flow is highly intermittent (episodic) and the dynamic angle of repose varies over time with a large amplitude. In FIG. 3.16a(c), it is noticeable that the free surface is close to vertical.

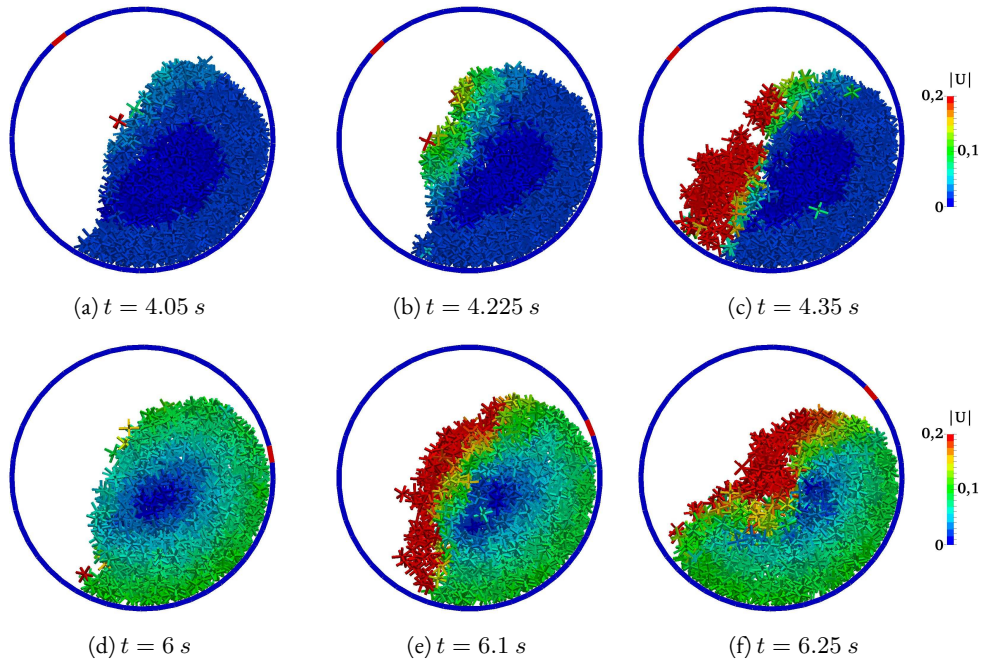


Figure 3.18 – Snapshots of the pattern of the "3D cross" shaped particles coloured by their translational velocity magnitude (from blue (min) to red (max)) at $\Omega = 5 \text{ rpm}$ (a,b,c) and at $\Omega = 20 \text{ rpm}$ (d,e,f).

“2D cross” shape

The overall picture of 2D crosses is qualitatively similar to the picture of 3D crosses. Since 2D crosses have a higher sphericity than 3D crosses and a lower tendency to entangle, the original features observed for 3D crosses are also observed but less marked for 2D crosses. We notice the same transitions from avalanching to cataracting, then to pseudo-cataracting and eventually to centrifuging as the drum rotation rate increases, but these transitions occur for slightly different critical rotation rates. The different flow regimes for 2D crosses are shown in FIG. 3.19.

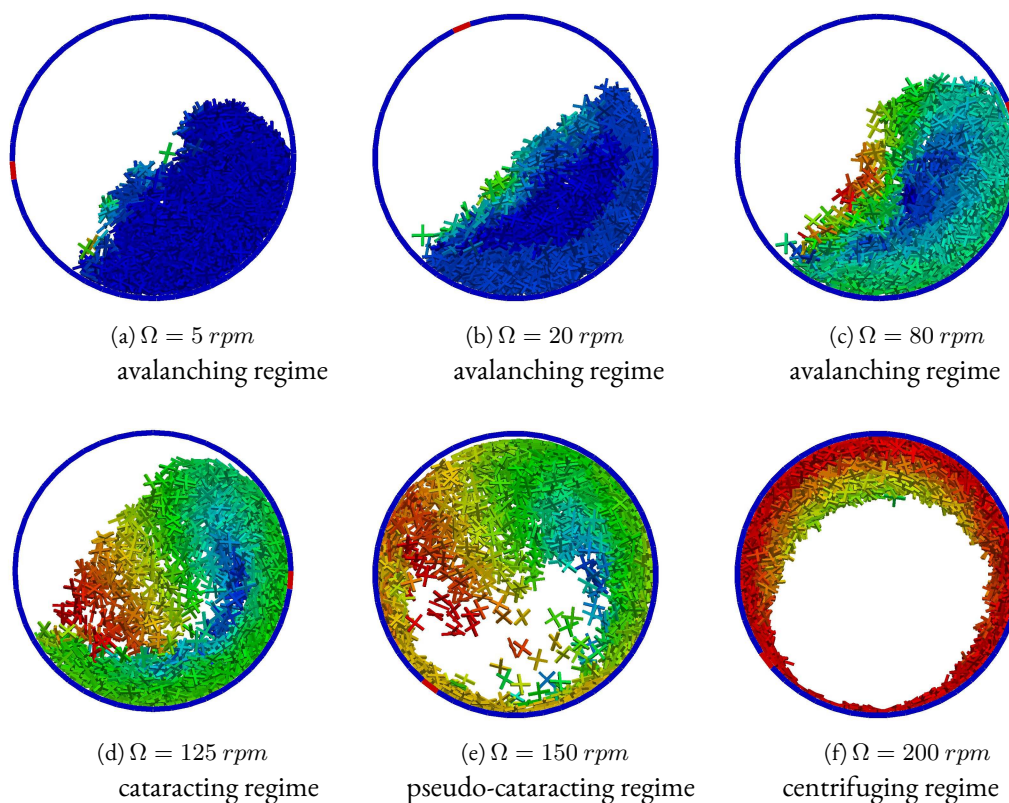


Figure 3.19 – Rotating drum filled with “2D cross” shaped particles at various rotation rates: snapshots of the pattern of particles coloured by their translational velocity magnitude (from blue (min) to red (max))

In general, the pack of 2D crosses is less cohesive than the pack of 3D crosses, in the sense that the strength of the entangled network of particles is weaker. This difference manifests very visibly in FIG. 3.20 where we illustrate the transient flow dynamics in the drum. The dynamic angle of repose of 2D crosses, although pretty high compared to convex shapes, is lower than that of 3D crosses. It also seems that the free surface, although not very flat, is significantly flatter than that of 3D crosses. Finally, FIG. 3.22 suggests that avalanches are more regular and that the avalanching regime can be classified as periodic avalanching, in contrast to episodic avalanching for 3D crosses. At $\Omega = 5 \text{ rpm}$ a single avalanching frequency for 2D crosses can be more clearly defined than for 3D crosses, although this is not totally obvious. Finally, cataracting, pseudo-cataracting and centrifuging regimes of 2D crosses are very similar to those of 3D crosses.

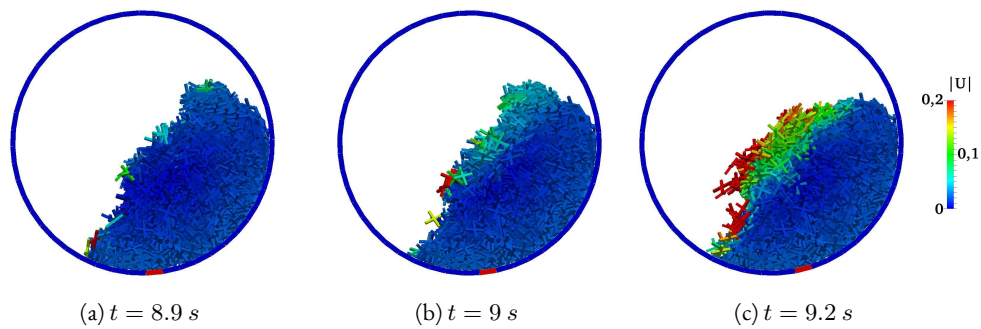


Figure 3.20 – Snapshots of the pattern of the “2D cross” shaped particles coloured by their translational velocity magnitude (from blue (min) to red (max)) at $\Omega = 5 \text{ rpm}$

Further comments

We plot in FIG. 3.21 the averaged in time coordination number as a function of rotation rate for all shapes. In general, 2D and 3D crosses exhibit a higher coordination number than other shapes regardless of the rotation rate, as a result of the highly entangled micro-structure. However, up to $\Omega = 150 \text{ rpm}$, the trend is very similar to convex particles and there is no major signature of non-convexity in the variation of the coordination with Ω . The plots for the 2 non-convex shapes are simply shifted to higher values of coordination number. The only signature of non-convexity pertains to the transition to cataracting/pseudo-cataracting regime and then to centrifuging regime. However, we run additional simulations for tetrahedra and notice the same trend than for 2D/3D crosses. Hence, this suggests that this signature is actually not relevant of non-convexity only, but more generally of non-sphericity. This emphasises again that the transitions to cataracting/pseudo-cataracting and to centrifuging are not easy to define. The increase of the coordination number above $\Omega = 150 \text{ rpm}$ might however indicate the onset of transition to centrifuging. At high $\Omega \geq 200 \text{ rpm}$, the absence of a neat plateau (as visible as for spheres) does not allow us to determine from this plot only when the fully centrifuging regime really starts.

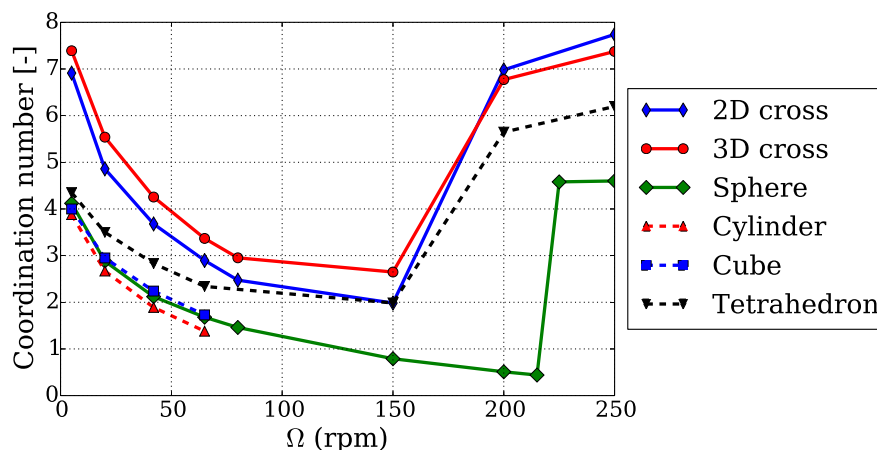


Figure 3.21 – Time averaged variation of the coordination number. Data are from [Wachs \(2011\)](#)

We plot in FIG. 3.22 the mean translational particle velocity as a function of time for different rotation rates. The interesting and already described in the above features of 2D and

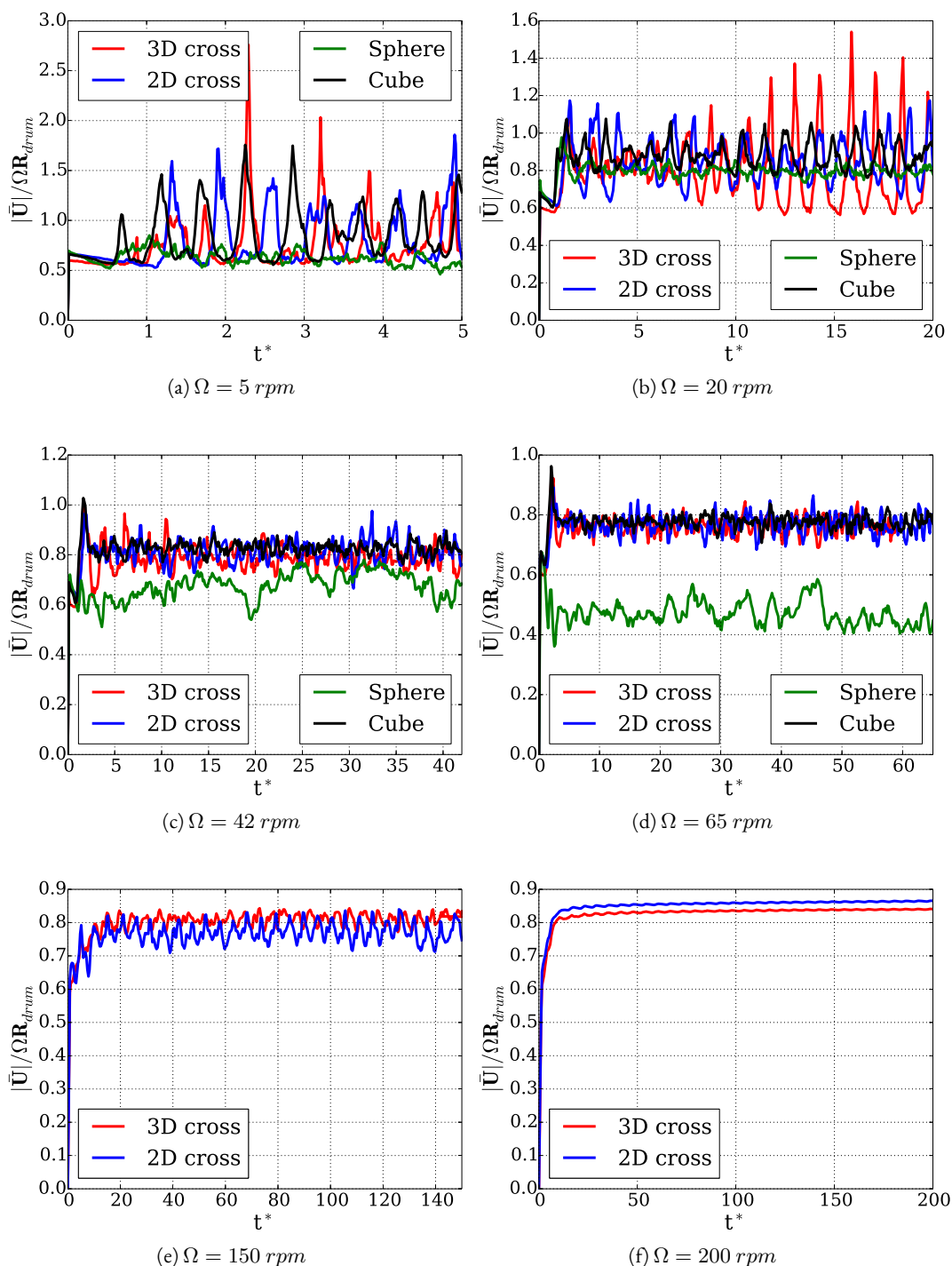


Figure 3.22 – Evolution of dimensionless mean translational velocity as a function of dimensionless time $t^* = t\Omega$. Data for spheres and cubes are from [Wachs et al. \(2012\)](#).

3D crosses flow dynamics occur at low rotation rates $\Omega = 5 \text{ rpm}$ and $\Omega = 20 \text{ rpm}$. From $\Omega = 42 \text{ rpm}$, the mean translational particle velocity of the 2 non-convex shape is very similar to that of any of the 3 non-spherical convex shapes. $\Omega = 5 \text{ rpm}$ reveals that 3D crosses undergo more chaotic, in the sense of larger amplitude and more episodic, avalanches than 2D crosses and convex shapes. The peaks of mean translational particle velocity represent rapid

avalanches of particles triggered by a very high dynamic angle of repose (up to $\sim 90^\circ$). The most remarkable manifestation of resistance to slump or to flow from the top right to the bottom left of the drum of the highly entangled pack of 3D crosses occurs at $\Omega = 20 \text{ rpm}$. While 2D crosses and cubes both exhibit a moderate avalanching dynamics, 3D crosses still undergo large amplitude and well defined avalanches characterized by large amplitude fluctuations of the mean translational particle velocity with time. At high rotation rates, the mean translational particle velocity progressively tends to a constant value over time. For instance, at $\Omega = 200 \text{ rpm}$, the mean translational particle velocity does not vary with time anymore. This represents a much more reliable signature of the onset of fully centrifuging regime than what we could extract from the coordination number analysis.

5 CONCLUSION AND DISCUSSION

We suggested an extension of our DEM from convex to non-convex shapes. As a reference to the glued spheres model, the novel method is called *glued convex* method as convex particles are “glued” together to create any non-convex shape. Our novel method for non-convex shapes relies on the same tools we used for convex shapes in [Wachs et al. \(2012\)](#). In fact, contact detection between two non-convex bodies relies on contact detection between all the pairs of elementary convex components that compose each composite non-convex body. This reduces the complexity of the problem of contact detection between non-convex bodies to the problem of contact detection between convex bodies, a problem for which we have already suggested a reliable and accurate solution method in [Wachs et al. \(2012\)](#) using a Gilbert-Johnson-Keerthi algorithm. The novel method is extremely versatile as virtually any non-convex shape can be considered. We illustrated the new simulation capabilities of our in-house code Grains3D in two flow configurations: (i) filling of a reactor and (ii) flow dynamics in a rotating drum. The simulation results we presented for non-convex 2D and 3D crosses are unprecedented in the literature.

We suggested a simple but robust solution to the problem of multi-contact points that enables us to keep using analytical estimates of contact features and in particular of contact duration. This significantly facilitates the estimation of the time-step magnitude in DEM simulations of non-convex bodies. We considered a normal cylinder-wall impact test case to illustrate the validation of our implementation. Along the way, we confirmed, as other works of the literature already showed [Kodam et al. \(2010b\)](#), that the accuracy of the glued sphere method to model particles of arbitrary shape is highly questionable as it rounds sharp angles and introduce an artificial rugosity. Conversely, our glued convex approach preserves angularity since a non-convex composite particle is decomposed into a set of elementary convex shapes, that are by essence sharp. A side effect of composite particles is their intrinsic ability to better handle contact configurations in which the contact zone cannot be modelled as a point, but rather as a line or a surface. In fact, composite particles naturally introduce multiple contact points corresponding to the contact points of their elementary components. Although decomposing an already convex particle in a set of smaller elementary convex particles is not the most promising path from a computational viewpoint, this property can still be exploited to improve the stability of static heap of particles and somehow circumvent the conceptual inability of our Gilbert-Johnson-Keerthi-based contact detection strategy to provide a line of contact, a surface of contact or multiple contact points from two simple convex bodies that overlap.

Although our new DEM for non-convex bodies opens up unprecedented numerical modelling perspectives, the computing cost is still prohibitive. In fact, the computing cost of con-

tact detection between two non-convex bodies scales as $N \times M$, where N denotes the number of elementary components of the first particle and M that of the second particle. Another computational drawback of the current implementation is that potential contacts are assessed with the circumscribed sphere to the non-convex particles, and then if they overlap with the circumscribed sphere to the convex elementary components (see FIG. 3.23). If the non-convex or elementary convex bodies are elongated, our method is not optimised and many contacts that actually do not exist are considered at the detection step. This undesirably slows down computations. An alternative solution would be to use oriented bounding boxes, with however no guarantee that the overall computing time will be lower as an oriented bounding box overlap test is more time consuming than a two sphere overlap test. In Chapter 5, we elaborate on the parallel implementation of the method. Although this could be a valuable way to speed up computations, we also show that scalability is satisfactory only for a minimum number of particles, as otherwise the MPI communication overhead is too high. We believe that contact detection between two non-convex bodies should be speeded up at the serial level.

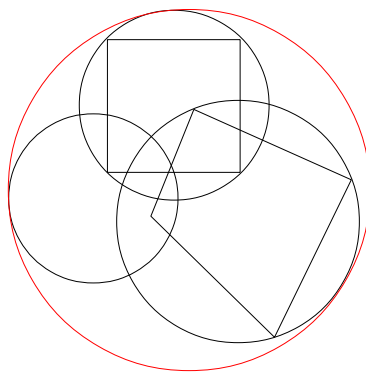


Figure 3.23 – *Circumscribed sphere illustrated in 2D.*

Potential applications of Grains3D were already quite broad, and the new *glued convex* model broadens even more its range of applicability. Only two examples of application were considered in this study that adequately illustrated the visible effect of particle non-convex shape on flow dynamics. Results from the rotating drum as shown in FIGS. 3.21 and 3.22 emphasise how flow dynamics differs from convex particles to non-convex particles. Our analysis could easily be extended to gain more insight into regime transitions and overall flow dynamics. One first step in that direction would be to analyse the PDF (Probability Density Function) of the time averaged particle translational and angular velocity and to seek in these plots any signatures of non-convexity. This is an on-going work in our research group.

RÉSUMÉ

Dans ce chapitre, les détails du modèle *glued convex* sont exposés avec toute la stratégie derrière cette approche. En effet, elle est basée sur le fait que la particule non-convexe peut être décomposée en plusieurs formes élémentaires arbitrairement convexes. Ainsi, elle peut être considérée comme une extension de la célèbre approche nommée “glued sphere” (“sphères collées”). Pour ce modèle la détection de contact se fait au niveau des particules élémentaires utilisant l’algorithme Gilbert-Johnson-Keerthi. La détection de contact s’appuie sur l’algorithme “Linked-Cell” pour pouvoir accélérer la phase de recherche de collisions potentielles. Une importance particulière est dédiée aux interactions impliquant de plusieurs points de contact.

Le modèle est validé sur quelques cas tests, par exemple, la comparaison de l’évolution de la force de contact lors de modélisation de l’interaction dans le cas d’un simple cylindre et celui d’un cylindre formé de cylindres collés avec une paroi.

L’approche est ensuite utilisée pour montrer l’impact de la forme sur les taux de vide dans des lits constitués de différentes formes de particules. Elle a aussi permis de mettre en évidence le changement de la dynamique des milieux granulaires dans un tambour tournant en fonction des formes des particules. Ces études ont illustré que non seulement la forme influence la dynamique mais elle fait aussi apparaître de nouveaux régimes d’écoulement selon l’angularité des particules (allant de la particule sphérique en passant par des formes convexes arbitraires telles que des cubes et des tétraèdre jusqu’aux particules en forme de croix).

OPTIMIZING PARTICLE SHAPE IN FIXED BEDS: SIMULATION OF VOID FRACTION WITH POLY-LOBED PARTICLES

4

CONTENTS

1	INTRODUCTION	56
2	METHODS AND MATERIAL	57
2.1	DEM with non-convex particles	57
2.2	Simulation principle	58
2.3	Void fraction analysis	58
2.4	Cases description	59
3	SIMULATIONS WITH RANDOM INSERTION AND DATA ANALYSIS	60
3.1	Repeating the packing	61
3.2	Effect of insertion window size	61
3.3	Overall uncertainty	62
4	RESULTS	63
4.1	Bi-periodic container	63
4.2	Cylindrical container	64
5	DISCUSSION	65
5.1	Effect of domain size in bi-periodic directions?	66
5.2	Remark on the effect of container size	66
6	CONCLUSION	67

This chapter has been submitted for publication in *Chemical Engineering Science*:

M. Rolland, A. D. Rakotonirina, A. Devousassoux, J.L. Barrios Goicetty, A. Wachs, J.-Y. Delenne. Optimizing particle shape in fixed beds: simulation of void fraction with lobed particles.

This paper presents the use of the *glued convex* method to simulate packing of poly-lobed particles. The simulations are carried out in bi-periodic domains in the aim of simulating a large fixed bed (industrial) and in small cylindrical containers that have the exact dimensions of a pilot unit at IFPEN. The work was performed in collaboration with 2 internships that I co-supervised.

I INTRODUCTION

Numerous chemical reactions are industrially performed using heterogeneous catalyst. Catalyst pellets can be shaped as spheres or extruded shapes (extrudates) or molded shapes (Moyses (1984), Cooper et al. (1986), Afandizadeh and Foumeny (2001), Mohammadzadeh and Zamaniyan (2002)). Due to the use of extrusion machines, extrudates are cheaper to produce in high quantities. They can have various shapes: cylinders, trilobes, and more recently quadralobes. Molded shapes include holes to improve internal transport. The best catalyst shape is a compromise between catalyst cost, catalyst efficiency, pressure drop, attrition, and bed plugging (Moyses (1984), Cooper et al. (1986), Afandizadeh and Foumeny (2001), Mohammadzadeh and Zamaniyan (2002)). Thus, it is application dependent. The challenge to design a better shape is to be able to predict the gains based only on the shape knowledge.

Catalyst efficiency is a measure of internal mass transfer limitation. It is defined as the actual reaction rate (in $\text{mol}/\text{m}^3/\text{s}$) divided by the reaction rate that would be achieved if the concentration inside the pellet was homogeneous and equal to that of the surface. If the reaction is fast enough, reactants may be consumed faster than they diffuse so that they have a lower concentration at the pellet centre than at its boundary. The active (expensive) phase located at the pellet centre is not used as efficiently as at its surface. The engineering pathways to improve efficiency are: (i) improving effective diffusion in the pellet by changing the pore size distribution and (ii) changing the shape, including size and introducing holes, to reduce the volume to external surface ratio. For a given shape, the catalyst efficiency can be numerically predicted by solving the diffusion equation in the grains assuming kinetic schemes (Mariani et al. (2009)). With a little less accuracy, it can be reasonably predicted for any particle shape without holes using the generalized Thiele modulus as proposed by Aris (1957), that can be written for a 1st order reaction:

$$\Phi = \frac{V_p}{S_p} \sqrt{\frac{k}{D_{eff}}} \quad (4.1)$$

$$\eta = \frac{1}{\Phi} \frac{I_1(2\Phi)}{I_0(2\Phi)} \quad (4.2)$$

where V_p , S_p , k and D_{eff} denote particle volume, particle surface, intrinsic kinetic constant and effectiveness coefficient respectively. I_n is the Bessel function of order n . Reducing the particle diameter results in an improvement of the catalyst efficiency due to a lower V_p/S_p , unfortunately at the cost of a higher pressure drop. But it still an efficient way to improve efficiency.

Gas-Liquid pressure drop in tricked bed reactors has been the subject of many publications. Their estimations are always performed using at some point the single phase predictions, so that for our purpose, optimizing trickle bed pressure drop is the same as optimizing single phase pressure drop (see for example Attou et al. (1999)). Pressure drop predictions are usually performed using correlations with a form following the Ergun's one (Ergun (1952)):

$$\frac{\Delta P}{H} = \alpha \frac{\mu(1 - \varepsilon)^2 u}{\varepsilon^3 d_p^2} + \beta \frac{\rho(1 - \varepsilon) u^2}{\varepsilon^3 d_p} \quad (4.3)$$

In the formulation EQ. 7.23, the pressure drop is the combination of a frictional viscous term proportional to the velocity and a quadratic term on velocity accounting for flow direction and section changes (Larachi et al. (2014)). Ergun (1952) proposed the constants $\alpha = 150$

and $\beta = 1.75$ to describe the pressure drop for spheres, cylinders and crushed particles. The diameter for non-spherical particles is the equivalent diameter defined as:

$$d_e = \frac{6V_p}{S_p} \quad (4.4)$$

Earlier [Carman \(1937\)](#) proposed $\alpha = 180$ and $\beta = 0$ for Stokes flows ($Re \sim 0$) in packed beds of spheres, which is more accurate than Ergun's coefficients in these conditions. For non-spherical particles, [Nemec and Levec \(2005\)](#) extended the correlation by introducing the sphericity:

$$\Psi = \left(\frac{36\pi V_p^2}{S_p^3} \right)^{\frac{1}{3}} \quad (4.5)$$

$$\frac{\Delta P}{H} = \frac{150}{\Psi^a} \frac{\mu(1-\varepsilon)^2 u}{\varepsilon^3 d_e^2} + \frac{1.75}{\Psi^b} \frac{\rho(1-\varepsilon)u^2}{\varepsilon^3 d_e} \quad (4.6)$$

The coefficients a and b have been subjected to some modifications by few authors, among others [Nemec and Levec \(2005\)](#) and [Dorai et al. \(2015\)](#). Other formulations have been proposed that take into account various shapes. Nevertheless, there is so far no universal method to precisely predict the Ergun's equation coefficients based only on particle shape.

As it can be noticed in EQ. 4.6, the pressure drop presents a very strong dependency on the void fraction which has been until recently measured experimentally. Due to the manufacturing process, the extrudates have random length. Therefore, length distribution may differ from an experiment to another, especially for particles produced on different extrusion dies. Automated sorting can be performed to narrow down the length distribution but this is not sufficient to prevent differences from experiment to experiment. Therefore, the comparison of the void fraction (and the pressure drop) is always based on measurements with different length distribution. As the differences between most efficient shapes are small, it is difficult to decouple shape and length effects when measuring the packed bed void fraction. In addition, the void fraction is highly dependent on the loading procedure leading to some discrepancies between operators. Repetition effects are barely quantified and are usually neglected, although we have no information on their magnitude compared to differences between shapes.

To summarize, it is yet impossible to predict the void fraction (and the pressure drop) accurately enough to rank innovative catalyst shapes without experiments. New numerical tools are required to optimise the particle shape "in silico". In this chapter, we present the use of DEM to estimate the void fraction for any trilobed and quadrilobed shapes, as well as an analysis of the trends in void fraction dependency.

2 METHODS AND MATERIAL

2.1 DEM with non-convex particles

Several numerical methods to produce packing of spheres have been published. Thanks to its flexibility the Discrete Element Method (DEM) can be extended to more complex shapes and thus will be presented. This method ([Cundall and Strack \(1979\)](#), [Cundall \(1988\)](#), [Wachs et al. \(2012\)](#)) is a Lagrangian particle tracking method which computes the particle velocities, trajectories and orientations. A key feature of any DEM tool is its ability to detect collisions, determine the contact point(s) and compute the resulting contact forces. This is done for example

using the Gilbert-Johnson-Keerthi algorithm [Gilbert et al. \(1988\)](#), [Gilbert and Foo \(1990\)](#). Recent developments of DEM allow the use of non-spherical particles, such as the glued spheres model which is a loose approximation of a complex shape [Nolan and Kavanagh \(1995\)](#), or by an accurate description of arbitrary convex particles [Wachs et al. \(2012\)](#). Recent development by our group ([Chapter 3](#)) allows the simulation of non-convex particles composed of a collection of convex particles. This method, called “glued convex”, is an extension of the glued spheres method of [Nolan and Kavanagh \(1995\)](#). It allows the use of the existing methods, models and algorithms already implemented in Grains3D ([Wachs et al. \(2012\)](#)) such as the equations of motion, time integration, collision resolution and particularly the Gilbert-Johnson-Keerthi algorithm for collision detection. Detailed information about the extension to non convex shape and the DEM features can be found in [Wachs et al. \(2012\)](#) and in [Chapter 3](#).

2.2 Simulation principle

Fixed beds of non-convex particles are computed using Grains3D. An insertion window is defined at the top of the domain ([FIG. 4.1](#)). It can be a box-like window or a flat surface, or a single point. The particles are inserted in the simulation in the following sequence:

- for the subsequent particle to be inserted, the code draws randomly its position and orientation,
- the particle is inserted as soon as there is enough space,
- the particle are subjected to the gravity force and leave the vicinity of the insertion zone.

A larger insertion zone results in more particles inserted simultaneously. During their free fall, the particles will experience inelastic collisions with walls and other particles. The total kinetic energy of the system decreases exponentially with time. The simulations are completed when the maximum of the particle velocities is below $10^{-5} m/s$. The output of the simulations is a file containing final positions, velocities and orientation for each particle. The domain geometry can be either constrained with rigid walls or using periodic conditions in the horizontal directions (bi-periodic).

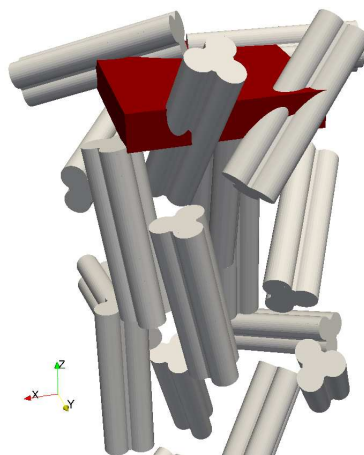


Figure 4.1 – Illustration of a box-like insertion window in DEM simulations.

2.3 Void fraction analysis

The average void fraction (porosity) is computed by two methods: (i) performing a 3D discretization of the space and counting the number of cells occupied by particles. Provided

sufficiently small grid cells, this method is very accurate but computationally expensive (*Chapter 3*). (ii) sorting all the particles according to their vertical position z and plotting that vertical position (vertical axis) against the particle ranking (horizontal axis) as illustrated in FIG. 4.2. For a random packing, the plot is a straight line whose slope is related to the void fraction as follow: the volume occupied by the particles scales with the number of the particles times the volume of a particle, the volume of the container scales with the container cross-section times the distance between particles. Thus, the void fraction ε reads:

$$\varepsilon = 1 - \frac{N V_p}{\Delta z S_p} = 1 - \frac{V_p}{S_p s} \quad (4.7)$$

where N , Δz , V_p , S_p and s denote respectively total number of particles, height of the cropped bed, particle volume, particle surface and slope related to void fraction.

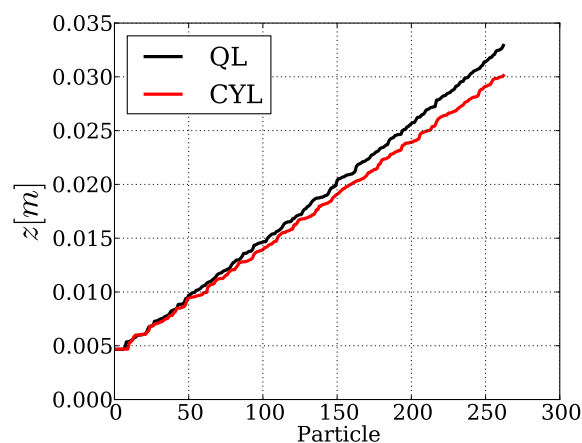


Figure 4.2 – Examples of plots resulting from the method (ii) of the void fraction analysis. Here QL and CYL have the same volume and same length L_p .

Incidentally, a non-linear trend in the ranking plot brings information about the structure: steps indicate “structured packing”, a changing slope indicates a change in the average void fraction. This method neglects the volume of particles located near the ends of the control volume and is as accurate as the discretization method when the control volume is large enough. As a last remark: a correct estimation of void fraction has to be performed discarding a few layers at the top and bottom of packing (Dorai et al. (2012)), avoiding end effects (flat bottom influence at the bottom and free surface at the top).

2.4 Cases description

A first set of simulations is performed using bi-periodic boundary conditions. This simulates a semi-infinite container, and models the packing in a large reactor. The container size is set to 18 mm after checking that this parameter has no effect of the void fraction. Another set of simulation is ran in a small size cylindrical reactors using solid walls. The vessel diameters are 14 mm, 16 mm and 19 mm.

Simulations are performed on the following shapes (FIG. 4.3): Cylinders (CYL), trilobes (TL) and quadralobes (QL). The particle cross-sectional diameter of trilobes and quadralobes is defined as that of circumscribed cylinder (FIG. 4.3d). For identical diameter and length, TL and QL occupy a volume of respectively 69% and 74% of the cylinder. The particle diameter is varying in the range [1.0, 2.5] mm and its length is set to 3 mm, 4 mm and 5 mm.

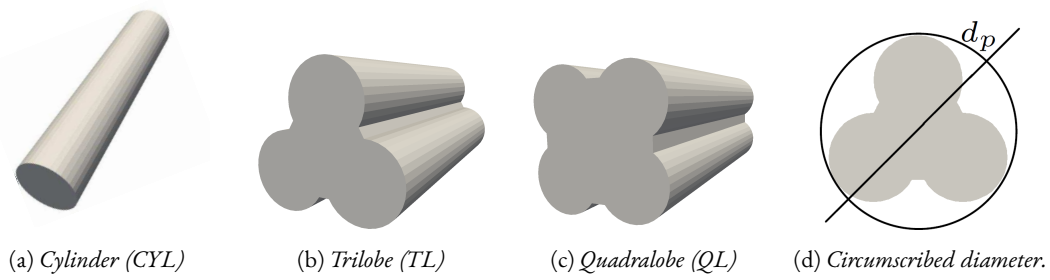


Figure 4.3 – Particle shapes in this study.

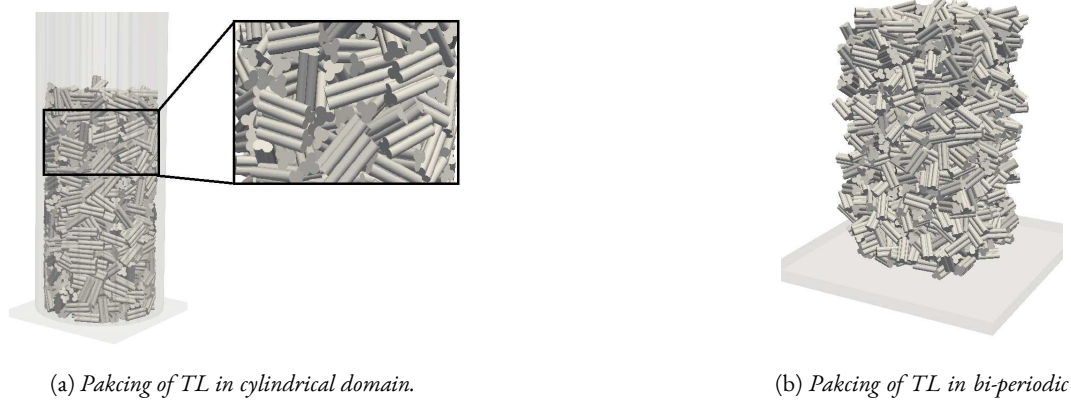


Figure 4.4 – Type of domains in this study.

In each simulation at least 1000 particles are inserted to fill either a bi-periodic domain or a cylindrical vessel (FIG. 4.4). The parameters of all numerical simulations are listed in TAB. 4.1.

Parameter	Value
$k_n (N m^{-1})$	1×10^5
e_n	0.7
μ_c	0.55
$\mu_t (s^{-1})$	1×10^5
$\delta_{max} (m), \delta_{max}/R_e$	$1.5 \times 10^{-5}, 0.005$
$T_C (s)$	2.01×10^{-5}
$\Delta t (s)$	1×10^{-6}

Table 4.1 – Contact force model parameters, estimate of contact features at $v_0 = 2 m s^{-1}$ for static packings.

3 SIMULATIONS WITH RANDOM INSERTION AND DATA ANALYSIS

As mentioned earlier, the particles are inserted in the simulation with a random position and orientation. Afterwards, the simulations and measurements are deterministic and accurate. Every packed bed has a different void fraction. As we are interested in comparing the effects

of shape on void fraction, we must be able to quantify which part of the differences between two simulations are due to the shape or to the random insertion at the top of the domain.

3.1 Repeating the packing

Several loadings with the same set of 1000 particles are repeated for the 3 shapes (TAB. 4.2). As the particle shape and dimension differ from one case to another, the average void fractions should not be compared for the moment but the reader should focus on the void fraction standard deviation ($\sigma < 0.0053$) which reads:

$$\sigma = \sqrt{\frac{1}{N} \sum_{i=1}^N (\varepsilon_i - \mu)^2}, \quad \text{where } \mu = \frac{1}{N} \sum_{i=1}^N \varepsilon_i \quad (4.8)$$

where N and ε_i stand for total number of simulations and void fraction of the simulation i respectively.

As the number of repetitions is not large, this estimation of repeatability can be improved by aggregating data and removing the average of each sub-set (shape effect). The standard deviation of the whole ensemble (18 elements) is indeed lower than $\sigma_1 = 0.0042$. At this point, it is worth reminding that once the particles are inserted in the simulation, the solver is deterministic and exact: σ_1 is a measure of the effect of the random initial conditions.

Shape	Length [mm]	Diameter [mm]	Number of repetition	Void fraction			
				Average	Std dev.	Min.	Max.
CYL	3	1.6	7	0.3829	0.0053	0.3752	0.3921
TL	3	2.2	5	0.4127	0.0007	0.4118	0.4136
QL	3	2.2	6	0.4085	0.0050	0.4026	0.4150

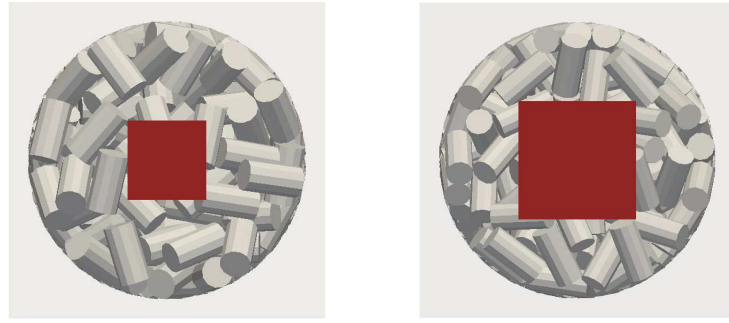
Table 4.2 – Repetition of random packing with identical particles.

3.2 Effect of insertion window size

We estimated the effects of insertion window size for various geometric configurations of the container (cylindrical / bi-periodic and its size), and the particle shape and its size (TAB. 4.3). In this work, we only use a planar 2D square insertion window and an insertion point (see FIG. 4.5 for reference).

According to an analysis of variance (ANOVA), the void fraction difference is statistically non zero. A larger window results in a higher void fraction. We propose the following mechanism: a larger window results in more particles inserted simultaneously, leaving less time for a particle at the top of the stack to reach the most stable position before the arrival of the subsequent ones. The standard deviation on the void fraction difference is 0.0049.

Choosing the proper insertion geometry is a matter of compromise for the several reasons. First, none of the methods is more realistic than another: in the laboratories, reactor loading is not standardized and is often manual. A change in particle size while keeping the insertion window size the same results in a change in the number of particles that are inserted simultaneously, which yields more or less compact beds. An obvious geometrical constraint is that the insertion window must be smaller than the reactor: smaller reactors need smaller insertion windows which leads to denser beds. This is similar to the reduction of the funnel diameter during an experimental loading. Last, a small insertion window requires a long loading time,



(a) An insertion window of 4 mm length in a cylindrical vessel of 14 mm diameter.

(b) An insertion window of 6 mm length in a cylindrical vessel of 14 mm diameter.

Figure 4.5 – Top view of two simulation domains with their corresponding insertion windows.

Case	Window 1 length [mm]	Window 2 length [mm]	Void fraction difference ($\times 10^{-3}$)
D14-CYL-L4, $d_p = 1.8$	4	6	0.3
D14-CYL-L3, $d_p = 1.6$	0	4	14.8
D14-CYL-L3, $d_p = 1.6$	0	6	6.9
D14-CYL-L3, $d_p = 1.6$	4	6	7.9
D14-CYL-L3, $d_p = 1.6$	4	6	7.4
D16-CYL-L3, $d_p = 1.8$	4	6	3.4
D16-CYL-L3, $d_p = 1.6$	4	6	0.7
D16-CYL-L3, $d_p = 1.8$	4	6	1.8
BIP16-CYL-L3, $d_p = 1.6$	4	10	5.8
BIP18-CYL-L3, $d_p = 1.4$	4	10	6.6
BIP16-CYL-L3, $d_p = 1$	4	10	16.3
BIP18-QL-L3, $d_p = 1.9$	7	10	1.9
BIP18-QL-L3, $d_p = 2.2$	6	10	6.9
		Average	6.2
		Std dev.	4.9

Table 4.3 – Effect of insertion window size on void fraction. Insertion window is 2D square of length comprised between 0 mm to 10 mm.

whereas a larger one permits a fast loading. In order to decrease the computing time, the simulations are performed with a medium size planar square insertion window (4 mm and 6 mm wide) that fits in all geometries. This choice will overestimate the void fraction compared to a point insertion and underestimate the void fraction for large particles. If we assume that this insertion effect can be modelled by a Gaussian random variable (of null average), then its standard deviation σ_2 must be equal to $1/\sqrt{2}$ of the standard deviation of the “void fraction difference” (see Appendix for details): $\sigma_2 = 0.00346 = 0.0049/\sqrt{2}$. σ_2 measures the unknown bias on the simulation induced by the choice of the insertion window size.

3.3 Overall uncertainty

An overall uncertainty on a single void fraction simulation result can now be estimated from σ_1 (random initial conditions) and σ_2 (bias induced by insertion window size). As both un-

certainties are independent, a classical measurement statistic theory gives an estimate of the overall standard deviation: $\sigma = \sqrt{\sigma_1^2 + \sigma_2^2} = 0.0054$. An estimation of the overall uncertainty on a single measurement I is $I = 2\sigma = 0.011$ (see Appendix for details). According to this analysis, there is a 95% probability that, given the output ϵ of a single experiment, the average void fraction of a large number of simulations falls in the interval $\epsilon \pm 0.011$ (with $\epsilon = 0.42$, this gives an estimate of 0.409 and 0.431). In other words, this corresponds to a relative uncertainty on the void fraction of less than 2.5%.

4 RESULTS

4.1 Bi-periodic container

The average void fraction for various shapes, length and diameters simulated in a bi-periodic container are presented in FIG. 4.6. This case corresponds to large containers similar to industrial reactors. The void fraction is linearly correlated with particle aspect ratio (L_p/d_p). Bulkier, rounder particles are easier to pack, whereas cylindrical particles present a lower void fraction and lower dependence on the aspect ratio than poly-lobed shapes. Surprisingly, the void fraction of trilobes and quadrilobes can not be distinguished.

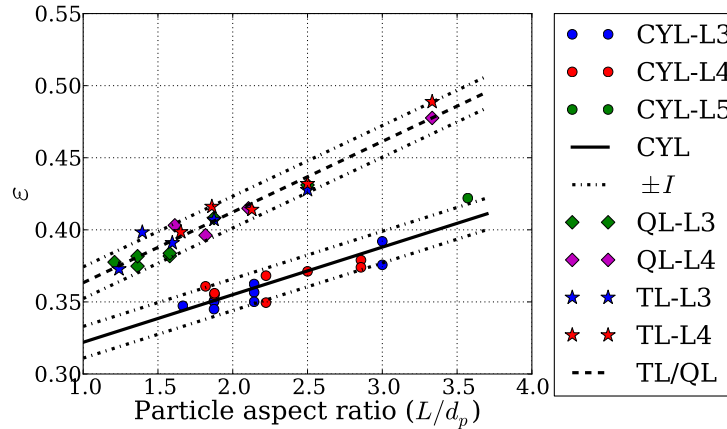


Figure 4.6 – Average void fraction in a bi-periodic container for particles of various shape, length and diameter.

Two correlations are proposed to predict the void fractions in large containers with an accuracy better than the overall uncertainty:

$$\text{CYL: } \epsilon = 0.289 + 0.033 \frac{L_p}{d_p} \quad (4.9)$$

$$\text{TL \& QL: } \epsilon = 0.314 + 0.049 \frac{L_p}{d_p} \quad (4.10)$$

In FIG. 4.6 the slope for the poly-lobed particles is much larger than that of the cylindrical ones. We suggest that during the packing, the lobes hinder rotation and result in a quick damping of the vibrations induced by impacts. This results in less compact beds for poly-lobed particles.

Extending the trends to near spherical shape ($L_p/d_p = 1$) leads to a void fraction of 0.32 (CYL) and 0.36 (TL/QL) which are values close to dense packings of spheres.

4.2 Cylindrical container

Cylindrical particles

The void fraction of a packed bed of cylindrical particles in a cylindrical reactor is in line with experimental measurements [Leva and Grummer \(1947\)](#) (our values are in the range of $d_p/D < 0.3$). It increases with the particle aspect ratio and seems to decrease with increasing reactor diameter D . However in the studied range, the effect is barely larger than the repeatability. Following [Leva and Grummer \(1947\)](#), whose results suggest a proportional relationship to the inverse of vessel diameter, we propose the correlation in EQ. 4.11. It describes all the data set with a maximum absolute error of 0.014 and a standard deviation of 0.006, which is about half of the uncertainty (FIG. 4.7). The correlation is written as follows:

$$\text{CYL: } \varepsilon = 0.315 + 0.0244 \frac{L_p}{d_p} + 0.141 \frac{L_p}{D} \quad (4.11)$$

$$10 < D[\text{mm}] < 19, \quad 1 < L_p/d_p < 5, \quad 3 < L_p[\text{mm}] < 4$$

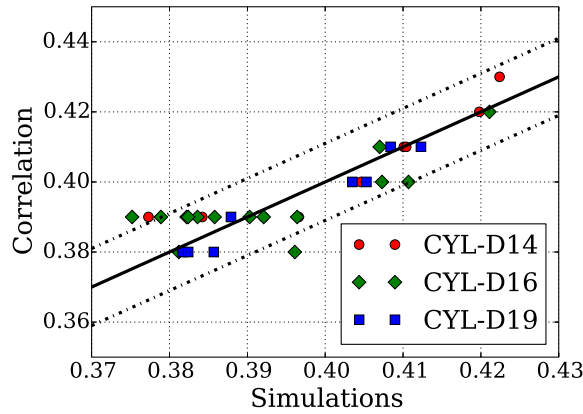


Figure 4.7 – Void fraction for packed beds of cylindrical particles in a cylindrical reactor for various reactor diameters, particle lengths and aspect ratios: correlation vs. simulations. Dashed lines are parity ± 1 .

In our data range, a simplified correlation that does not take into account the cylindrical vessel diameter predicts the void fraction (EQ. 4.12) with good accuracy (standard deviation of 0.0077).

In our limited diameter range, a simplified correlation that does not take into account the reactor diameter predicts the void fraction with a slightly higher identical relative standard deviation (2%). It reads:

$$\text{CYL: } \varepsilon = 0.327 + 0.033 \frac{L_p}{d_p} \quad (4.12)$$

$$10 < D[\text{mm}] < 19, \quad 1 < \frac{L_p}{d_p} < 5, \quad 3 < L_p[\text{mm}] < 4$$

Poly-lobed particles

The following linear correlation (EQ. 4.13) predicts the void fraction with a lower accuracy (equal to the uncertainty) (see FIG. 4.8):

$$\text{QL: } \varepsilon = 0.33 + 0.0328 \frac{L_p}{d_p} + 0.212 \frac{L_p}{D} \quad (4.13)$$

$$10 < D[\text{mm}] < 19, \quad 1.2 < L/d_p < 3.33, \quad 3 < L_p[\text{mm}] < 4$$

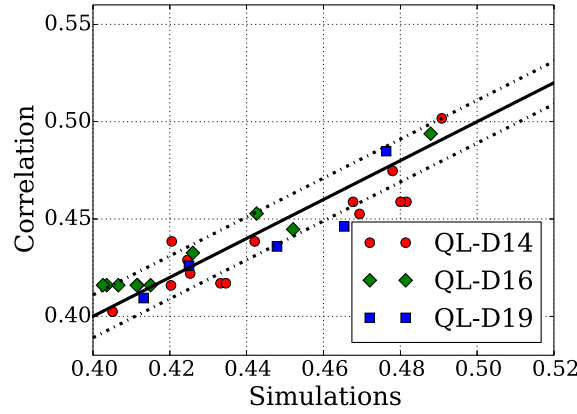


Figure 4.8 – Void fraction for packed beds of quadralobal particles in a cylindrical reactor for various reactor diameters, particle lengths and aspect ratios: correlation vs. simulations. Dashed lines are parity ± 1 .

The results for TL particles are presented in FIG. 4.9. The following linear correlation (EQ. 4.16) describes the data with an accuracy equal to the uncertainty:

$$\text{TL: } \varepsilon = 0.345 + 0.0289 \frac{L_p}{d_p} + 0.15 \frac{L_p}{D} \quad (4.14)$$

$$10 < D[\text{mm}] < 19, \quad 1.2 < L/d_p < 3.3, \quad 3 < L_p[\text{mm}] < 4$$

A simplified correlation based only on aspect ratio predicts almost as well void fractions with relative standard deviation of 2.5%. It reads:

$$\text{TL: } \varepsilon = 0.366 + 0.035 \frac{L_p}{d_p} \quad (4.15)$$

A unified correlation predicting the void fraction for TL and QL regardless of the shape has the same accuracy as that of the TL. It is defined as follows:

$$\text{QL \& TL: } \varepsilon = 0.329 + 0.0289 \frac{L_p}{d_p} + 0.15 \frac{L_p}{D} \quad (4.16)$$

$$10 < D[\text{mm}] < 19, 1.2 < L_p/d_p < 3.33,$$

$$2 < L_p[\text{mm}] < 4, 1.2 < d_p[\text{mm}] < 2.48$$

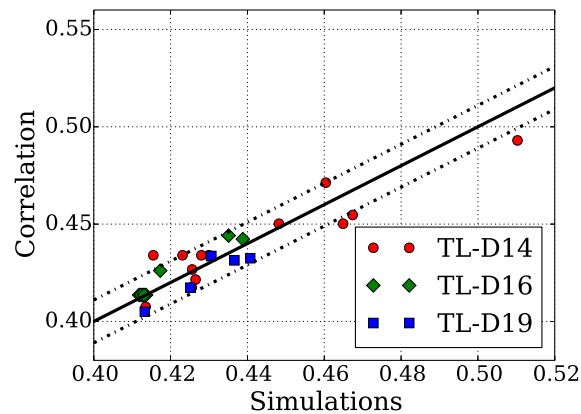


Figure 4.9 – Void fraction for TL packed beds for various reactor diameters, particle lengths (not shown) and aspect ratio.

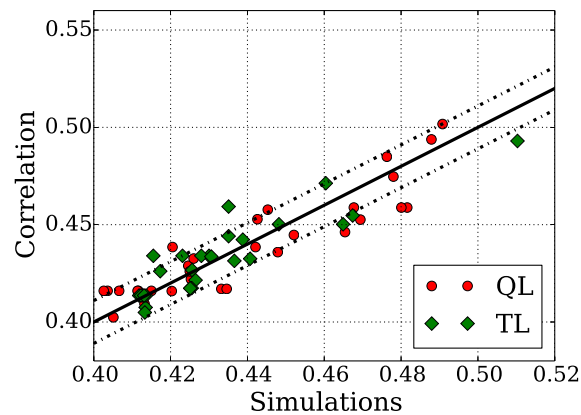


Figure 4.10 – Comparison of a unified correlation with numerical simulations for TL and QL in small size cylindrical reactors.

5.1 Effect of domain size in bi-periodic directions?

Most of the bi-periodic simulations have been performed with a domain with a transverse size of 18 mm. 4 simulations have been repeated using smaller domains (8 mm and 10 mm) with CYL and QL with an aspect ratio 3. The void fraction in smaller domains is within the repeatability of that in the large domain with a transverse size of 18 mm. We have so far no indication of an effect of bi-periodic domain size in the range 8 mm to 18 mm. It seems that performing simulations in the chosen domains does not impose any particular micro-structure in the bed with a wave length correlated to the transverse domain size. Simulation results indicate that even a transverse size of 8 mm is large enough to represent an infinitely large domain in the transverse direction.

5.2 Remark on the effect of container size

For all three particle shapes (CYL, TL and QL), the void fraction is higher in small reactors than in semi-infinite vessels as expected. When the reactor diameter increases, none of the correlations for cylindrical reactors so far converges to the correlation proposed for infinite

vessels. This was however expected as our cylindrical reactors are quite small compared to the particle length. In fact, the minimum L_p/D in our simulations is $3/18 = 0.167$, which suggests that wall effects are strong in these small reactors. To get asymptotically vanishing wall effects in a reactor, L_p/D is probably required to be at least as small as 0.05.

More simulations at large reactor diameters and probably non-linear relationships would be necessary to propose a unified correlation.

6 CONCLUSION

DEM has been used to prepare packed beds of poly-lobed particles. Although the simulations are deterministic, random input parameters (location and orientation of particles) as well as simulation parameters (insertion window) lead to an overall uncertainty that has been estimated at 0.0011. A subsequent analysis of the void fraction and its dependence on the particle shape and reactor size showed that TL and QL present statistically identical void fractions. The effects of random insertion, i.e. filling procedure, in packed beds mask the shape induced effect for optimised particles. We suggested linear correlations to predict the void fraction for cylinders, trilobes and quadralobes in semi-infinite and small size cylindrical reactor that showed a reasonably satisfactory level of reliability. More simulations and probably non-linear regressions are necessary to unify these correlations.

Ranking TL and QL and their chemical efficiencies are not possible based only on void fraction. A precise knowledge of the relationship between shape and pressure drop is necessary to conclude. An ongoing work is to perform a similar study on poly-disperse beds. Another ongoing work is to use Direct Numerical Simulation to evaluate the pressure drop in beds of poly-lobed particles, which is an extension of the work presented in [Dorai et al. \(2015\)](#). The next step will be the use of DNS in reactive flows as demonstrated in [Dorai et al. \(2014\)](#), which is probably more in the aim of assessing random induced uncertainty rather than predicting the fixed bed performance.

APPENDIX

In this work, simulations and measurements are deterministic and accurate. The resulting void fraction is different each time a simulation is performed with the same particles, but inserted with different (random) orientations and positions. Void fraction values appear as a random variable. Our interest is to compare the effects of shape on the void fraction. Thus we want to quantify how much of the difference between two simulations with different shapes are due to the shape or to the random insertion effects.

By definition, the uncertainty is the value I so that 95% of the random values of the void fraction will be within $\pm I$ of the average. With a Gaussian probability law, this definition is equivalent to $I = 1.96\sigma$ which is classically simplified to $I = 2\sigma$. In mathematical terms, 95% of the area under the Gaussian probability curve is within average $\pm I$. In our study, the effect of particle position and orientation is estimated by repeating simulations and estimating the standard deviation.

The standard deviation of the sum or difference of two independent Gaussian random variables is given by $\sigma_{X-Y} = \sigma_{X+Y} = \sqrt{\sigma_1^2 + \sigma_2^2}$, yielding $\sigma_{X-Y} = \sigma_{X+Y} = \sigma_X\sqrt{2}$ when $X1$ and $X2$ follow the same probability law with standard deviation σ_X . The effect of insertion window size is estimated using the difference between two simulations, hence the introduction of a $\sqrt{2}$ in the calculations.

RÉSUMÉ

Dans ce chapitre, le modèle *glued convex* est utilisé pour optimiser les formes de particules rencontrées dans l'industrie du raffinage. L'intérêt de ce chapitre est particulièrement porté sur la mise en évidence des différences sur le taux de vide dans des réacteurs à lit fixe en fonction des formes des particules (ici, cylindre, trilobe et quadrilobe), du mode d'insertion des particules et enfin la quantification de l'aspect aléatoire de la procédure de remplissage des réacteurs. En effet, Grains3D dispose d'un algorithme qui joue le rôle de fenêtre d'insertion de particules dans le système étudié. Les particules sont créées avec une orientation aléatoire et tombent dans les réacteurs une par une si la taille caractéristique de la fenêtre est du même ordre que celle des particules ou par pluviation si elle est de quelques ordres de grandeur de celle des particules.

Le taux de vide dans un lit est calculé à l'aide d'une discrétisation spatiale du système étudié. Cette méthode repose ensuite sur l'aspect parallèle du code Grains3D pour la prise en compte de gros systèmes ainsi que pour l'accélération des simulations.

Ce chapitre a alors permis de mettre en évidence que les taux de vide calculés sont statistiquement identiques pour les particules multi-lobées et sont différents de ceux des particules cylindriques dans les mêmes conditions. Grâce à ces observations, des corrélations linéaires ont été mises en place pour prédire le taux de vide dans des réacteurs à lit fixe.

GRAINS₃D: A MASSIVELY PARALLEL 3D DEM CODE

5

CONTENTS

1	INTRODUCTION	70
2	NUMERICAL MODEL	71
3	DOMAIN DECOMPOSITION PARALLEL STRATEGY	72
4	COMPUTATIONAL PERFORMANCE	77
4.1	Assessing memory management on multi-core node architecture	77
4.2	Granular slumping	85
4.3	Coupling with a fluid in an Euler/Lagrange framework, application to fluidized beds	91
5	DISCUSSION AND PERSPECTIVES	97

This chapter has been submitted for publication in *Powder Technology*:

A. D. Rakotonirina, A. Wachs. Grains₃D, a flexible DEM approach for particles of arbitrary convex shape - Part II: parallel implementation and scalable performances.

In this paper, we present the parallelisation strategy to be able to handle large numbers of particles. We also present simulations on silo discharge, dam breaking, fluidization.

ABSTRACT

IN [Wachs et al. \(2012\)](#) we suggested an original Discrete Element Method that offers the capability to consider non-spherical particles of arbitrary convex shape. We elaborated on the foundations of our numerical method and validated it on assorted test cases. However, the implementation was serial and impeded to examine large systems. Here we extend our method to parallel computing using a classical domain decomposition approach and inter-domain MPI communication. The code is implemented in C++ for multi-CPU architecture. Although object-oriented C++ offers high-level programming concepts that enhance the versatility required to treat multi-shape and multi-size granular systems, particular care has to be devoted to memory management on multi-core architecture to achieve reasonable computing efficiency. The parallel performance of our code Grains3D is assessed on various granular flow configurations comprising both spherical and angular particles. We show that our parallel granular solver is able to compute systems with up to a few hundreds of millions of particles. This opens up new perspectives in the study of granular material dynamics.

1 INTRODUCTION

Discrete Element Method (DEM) based simulations are a very powerful tool to simulate the flow of a granular media. The foundations of the method were introduced by [Cundall and Strack \(1979\)](#) in the late seventies. Originally developed for contacts between spherical particles, the method was later extended to polyhedra by [Cundall \(1988\)](#). The conceptual simplicity combined with a high degree of efficiency has rendered DEM very popular. However, there are essentially still two bottlenecks in DEM simulations: (i) the non-sphericity of most real life particles and (ii) the generally large number of particles involved even in a small system.

In [Wachs et al. \(2012\)](#) we addressed issue (i), i.e., the non-sphericity of particles by reviewing the various existing techniques to detect collisions between two non-spherical particles and by suggesting our own collision detection strategy that enables one to consider any convex shape and any size. Issue (ii) can be tackled in two different and complementary ways. The former involves improving the computational speed of classical serial implementations of DEM. This can be achieved by a higher quality programming and smarter algorithms, but there is admittedly a limit in that direction, even with the most advanced implementations. The latter involves dividing the work load between different computing units and hence using distributed computing. Nowadays, there are two competing technologies for DEM distributed computing: CPU ([Walther and Sbalzarini \(2009\)](#), [Iglberger and Rde \(2009; 2011\)](#)) vs GPU ([Radeke et al. \(2010\)](#), [Govender et al. \(2015\)](#)). Both technologies have assets and drawbacks. While GPU is parallel in essence (multi-threaded), fast on-chip memory is limited in size and global memory access is very slow, which can result in a weak performance of the code ([Govender et al. \(2015\)](#)). Besides, the built-in parallelism of GPU is not designed (yet) for multi-GPU computations, which limits the overall performance to that of a single GPU, in particular in terms of system size, i.e., number of particles. Conversely, CPU-based DEM codes, generally implemented with a domain decomposition technique, exhibit no limit in number of communicating CPUs (cores) and hence no limit in number of particles, provided the scalability is maintained at a reasonable level. Communications between cores is generally achieved using the Message Passing Interface (MPI) ([Gropp et al. \(1999\)](#)). While simulations with up to a few tens to hundreds of thousands of particles is attainable with GPU-based implementations ([Radeke et al. \(2010\)](#), [Govender et al. \(2015\)](#)), simulations with up to a few billions of particles can be envisioned with CPU-based implementations, provided computational practitioners

have access to large supercomputers with many thousands of cores (Walther and Sbalzarini (2009), Iglberger and Rde (2009; 2011)). The forthcoming new GPU technology is likely to offer similar parallel computing capabilities as CPU by improving inter-GPU communications but at the time we write this article, this enhanced GPU technology is not available yet.

The primary motivations for developing a parallel implementation of a serial code is either (i) to lower the computing time for a given system size by using more cores or (ii) to increase the size of the simulated system for a given computing time. In general, it is rather hard to define what is a "rationally acceptable computing time". Talking about the number of particles that one can simulate on a single-core computer in number of minutes/hours/days is meaningless without mentioning as well the time step magnitude and simulated physical time. In other words, the only rational measure of performance is the wall clock time per time step and per particle. Ironically, a highly efficient serial implementation might not scale well in parallel as the communication overhead will be significant, and conversely a time consuming (and/or badly programmed) serial implementation might scale much better. Obviously, this statement is not an incentive to write poor serial implementation or slow collision detection algorithm to get at a later stage a good scalability but simply underlines the fact that systems made of non-spherical particles have a chance to scale better than systems comprising spheres, as the collision detection step is a local (in the sense on each core without any communication) time-consuming operation.

Our goal in the paper is to elaborate on a simple domain decomposition based parallel extension of our granular code Grains3D and to assess its computing performance on systems of up to a few hundreds of millions of particles. In *Section 3*, we quickly recall the features of our numerical model as already explained in Wachs et al. (2012). We then present our parallel strategy in *Section 3*. In *Section 4* we measure the computing performance of our parallel implementation in various granular flow configurations (particle shape, particle load by core, weak scalability). Finally, we discuss parallel computing performances exhibited by Grains3D in *Section 5* and highlight the remaining intrinsic limitations of Grains3D and how to relax them.

2 NUMERICAL MODEL

The motion of the granular material is determined by applying Newton's second law to each particle $i \in \llbracket 0, N - 1 \rrbracket$, where N is the total number of particles. The rigid body motion assumption leads to the decomposition of the velocity vector \mathbf{v} as $\mathbf{v} = \mathbf{U} + \boldsymbol{\omega} \wedge \mathbf{R}$, where \mathbf{U} , $\boldsymbol{\omega}$ and \mathbf{R} denote the translational velocity vector of the center of mass, the angular velocity vector of the center of mass and the position vector with respect to the center of mass, respectively. The complete set of equations to be considered is the following one:

$$M_i \frac{d\mathbf{U}_i}{dt} = \mathbf{F}_i \quad (5.1)$$

$$\mathbf{J}_i \frac{d\boldsymbol{\omega}_i}{dt} + \boldsymbol{\omega}_i \wedge \mathbf{J}_i \boldsymbol{\omega}_i = \mathbf{M}_i \quad (5.2)$$

$$\frac{d\mathbf{x}_i}{dt} = \mathbf{U}_i \quad (5.3)$$

$$\frac{d\boldsymbol{\theta}_i}{dt} = \boldsymbol{\omega}_i \quad (5.4)$$

where M_i , \mathbf{J}_i , \mathbf{x}_i and $\boldsymbol{\theta}_i$ stand for the mass, inertia tensor, center of mass position and angular position of particle i . \mathbf{F}_i and \mathbf{M}_i are the sum of all forces and torques applied on particle i , respectively, and can be further decomposed in purely granular dynamics (i.e., without

accounting for any external forcing as e.g. hydrodynamic or electrostatic) into a torque-free gravity contribution and a contact force contribution as:

$$\mathbf{F}_i = M_i \mathbf{g} + \sum_{j=0, j \neq i}^{N-1} \mathbf{F}_{ij} \quad (5.5)$$

$$\mathbf{M}_i = \sum_{j=0, j \neq i}^{N-1} \mathbf{R}_j \wedge \mathbf{F}_{ij} \quad (5.6)$$

where \mathbf{F}_{ij} is the force due to collision with particle j and \mathbf{R}_j is a vector pointing from the center of mass of particle i to the contact point with particle j . In our model, \mathbf{F}_{ij} comprises a normal Hookean elastic restoring force, a normal dissipative force and a tangential friction force.

The set of equations EQ. 5.1-EQ. 5.4 is integrated in time using a second order leap-frog Verlet scheme. Rotations of particles are computed using quaternions for computational efficiency as well as to avoid any gimbal lock configurations. The collision detection algorithm is a classical two-step process. Potential collisions are first detected via a linked-cell list and then actual collisions are determined using a GJK algorithm. Our GJK-based collision detection strategy enables us to consider any convex shape and size. For more detail, we refer the reader to Grains3D-Part I [Wachs et al. \(2012\)](#) and the references therein.

3 DOMAIN DECOMPOSITION PARALLEL STRATEGY

Our parallel strategy is classical and is based on a domain decomposition technique. We consider below only the case of a constant in time domain decomposition, assuming that we know how to guarantee a reasonable load balancing of number of particles between subdomains over the whole simulation. The extension to dynamic load balancing in granular flows with large particle volume fraction heterogeneities will be shortly discussed in [Section 5](#) as an extension of this work.

We employ a cartesian domain decomposition. Each process hosts a single subdomain and we hence define a cartesian MPI communicator using the `MPI_Cart_create` command. It is then very convenient to identify the neighbouring subdomains on each subdomain as well as to implement multi-periodic boundary conditions. On each subdomain, we construct a cartesian linked-cell list with an additional layer of cells at the boundary with neighbouring subdomain to serve as an overlapping zone. This overlapping zone hosts clone particles used to compute collisions with particles located on a neighbouring subdomain (process). As a consequence, cells in a linked-cell list are tagged based on their location on the subdomain: 0 = interior, 1 = buffer and 2 = clone, as illustrated on [FIG. 5.1](#). At each time step, clone particles are either created, deleted or updated. All particles are tagged based on the cell they belong to. Hence they constantly change status as they move in the subdomain. Corresponding operations are performed on neighbouring subdomains when a particle change status. For instance, if a particle moves from an interior cell (tag = 0) to a buffer cell (tag = 1), a clone particle (tag = 2) is automatically created on the neighbouring subdomain.

The serial code is implemented in C++ which equips us with the required versatility to handle multiple particle shapes and sizes, based on inheritance mechanism, virtual classes and dynamic typing. Each particle is an instance of a C++ class and all active particles on a subdomain, including particles in buffer and clone zones, are stored in a primary list. Two additional separate lists for buffer and clone particles, respectively, are also created. As a consequence, when information of buffer particles needs to be sent to a neighbouring subdomain, we first

loop on the list of buffer particles, extract the relevant information and copy it to a buffer memory container (a standard 1D array, i.e., a standard vector, of doubles or integers). Each subdomain keeps a list of reference particles corresponding to all the types of particle in the simulation. These reference particles store generic data as mass, moment of inertia tensor and geometric features, such that MPI messages contain velocity and position information only and their size is reduced to the minimum.

Assorted communication strategies between processes (subdomains) can be designed, ranging from the simplest strategy to the most advanced (to the best of our knowledge for a cartesian MPI decomposition) strategy. We list below the different strategies we implemented and tested, ranked in growing complexity:

- the `AllGatherGlobal` strategy
All processes send information from their buffer particles to all other processes, regardless of their location in the MPI cartesian grid using a `MPI_Allgather` command. A huge amount of useless information is sent, received and treated by each process. It is however a good starting point and performs well up to 8 (maybe 16) processes maximum.
- the `AllGatherLocal` strategy
All processes send information from their buffer particles to all their neighbouring processes. The amount of useless information is reduced, but it is still far from optimal. This can be achieved by creating local communicator for each process including itself and its neighbours and performing the `MPI_Allgather` command using this local communicator. This strategy performs reasonably well up to 16 (maybe 32) processes, but beyond the scalability markedly deteriorates.
- the `AllGatherLocal` strategy with non-blocking sending
The next level of sophistication consists in replacing the `MPI_Allgather` command performed on the local communicator by a first stage of non-blocking sending of messages with the `MPI_Isend` command combined with a classical blocking receiving stage with the `MPI_Recv` command. Incoming messages are first checked with the `MPI_Probe` command and their size is detected with the `MPI_Get_count` command such that the receiving buffer is properly allocated for each received message [Iglberger and Rude \(2009; 2011\)](#). Using non-blocking sending speeds up communications as the MPI scheduler can initiate the receiving operations even if the sending operations are not completed, but still a large amount of useless information is sent, received and treated.
- the adopted optimal strategy called `SendRecv_Local_Geoloc`
Not only cells (and hence particles belonging to these cells) are tagged in terms of their status (0 = interior, 1 = buffer and 2 = clone, see [FIG. 5.1](#)) but cells in the buffer zone are also tagged in terms of their location with respect to the neighbouring subdomains using a second tag, named `GEOLoc` for geographic location, that takes the 26 following values (whose meaning is rather obvious on a 3D cartesian grid as can be seen in [FIG. 5.2](#)): `EAST` & `WEST` in the x direction, `NORTH` & `SOUTH` in the y direction, `TOP` & `BOTTOM` in the z direction are the main neighbours, `NORTH_EAST`, `NORTH_WEST`, `SOUTH_EAST`, `SOUTH_WEST`, `NORTH_BOTTOM`, `NORTH_TOP`, `SOUTH_BOTTOM`, `SOUTH_TOP` are the edge neighbours, and `NORTH_WEST_TOP`, `NORTH_WEST_BOTTOM`, `SOUTH_WEST_TOP`, `SOUTH_WEST_BOTTOM`, `NORTH_EAST_TOP`, `NORTH_EAST_BOTTOM`, `SOUTH_EAST_TOP`,

SOUTH_EAST_BOTTOM are the corner neighbours. The aftermath is an exact tailoring of sent messages with the appropriate information only, thus reducing the size of each sent message to the minimum.

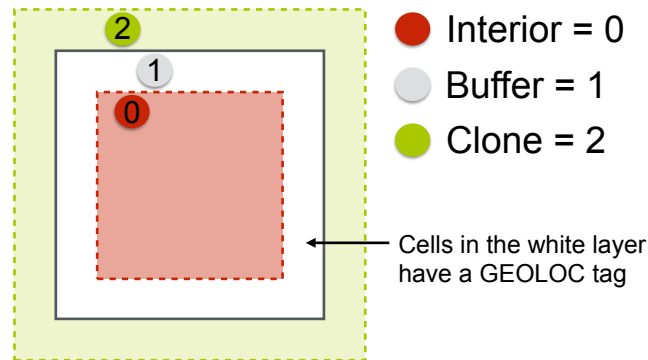


Figure 5.1 – Illustration of the status of a particle in a tagged cell.

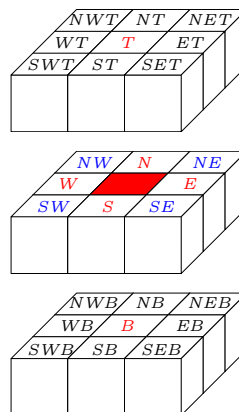


Figure 5.2 – Sketch of the communications between a cell in a buffer zone and its neighbouring cells with respect to the neighbouring subdomains. N, S, W, E, T and B denote respectively the North, South, West, East, Top and Bottom directions.

Depending on the particle's GEOLoc tag, information from a buffer particle is copied to one or more buffer vectors to be sent to neighbouring subdomains. There are essentially three situations as illustrated below:

- a buffer particle with a main GEOLOC tag: for instance a particle tagged SOUTH is sent to the SOUTH neighbouring subdomain only (FIG. 5.3),

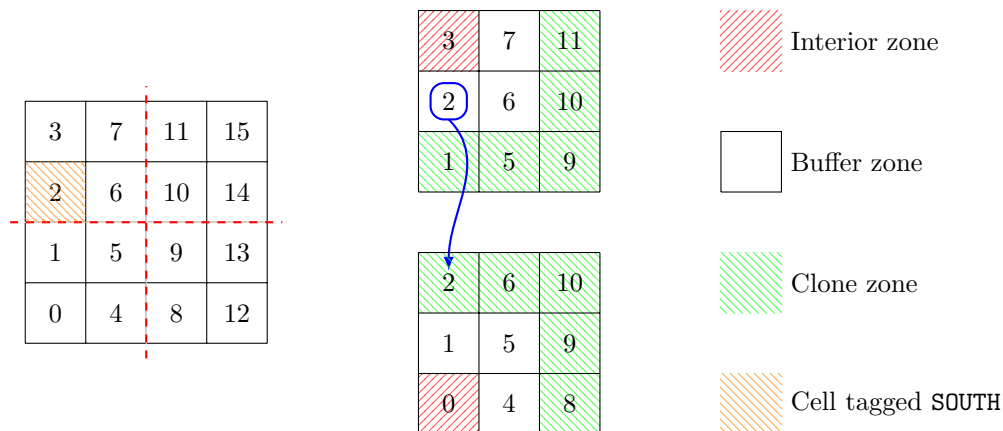


Figure 5.3 – 2D illustration of inter-process communication for a particle tagged SOUTH.

- a buffer particle with an edge GEOLOC tag: for instance a particle tagged SOUTH_EAST is sent to the SOUTH, EAST and SOUTH_EAST neighbouring subdomains only (FIG. 5.4),

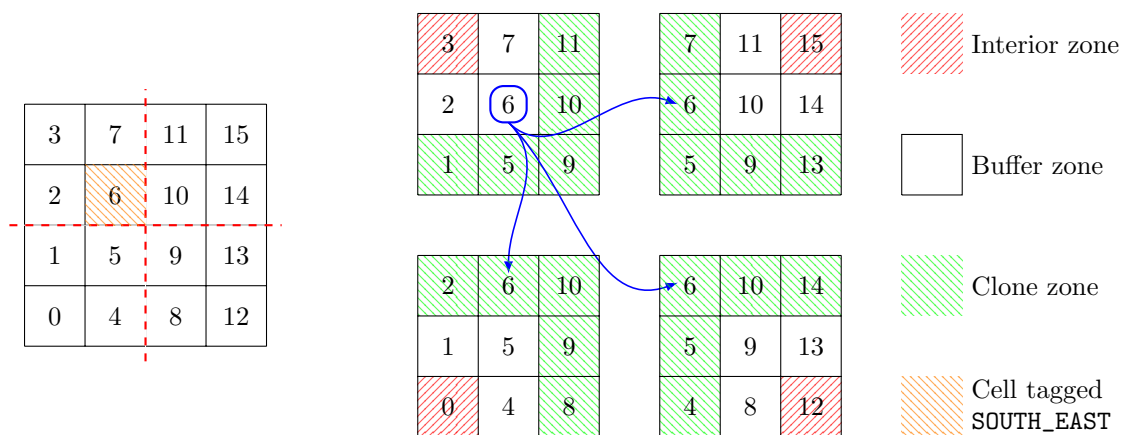


Figure 5.4 – 2D illustration of inter-process communication for a particle tagged SOUTH_EAST.

- a buffer particle with a corner GEOLOC tag: for instance a particle tagged SOUTH_WEST_TOP is sent to the SOUTH, WEST, TOP, WEST_TOP, SOUTH_WEST, SOUTH_TOP and SOUTH_WEST_TOP neighbouring subdomains only.

Similarly to the `AllGatherLocal` strategy, exchange of information between neighbouring subdomains is performed by a combination of non-blocking sending operations using `MPI_Isend` and blocking receiving operations using `MPI_Recv`.

The buffer vectors sent and received by processes are of the C double type. A buffer vector contains for each particle the following data: particle identity number, particle reference type, MPI rank of sending process, velocity, position and orientation for a total of 29 numbers. Particle identity number, particle reference type and MPI rank of sending process are integer numbers and are cast into double numbers such that all features can be concatenated into a single vector of doubles. Hence each process sends to and receives from another neighbouring process a single message containing a vector of doubles with the `MPI_DOUBLE` data

type (instead of sending and receiving separately in two different messages a vector of doubles with the `MPI_DOUBLE` data type and a vector of integers with the `MPI_INT` data type, respectively). Each message size is then 29 times the size of a double times the number of buffer particles with the appropriate `GEOLOC` tag. Due to the considerable latency involved in any MPI message, efficient parallel performance involves keeping the number of messages as low as possible. This explains why we cast integer to double as a way to avoid heterogeneous data types and/or twice more messages (the computing cost of the cast operation from integer to double when sending and back from double to integer when receiving is much smaller than the one associated to sending and receiving 2 messages instead of 1). Another option that we have not tried is to convert all data types to raw bytes and send a single vector of raw bytes using the `MPI_BYTE` data type. Each neighbouring process is then responsible to convert back the received raw byte messages to their original data types. This strategy has been successfully implemented in [Iglberger and Rde \(2009; 2011\)](#).

At each time step, the full solving algorithm on each subdomain reads as follows:

1. for all particles with status 0 or 1: initialize force to gravity and torque to 0
2. for all particles:
 - (i) detect collisions
 - (ii) compute contact forces & torques
3. for all particles with status 0 or 1:
 - (i) solve Newton's law: EQ. 5.1 for translational velocity and EQ. 5.2 for angular velocity
 - (ii) update position EQ. 5.3 and orientation EQ. 5.4
4. search for particles whose status changed from 0 to 1 add them to the list of buffer particles
5. MPI step using the `SendRecv_Local_Geoloc` strategy (in the 3D general case of 26 neighbouring subdomains):
 - (i) copy buffer particles features into the different buffer vectors of doubles depending on their `GEOLOC` tag,
 - (ii) perform non-blocking sendings of each of the 26 buffer vectors of doubles to the corresponding neighbouring subdomains,
 - (iii) for $j = 0$ to 25 (i.e., for each of the 26 neighbouring subdomains):
 - (I) perform a blocking receiving of the vector of doubles sent by neighbouring subdomain j ,
 - (II) Treat the received vector of doubles containing particles information
 - Create or update clone particles
 - Delete clone particles moved out of the subdomain
6. for all particles: based on their new position, update status and `GEOLOC` tags and the corresponding lists of buffer and clone particles

4 COMPUTATIONAL PERFORMANCE

In this section, we assess the computational performance of our parallel DEM code Grains3D on assorted flow configurations in which load balancing in terms of number of particles per subdomain (process) is approximately constant over the whole simulation. All the test cases considered thereafter are fully three-dimensional. In all computations, each core hosts a single subdomain and a single process. Hence, the terms “per core”, “per subdomain” and “per process” are equivalent. Computations are performed on a 16-core per node supercomputer.

Our primary goal is to compute larger systems for a given computing time. We therefore assess the computational performance of Grains3D in terms of weak scaling. We compute the parallel scalability factor $S(n)$ by the following expression:

$$S(n) = \frac{T(1, N)}{T(n, N \times n)} \quad (5.7)$$

where $T(1, N)$ denotes the computing time for a problem with N particles computed on a single core or a single full node and $T(n, N \times n)$ denotes the computing time for a similar problem with $N \times n$ particles computed on n cores or nodes.

4.1 Assessing memory management on multi-core node architecture

Discharge flow in silos

The first test case is a discharge of particles from a silo. Before performing weak scaling tests, we validate our DEM solver versus experimental data. For that purpose, we select the work of [González-Montellano et al. \(2011\)](#) as a reference because of its conceptual simplicity. Their study consists in comparing their own DEM simulation results to experimental data of spherical glass beads of 13.8 mm diameter discharging from a silo. The silo has a 0.5 m height (H) and 0.25 m sides (L) (FIG. 5.5a). The bottom has a truncated pyramid shape with a square hopper opening of 57 mm sides whose walls make an angle $\theta = 62.5^\circ$ with respect to the horizontal plane. In our simulations, we extend the bottom of the silo to collect all particles flowing through the opening of the hopper (see FIG. 5.5b). Obviously, this does not affect the discharge dynamics and rate.

As in [González-Montellano et al. \(2011\)](#), we fill the silo with 14000 spherical particles by performing a first granular simulation with the opening of the hopper sealed by a plate. In this preliminary simulation, we insert all particles together as a structured array in order to reduce the computing time (see FIG. 5.6 at $t = 0$). To this end, we extend the height of the silo in a way that all particles fit into the silo before they start to settle. The initial particles positions at the insertion time are actually slightly perturbed with a low amplitude random noise in order to avoid any artificial microstructural effect. Particles then settle by gravity and collide until the system reaches a pseudo steady state corresponding to a negligible total kinetic energy (see FIG. 5.6 at $t = T_{fill}$). As observed in [González-Montellano et al. \(2011\)](#), the 14000 spherical particles fill the silo up to $H_m \simeq 0.86H$. After the filling of the silo, the plate that blocks the particles is removed by imposing a fast translational frictionless displacement to start the discharge. Simulations are run until all particles have exited the silo (see FIG. 5.6 at $t = T_{dis}$).

As in [Wachs et al. \(2012\)](#) our contact model is the linear damped spring with tangential Coulomb friction for both particle-particle and particle-wall contacts. The magnitude of the parameters involved in the silo discharge simulations is given in TAB. 5.1. In [Wachs et al. \(2012\)](#), we elaborated on the fact that the spring stiffness k_n in our contact model can be linearly related to the Young modulus E of the material. Since the contact duration is inversely proportional to k_n , a high E leads to a short contact duration, and hence a correspondingly small

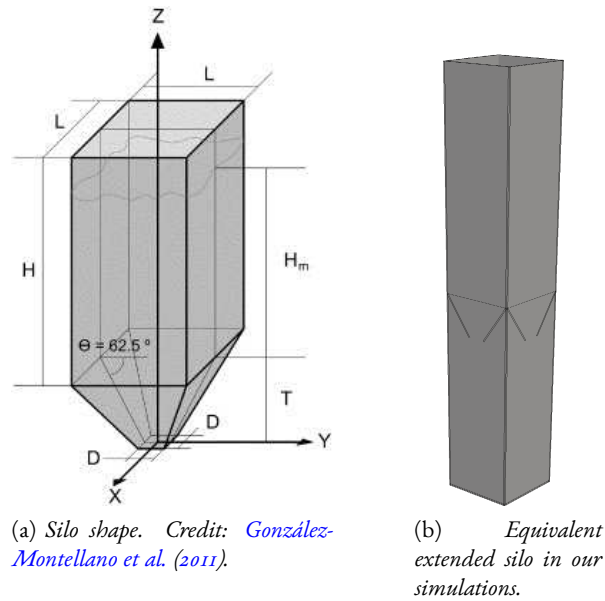


Figure 5.5 – Shape and dimensions of the 3D silo.

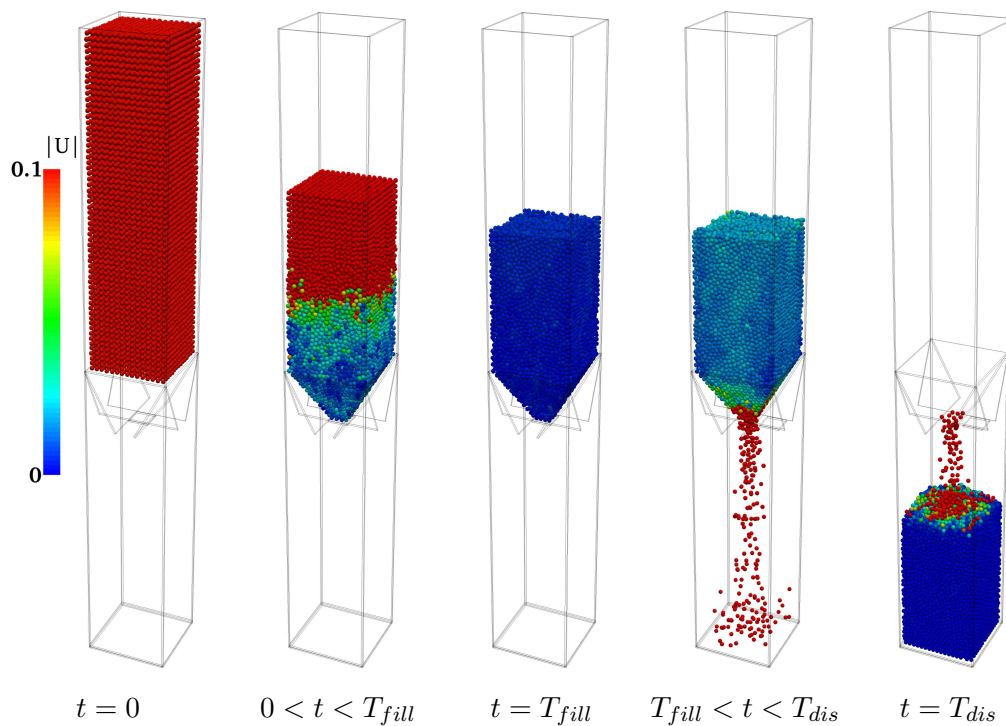


Figure 5.6 – Simulation results of filling and discharge of the 3D silo with Grains3D. Coloured by the particle velocity magnitude.

time-step Δt . For glass beads, the Young modulus E is approximately 50 GPa. It leads to a time step magnitude of the order of $\Delta t \sim 10^{-7} s$, which would require to compute an unnecessary large number of time steps to simulate the whole discharge of the silo. In fact, as explained in [Wachs et al. \(2012\)](#), the stiffness coefficient k_n is generally not set in accordance with Hooke's law and Hertzian theory, but rather in a way to control the maximum overlap between particles as they collide. The meaningful parameters from a physical viewpoint are

the coefficient of restitution e_n and the Coulomb friction coefficient μ_c . A smaller k_n enables us to use much larger time steps without affecting the whole dynamics of the system. This is rather customary in DEM simulations of non-cohesive materials. For more detail about how to determine k_n , the reader is referred to [Wachs et al. \(2012\)](#), [Cleary and Sawley \(2002\)](#), [Cleary \(2009; 2010\)](#) and the references therein. In [TAB. 5.2](#), the meaningful physical parameters e_n and μ_c are set to exactly same values as those selected by [González-Montellano et al. \(2011\)](#). Using an estimate of the maximum collisional velocity of $v_{col} = 4.5 \text{ m/s}$, the selected value of k_n leads to a maximum overlap distance of 3% of the sphere radius. Please note that this estimate is highly conservative as $v_{col} = 4.5 \text{ m/s}$ is the free fall velocity of particles as they collide with the bottom wall of the collecting bin underneath the hopper opening. In fact, the collecting bin height is $\approx 1 \text{ m}$, hence we get $\sqrt{2 \times 9.81 \times 1} \approx \sqrt{20} \approx 4.5 \text{ m/s}$. In the dense discharging granular material above the hopper opening, the actual collisional velocity is much less. As a result, the maximum overlap between colliding particles in this part of the granular flow is less than 0.1% of the sphere radius, a value commonly deemed to be a very satisfactory (and almost over-conservative) approximation of rigid bodies in DEM simulations.

Parameter	Value
Particle-Wall	
$k_n (N \text{ m}^{-1})$	1×10^6
$e_n, \mu_n (s^{-1})$	$0.62, 3.63 \times 10^3$
μ_c	0.3
k_{ms}	1×10^{-5}
$\delta_{max} (m), \delta_{max}/R$	$2.25 \times 10^{-4}, 0.033$
$T_C (s)$	1.85×10^{-4}
Particle-Particle	
$k_n (N \text{ m}^{-1})$	7.2×10^5
$e_n, \mu_n (s^{-1})$	$0.75, 1.87 \times 10^3$
μ_c	0.3
k_{ms}	1×10^{-5}
$\delta_{max} (m), \delta_{max}/R$	$1.92 \times 10^{-4}, 0.028$
$T_C (s)$	1.55×10^{-4}
$\Delta t (s)$	1×10^{-5}

Table 5.1 – Contact force model parameters, estimate of contact features at $v_{col} = 4.5 \text{ m/s}$ and time step magnitude used in the silo discharge simulation.

Repetition	Experiments (s)	Grains3D (s)
1	29.32	29.36
2	29.28	
3	29.2	
Mean discharge time (s)	29.27	29.36

Table 5.2 – Comparison between experimental data of [González-Montellano et al. \(2011\)](#) and our simulation results with *Grains3D* for the discharge time of the silo.

We report in [TAB. 5.2](#) the values of the discharge time experimentally measured by [González-Montellano et al. \(2011\)](#) together with our simulation result. [González-Montellano et al. \(2011\)](#) carried out three times the same experiment but it seems that the observed devia-

tion of the discharge time with respect to the mean value is very limited (of the order of 0.2%). In other words, the initial microstructure of the particles in the silo before removing the hopper gate is essentially similar and does not markedly affect the discharge process. Based on this observation, we perform a single discharge simulation. Our model shows a (even surprisingly) good agreement with the discharge time measured in the experiments of [González-Montellano et al. \(2011\)](#). Snapshots of the discharge process also exhibit a highly satisfactory agreement between our simulations and the experiments in [González-Montellano et al. \(2011\)](#), as presented in FIG. 5.7. Although our goal in this work is not to carry out an extensive analysis of the discharge, it is computationally cheap and important to validate our model and gain confidence in the computed results. We are now in a sensible position to perform weak scaling tests and assess the scalability properties of our parallel DEM solver.

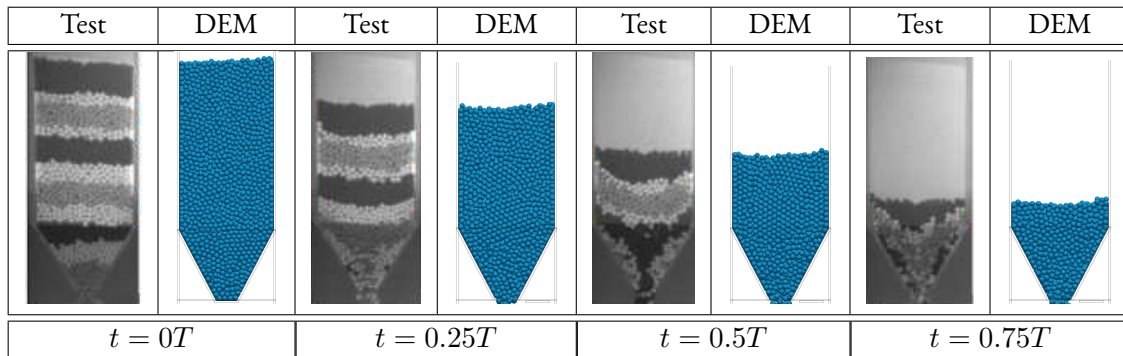


Figure 5.7 – Comparison between experimental data of [González-Montellano et al. \(2011\)](#) and our simulation results with *Grains3D*: snapshots of discharge dynamics at different times.

Parallel scalability

On the single-core architecture of the 90s, each core had its own levels of cache and its own random-access memory (RAM). The limitation of parallel implementations was hence essentially the communication overhead. This overhead depends on the MPI strategy (size of message, synchronous/asynchronous communication, blocking/non-blocking communication, etc). Since the early 2000s, the new emerging architecture relies on multi-core processors. In a supercomputer, these multi-core processors are bundled in computing nodes, i.e., a computing node hosts multiple processors that each hosts multiple cores. Cores share levels of cache on the processor they belong to and processors share RAM on the computing node they belong to. The aftermath is a more complex and competitive access to memory by all the cores of a computing node. Hence, parallel implementations running on modern supercomputers can be limited as much by the communication overhead as by the intra-processor and intra-node memory management and access. Our parallel DEM solver *Grains3D* is programmed in C++. C++ equips programmers with a formidable level of flexibility to handle multi-shape and multi-size granular flows with well-known object-oriented mechanisms as inheritance, virtual classes and dynamic typing. Another enjoyable tool of C++ is constructors and destructors that enables one to create and delete instances of object with a high level of control on memory allocation (provided the constructor and destructor are properly programmed). However, dynamic memory allocation/deallocation, even with absolutely no memory leak, can literally kill the parallel performance of a numerical code. This has nothing to do with inter- and intra-node MPI communications between cores but rather with the management and competitive access to memory. The first parallel version of *Grains3D* exhibited dramatically poor scalability properties. It took us a while to realize that the limitation was coming from an excessive use

of constructors/destructors while our MPI strategy was performing quite well from the start. Complete refactoring of the code with use of dynamic memory allocation/deallocation only when absolutely necessary and partial over-allocation strikingly improved the scalability properties. It is hard to get here into the details of our C++ implementation but Grains3D is now programmed with the following guidelines: (i) use object-oriented programming concepts at a very high level of design only, (ii) use standard old-fashioned C/F77-like containers whenever possible and (iii) slightly over-allocate memory and reduce to the absolute minimum dynamic memory management. There is still room for improvement in our implementation but we are now in a position to present acceptable parallel properties. It is this new version of the code with enhanced memory management that we assess the scalability properties of in the rest of the paper. In this section, we design two slightly different multi-silo discharge configurations in order to discriminate the computing overhead related to (i) memory competitive access and management and pure MPI communication latency from (ii) actual MPI communications and treatment of received information.

The first flow configuration consists in discharging particles from several silos using the previous configuration (FIG. 5.5). The multiple silos case is designed in a way that a silo is handled by a single core without any actual communication with neighbouring sub-domains (FIG. 5.8). In fact, silos are located far enough from each other to avoid the creation and destruction of clone particles. This flow configuration is hence illustrative of case (i): memory competitive access and management and MPI communication latency. In fact, the code runs in MPI but messages are empty. The overhead coming from MPI is hence essentially related to the latency of the MPI scheduler to send and receive messages. We adopt a two dimensional domain decomposition ($N_{cores,x} \times N_{cores,y} \times 1 = N_{cores}$) to guarantee exact load balancing between the cores. We evaluate the scalability of our code by gradually increasing the size of our system. To this end, we perform discharge simulations of 2, 000 cubic particles and 2, 000, 14, 000, and 100, 000 spherical particles per silo, starting from one silo till 256 silos. Varying the load of particles per core changes the amount of memory allocated, managed and accessed by the code on each core. This enables us to discriminate further between memory management and MPI latency so that the effects of these two factors are not mixed up. In fact, MPI latency is independent of the particle load as the number of messages sent and received scales with the number of cores. The total number of particles N_T in the system is a multiple of that in a single core system and is defined as follows:

$$N_T = N_{p,1} \times N_{cores} \quad (5.8)$$

where $N_{p,1}$ and N_{cores} are respectively the number of particles on a single core system and the number of cores. The largest system comprises $100, 000 \times 256 = 25, 600, 000$ of spherical particles. As the granular media is dense in most of the domain, the largest part of the computing time (more than 85%) is spent in computing interactions between particles, i.e., contact detection and contact forces. For the weak scaling tests, we run all discharge simulations over 300, 000 time steps. Reference times on a single core job are listed in TAB. 5.3. A first interesting comment about TAB. 5.3 is that the computing time per particle and per time step is not constant and slightly increases with the size of the system. Even when running in serial mode, memory access is apparently not optimal as containers of larger size (as e.g. a larger list of particles) seem to slow down the computation. Some additional efforts in refactoring the serial implementation of the code are required but this is beyond the scope of the present paper.

The second flow configuration is very similar except that right now all silos are merged together into a big silo. The whole domain is thus shared by each core and actual communications (in the sense of communications with non-empty messages) between sub-domains are exchanged (see FIGS. 5.9 and 5.10). For this purpose, we performed discharge simulations of

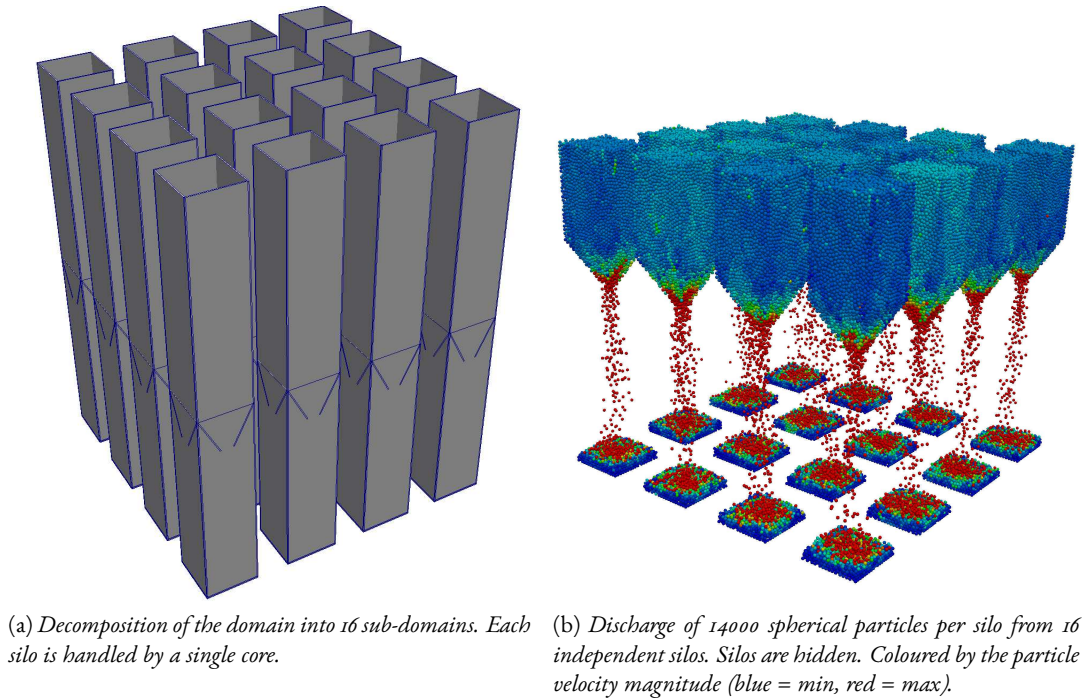


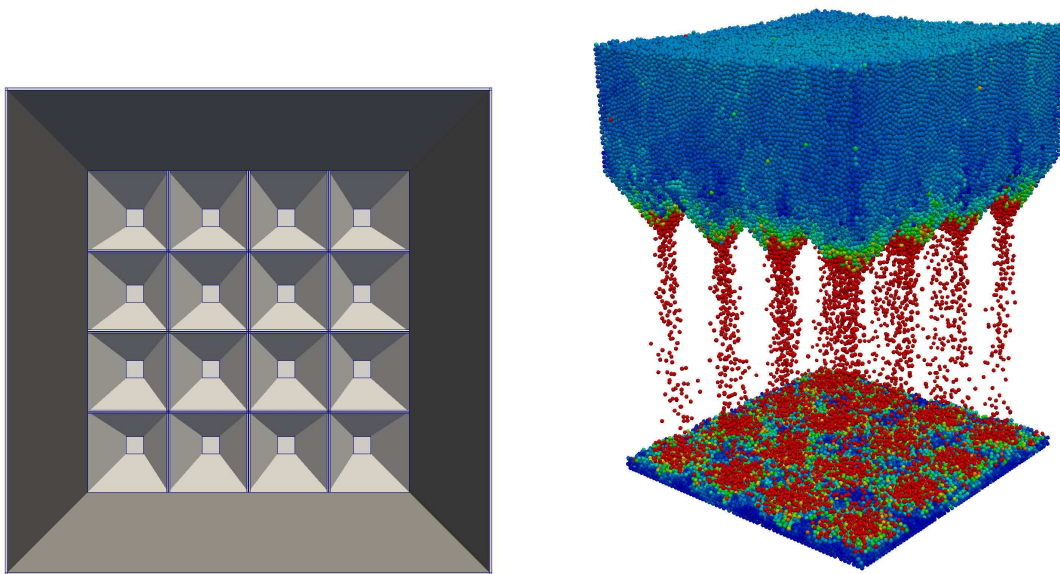
Figure 5.8 – Multi-silo simulation set-up without overlap between silos (communications with empty messages between sub-domains).

Configuration/core	Total computing time	Computing time per particle and per time step
2000 spheres	59min 56s	$6\mu s$
14000 spheres	12h 24min 27s	$10\mu s$
100000 spheres	104h 41min 12s	$12\mu s$
2000 cubes	3h 58min 32s	$24\mu s$
10000 cubes	30h 30min 16s	$36\mu s$

Table 5.3 – Silo discharge for different systems: reference times of a serial job over 300,000 time steps of 10^{-5} s.

10,000 cubic particles, 2,000, 14,000 and 100,000 spherical particles. As for the first flow configuration, a two dimensional domain decomposition is chosen such that each sub-domain has approximately the same number of particles as if the silos were independent. This hence guarantees again an almost perfect load balancing between the cores.

FIG. 5.11 illustrates the scalability of our code of these two flow configurations. At first sight, results are very similar without (separate silos) and with (merged silos into a big silo) actual communications. We plot in FIG. 5.11a the parallel performance of Grains3D on the first test case, i.e., without any overlap between separate silos and empty MPI messages. This figure indicates that for low numbers of particles per core, the limiting factor is clearly MPI latency while for high numbers of particle per core, the serial computations per core prevail and the MPI latency becomes negligible. Hence, the loss of performance is primarily related to a yet non-optimal memory access and management on multi-core architectures. However, for a high enough number of particles per core as e.g. 100,000 spheres, the scaling factor $S(n = N_{cores})$ is independent of n up to $n = 256$ cores and is around 0.85. As the contact detection of convex bodies is more time-consuming than that of spheres, $S(n)$ for cubes is



(a) Top view of the simulation domain in which 16 silos are merged into one big silo.

(b) Discharge of 16000 spherical particles per sub-domain from 16 connected hoppers. Hoppers are hidden. Coloured by the particle velocity magnitude (blue = min, red = max).

Figure 5.9 – Multi-silo simulation set-up with all silos merged (connected hoppers) into one big silo (actual communications with non-empty messages between sub-domains). Each hopper corresponds to a sub-domain.

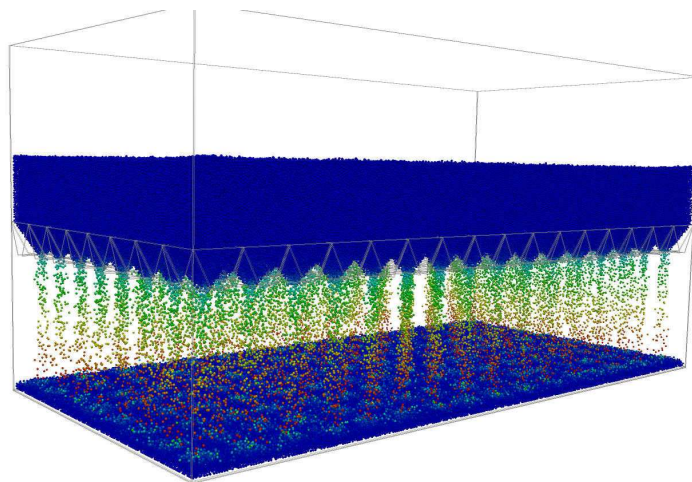


Figure 5.10 – Discharge of 1,792,000 spherical particles from 128 merged silos (connected hoppers). Coloured by the particle velocity magnitude (blue = min, red = max).

higher than $S(n)$ for spheres for the same number of particles per core. Hence, we expect that for more than 100,000 particles per core, the observed scaling factor of 0.85 for spheres is actually a lower bound and that the scaling factor for non-spherical particles should be higher. We plot in FIG. 5.11b the parallel performance of Grains3D on the second test case, i.e., a big silo split into sub-domains and non-empty MPI messages. The 2000 spheres per core is a special case as on each sub-domain there are almost as many particles on the actual sub-domain, i.e., interior and buffer zones, than in the clone layer, leading to a high global communication

overhead (size of messages and treatment of information received). This is getting worse and worse as the number of cores increases (see blue line in FIG. 5.11b). The general outcome is in line with the first test case with empty messages: for a large enough number of particles per core, the scaling factor $S(n)$ is satisfactory (it is actually 0.78 for 100,000 spheres and is likely to be higher for 100,000 non-spherical particles). This is again emphasized in FIG. 5.12 where we compare the communication overhead to the serial computational task for a sphere and a polyhedron. The difference shown there is primarily due to the contact detection that requires to use a GJK algorithm for non-spherical particles while it is analytical (and hence faster) for spheres (see Wachs et al. (2012) for more detail). Interestingly, for 100,000 spheres, the scaling factor $S(n)$ drops from 0.85 with empty messages to 0.78 with non-empty messages and treatment of the received information. Therefore, the actual overall parallel overhead is around 7% and the rest of the loss of performance, i.e., the remaining 15%, is predominantly due to non-optimal memory access and management on multi-core chips.

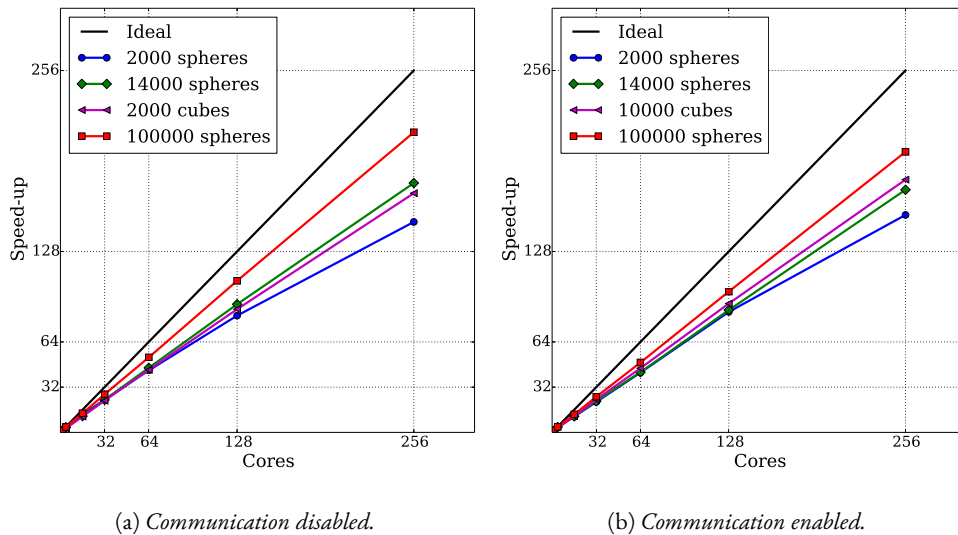


Figure 5.11 – Weak scaling parallel performance of Grains3D in the multi-silo configurations with (a) disconnected silos and (b) merged silos into one big silo.

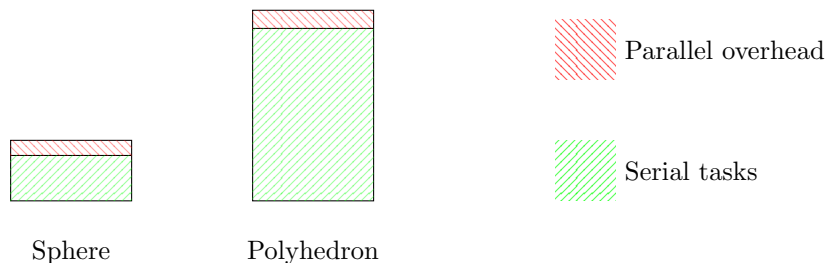


Figure 5.12 – Ratio between parallel overhead and serial tasks for systems made of spherical particles and polyhedral particles.

These two first test cases are extremely informative. They show that for a dense granular flow with a minimum load of 100,000 of particles per core, we can expect a good overall parallel performance with a scaling factor $S(n) \gtrsim 0.75$ on up to 512 to 1024 cores. Systems with a low particles load per core, i.e., of the order of a few thousands, show an unsatisfac-

tory, although not dramatically poor, parallel performance that exhibits the obvious tendency to degrade with the number of cores n . Overall, the MPI strategy presented in *Section 3* is deemed to perform very well while additional efforts in serial programming are required to improve memory access and management. Systems with up to 100,000,000 of particles can be computed with a scaling factor of at least 0.75, which is deemed to be very satisfactory for engineering and fundamental physics purposes.

4.2 Granular slumping

Dam break collapse

Granular column collapse is a very classical flow configuration to understand the fundamental dynamics of granular media [Ritter \(1892\)](#), [Balmforth and Kerswell \(2005\)](#), [Ancy et al., Lajeunesse et al. \(2005\)](#), [Lube et al. \(2005\)](#). The "dam break" configuration in a rectangular channel has been extensively studied by many authors, experimentally ([Lajeunesse et al. \(2005\)](#), [Lube et al. \(2005\)](#), [Balmforth and Kerswell \(2005\)](#)), analytically ([Balmforth and Kerswell \(2005\)](#)) and numerically ([Girolami et al. \(2012\)](#)), among others. The experimental set up is cheap and experiments are easy to conduct. The overall picture of granular column collapse has been described in many papers and books (and in particular in the aforementioned papers) but a fully comprehensive understanding is still lacking. To summarize, the macroscopic features of the collapse, i.e., the final height H_∞/H and the run-out distance $(L_\infty - L)/L = X_f/L$, scale with the initial aspect ratio $a = H/L$ of the column, where H and L denote the initial height and initial length of the column, respectively, and H_∞ and L_∞ denote the final height and final length of the column, respectively. It has been established and verified by many authors that H_∞/H and $(L_\infty - L)/L$ are essentially functions of a and vary as $H_\infty/H \simeq \lambda_1 a^\alpha$ and $(L_\infty - L)/L \simeq \lambda_2 a^\beta$, with $\alpha \approx 1$ for $a \lesssim 0.7$ and $\alpha \approx 1/3$ for $a \gtrsim 0.7$, and $\beta \approx 1$ for $a \lesssim 3$ and $\beta \approx 2/3$ for $a \gtrsim 3$, although Balmforth and Kerswell found slightly different exponents ([Balmforth and Kerswell \(2005\)](#)). Anyhow, the constants λ_1 and λ_2 are largely undetermined. In the inertia dominated regime $a \gtrsim 3$, [Lube et al. \(2005\)](#) suggested that $\lambda_2 = 1.9$. Although the qualitative description of granular column collapse in a rectangular channel is acknowledged by all contributors to the field, significant quantitative discrepancies can be found in terms of experimentally measured run-out distances between e.g. [Lube et al. \(2005\)](#) and [Balmforth and Kerswell \(2005\)](#). It is admitted that the problem is primarily governed by the initial aspect ratio a but the various existing studies also suggest that λ_1 and λ_2 might not be true constants but functions of the transverse dimension of the channel (narrow or wide slots), the type of material and the shape of the particles, although this functional dependence might be weak. In any case, the scaling analysis is assumed to be valid, which implies that the general behaviour and hence H_∞/H and $(L_\infty - L)/L$ are independent of the dimensional system size.

In [Girolami et al. \(2012\)](#), we used Grains3D to carry out an extensive analysis of dam break granular collapses in a rectangular channel and satisfactorily reproduced the experimental data of [Lajeunesse et al. \(2005\)](#). Here our objective is twofold: (i) show that the scaling analysis is indeed valid by computing systems of increasing size but constant a and that the computed run-out distance is within the reported experimental range of values, and (ii) use the largest system as a reference point for weak scaling parallel tests.

Numerical simulation

Simulations are performed based on a well-known experimental set-up: a box with a lifting gate (see [FIG. 5.13](#)). The simulation procedure consists in filling the parallelepipedic reservoir

of length L and width W up to a height H with granular media. Particles are inserted at the top of the reservoir. They settle by gravity and collide until the system reaches a pseudo steady state corresponding to a negligible total kinetic energy. Then, the gate is lifted over a time scale much smaller than that of the collapsing media in a sense that it does not affect the dynamics of the whole system. The moving gate is also chosen to be frictionless to avoid particle located close to the gate to be artificially lifted in the air. The lateral boundaries of our system are subjected to periodic condition to mimic an infinite granular media in the transverse direction to the flow. Particles are assumed to have a mono-sized icosahedral shape that mimics quartz-sand grains. Icosahedral particles have an equivalent diameter d_p (diameter of a sphere of same volume as the icosahedron) of 3 mm . The magnitude of the parameters involved in the granular collapse simulations is given in TAB. 5.4. We take the free-fall settling velocity of the highest heap of particles (Size 5, $H = 0.905\text{m}$) as an estimate of the maximum collisional velocity. We hence get $v_{col} = \sqrt{2 \times 9.81 \times 0.905} \approx 4.2\text{ m/s}$. The theoretical maximum overlap is of the order of maximum 5% of the particle equivalent radius as shown in Table 5.4. In practice, the average overlap and maximum overlap in all simulation are of the order of 0.1% and 1%, respectively.

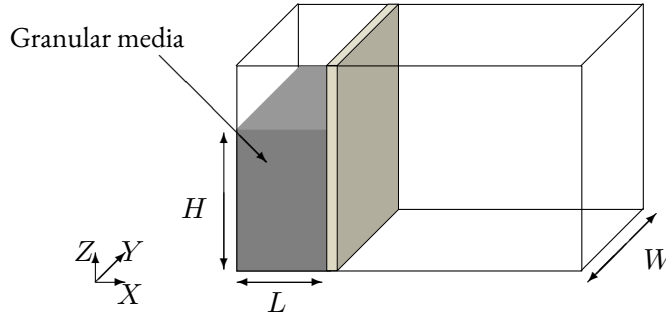


Figure 5.13 – Granular dam break set-up.

Parameter	Value
Particle-Box (PB) & Particle-Gate (PG)	
$k_n (N\ m^{-1})$	1×10^5
$e_n, \mu_n (s^{-1})$	$0.75, 6.86 \times 10^3$
$\mu_{c,PB}, \mu_{c,PG}$	$0.5, 0$
k_{ms}	0
$\delta_{max} (m), \delta_{max}/R$	$7.16 \times 10^{-5}, 0.048$
$T_C (s)$	5.91×10^{-5}
Particle-Particle	
$k_n (N\ m^{-1})$	1×10^5
$e_n, \mu_n (s^{-1})$	$0.75, 6.86 \times 10^3$
μ_c	0.5
k_{ms}	0
$\delta_{max} (m), \delta_{max}/R$	$4.87 \times 10^{-5}, 0.0325$
$T_C (s)$	4.19×10^{-5}
$\Delta t (s)$	2.5×10^{-6}

Table 5.4 – Contact force model parameters, estimate of contact features at $v_{col} = 4.2\text{ m/s}$ and time step magnitude used in the dam break simulations.

We fix a to roughly 7.3 and select five systems of increasing dimensional size. The way we proceed is as follows: we set $W = 0.5 m$ and select $L = L_1 = 0.025m$ has the length of the smallest system. We fill the reservoir with $N_1 = 98,000$ mono-disperse icosahedral particles and the resulting height is $H = H_1 = 0.187 m$. The 4 other systems have the following features: $i \in \langle 2, 5 \rangle$, $L_i = iL_1$, $N_i = i^2 N_1$, $H_i \approx iH_1$. The simulation of the filling process results in the following actual height and aspect ratio of the reservoir of particles for the different systems:

- Size 1: 98000 particles ($H = 0.187m$, $L = 0.025m$, $a = 7.475$)
- Size 2: 392000 particles ($H = 0.365m$, $L = 0.05m$, $a = 7.305$)
- Size 3: 882000 particles ($H = 0.547m$, $L = 0.075m$, $a = 7.296$)
- Size 4: 1568000 particles ($H = 0.731m$, $L = 0.1m$, $a = 7.31$)
- Size 5: 2450000 particles ($H = 0.905m$, $L = 0.125m$, $a = 7.238$)

The resulting aspect ratio a is $7.3 \pm 2.3\%$. The observed limited deviation of 2.3% is the aftermath of systems of slightly different compaction. In fact, the initial height is a result of the filling simulation and cannot be set a priori. It is only known after all particles have settled in the reservoir and the system exhibits a negligible total kinetic energy. It has been noticed that once the free fall phase of all particles is complete, the system relaxes and densifies extremely slowly over a time scale of a few seconds at least. Slow microstructural re-arrangements lead to a progressively more compact granular media in the reservoir. Actually, starting from a loose packing, the compaction of the system can be very slow, even with a successive vertical taps (Knight et al. (1995)). In terms of computational cost, this situation may lead to an extremely long simulation time since the typical time step is in the order of a micro-second. We assume that these slight variations of the initial aspect ratio a and correspondingly of the initial volume fraction and microstructure of the granular media have a very low impact on the whole granular collapse. In the worst case, it will result in similar slight variations of the final height and the final run-out distance.

Measuring the run-out distance in an unbiased way is not straightforward as once the collapse is complete the front of the deposit of particles is diffused (detached particles are spread out). In order to determine the total length of the final deposit, we employ the following procedure:

- we consider the bottom layer of particles whose thickness is roughly a particle equivalent diameter d_p ,
- we translate along the bottom wall a box-like control volume that spans the whole transverse dimension of the flow domain ($V_b = d_p \times W \times d_p$) from the origin of the X -axis and compute the solid volume fraction as a function of X as follows:

$$\phi(X) = \frac{\sum_{i=1}^N V_i}{V_b}, \quad (5.9)$$

where $V_i = \pi d_p^3/6$ is the particle volume and N is the number of particles whose center of mass belongs to V_b .

- the total length of the final deposit L_∞ is determined once the condition $\phi(L_\infty) \leq 0.1$ is satisfied.

Note that changing the critical value of the average solid volume fraction in the control volume V_b from 0.1 to 0.05 or 0.025 does not change significantly the estimation of L_∞ .

FIG. 5.14 and FIG. 5.15 illustrate the dynamics of the granular collapse and the time evolution of the free surface in a 2D $X - Z$ cut plane and in 3D, respectively, for case Size 4. As observed by Lube et al. (2005), the early transient of the collapse correspond to a free-fall

regime (FIG. 5.14 (a)-(c)) until the flow transitions to a phase over which the advancing front of the collapsing granular media reaches a quasi-constant velocity (FIG. 5.14 (d)-(f)), and finally the flow is friction-dominated and slows down to rest. Interestingly, over the second phase, the front of the collapsing granular media shows a rather chaotic dynamics. Although the front advances at a quasi-constant velocity, the singularity that the front represents leads to a high level of particles agitation with many particles being ejected/detached from the mass to ballistically free-fly until they settle back on the deposit.

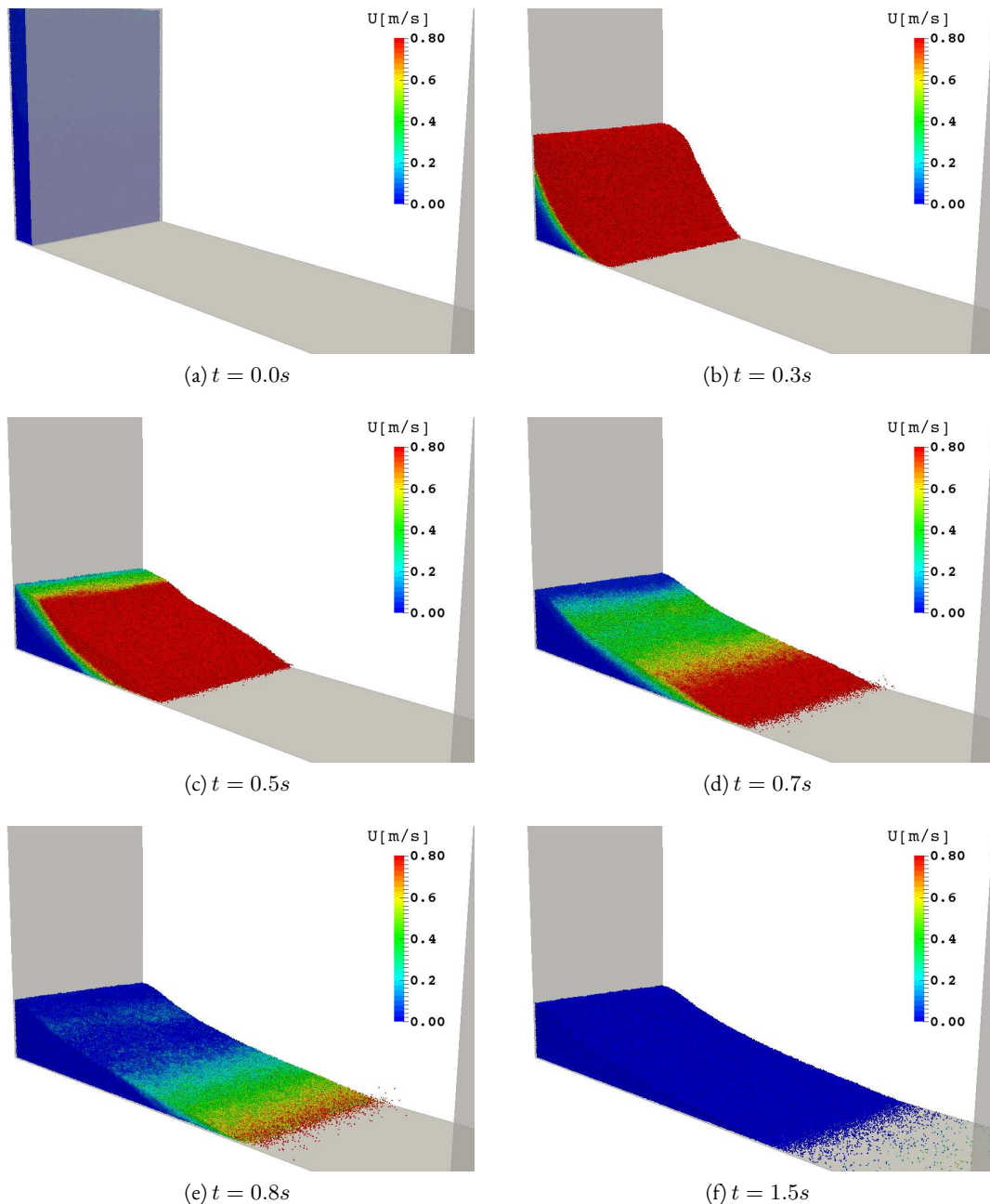


Figure 5.14 – 3D view of the granular dam break flow for Size 4 case.

As experimentally observed by many authors, our computed results confirm that the overall dynamics and in particular the final height, run-out distance and cross-sectional profile of the deposit are independent of the size of the system and solely controlled by the initial as-

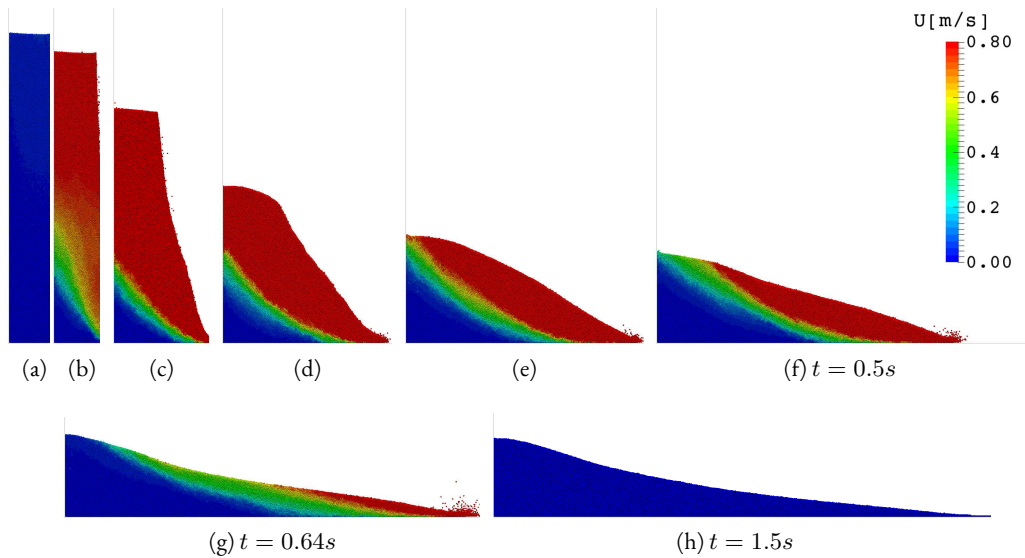


Figure 5.15 – 2D view of the granular dam break flow for Size 4 case. (a)-(f) correspond to snapshots every 0.1s.

pect ratio a . We present in FIG. 5.16 a view from the top of the final deposit together with the scaled total length of the deposit L_∞/L obtained with the criterion $\phi \leq 0.1$ (red line) for all systems. The variation of the run-out distance $(L_\infty - L)/L$ is quantitatively plotted in FIG. 5.17. It is pretty obvious that $(L_\infty - L)/L$ is quasi-constant as a function of the size of the system. The limited variations obtained are primarily a result of the slight variations of a for the different sizes in the computations.

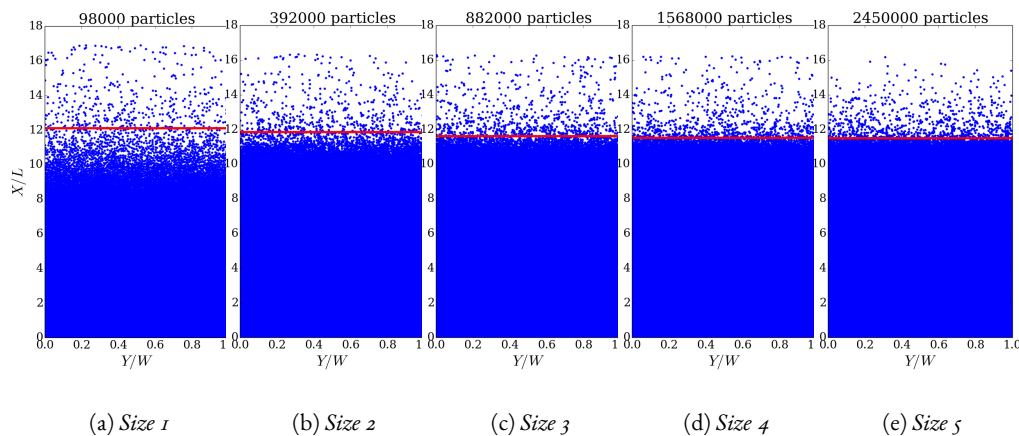


Figure 5.16 – Variation of L_∞/L . L_∞ (red) for $\varepsilon \leq 0.1$. Blue dots are particles positions.

Finally, the final scaled cross-sectional profiles of the deposit for all system sizes nicely collapse on a unique master plot, as shown in FIG. 5.18, emphasizing once again the dependence to a and not to the dimensional size of the system. Let us complete this subsection by shortly discussing the value of the obtained run-out distance. Lajeunesse et al. (2005) and Lube et al. (2005) agree on the scaling exponents while Balmforth and Kerswell (2005) suggests slightly different values. Please note that all these works are experimental. For inertia-dominated regimes $a \gtrsim 3$, Lube et al. (2005) even determine that the value of the constant λ_2 is around 1.9 and independent of the granular material properties and shape. Using their correlation

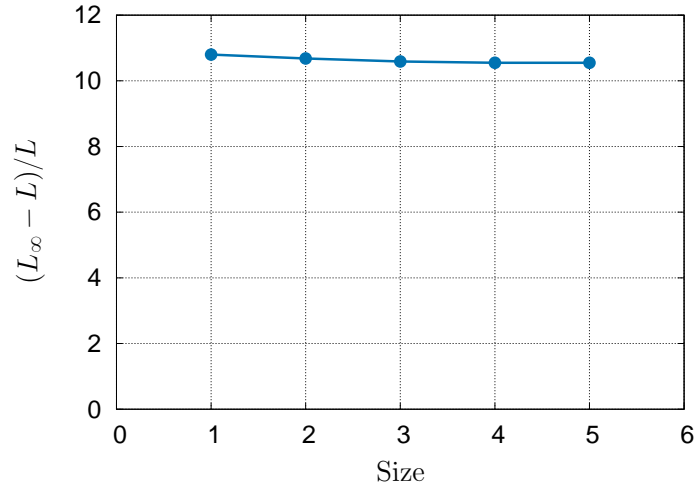


Figure 5.17 – Variation of run-out distance $(L_\infty - L)/L$ with dimensional size of the system for $a \approx 7.3$.

$(L_\infty - L)/L \simeq 1.9a^{2/3}$, we get for $a \approx 7.3$, $(L_\infty - L)/L = 1.9 \times 7.3^{2/3} \simeq 7.15$, a value significantly less than our numerical prediction of ≈ 10.5 . In their experiments, Lube *et al.* have lateral walls while we have periodic boundary conditions, i.e., no frictional resistance from any lateral walls. This difference in the flow configuration qualitatively justifies that our run-out distance is larger (less frictional resistance leads to a larger spread out of the granular media) but is probably not sufficient to quantitatively explain the discrepancy. Although Lube *et al.* have lateral walls, their channel looks rather wide, so the additional frictional flow resistance is likely to be limited. In Balmforth and Kerswell (2005), Balmforth and Kerswell claim that λ_2 is a function of the granular material properties and shape, based on their own experimental results. Figure 11 in Balmforth and Kerswell (2005) suggests that for $a = 7.3$, the run-out distance roughly spans the range $[7 : 13]$ for wide channels, with the largest value found for fine glass. Fine glass grains seem to look moderately angular (see Figure 3 in Balmforth and Kerswell (2005)) and could presumably be well represented by icosahedra. Our computed run-out distance hence falls almost in the middle of the range of values reported in Balmforth and Kerswell (2005). Overall, our numerical prediction is in good agreement with the assorted experimental values reported in the literature. But additional simulations are required to further determine the right scaling and the potential dependence of that scaling to the granular material properties and shape.

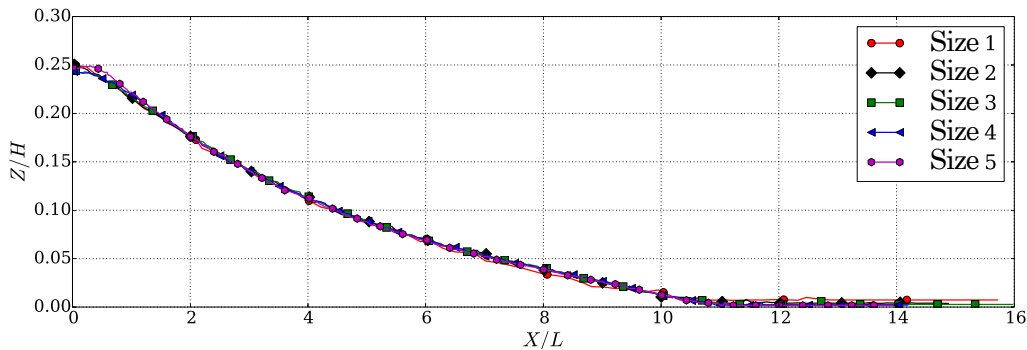


Figure 5.18 – Final scaled profiles of the deposit as a function of dimensional size of the system for $a \approx 7.3$. All profiles collapse on a single master profile.

Parallel scalability

We use the Size 5 granular column collapse flow configuration to perform weak scaling tests and further assess the parallel scalability of Grains3D. From [Section 4.1](#), we learnt that a good parallel performance requires a minimum of $\approx 100,000$ particles per core. Therefore our reference case on a single core approximately corresponds to Size 5 case of [Section 4.2](#) but 24 times narrower. The system on a single core comprises $N_{p,1} = 101850$ icosahedra and its width is $W_1 = 0.021875m$. For parallel computing, we increase the system width and the number of particles accordingly. We adopt a 1D domain decomposition in the Y direction such that each core hosts approximately 101850 particles. Hence, a N_{cores} -core computation corresponds to a system with $N_T = N_{p,1} \times N_{cores}$ particles and of width $W = N_{cores} \times W_1$ as detailed in [TAB. 5.5](#). The weak scaling tests are performed over the 20,000 first time steps of the collapse.

N_{cores}	1	16	32	64	128	256	512
$W(m)$	0.021875	0.35	0.7	1.4	2.8	5.6	11.2
N_T	101,850	1,627,500	3,255,000	6,510,000	13,020,000	26,040,000	52,080,000

Table 5.5 – System size in granular dam break weak scaling tests.

[FIG. 5.19](#) shows the overall scalability of our code Grains3D. The code exhibits a very satisfactory performance for a particles load per core of $\approx 100,000$ of regular polyhedra. The scaling factor $S(n = N_{cores})$ is ≈ 0.93 on 512 cores for a system with a quasi-perfect load balancing. The plot seems to indicate a very slight degradation of the performance above 256 cores but the general trend suggests that $S(n)$ should still be $\gtrsim 0.9$ on 1024 cores for a system comprising more than 100,000,000 of regular polyhedra.

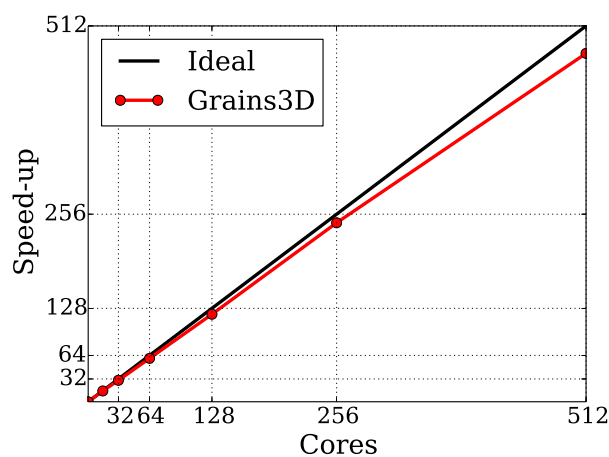


Figure 5.19 – Weak scaling parallel performance of Grains3D in granular dam break computations.

4.3 Coupling with a fluid in an Euler/Lagrange framework, application to fluidized beds

The final test case is a fluidized bed, i.e., a flow configuration in which the particles dynamics is not only driven by collisions by also by hydrodynamic interactions with the surrounding fluid. The model implemented here is of the two-way Euler/Lagrange or DEM-CFD type ([Anderson and Jackson \(1967\)](#), [Kawaguchi et al. \(1998\)](#), [Tsuji et al. \(2008\)](#), [Pepiot and Desjardins](#)

(2011)). The principle of the formulation is to write fluid porosity averaged conservation equations with an additional source representing the reaction of the particles on the fluid and to add a hydrodynamic force to the translational Newton's equation for the particles representing the action of the fluid on the particles. In our weak scaling tests below, we evaluate the parallel scalability of the solid solver only.

Formulation

The formulation of the set of governing equations dates from Anderson and Jackson [Anderson and Jackson \(1967\)](#) in the late 60s and was recently clarified in [Capecelatro and Desjardins \(2013\)](#). In essence, for the fluid part, the mass conservation equation and the momentum conservation equation are averaged by the local fluid porosity. In most formulations, the set of governing equations is integrated in control volumes larger than the particle diameter, although recent advances in this field have shown that it is possible to use a projection kernel disconnected from the grid size ([Pepiot and Desjardins \(2011\)](#), [Capecelatro and Desjardins \(2013\)](#)). Particles trajectories with collisions and hydrodynamic forces are tracked individually and computed by our granular dynamics code Grains3D. The two-way Euler/Lagrange formulation has been detailed many times in the past literature (see [Kawaguchi et al. \(1998\)](#), [Tsuji et al. \(2008\)](#), [Xu and Yu \(1997\)](#) among many others) and we shortly summarize the main features of our own two-way Euler/Lagrange numerical model.

The fluid is assumed to be Newtonian and incompressible. The set of governing equations for the fluid-solid coupled problem reads as follows:

- Fluid equations

We solve the following fluid porosity averaged mass and momentum conservation equations:

$$\frac{\partial \varepsilon}{\partial t} + \nabla \cdot \varepsilon \mathbf{u} = 0 \quad (5.10)$$

$$\rho_f \left(\frac{\partial (\varepsilon \mathbf{u})}{\partial t} + \nabla \cdot (\varepsilon \mathbf{u} \mathbf{u}) \right) = -\nabla p - \mathbf{F}_{fp} + 2\mu \nabla \cdot (\varepsilon \mathbf{D}) \quad (5.11)$$

where ρ_f , μ , ε and \mathbf{D} stand for the fluid density, the fluid viscosity, the fluid porosity (also referred to as fluid volume fraction) and the rate-of-strain tensor, respectively. The pressure gradient term only contains the hydrodynamic pressure and \mathbf{F}_{fp} represents the fluid-particle hydrodynamic interaction force.

- Particles equations

We solve [EQ. 5.1](#) and [EQ. 5.2](#) with additional hydrodynamic interaction contributions \mathbf{F}_i and \mathbf{M}_i , respectively. The translational and angular momentum conservation equations of particle i hence read as follows:

$$M_i \frac{d\mathbf{U}_i}{dt} = M_i (1 - \rho_f / \rho_p) \mathbf{g} + \sum_{j=0, j \neq i}^{N-1} \mathbf{F}_{ij} + \mathbf{F}_{fp,i} \quad (5.12)$$

$$\mathbf{J}_i \frac{d\boldsymbol{\omega}_i}{dt} + \boldsymbol{\omega}_i \wedge \mathbf{J}_i \boldsymbol{\omega}_i = \sum_{j=0, j \neq i}^{N-1} \mathbf{R}_j \wedge \mathbf{F}_{ij} + \mathbf{M}_{fp,i} \quad (5.13)$$

where ρ_p , $\mathbf{F}_{fp,i}$ and $\mathbf{M}_{fp,i}$ stand for the particle density, the fluid-particle hydrodynamic interaction force exerted on particle i and the fluid-particle hydrodynamic interaction torque exerted on particle i , respectively.

The fluid-particle hydrodynamic interaction force $\mathbf{F}_{fp,i}$ exerted on particle i (and similarly for the torque) derives from the momentum exchange at the particle surface:

$$\mathbf{F}_{fp,i} = \int_{\partial\mathcal{P}_i} \boldsymbol{\tau} \cdot \mathbf{n} \, dS \quad (5.14)$$

where $\boldsymbol{\tau}$ denotes the point-wise fluid stress tensor and \mathbf{n} is the normal vector to the particle surface $\partial\mathcal{P}_i$. In the two-way Euler-Lagrange framework, point-wise variables are not resolved. A closure law is hence needed to compute the fluid-solid interaction at the position of each particle (Kawaguchi et al. (1998), Tsuji et al. (2008), Pepiot and Desjardins (2011)). Following previous contributions to the literature, we assume that the dominant contribution to the hydrodynamic interaction is the drag and that the hydrodynamic torque is small enough to be neglected, i.e., we set $\mathbf{M}_{fp,i} = \mathbf{0}$. In our fluidized bed simulations, particles are spherical and we select the drag correlation proposed by Beetstra et al. (2007a,b) which reads as follows:

$$\mathbf{F}_{i,fp} = \mathbf{F}_{d,i} = 3\pi d\mu(\mathbf{u} - \mathbf{U}_i)g(\varepsilon, \mathcal{R}e_{p,i}) \quad (5.15)$$

$$g(\varepsilon, \mathcal{R}e_p) = \frac{10(1-\varepsilon)}{\varepsilon^2} + \varepsilon^2(1 + 1.5\sqrt{1-\varepsilon}) + \frac{0.413\mathcal{R}e_p}{24\varepsilon^2} \left(\frac{\varepsilon^{-1} + 3\varepsilon(1-\varepsilon) + 8.4\mathcal{R}e_p^{-0.343}}{1 + 10^{3(1-\varepsilon)}\mathcal{R}e_p^{-0.5-2(1-\varepsilon)}} \right) \quad (5.16)$$

$$\mathcal{R}e_{p,i} = \frac{\rho_f d_p \varepsilon |\mathbf{u} - \mathbf{U}_i|}{\mu}$$

To compute the reaction term $-\mathbf{F}_{fp}$ of the particles on the fluid flow, we need to use a projection operator from the Lagrangian description of the particles motion to the Eulerian description of the fluid flow. Here we use the simple embedded cube projection kernel introduced by Bernard (2014), Bernard et al. (2016). The fluid equations are discretized with a classical second-order in space Finite Volume/Staggered Grid discretization scheme and the solution algorithm is of the first-order operator splitting type. The two-way Euler/Lagrange model used here is implemented in the PeliGRIFF platform to which Grains3D is plugged to compute particles trajectories, see Wachs (2009), Wachs et al. (2007-2016) among others. For more detail about the formulation of the model and its implementation, the interested reader is referred to Bernard (2014), Esteghamatian et al. (2016), Bernard et al. (2016).

The set of governing equations above can be easily made dimensionless by introducing the following scales: L_c for length, V_c for velocity, L_c/V_c for time, $\rho_f V_c^2$ for pressure and $\rho_f V_c^2 L_c^2$ for forces. In a dimensionless form, the governing equations contain the following dimensionless numbers: the Reynolds number $\mathcal{R}e_c = \frac{\rho_f V_c L_c}{\mu}$, the density ratio $\rho_r = \frac{\rho_p}{\rho_f}$

and the Froude number $\mathcal{F}r = \frac{gL_c}{V_c^2}$.

Simulation set-up and parameters

We consider the fluidization of mono-disperse solid spherical particles in a simple box-like reactor. We use the uniform inlet velocity U_{in} as the characteristic velocity V_c and the spherical particle diameter d_p as the characteristic length L_c . The Reynolds and Froude numbers hence

read as follows:

$$\mathcal{R}e_{in} = \frac{\rho_f U_{in} d_p}{\mu} \quad (5.17)$$

$$\mathcal{F}r_{in} = \frac{g d_p}{U_{in}^2} \quad (5.18)$$

Results hereafter are presented in a dimensionless form and dimensionless variables are written with a $\tilde{\cdot}$ symbol. Particles positions are initialized as a cubic array arrangement with a solid volume fraction of $\pi/6$. The computational domain is shown in FIG. 5.20. Inlet boundary condition corresponds to an imposed velocity $\mathbf{u} = (0, 0, 1)$ and outlet boundary condition corresponds to a standard free-flow condition with an imposed reference pressure. Lateral (vertical) boundaries are periodic.

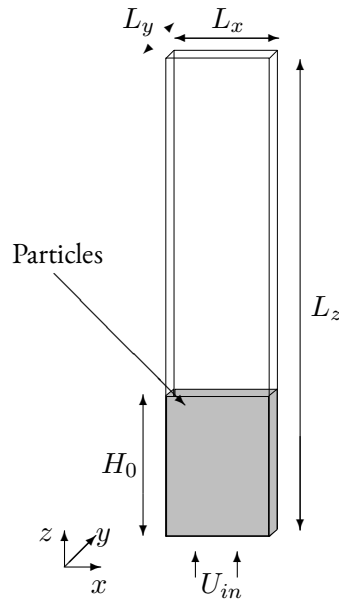


Figure 5.20 – Fluidized bed computational domain.

The principle of our weak scaling tests is similar to the one adopted in the scaling tests of the previous sections except that here the reference case is a full node that comprises 16 cores. The domain is evenly decomposed and distributed in the horizontal $x - y$ plane to guarantee an optimal load balancing over the whole simulation, i.e., we adopt a $N_{cores,x} \times N_{cores,y} \times 1 = N_{cores}$ domain decomposition. The reference case on a full 16-core node has the following dimensionless size: $\tilde{L}_x = 200$, $\tilde{L}_y = 80$ and $\tilde{L}_z = 1500$ and initially hosts $200 \times 80 \times 300 = 4,800,000$ of spheres. With a $4 \times 4 \times 1$ domain decomposition, each sub-domain has the following dimensionless size $50 \times 20 \times 1500$ and hosts initially $N_{p,1} = 50 \times 20 \times 300 = 300,000$ of spheres. The total number of particles in a system is $N_T = 300,000 \times N_{cores} = 4,800,000 \times N_{nodes}$. The initial height \tilde{H}_0 of the bed is 300, such that we also have $\tilde{L}_z/\tilde{H}_0 = 5$. The additional physical and numerical dimensionless parameters of our simulations are listed in TAB. 5.6. We use the same contact parameters for particle-bottom wall and particle-particle collisions.

Another important dimensionless parameter is the ratio of the inlet velocity U_{in} to the minimum fluidization velocity of the system U_{mf} . Here we select $U_{in}/U_{mf} = 3$ to run our weak scaling tests. To avoid a strong overshoot of the bed over the early transients, we first set $U_{in}/U_{mf} = 2$ for $\tilde{t} \in [0 : 1785]$ and then $U_{in}/U_{mf} = 3$ for $\tilde{t} > 1785$. The weak scaling

Parameter	Value
Fluid	
ρ_r	2083.333
$\mathcal{R}e_{in}$	79.333
$\mathcal{F}r_{in}$	6.927×10^{-3}
$\Delta \tilde{t}_f$	0.0119
Particle	
e_n	0.9
μ_c	0.1
k_{ms}	0
$\tilde{\delta}_{max}$	0.025
$\Delta \tilde{t}_p$	0.00595

Table 5.6 – Fluid and particles physical and numerical dimensionless parameters.

tests are performed by increasing the length \tilde{L}_x of the system together with the number of particles, as shown in TAB. 5.7, with \tilde{L}_y and \tilde{L}_z kept unchanged. As \tilde{L}_x increases, the domain horizontal cross-section looks more and more like a narrow rectangle and the bed behaves like a pseudo-3D/quasi-2D bed, as transverse secondary instabilities in the y direction are artificially strongly damped by the narrow periodic length \tilde{L}_y while transverse secondary instabilities in the x direction are free to develop. This configuration is purposely selected to facilitate the visualisation of the bubbles dynamics inside the bed. As expected, the flow field does not vary much in the y direction (see FIG. 5.21). Note that this does not affect our weak scaling tests since with 4 sub-domains in the y direction and bi-periodic boundary conditions, each sub-domain has exactly 8 neighbors, regardless of the fact that the cross-section is a narrow rectangle or a square. In other words, the cartesian domain decomposition is fully 2D. The evaluation of the scaling factor is carried out over 20, 000 time-steps as $U_{in}/U_{mf} = 3$ for $\tilde{t} > 1785$.

\tilde{L}_x	200	400	800	1600	3200	9600
N_{nodes}	1	2	4	8	16	48
N_{cores}	16	32	64	128	256	768
N_T (million)	4.8	9.6	19.2	38.4	76.8	230.4

Table 5.7 – System size in the fluidized bed weak scaling tests. Each node hosts 16 cores, i.e., $N_{cores} = 16 \times N_{nodes}$, and each core initially hosts $N_{p,1} = 300,000$ of spheres, thus $N_T = 300,000 \times N_{cores} = 4,800,000 \times N_{nodes}$.

FIG. 5.21 illustrates the early transients for $U_{in}/U_{mf} = 2$ of the simulation with 19, 200, 000 of particles over which the primary streamwise (in the z direction) instability develops, as well documented in the literature. Then a secondary transversal (horizontal in the x direction) instability triggers, grows and leads to the creation of a first big bubble that eventually bursts. FIG. 5.21 shows the time evolution of the fluid porosity in a $x - z$ cut plane located at $\tilde{L}_y/2$ over the transition from $U_{in}/U_{mf} = 2$ to $U_{in}/U_{mf} = 3$. For $\tilde{t} > 1785$, the system progressively transitions to its bubbling regime. The level of intermittency decreases with time until the system reaches a pseudo-stationary bubbling regime. FIG. 5.22 shows a 3D snapshot of the flow field (velocity contours in a $x - z$ cut plane located at \tilde{L}_y and 3D contours of $\varepsilon = 0.75$) at $\tilde{t} = 2142$. The presented results are qualitatively in line with the expected behaviour of a fluidized in the selected flow regime (Pepiot and Desjardins (2011)).

FIG. 5.23 shows the parallel scalability of our granular solver Grains3D in our fluidized

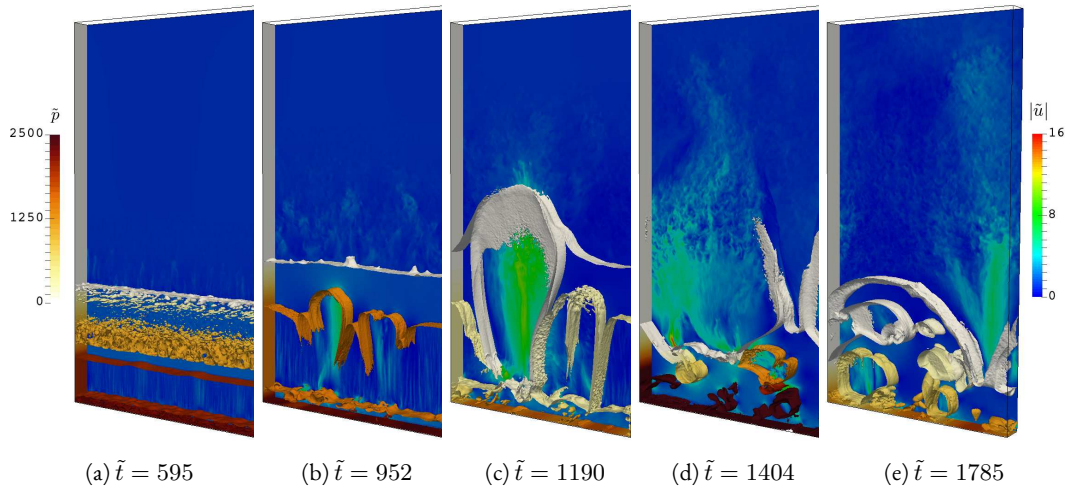


Figure 5.21 – 3D snapshots of fluidized bed fluid flow over the early transients with $U_{in}/U_{mf} = 2$ in the case $N_{cores} = 64$, $N_T = 19,200,000$: $\varepsilon = 0.75$ fluid porosity contours colored by pressure magnitude, velocity contours in a $x - z$ cut plane located at $\tilde{y} = \tilde{L}_y$ and pressure contours in a $y - z$ cut plane located at $\tilde{x} = 0$.

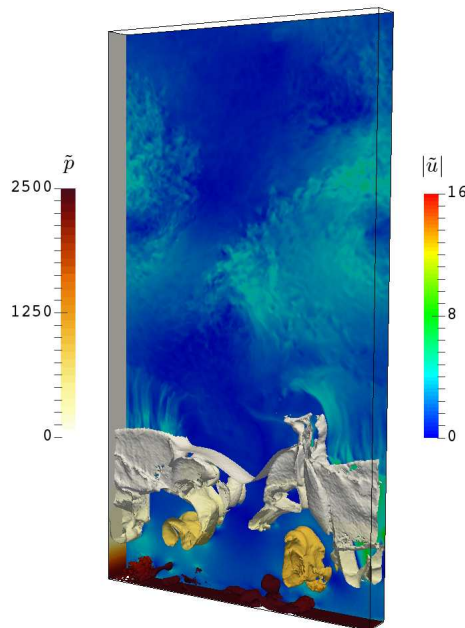


Figure 5.22 – A 3D snapshot of fluidized bed fluid flow at $\tilde{t} = 2142$ and $U_{in}/U_{mf} = 3$ in the case $N_{cores} = 64$, $N_T = 19,200,000$: $\varepsilon = 0.75$ fluid porosity contours colored by pressure magnitude, velocity contours in a $x - z$ cut plane located at \tilde{L}_y and pressure contours in a $y - z$ cut plane located at $\tilde{x} = 0$.

bed parallel simulations. The overall parallel efficiency of our granular solver is very satisfactory. The scaling factor $S(n = N_{nodes})$ is 0.91 for the largest system investigated, i.e., for 230,400,000 of particles and 48 nodes/768 cores. This very high scalability for such a high number of particles derives from less frequent collisions between particles than in a dense granular media. Although collisions are constantly happening in the system, the presence of the fluid and the overall observed dynamics lead to particles often advancing over a few solid time steps without collide with another particle. We would like to emphasize that, in such a flu-

idized bed simulation, most of the computing time is spent in computing particles trajectories with collisions, i.e., in the granular solver. This has been shown as well in a companion paper (Bernard et al. (2016)). So overall, measuring the parallel efficiency of the granular solver only in such systems still supplies a rather reliable indication of how the whole fluid-solid solver scales. Although FIG. 5.23 shows that the scaling factor seems to slightly degrade with increasing the number of nodes, the trend reveals that simulations with a 1 billion of particles on a few thousands of cores can be performed with a reasonably satisfactory scalability. This is indeed very encouraging.

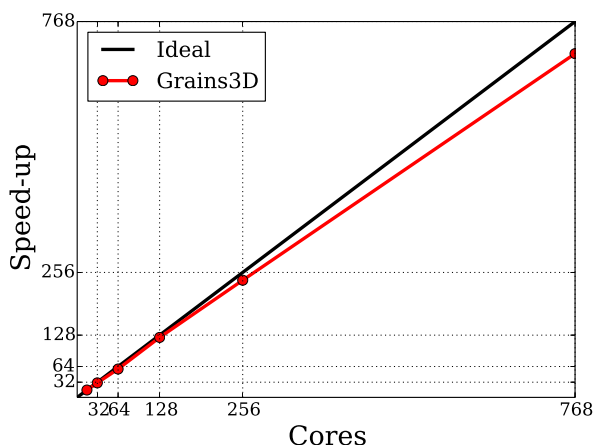


Figure 5.23 – Weak scaling parallel performance of *Grains3D* relative to a full 16-core node in fluidized bed computations.

5 DISCUSSION AND PERSPECTIVES

We have suggested a simple parallel implementation of our granular solver *Grains3D* based on a fixed cartesian domain decomposition and MPI communications between subdomains. The MPI strategy with tailored messages, non-blocking sendings and type conversion has proven to be particularly efficient when the flow configuration does not require any particular dynamic load balancing of the number of particles per core. In the three flow configurations investigated in this work, the parallel performance of the code is deemed to be more that acceptable, and even satisfactory to very satisfactory. For systems with more than 100, 000 particles per core, the scaling factor $S(n)$ is constantly larger than 0.75. In case particles are non-spherical, $S(n)$ is actually larger than 0.9 for computations on up to a few hundreds of cores.

We have also shown than the parallel performance is not only limited by the parallel overhead in terms of messages sent by and received from cores combined to copying the required information in buffers before sending and treating the information received, but also by the competitive access to and proper management of random-access memory on a multi-core architecture. The aftermath of this known limitation is the requirement to enhance even the serial parts of the code. This reprogramming task might be tedious but should be very beneficial on the long run as new architectures are likely to have more and more cores per processor and more and more processors per node. Although *Grains3D* went through this refactoring process, there is still room for further improvement.

In its current state, *Grains3D* offers unprecedented computing capabilities. Systems with up to 100, 000, 000 of non-spherical particles can be simulated on a few hundreds of cores.

Besides, the trend shown by the scaling factor as a function of the number of cores or nodes suggests that the milestone of a billion of particles is attainable with a decent parallel performance, without fluid or with fluid in the framework of a two-way Euler/Lagrange coupling method. This will create incentives to examine flow configurations that were beyond reach before and strengthen the position of numerical simulation associated to high performance computing as an indispensable tool to extend our comprehension of granular flow dynamics.

The next research directions that we will explore short-term on the purely computing side to further enhance the computing capabilities of Grains3D are the following ones:

- the development of a dynamic load balancing algorithm to supply a good parallel performance in flow configurations with high particle volume fraction heterogeneities and significant particle volume fraction time variations. We will proceed in two steps. First, we will implement an algorithm that dynamically balances the load of particles per core in one direction only and make sure this algorithm exhibits a good parallel performance. Second, we will extend this algorithm to dynamic load balancing in 3 directions. Conceptually, dynamic load balancing is not particularly complex but a parallel implementation that scales well is the true challenge,
- the intra-processor and intra-node limitation due to competitive access to memory and/or MPI latency may be partly corrected by moving to an hybrid OpenMP/MPI parallelisation instead of an all-MPI one, such as the one suggested by [Berger et al. \(2015\)](#),
- as the number of cores attains a few thousands, the MPI latency as well as the number of messages sent and received might start to become a serious limitation, although we have not explored yet this range of number of cores. In case this should happen, our simple though very efficient so far MPI strategy might necessitate to be upgraded too, with at least improvements in the scheduling of messages or other techniques,
- finally, although the ability to compute granular flows with non-spherical convex shape opens up fascinating perspectives to address many open questions in the dynamics of real life granular systems, this does not cover all possible particle shapes. In fact, many non-spherical particles are also non-convex. There is hence a strong incentive to devise a contact detection algorithm that can address granular media made of non-convex particles. We will examine this issue in *Grains3D-Part III: extension to non-convex particles*.

ACKNOWLEDGEMENTS

This work was granted access to the HPC resources of CINES under the allocations 2013-c20132b6699 and 2014-c20142b6699 made by GENCI. The authors would like to thank Dr. Manuel Bernard who developed the two-way Euler/Lagrange numerical model for the coupled fluid/particles numerical simulations.

RÉSUMÉ

Ce chapitre est dédié à l'aspect parallèle du code Grains3D. Effectivement, il décrit une nouvelle stratégie d'implémentation parallèle du code Grains3D. Le travail est effectué en adoptant une approche classique de décomposition de domaine, une communication MPI (Message Passing Interface) entre sous-domaine et une implémentation utilisant un système de "géolocalisation" des particules. C'est-à-dire que les particules sont géolocalisées lorsque celles-ci se retrouvent dans le voisinage des interfaces entre sous-domaines pour optimiser ainsi les messages entre les processeurs. Le problème gestion de mémoire est aussi abordée. L'implémentation a été testée sur quelques configurations d'écoulements granulaires tels que vidanges de silos, effondrements de colonnes de particules et lits fluidisés. Ces tests ont pu montrer que le code Grains3D est capable de simuler des systèmes contenant quelques centaines de millions de particules ouvrant ainsi la voie à des simulations numériques de systèmes de milliard de particules.

PARTICLE-RESOLVED SIMULATION: STATE OF THE ART

6

CONTENTS

1	BODY CONFORMAL MESH METHOD	103
1.1	Arbitrary-Lagrangian-Eulerian (ALE)	103
1.2	Deforming-Spatial-Domain/Stabilized Space-Time (DSD/SST)	103
2	FIXED MESH METHODS	104
2.1	Lattice-Boltzmann Method (LBM)	104
2.2	Immersed Boundary Method (IBM)	105
2.3	Distributed Lagrange Multiplier / Fictitious Domain (DLM/FD)	105
3	ADAPTIVE MESH REFINEMENT (AMR)	106
4	CONCLUSION	107

For decades most catalytic refining and petrochemical reactions have been processed in fixed bed reactors. In the downstream oil and gas industries, these reactors represent the majority of reactor plants. Particles (catalyst pellets) are randomly stacked in these reactors and reactants, such as liquid or gas flow through these packed beds in the upward direction or the downward direction. It is known that these particles are made of porous medium in which the pores hold noble active materials. Usually, particle length is in the order of few millimetres.

Traditionally, the chemical industry is always looking for optimised and economical processes. For example, long lasting efficient catalysts. It is a matter of interest to investigate at the fundamental level the physics that govern these industrial plants. Afterwards, based on these investigations engineers can improve the performances of the reactors both in terms of chemical reactions and in terms of mechanical behaviour.

Until late 90's all the studies aimed at optimising processes in fixed beds were done experimentally and analytically. Later on, numerical approach has been gradually introduced in the community. Among others, [Kuipers and Van Swaaij \(1998\)](#) presented the future of numerical simulation in chemical engineering and [Logtenberg and Dixon \(1998\)](#) explored the use of numerical simulation to study heat transfer in fixed bed reactors. They used a finite element commercial code to solve the 3D Navier-Stokes equations. The simulation consisted of an arrangement of 8 spherical particles only. Afterwards, [Dixon and Nijemeisland \(2001\)](#) presented Computational Fluid Dynamics as a design tool for fixed bed reactors, still limited to low tube-to-particle diameter ratio ($N \in [2; 4]$). [Romkes et al. \(2003\)](#) extended this limitation to a channel-to-particle-diameter ratio N of $1 < N < 5$ and compared their numerical results to experimental data. They found that their tool could predict the particle-to-fluid heat transfer with an average of 15% of relative discrepancy with the experimental data. [Gunjal et al. \(2005\)](#) studied the fluid flow through an arrangement of spherical particles to understand the interstitial heat and mass transfer. Particles were arranged periodically following a simple cubical, a 1D rhombohedral, a 3D rhombohedral, and a face-centered cubical geometries. In this framework of finding the best particle arrangement that can represents a whole industrial bed, [Freund et al. \(2005\)](#) presented their work applied to a structured simple cubic packing and a random packing. In addition, they highlighted the advantages of modelling approaches such as deriving reliable correlations from “numerical experiments”.

In the literature, the use of Discrete Particle modelling is becoming more and more undeniable due its conceptual simplicity. This method combined with Computational Fluid Dynamics has been proven to be an efficient and powerful tool for the study of the physics behind numerous industrial processes (among others [van Buijtenen et al. \(2009\)](#), [Deen and Kuipers \(2013\)](#), [Sutkar et al. \(2013\)](#), [Rahmani and Wachs \(2014\)](#), [Dorai et al. \(2015\)](#)). With the growth of computing capabilities, many research groups adopted a multi-scale strategy ([Deen et al. \(2004\)](#), [Van der Hoef et al. \(2008\)](#)) which targets the up-scaling of local information (at the particle scale), known as micro-scale, to the intermediate scale, known as meso-scale (usually laboratory scale) and later on to the macro-scale (industrial plant). FIG. 6.1 illustrates the aforementioned strategy where the micro-scale is usually resolved with Direct Numerical Simulation (DNS), called also Particle Resolved Simulation (PRS). The power of this method relies on the fact that the momentum, heat or mass transfer are fully resolved without almost any assumption (see for example the works of [Deen and Kuipers \(2013\)](#), [Wachs et al. \(2015\)](#)). The PRS solutions serve as a benchmark to create correlations that will be implemented in the meso-scale model ([Beetstra et al. \(2007a;b\)](#), [Esteghamatian et al. \(2016\)](#)) and the macro-scale one.

Finally, coming back to fixed bed numerical simulation, the DEM approach combined with the PRS method enables researchers to simulate from the filling of reactors with particles, the flow through the packed bed to the chemical reaction and heat transfers between the bed

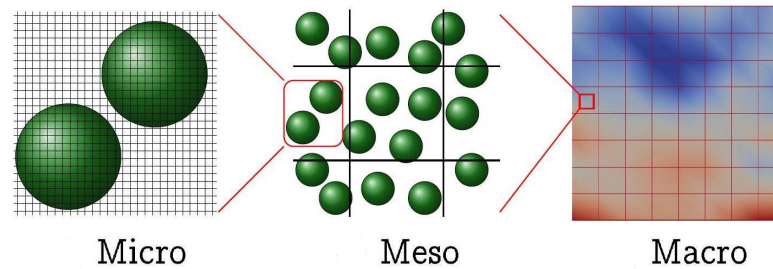


Figure 6.1 – Illustration of the up-scaling procedure. *Micro: DNS approach, Meso: Euler-Lagrange approach, Macro: Euler-Euler approach.*

and the fluid. In the PRS level, various methods have been developed during the last two decades.

1 BODY CONFORMAL MESH METHOD

One of the earliest method is the body-conformal mesh or boundary fitted methods (among others see the works of [Johnson and Tezduyar \(1996\)](#) or [Wan and Turek \(2007\)](#)). The boundary fitted methods have the advantage of capturing the details of the flow dynamics around rigid bodies. Indeed this method is very powerful to capture momentum, heat and mass boundary layers around immersed objects but suffers from a weak on computational performance since a re-meshing process is needed at each time step. This method is often combined with various numerical schemes that have been suggested in the literature, the most famous ones are the Arbitrary-Lagrangian-Eulerian (ALE) formulation and the Deforming-Spatial-Domain/Stabilized Space-Time (DSD/SST) which is generally used in combination with a Finite Element discretization.

1.1 Arbitrary-Lagrangian-Eulerian (ALE)

The ALE is an hybrid method which combines the Lagrangian description of the grid cell where there is a “small” motion and its Eulerian description where it is almost impossible for the mesh to track the motion. In this method the boundary nodes are treated as Lagrangian and the intermediate node velocities are interpolated between the boundary node velocities. This method was initially established by [Christie et al. \(1976\)](#), [Belytschko et al. \(1980\)](#), [Liu et al. \(1988\)](#) for Finite Element formulation. The works of [Feng et al. \(1994a;b\)](#), [Hu \(1996\)](#), [Hu et al. \(2001\)](#) are among others the first studies to apply the method to particulate flow (Newtonian and non-Newtonian) problems. On unstructured grids (FIG. 6.2) they have the advantage of capturing precisely the fluid-solid interface. It is well known that despite the exceptional accuracy of this method, simulations of dense particulate systems are computationally expensive. This limits their use to study a small system of particulate flows. In particular, the re-meshing step in the simulation algorithm scales poorly on parallel computers.

1.2 Deforming-Spatial-Domain/Stabilized Space-Time (DSD/SST)

The DSD/SST was first introduced by [Tezduyar et al. \(1992\)](#) for problems related to deforming spatial domain in a Finite Element framework. In this formulation, the problem is written in its variational form over the associated space-time domain. This implies that the deformation of the spatial domain is taken into account. The space-time mesh is generated over the space-time domain of the problem, within each time step, the interface nodes move with the interface

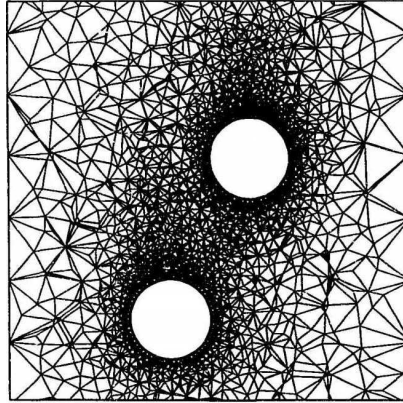


Figure 6.2 – *Arbitrary-Lagrangian-Eulerian*. Credits: *Johnson and Tezduyar (1996)*.

(FIG. 6.3). Hence, during a time step, the interface nodes move with the interface. After each time step, a new distribution of mesh covers the new spatial domain when there is a motion. Details and extension of the DSD/SST can be found in *Johnson and Tezduyar (1996; 1997; 1999)*.

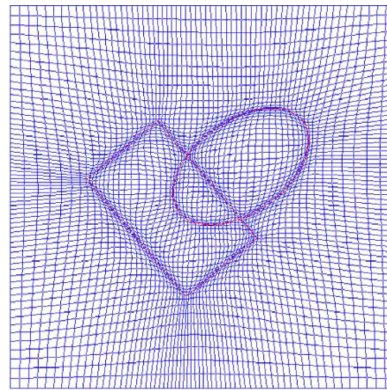


Figure 6.3 – *Deforming-Spatial-Domain / Stabilized Space-Time*. Credits: *Wan and Turek (2007)*.

2 FIXED MESH METHODS

Fixed mesh methods have a non negligible advantage since they scale well on large supercomputers but with the price of low accuracy at the fluid-solid interface as a local reconstruction is required.

2.1 Lattice-Boltzmann Method (LBM)

The LBM (*Ladd (1997)*, *Ladd and Verberg (2001)*, *Feng and Michaelides (2004)*, *Derksen and Sundaresan (2007)*, *Van der Hoef et al. (2005)*, *Hill et al. (2001b;a)*, *Third et al. (2016)*) has proven to be successful for the numerical simulation of particle-laden flows. This method is a relatively new technique for complex fluid systems. Unlike the traditional CFD methods, LBM consists in modelling the fluid with fictive particles undergoing consecutive propagation and collision processes over a discrete lattice mesh (FIG. 6.4). In this method, the fluid variables are considered as distribution functions. A “Bounce Back” method (*Ladd (1994)*, *Ladd and Verberg (2001)*) is often used to account for rigid particles.

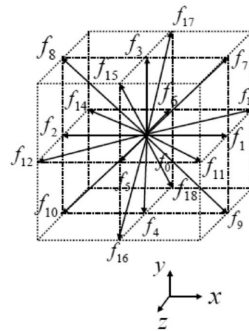


Figure 6.4 – Lattice structure for a "D₃Q₁₉" model. Credits: *Third et al. (2016)*.

By means of LBM, [Hölzer and Sommerfeld \(2009\)](#) determined correlations for the forces acting on a non-spherical particles. [Günther et al. \(2013\)](#) used the LBM to simulate anisotropic ellipsoidal particles to mimic the shape of clay particles. Using LBM, [Janoschek et al. \(2013\)](#) investigated the lubrication corrections on the non-normal direction on spheroids. [Hill et al. \(2001a;b\)](#) also demonstrated the ability of the method to computed fluid flows through porous media made of assemblies of spherical particles.

2.2 Immersed Boundary Method (IBM)

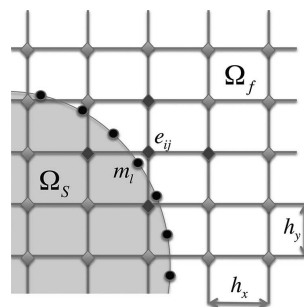


Figure 6.5 – Illustration of the IBM on a disk. The Lagrangian points are distributed on the boundary. Credits: *Vanella et al. (2014)*.

IBM was primarily introduced by [Peskin \(1977; 2002\)](#) for biological fluid flow simulations in which the method handles very thin interfaces. In IBM the fluid flow is solved on the Eulerian grid and the immersed body boundary is represented with Lagrangian points at its surface. Then approximations of the Delta distribution by smoother functions allow the interpolation between the two grids (FIG. 6.5). Later on the method was extended to suspension flow problems ([Peskin \(1977; 2002\)](#), [Kim and Choi \(2006\)](#), [Uhlmann \(2005\)](#)). [Zastawny et al. \(2012\)](#) utilised IBM to propose correlations for drag force, lift force and torques for four different type of non-spherical particles (FIG. 6.6).

2.3 Distributed Lagrange Multiplier / Fictitious Domain (DLM/FD)

The Distributed Lagrange Multiplier / Fictitious Domain (DLM/FD) (FIG. 6.7) method initially introduced by [Glowinski et al. \(1999; 2001\)](#).

Unlike the IBM, the DLM/FD formulation treats the particle boundary and volume as an object under solid body motion ([Patankar et al. \(2000\)](#), [Yu et al. \(2002\)](#), [Yu and Shao \(2007\)](#),

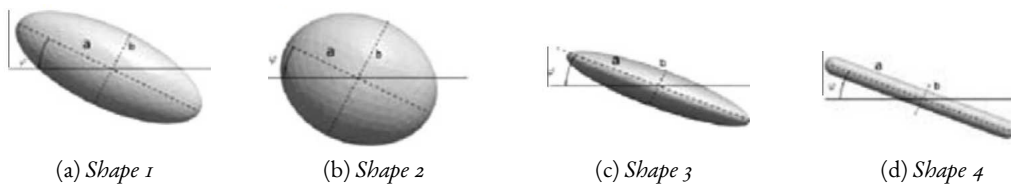


Figure 6.6 – Example of non-spherical particles used in IBM studies. Credits: [Zastawny et al. \(2012\)](#).

[Wachs \(2009; 2011\)](#)). In fact, Lagrangian points are distributed not only on the boundary but in the volume occupied by the particle too.

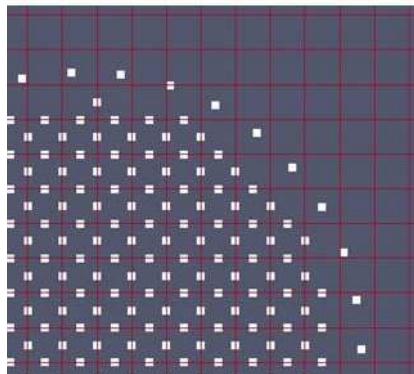


Figure 6.7 – Illustration of the DLM/FD method on a disk. The Lagrangian points are distributed all over the rigid body. Credits: [Wachs et al. \(2015\)](#).

[Segers et al. \(2013\)](#) used IBM to study the fluid-structure interaction of single phase flow past crossing cylinders. [Tavassoli et al. \(2015\)](#) carried out DNS of the heat transfer in fixed random arrays of spherocylinders in order to characterize the fluid-solid heat transfer coefficient.

So far, the most complex particle shapes in particulate flow in the literature using fixed mesh methods can be seen in the works of [Rahmani and Wachs \(2014\)](#) and [Wachs et al. \(2015\)](#). In fact, [Rahmani and Wachs \(2014\)](#) showed the influence of particle shape in the path instabilities of free raising or settling of angular particles (FIG. 6.8), whereas [Wachs et al. \(2015\)](#) highlighted the accuracy of the DLM/FD method on spherical and angular particles from low to high solid volume fractions and from Stokes to moderate Reynolds regimes. In [Dorai et al. \(2015\)](#), PRS of packed beds of cylinders are performed using the DLM/FD formulation. They showed the accuracy of the method on the computed pressure drop.

3 ADAPTIVE MESH REFINEMENT (AMR)

The AMR method was first introduced by [Berger and Oliger \(1984\)](#) and [Berger and Colella \(1989\)](#). Their original work consists in creating a fine Cartesian grid which is embedded into a coarser grid. Pursuing the concept of [Berger and Oliger \(1984\)](#), [Almgren et al. \(1998\)](#) extended the method to solve the variable density incompressible Navier–Stokes equations which was later on extended to two-phase flow (fluid-fluid) problems ([Sussman et al. \(1999\)](#)). The method suggests that local grid refinement should be performed when needed depending on the flow conditions at the interface and the far field mesh remains coarse. The major advantages of the AMR lie on the fact that the subcategories of methods of fixed mesh can be incorporated in it. That is to say that IBM and AMR ([Roma et al. \(1999\)](#), [Vanella et al. \(2014\)](#)) or DLM/FD and AMR ([Van Loon et al. \(2004\)](#), [Kanarska et al. \(2011\)](#)) can be combined so

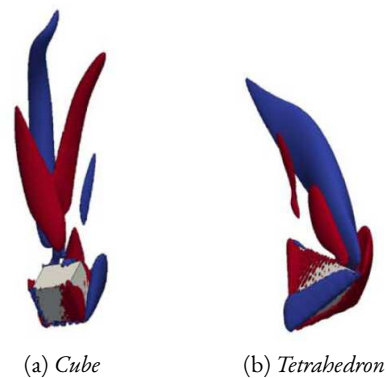
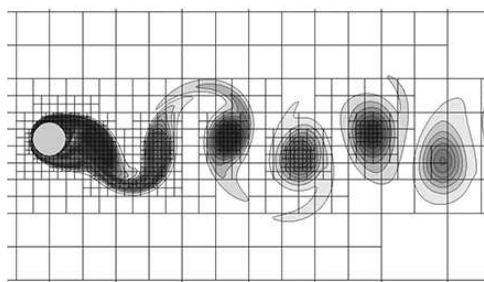
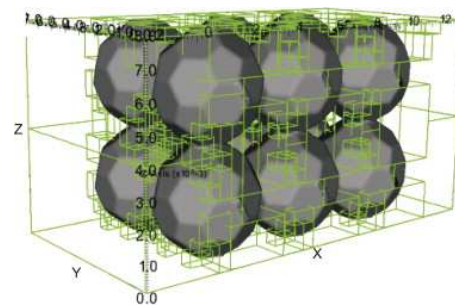


Figure 6.8 – Chaotic motion of a cube and a tetrahedron. Credits: [Rahmani and Wachs \(2014\)](#).

that when a mesh refinement is needed in the vicinity of the interface, additional Lagrangian points are added, hence locally improving the accuracy of the computed solutions (FIG. 6.9). However, one of the challenges of AMR is to make it scale well on supercomputers ([Kanarska et al. \(2011\)](#)).



(a) Computational domain and flow around a sphere (IBM). Credits: [Vanella et al. \(2014\)](#).



(b) Flow through a cubic array of spheres (DLM/FD). Credits: [Kanarska et al. \(2011\)](#).

Figure 6.9 – Illustration of the adaptive mesh refinement technique.

4 CONCLUSION

According to the purpose of the second part of this thesis, i.e. the modelling of fluid flow through packed beds of particles, the well suited numerical technique is the boundary fitted method. Indeed, it offers the best accuracy among the three aforementioned methods especially for particles of complex shape. After this method would come the adaptive mesh refinement combined either with the DLM/FD formulation or the IB formulation. Then the DLM/FD or the IB method would be the last one to achieve the goal of this study. Having said that, the method we plan to develop must also be applicable to freely-moving particles. This hence disqualifies the use of a boundary fitted method, due to the aforementioned low computing performance related to constant re-meshing needs. For the same reason, a combined AMR-DLM/FD approach would require the AMR part to be dynamic. As far as we know, this has never been done yet in the literature. Finally, our granular solver Grains3D is already fully coupled with an Eulerian Navier–Stokes solver by means of a DLM/FD method combined with a Finite Volume Staggered Grid scheme and a second order interpolation operator to impose the rigid body motion constraint at the particle boundary based on Finite

Element cubic quadratic basis functions. This constitutes the PRS model of the PeliGRIFF platform. It has proven to supply computed solutions of satisfactory accuracy for spherical and non-spherical convex bodies. It is hence sensible to build up on the existing tools and to extend the DLM/FD method in PeliGRIFF to non-convex particle shapes. As seen in the previous part of this thesis, Grains3D possesses now the capability to handle non-convex particles enhances and justifies the use of PeliGRIFF to resolve the intricate flow dynamics through fixed bed reactors made of non-convex particles.

RÉSUMÉ

Ce chapitre propose une revue de la littérature sur la modélisation des écoulements fluide-particules en utilisant la méthode de résolution directe. En effet, depuis quelques décennies ces écoulements sont souvent modélisés avec des particules sphériques. Grâce à l'avènement du calcul haute performance, les chercheurs proposent des modèles avec des particules non sphériques. Pour cela, plusieurs méthodes sont rentrées dans la communauté telles que les méthodes à maillage adaptatif qui suivent les déplacements des particules de façon lagrangienne parmi lesquelles la célèbre "Arbitrary Lagrangian Eulerian" (ALE) ou encore la "Deforming-Spatial-Domain/Stabilized Space-Time" (DSD/SST). Les méthodes à maillage fixe sont aussi très courantes grâce au fait qu'elles éliminent le remaillage des particules engendrant ainsi un gain précieux du temps de calcul; parmi lesquelles on trouve la méthode "Immersed Boundary" (IBM) ou la méthode "Distributed Lagrange Multiplier/Fictitious Domain (DLM-FD)" ou la méthode "Lattice Boltzmann". Les deux dernières décennies ont vu naître la méthode "Adaptive Mesh Refinement".

Cette revue de littérature a conduit à conclure que la méthode "Distributed Lagrange Multiplier/Fictitious Domain (DLM-FD)" est compatible aux problèmes qui font l'objet de cette thèse car elle est déjà existante sur la plateforme PeliGRIFF-Grains3D moyennant une certaine adaptation tout en bénéficiant ainsi de nouvelle extension du code Grains3D.

NON-CONVEX PARTICLES WITH PELIGRIF AND PRESSURE DROP IN FIXED BED REACTORS

CONTENTS

1	INTRODUCTION	ii2
2	A DLM/FD METHOD FOR PRS OF PARTICULATE FLOWS WITH NON-CONVEX PARTICLES	ii3
3	NUMERICAL MODEL	ii4
3.1	Introduction to PeliGRIF	ii4
3.2	Governing equations for the fluid flow solver	ii4
3.3	Time discretization scheme	ii5
3.4	Colocation Points on non-convex particles	ii6
4	ACCURACY OF THE COMPUTED SOLUTIONS	ii8
4.1	Methodology	ii8
4.2	Flow past a single poly-lobed particle in a tri-periodic domain	ii9
4.3	Flow past a small packed bed of poly-lobed particles	ii3
5	PRESSURE DROP THROUGH PACKED BEDS OF POLY-LOBED PARTICLES	ii4
5.1	A quick review of single phase pressure drop in fixed beds	ii4
5.2	Method	ii7
5.3	Results	ii8
6	CONCLUSION AND PERSPECTIVES	ii34

A part of this chapter has been written as a first draft of manuscript that I intend to submit with my co-authors for publication in *Chemical Engineering Science*. The provisional title of the manuscript is:

Particle Resolved Simulation of packed beds of trilobal/quadrilobal particles using a Finite Volume/Staggered Grid Distributed Lagrange Multiplier/Fictitious Domain formulation.

In this chapter we present the implementation of the numerical method to compute the flow around poly-lobed particles. Then we assess the space convergence studies of the computed solutions on assorted flow configurations and flow regimes. Finally we compute the pressure drop through packed beds of poly-lobed particles to study the effect of shape on the hydrodynamics.

ABSTRACT

Irregularly shaped particles are ubiquitous in many different real-life systems. For instance, in the downstream oil and gas industries, trilobal and quadralobal shaped particles are used in many chemical reactors for process purposes. Unfortunately, most of corresponding numerical simulations are carried out using idealized spherical particles, spheroids, cubes, or tetrahedron. Very often, the weakness relies on the modelling of the collisional behaviour either to create the packed bed of particles for flows through a fixed bed or to compute particle/particle collisions for freely-moving particles in a fluidized bed. In *Chapter 3*, we suggested a numerical technique implemented in our granular dynamics code Grains3D (Wachs et al. (2012)) to treat the collisional behaviour of particles of (almost) arbitrary shape even non-convex one. In Rahmani and Wachs (2014) have shown the successful implementation of our Distributed Lagrange Multiplier/Fictitious Domain method with a Finite Volume/Staggered Grid discretization scheme for polyhedral particles in the fully parallel numerical platform PeliGRIFF (Wachs (2011)) for multiphase flow simulations. Wachs et al. (2015) have shown that the method supplies solutions of satisfactory accuracy which puts us in a favourable position to suggest a similar Discrete Element Method - Particle-Resolved Simulation (DEM-PRS) approach. The aim of this study is to go one step further and to extend our numerical method to non-convex particles. Trilobal and quadralobal particles are chosen to illustrate the novel capabilities of PeliGRIFF. We keep our 2nd order interpolation operator for velocity reconstruction at the particle boundary and the solutions are computed without any hydrodynamic radius calibration. First, we assess the space convergence and overall accuracy of the computed solutions. Then, we show the shape effects on pressure drop through packed beds of trilobes and quadralobes with an uncertainty quantification for the effects of random packings encountered in these applications.

I INTRODUCTION

Flow through porous media made of assemblies of fixed particles is encountered in nature and in many industrial plants especially in the process industry, especially in the process industry. Many studies (analytical or numerical) were carried out for applications as e.g. chemical reactors, biomass converters and catalytic exhaust pipes. From numerical point of view, Direct Numerical Simulation tools referred to as Particle Resolved Simulation (PRS) appear to be a good candidate to solve the intricate momentum transfer between solid and fluid phases. In fact, numerous methods exist in the literature to simulate the flow dynamics around immersed objects.

This work is entirely focused on the use of a DLM/FD fixed mesh method combined with a FV/SG discretisation scheme and its application to complex particle geometry. The improvement of the DLM/FD method suggested in Wachs et al. (2015) does not require the use of any hydrodynamic radius calibration and is hence well suited to particles of arbitrary shape. In fact, the goal of this work is two-fold: (i) to examine again the accuracy of the method when it is extended to non-convex particle shapes. For that purpose, space convergence of computed solutions is assessed on assorted flow configurations and flow regimes, i.e. the flow through infinite arrays of trilobal/quadralobal particles of various orientation and volume fraction. Then the accuracy of the method is investigated in flows through a packed bed made of the same type of particles in Stokes regime and finite Reynolds number regime; (ii) to use the method to predict the pressure drop through packed bed reactors in order to discriminate new shapes of catalyst particle. For decades processes in the chemical industries always relied on analytical

and experimental works which often exhibit excessive costs. Therefore, it is of great interest to develop numerical tools to estimate the packing voidage and the pressure drop through the bed so that discrimination of new particle shapes can be carried out before prototyping and building expensive pilot units. Indeed the aforementioned PRS method combined with a Discrete Element Method granular solver can give an insight in local variables of the flow at the particle level and can be used as a tool to provide guidelines for up-scaling procedures to laboratory scale pilot plant and latter on to industrial pilot.

2 A DLM/FD METHOD FOR PRS OF PARTICULATE FLOWS WITH NON-CONVEX PARTICLES

[Glowinski et al. \(1999; 2001\)](#) were the first to introduce the concept of DLM/FD to the community of particulate flow modelling. It was originally combined with a Finite Element Method and latter on extend to Finite Volume method ([Wachs et al. \(2015\)](#)). The principle of the DLM/FD formulation consists in enforcing the rigid body motion on the particle domain within an Eulerian fixed-grid as a constraint. Solid objects are defined by using Lagrangian points over both their volume and their surface. In many works, authors point out the use of hydrodynamic radius calibration in order to correct the computed drag force on a fixed spherical particle in creeping flow regime and low solid volume fraction ϕ . Then the calibration is used for any flow regime and any solid volume fraction. [Wachs et al. \(2015\)](#) pointed out that the hydrodynamic radius calibration becomes questionable when it comes to deal with non-spherical shapes. Despite the work of [Breugem \(2012\)](#) that suggested a presumably optimal hydrodynamic radius for cubic particles, it is totally unclear how to determine a hydrodynamically calibrated radius for any non-spherical particle. It seems to us that for non-convex particle the concept of hydrodynamic radius calibration is almost meaningless. Therefore, correct and accurate methods without resorting to using any sort of geometric calibration should be selected to model the fluid-solid interaction. For instance, in [Deen et al. \(2012\)](#) and [Wachs et al. \(2015\)](#), the authors presented satisfactory method, respectively IBM and DLM/FD, without any such geometric calibration. The assets of the enhanced IB and DLM/FD methods suggested in these two works rely only on an accurate velocity reconstruction at the particle boundary and a distribution of Collocation Points (CP) on the solid domain compatible with the formulation of the problem and the discretization scheme adopted.

For spherical particles, it is well known ([Uhlmann \(2005\)](#), [Feng and Michaelides \(2009\)](#), [Wachs et al. \(2015\)](#)) in the community that the best way to distribute these CP on the particle surface is to perform a dynamic simulation of a system in which CPs are considered as charged particles. Then, the final state of the system corresponds to homogeneously distributed charged particles with minimum repulsion energy. Despite the accuracy of this method, the time scale of this type of simulation is very large and the method cannot be extended to non-spherical shape. There is hence a technical issue in distributing CPs as homogeneously as possible on the surface of a non-spherical particle while keeping the remarkable geometric features (edges, corners) of the shape at the discrete level. This is not an easy task and we will present a construction method for trilobes and quadralobes in this work. Recently, some studies other than those of our group extended the use of PRS methods to non-spherical particles but mostly for generalized ellipsoids/rounded particles ([Zastawny et al. \(2012\)](#), [Tavassoli et al. \(2015\)](#)).

3 NUMERICAL MODEL

In line with the work of [Wachs \(2009; 2011\)](#), [Wachs et al. \(2015\)](#), our numerical is based on the classical Distributed Lagrange Multiplier/Fictitious Domain method in which the Lagrange multiplier is implicitly computed to enforce the rigid body motion, combined with a FV/SG scheme and a L2-projection algorithm for the solution of the Navier-Stokes equations. The method is coupled with a granular solver to solve the particle-particle collisions. Hence, the granular solver is employed to fill the reactor and create the pack of particles while the flow solver computes the fluid flow through the packed bed of particles. In the rest of this chapter, we shortly remind the reader the formulation of both numerical methods and elaborate on their extension to poly-lobed particles. The collisional model for non-convex particles is based on the decomposition of the composite particle into a set of convex particles. The reader is referred to *Chapter 3* for more details of the collision model for non-convex rigid bodies.

3.1 Introduction to PeliGRIFF

PeliGRIFF (Parallel Efficient Library for GRains in Fluid Flow) ([Wachs et al. \(2007-2016\)](#)) is an object oriented code implemented in C++ for multi-core architecture. The discrete phase is handled by Grains3D. The open source library PELICANS is the kernel of PeliGRIFF which is used of PDE solvers. PeliGRIFF relies on different libraries for linear algebra such as PETSc (Portable, Extensible Toolkit for Scientific Computation), BLAS (Basic Linear Algebra Subprograms), LAPACK (Linear Algebra PACKage) and HYPRE BoomerAMG for preconditioners. The code can simulate fluid-solid, using a DLM/FD approach, and fluid-fluid, using a Level-Set approach, two-phase flows. In addition, new extensions of PeliGRIFF enable simulations of heat and mass transfers between phases.

3.2 Governing equations for the fluid flow solver

We shortly recall the general DLM/FD formulation for freely-moving particles. Then we present the first-order operator splitting solution algorithm in the particular case of fixed particles. Finally, we elaborate on our CP construction strategy for the case of poly-lobed particles.

Let Ω defines a domain of \mathbb{R}^d , $d \in \{2, 3\}$, $\partial\Omega$ its boundary. Then let be N_P the number of rigid bodies $P_i(t)$ ($i \in [1, N_P]$) that Ω is filled with. For the sack of simplicity, N_P is considered to be equal to 1. Dirichlet boundary conditions are set on $\partial\Omega$ for the fluid velocity field. In the rest of the chapter, the “star” symbol denotes any dimensional quantity.

Dimensionless variables are defined using the set of the following variables: L_c^* for length, U_c^* for velocity, $T_c = L_c^*/U_c^*$ for the convective time scale, $\rho_f^* U_c^{*2}$ for pressure and $\rho_f^* U_c^{*2}/L_c$ for rigid-body motion Lagrange multiplier, ρ_f^* denotes the fluid density. The combined conservation equations that govern both the fluid and solid motion is written as follows:

1. Combined momentum equations

$$\left(\frac{\partial \mathbf{u}}{\partial t} + \mathbf{u} \cdot \nabla \mathbf{u} \right) = -\nabla p + \frac{1}{Re_c} \nabla^2 \mathbf{u} - \boldsymbol{\lambda} \quad \text{over } \Omega \quad (7.1)$$

$$(\rho_r - 1)V_P \left(\frac{d\mathbf{U}}{dt} - \mathcal{F}_r \frac{\mathbf{g}^*}{g^*} \right) - \sum_j (\mathbf{F}_c)_j - \int_{P(t)} \boldsymbol{\lambda} d\mathbf{x} = \mathbf{0}, \quad \text{over } P(t) \quad (7.2)$$

$$\mathbf{I}_P \frac{d\boldsymbol{\omega}}{dt} + \boldsymbol{\omega} \times \mathbf{I}_P \cdot \boldsymbol{\omega} + \sum_j (\mathbf{F}_c)_j \times \mathbf{R}_j + \int_{P(t)} (\boldsymbol{\lambda} \times \mathbf{r}) \cdot d\mathbf{x} = \mathbf{0}, \quad \text{over } P(t), \quad (7.3)$$

$$\mathbf{u} - (\mathbf{U} + \boldsymbol{\omega} \times \mathbf{r}) = \mathbf{0}, \quad \text{over } P(t), \quad (7.4)$$

2. Continuity equation

$$\nabla \cdot \mathbf{u} = 0, \quad \text{over } \Omega. \quad (7.5)$$

where $\mathbf{u} \in \mathcal{V}_{\partial\Omega}(\Omega)$ stands for the fluid velocity vector, $p \in \mathcal{P}(\Omega)$ the pressure, $\boldsymbol{\lambda} \in \Lambda(t)$ the velocity distributed Lagrange multiplier vector, $\mathbf{U} \in \mathbb{R}^d$ the particle translational velocity vector, $\boldsymbol{\omega} \in \mathbb{R}^{\tilde{d}}$ the particle angular velocity vector, \tilde{d} the number of non-zero components of $\boldsymbol{\omega}$ (if $d = 2$: $\boldsymbol{\omega} = (0, 0, \omega_z)$ and $\tilde{d} = 1$; if $d = 3$: $\boldsymbol{\omega} = (\omega_x, \omega_y, \omega_z)$ and $\tilde{d} = 3 = d$), $\mathbf{F}_c \in \mathbb{R}^d$ the contact forces, $\mathbf{R} \in \mathbb{R}^d$ the vector between particle gravity center and contact point, \mathbf{r} the position vector with respect to particle gravity center, $V_P = M^*/(\rho_s^* L_c^{*d}) \in \mathbb{R}$ the dimensionless particle volume, M^* the particle mass, $\mathbf{I}_P = \mathbf{I}_P^*/(\rho_s^* L_c^{*(d+2)}) \in \mathbb{R}^{\tilde{d} \times \tilde{d}}$ the dimensionless particle inertia tensor, $\rho_s^* \in \mathbb{R}$ the particle density, $\mathbf{g}^* \in \mathbb{R}^d$ the gravity acceleration and $g^* \in \mathbb{R}$ the gravity acceleration magnitude.

The following dimensionless numbers are introduced in the above equations:

$$\text{Reynolds number } \mathcal{R}e_c = \frac{\rho_f^* U_c^* L_c^*}{\eta^*}, \quad (7.6)$$

$$\text{Froude number } \mathcal{F}r = \frac{g^* L_c^*}{U_c^{*2}}, \quad (7.7)$$

$$\text{density ratio } \rho_r = \frac{\rho_s^*}{\rho_f^*}, \quad (7.8)$$

where η^* denotes the fluid viscosity. In the following, $L_c^* = d^*$ is chosen for suspension flows, d^* denoting the diameter of the cylinder whose cross section circumscribes the extruded shapes (FIG. 7.1).

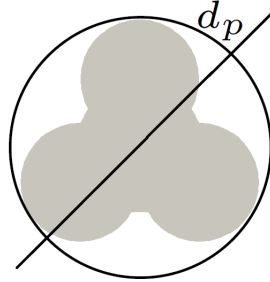


Figure 7.1 – Definition of the circumscribed diameter.

3.3 Time discretization scheme

The set of conservation equations is solved by a first-order operator splitting algorithm. Diffusion and advection terms are treated by a Crank-Nicholson and a Adams-Bashford scheme. Further details on the method and algorithm can be found in [Wachs et al. \(2015\)](#) and [Dorai et al. \(2015\)](#). In this study, since particles are fixed, our operator-splitting algorithm is comprised in two stages, written in a dimensionless form as follows:

1. A classical L2-projection scheme for the solution of the Navier-Stokes problem: find $\mathbf{u}^{n+1/2}$ and p^{n+1} such that

$$\begin{aligned} \frac{\tilde{\mathbf{u}} - \mathbf{u}^n}{\Delta t} - \frac{1}{2\mathcal{R}e_c} \nabla^2 \mathbf{u}^{n+1/2} &= -\nabla p^{n+1} + \frac{1}{2\mathcal{R}e_c} \nabla^2 \mathbf{u}^n, \\ &- \frac{1}{2} (3\mathbf{u}^n \cdot \nabla \mathbf{u}^n - \mathbf{u}^{n-1} \cdot \nabla \mathbf{u}^{n-1}) - \gamma \boldsymbol{\lambda}^n, \end{aligned} \quad (7.9)$$

$$\nabla^2 \psi = \frac{1}{\Delta t} \nabla \cdot \tilde{\mathbf{u}}, \quad \frac{\partial \psi}{\partial n} = 0 \text{ on } \partial\Omega, \quad (7.10)$$

$$\begin{aligned} \mathbf{u}^{n+1/2} &= \tilde{\mathbf{u}} - \Delta t \nabla \psi, \\ p^{n+1} &= p^n + \psi - \frac{\Delta t}{2\mathcal{R}e_c} \nabla^2 \psi. \end{aligned} \quad (7.11)$$

2. A fictitious domain problem: find \mathbf{u}^{n+1} and $\boldsymbol{\lambda}^{n+1}$ such that

$$\frac{\mathbf{u}^{n+1} - \mathbf{u}^{n+1/2}}{\Delta t} + \boldsymbol{\lambda}^{n+1} = \gamma \boldsymbol{\lambda}^n, \quad (7.12)$$

$$\mathbf{u}^{n+1} = \mathbf{0} \text{ in } P(t). \quad (7.13)$$

where \mathbf{u} , p , $\boldsymbol{\lambda}$, ψ and Δt denote the dimensionless fluid velocity, fluid pressure, DLM/FD Lagrange Multiplier to relax the constraint in EQ. 7.13, pseudo-pressure field and time step respectively. The term $\gamma \in [0 : 1]$ is a constant that sets the level of explicit direct forcing in the velocity prediction step. It has been shown that $\gamma = 1$ significantly improves the coupling between sub-problems (1) and (2) and allows the use of larger time steps Δt . In practice, all computations are performed with $\gamma = 1$ (see [Wachs et al. \(2015\)](#) for more details).

3.4 Colocation Points on non-convex particles

As explained in [Wachs \(2009; 2011\)](#), the set of CP comprises a set of interior points distributed in the solid volume using staggered fluid velocity nodes and a subset of boundary points distributed as uniformly as possible on the solid surface. An illustration on a 2D circular cylinder is shown in [FIG. 7.2](#).

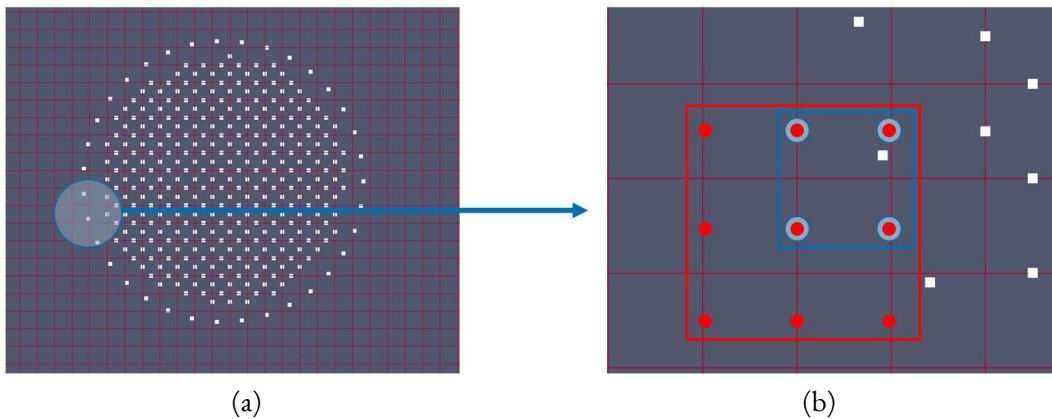


Figure 7.2 – DLM/FD points on the staggered grid for a 2D circular cylinder: (a) the set of interior and boundary points, (b) in blue the 4-point multi-linear interpolation stencil and in red the 9-point Q2 outwards-oriented interpolation stencil for the x velocity component. Adapted from [Wachs et al. \(2015\)](#).

In [Wachs et al. \(2015\)](#), two types of interpolation operator are considered ([FIG. 7.2](#)): a classical multi-linear operator ([Höfler and Schwarzer \(2000\)](#)) and a quadratic operator that uses

the basis functions of a cubic Q_2 finite element (9-point in 2D and 27-point in 3D stencil). The difficulty arises when the particle shape is not isotropic. Far from being understood, the repartition of CP on non-convex body is not straightforward. Even the simple case of spherical particle is still subjected to discussion in the literature. Therefore, a particular care is dedicated to equally distribute the CP in the best manner possible.

As the construction of a non-convex shape is based on decomposing it into convex shapes, the construction of the CP is performed as follows:

- trilobal particle is made of three cylinders with a triangular prism which fills the central gap forming the connection between the three cylinders (FIG. 7.3a). The same procedure is applied to quadralobal particle but instead of a triangular prism, a rectangular parallelepiped is used (FIG. 7.3b).

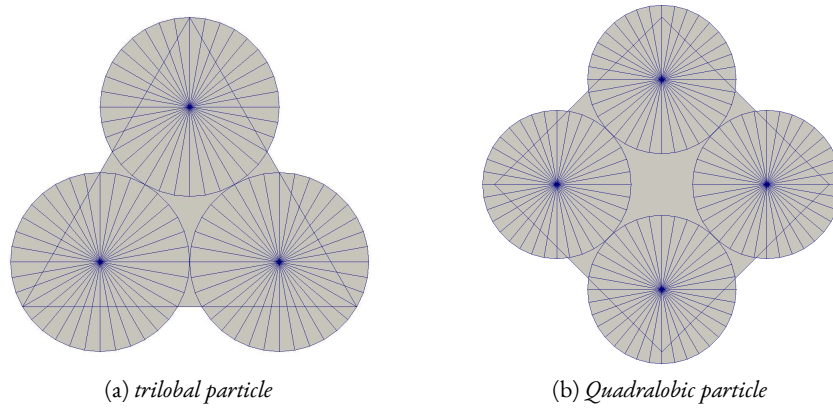


Figure 7.3 – Decomposition of trilobal and quadralobal particle shapes into convex shapes. View of the cross sections.

- the sets of interior CPs of all the components of the “composite” are merged by ensuring that they are neither overlapping.
- the set of boundary points is distributed as follows:
 - for the cylinders, the CPs are distributed in slices along the cylinder revolution axis with a constant distance. Let z be the revolution axis of the cylinder and $\mathbf{k} \in \mathbb{R}^d$ its unit vector and let $\mathbf{r} \in \mathbb{R}^d$ the radial vector. Then the CP are build using the parametric equation of each slice which reads, for $\zeta \in [0, 1]$: $\mathbf{P} = \cos(\zeta)\mathbf{r} + \sin(\zeta)\mathbf{k} \times \mathbf{r} + \mathbf{C}$, where $\mathbf{C} \in \mathbb{R}^d$ denotes the slice gravity center.
 - for the triangular prism and the rectangular parallelepiped, the points are distributed as follows: given the targeted point to point distance $l_{pp} = \tau h$, $\tau \in [1 : 2]$ and the rectangular or triangular edge length l_e , the actual point to point distance is $l_a = l_e / \mathbf{int}(l_e / l_{pp})$, where $\mathbf{int}(x)$ denotes the integer portion of x . On each face, the points are located at the nodes of a constant spacing ratio l_a lattice made of squares for the rectangular faces and equilateral triangles for the triangular faces (FIG. 7.4).
 - the boundary CPs are merged in the following manner: (i) the BP located in another convex component is discarded; (ii) the CPs on the edges of the components are kept to perfectly describe their shapes; (iii) the boundary CPs on the top and bottom disks of all the cylinders are kept except those on their edges which are on the cross-section of the polyhedron; (iv) the last empty area: on the top and the bottom of the shape is filled by the CPs of the polyhedron and we ensure that the CPs are not too close.



Figure 7.4 – Layout of boundary CP on: (a) rectangular face and (b) triangular face.

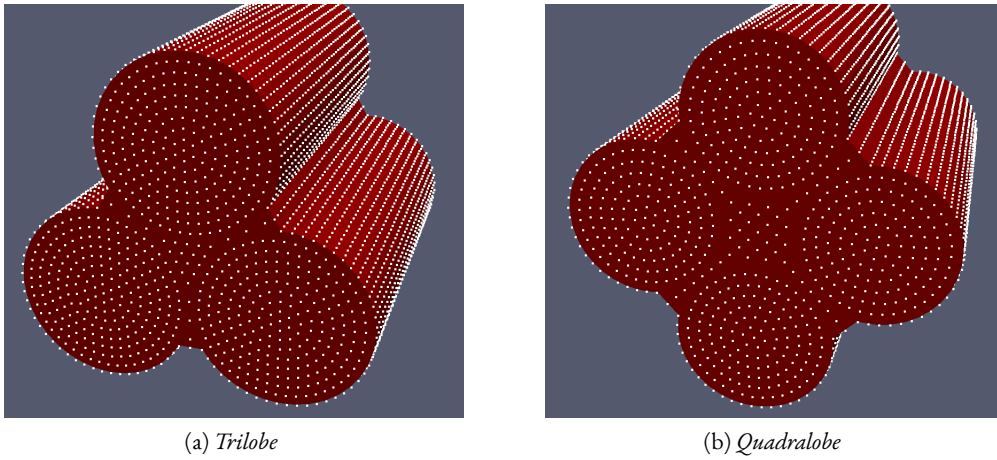


Figure 7.5 – Layout of boundary CP on a : (a) trilobal, (b) quadralobal particles

The resulting geometries are illustrated in FIG. 7.5

4 ACCURACY OF THE COMPUTED SOLUTIONS

4.1 Methodology

A space convergence study is now presented in the aim of knowing the accuracy as a function of the mesh size and minimizing the computing resources. Literature on the accuracy of solutions computed with a DLM/FD methods exists for spheres (Kanarska et al. (2011)) and cylinders (Dorai et al. (2014; 2015)). Intuitively, the space resolution for poly-lobed particles is expected to be even more demanding.

Due to the lack of analytical solution, the space convergence study is based on the approach proposed by Richardson (1911) which consists in (i) estimating the reference solution by extrapolating the numerical solutions to zero mesh size and (ii) evaluating the accuracy of the computed solutions against the reference. The extrapolation reads:

$$\Lambda = \Lambda(h) + Kh^\beta + \mathcal{O}(h^{\beta+1}), \quad \text{with } h = N_p^{-1} \quad (7.14)$$

where N_p , K and β denote respectively the number of CP on the circumscribed cylinder diameter d^* , pre-factor of the relative error and convergence rate. From the equation EQ. 7.14, $\Lambda_{ref} = \Lambda(0)$ gives the exact extrapolated solution. Hence, the convergence is evaluated in

terms of relative error e of the physical quantity Λ as follows:

$$e(\Lambda) = \frac{|\Lambda - \Lambda_{ref}|}{|\Lambda_{ref}|} \quad (7.15)$$

Here, the new shapes of particle are subjected to assorted flow regimes and flow configurations such as: (i) flows through an infinite structured array of poly-lobed particles at low Reynolds number ($\mathcal{R}e_c = 0.01$), (ii) flows through a packed bed of poly-lobed particles at low and moderate Reynolds numbers ($\mathcal{R}e_c = 0.01$ and $\mathcal{R}e_c = 16$).

4.2 Flow past a single poly-lobed particle in a tri-periodic domain

The first attempt to assess the accuracy of the presented extension of the DLM/FD formulation has been inspired by the work of [Zick and Homsy \(1982\)](#). The test consists in computing the friction coefficient for a single particle in a tri-periodic domain, in other words the flow through an infinite of particles. The friction coefficient is computed as the pressure drop based on the diameter of the equivalent sphere of same volume. The relationship between the mean velocity u^* , the imposed pressure drop Δp^* and the friction coefficient K for an infinite structured simple array of poly-lobed particles, modelled as a single particle centered in a tri-periodic domain, reads:

$$\frac{\Delta p^*}{l_s^*} = \frac{9}{2} \frac{\eta^*}{a^{*2}} \phi K u^* \quad (7.16)$$

where l_s^* , a^* , η^* , ϕ denote respectively the streamwise domain length, equivalent sphere radius, fluid viscosity and the solid volume fraction defined as $\phi = 1 - \varepsilon$ in which ε stands for the void fraction. Unlike spherical particles, there is an infinite way to orientate an elongated poly-lobed particle due to the anisotropy of its shape. In addition to the Reynolds number $\mathcal{R}e$ and the solid volume fraction ϕ , the Euler angles (φ, θ, ψ) and the aspect ratio a_r should be included in the study.

In general, the packed particles are arranged in a random way which enables the fluid to flow in a random interstitial pore shape and size. Depending on the latter the preferential streamwise directions are established, whereas in this test case the streamwise direction is only imposed by the geometry of the periodic domain. For the sake of simplicity and to cover a large range of all the parameters, two aspect ratios are chosen ($a_r = 1$ and $a_r = 5$), ϕ is varying from loose to dense packing and three sets of Euler angles are considered for the particle orientation (relative to the streamwise direction):

- parallel to the particle axis ($\varphi = 0^\circ, \theta = 0^\circ, \psi = 0^\circ$) denoted with the symbol “||” (FIG. 7.6a),
- perpendicular to the particle axis ($\varphi = 90^\circ, \theta = 0^\circ, \psi = 0^\circ$) denoted with the symbol “ \perp ” (FIG. 7.6b),
- a rotation of 20° about all the axis ($\varphi = 20^\circ, \theta = 20^\circ, \psi = 20^\circ$) denoted with the symbol “20” for moderate ϕ (FIG. 7.6c).

In the following, for Stokes regimes, a diffusive time scale is defined as $T_d = \rho_f d^{*2} / \eta^*$ and the Reynolds number $\mathcal{R}e_c$ is defined by using the following terms: $L_c^* = d^*$ for the characteristic length scale and $U_c^* = u_{in}^*$ for the characteristic velocity. d^* and u_{in}^* stand for the diameter of the circumscribed cylinder and the inlet fluid velocity respectively. Hence, the Reynolds number reads:

$$\mathcal{R}e_c = \frac{\rho_f^* u_{in}^* d^*}{\eta^*} \quad (7.17)$$

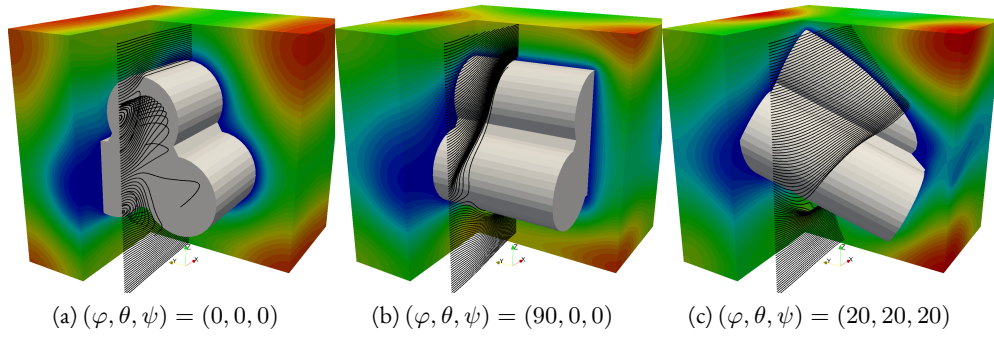


Figure 7.6 – Illustration of the three flow configurations for $\phi = 0.216$. Stream lines. Velocity field magnitude (red=max, blue=min).

First, we assess the accuracy of our method with particles of an aspect ratio $a_r = 1$. The computed solutions obtained from various ϕ are plotted on FIG. 7.8. Simulations are carried out for $Re_c = 0.01$ and $\Delta t/T_d = 10^{-2}$. The trilobe particle seems to have nicer convergence than the quadralobed one. As expected, for high ϕ , the error e is much higher for the same N_p i.e. a higher resolution is needed for dense particulate systems.

Since the space convergence study on $a_r = 1$ shows satisfying results, we now move on to the space convergence for $a_r = 5$. Again, the study is still performed from loose to dense packing. Due to the domain size and shape restriction, the particles are only oriented perpendicularly and collinearly to the flow direction (the “ \perp ” and the “ \parallel ” configurations). For the perpendicular configuration, a very high ϕ means that the fluid is not flowing any more because the orthographic projection of the particle is equal to that of the domain which is somehow “blocking” the fluid to flow properly. For the parallel configuration, the particle orthographic projection is the area with the lobes which enable the fluid to flow in the concavity of the particle even with high solid volume fraction. FIG. 7.7 plots the space convergence of the computed solutions. It can be observed that for $\phi = 0.59$ (dense packing) the solutions exhibit higher relative error compared to the other systems.

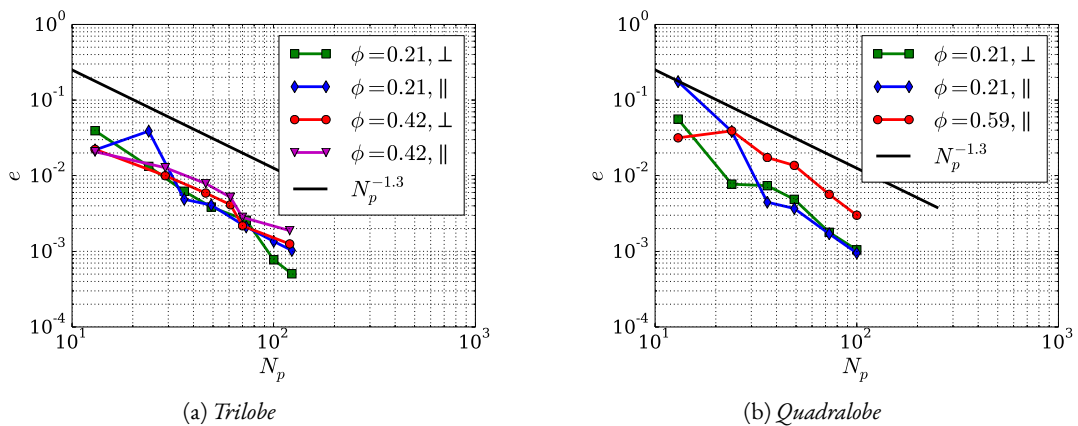


Figure 7.7 – Convergence of the computed solutions at $Re = 0.01$ for $a_r = 5$. N_p is the number of CP in the particle cross-section. $N_p^{-1.3}$ is the convergence rate of a spherical particle.

The previous numerical study can be summarized as follows:

- the most challenging cases are (i) when the particle axis is perpendicular to the main flow

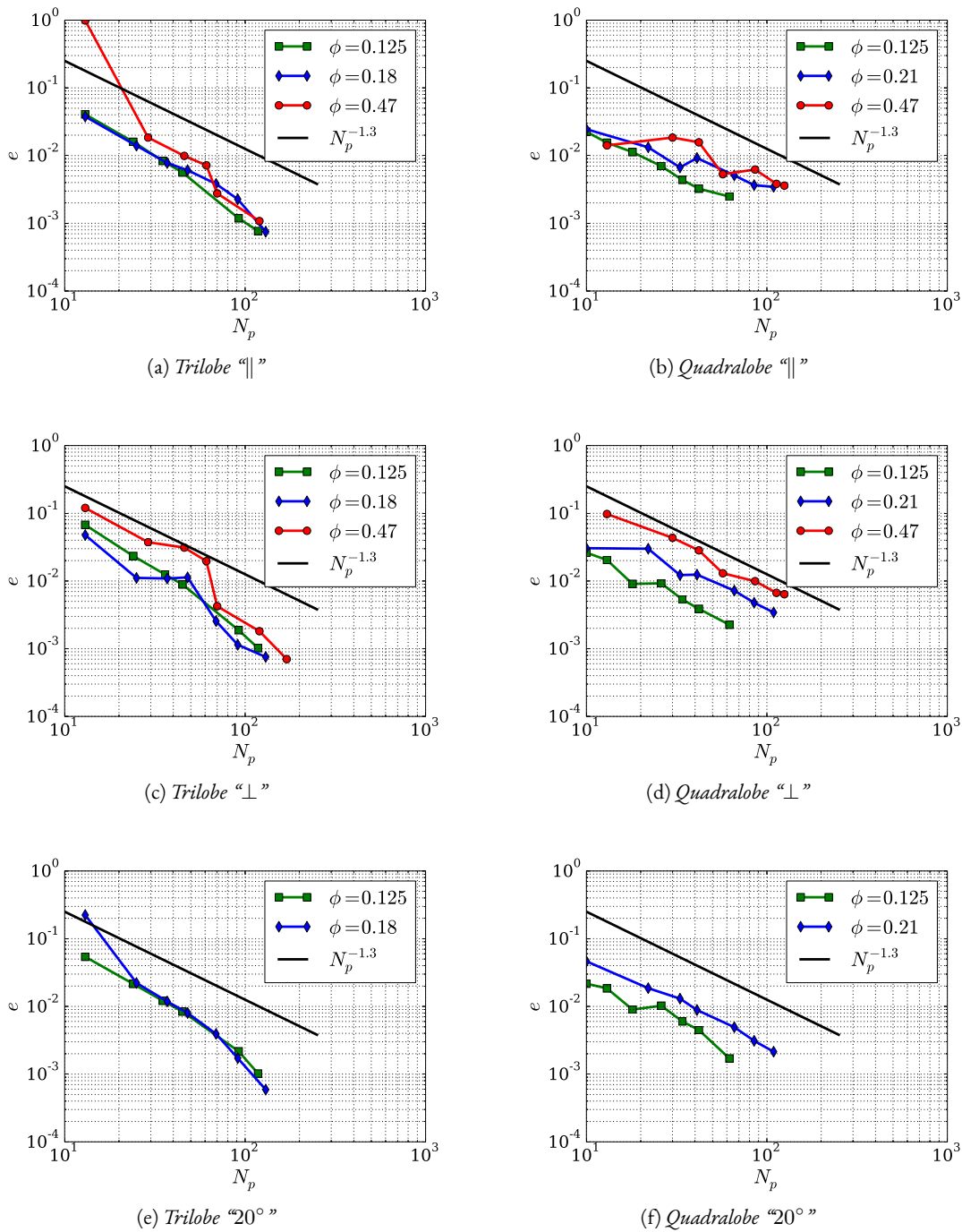


Figure 7.8 – Convergence of the computed solutions at $Re = 0.01$ for $a_r = 1$. N_p is the number of CP in the particle cross-section. $N_p^{-1.3}$ is the convergence rate of a spherical particle.

direction due to the lobe induced recirculation; (ii) when the particle axis is parallel to the main flow direction due to its flat orthogonal face which creates singularities all over the edge,

- all the simulations exhibit an average convergence rate of $N_p^{-1.3}$ which is in line with the work of [Wachs et al. \(2015\)](#) for spherical and polyhedral particles (see also the work of [D'Avino and Hulsen \(2010\)](#)),

- as expected, compared to low ϕ , simulations at high solid volume fraction require a higher N_p for the same accuracy.

For comparison purposes, we performed the simulations of flow past three different shapes (TL, QL, CYL) to have a first glance on the dependency of their friction coefficient on the solid volume fraction. The studied cases consist in comparing 3 elongated particles of the same volume and the same particle length L_p^* . It worth to remind that at the same volume a cylinder does not circumscribe neither the trilobe nor the quadralobe. In terms of particle orientations, two configurations are selected: particle axis perpendicular and parallel to the streamwise direction. $N_p = 45$ for a relative error $e \leq 5\%$ and $\mathcal{R}e_c = 0.01$. TAB. 7.1 summarises the differences between the three shapes.

Shape	Trilobe	Quadralobe	Cylinder
d^*/L_p^*	0.414	0.405	0.349

Table 7.1 – Configuration of the studied cases.

FIG. 7.11 depicts the results of our comparison. In FIG. 7.11a, it can be observed that when the particle axis is perpendicular to the flow the friction coefficient $K(\phi)$ is similar for $\phi \leq 0.34$. The difference is only noticed at high ϕ . In fact, in this configuration, the projected cross-sectional areas (FIG. 7.9) of the particles are different in the following order: $S_{TL}^\perp > S_{CYL}^\perp > S_{QL}^\perp$. This leads to the following classification of friction coefficients: $K_{TL}^\perp > K_{CYL}^\perp > K_{QL}^\perp$.

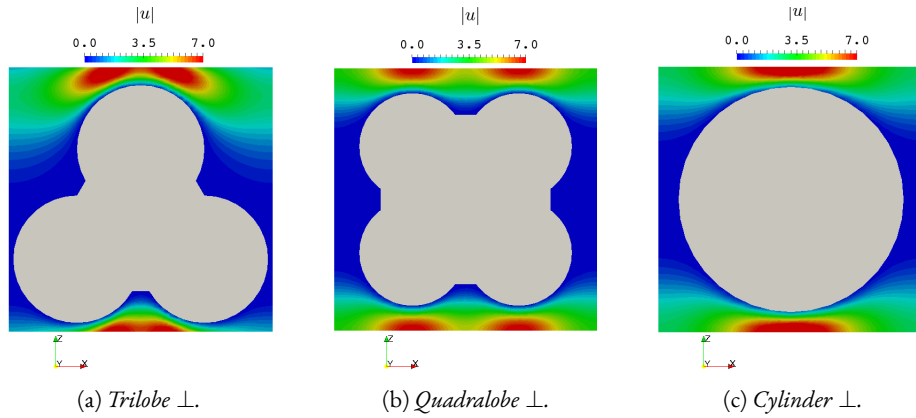


Figure 7.9 – 3-periodic array of particle for $\phi = 0.545$ and $\mathcal{R}e_c = 0.01$. Velocity field magnitude.

FIG. 7.11b, illustrates the computed friction coefficient $K(\phi)$ corresponding to a flow parallel to the particle axis. The orthogonal cross-sectional areas of the particles are classified in the following order: $S_{CYL}^\parallel < S_{TL}^\parallel < S_{QL}^\parallel$ (FIG. 7.10). Therefore, the resulting friction coefficients are classified as follows: $K_{CYL}^\parallel < K_{TL}^\parallel < K_{QL}^\parallel$.

The results presented in FIG. 7.11 show that the computed solutions depend drastically on the particle orientation, hence the projected cross-sectional area. At low concentration, there is no clear distinction between the shapes.

Based on these results, we would like to examine the accuracy of the solution computed by our numerical model in the case of the flow through a packed bed. In fact, a packed bed is representative of the real operating conditions regarding volume fraction, the position and orientation of particles.

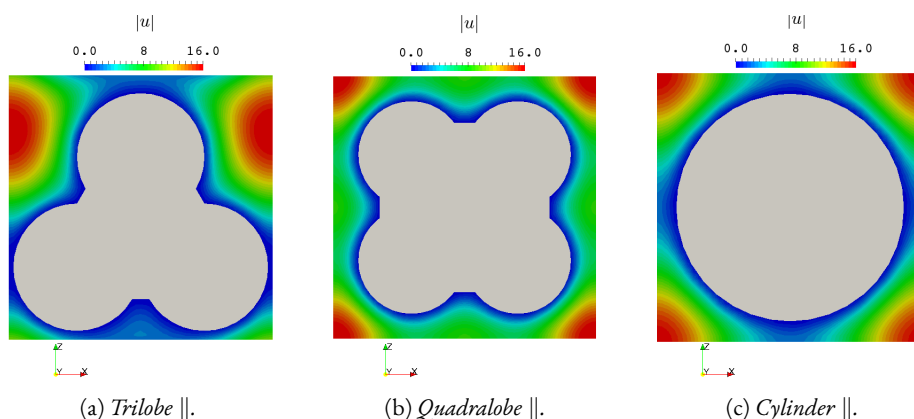


Figure 7.10 – 3-periodic array of particle for $\phi = 0.545$ and $\mathcal{R}e_c = 0.01$. Velocity field magnitude.

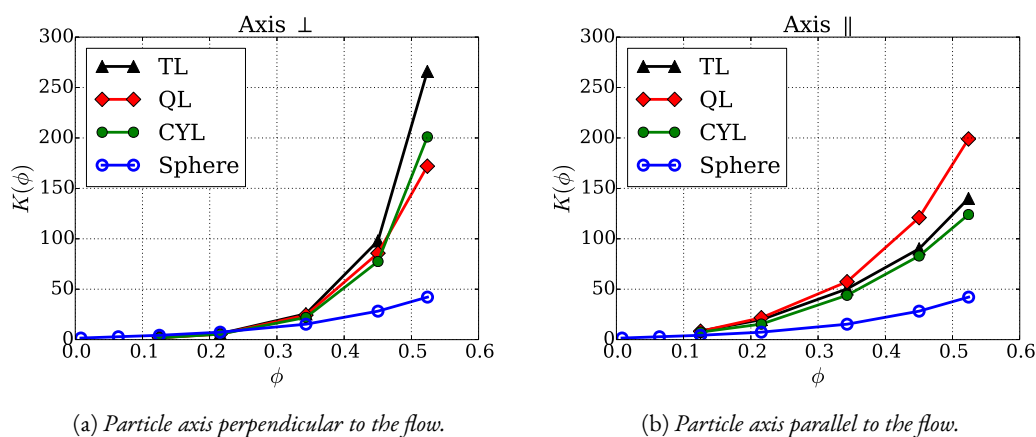


Figure 7.11 – Dependency of the friction coefficient K on the solid volume fraction ϕ .

4.3 Flow past a small packed bed of poly-lobed particles

For decades, predicting the flow through a packed bed of particles has been an interesting and challenging subject in the chemical engineering community. One of the major challenges is the effect of particle shape in these systems, where the bed porosity and pressure drop are very important for industrial operations. The second step of the space convergence study is performed on a small size bed of packed particles ($a_r = 2$). This case is more representative of fixed beds than the periodic array of a single particle as particles present random orientations forming a porous medium in which the fluid flow is more complex. Rules have been suggested in previous related works regarding the number of CP needed to discretize a particle and guarantee a computed solution of satisfactory accuracy. However the straightforward extrapolation from flow in beds of cylinders (Dorai et al. (2014; 2015)) and polyhedra (Wachs et al. (2015)) to beds of poly-lobed particles is rather questionable and might not be accurate enough. In fact, the lobes create additional complexity.

In this case, 40 trilobal particles ($a_r = 2$) are stacked in a bi-periodic domain of $5 \times 5 \times 10$ ($Lx \times Ly \times Lz$) (FIG. 7.12a). The corresponding solid volume fraction is $\phi \simeq 0.55$. The particles are located at $z = 3$ away from the inlet and the outlet of the system. The boundary conditions are set as follows:

- periodic boundary conditions in the horizontal direction

- a uniform upward inlet velocity at the bottom of the bed
- a zero pressure outlet and homogeneous Neumann boundary conditions for all velocity components at the top of the bed

The convergence is assessed on the inlet-outlet pressure drop.

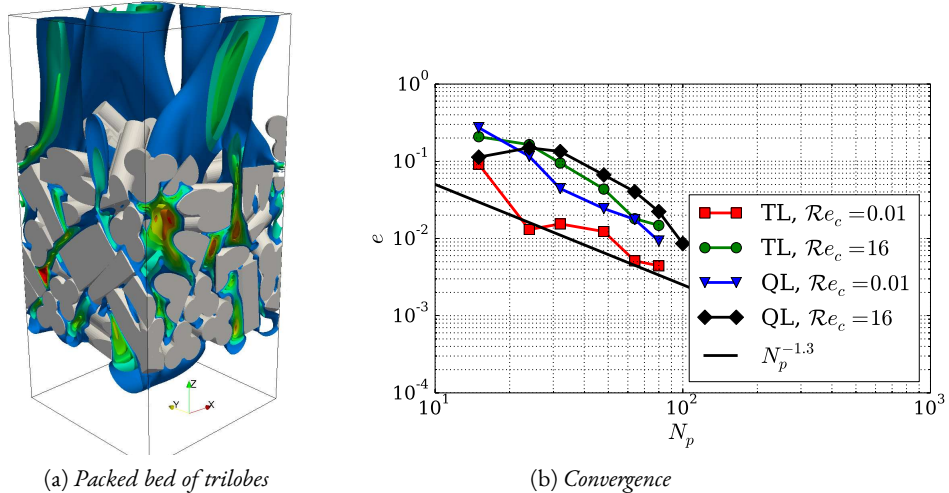


Figure 7.12 – Packed bed reactor of trilobal particles. (a) contour of the velocity magnitude at $\mathcal{R}e = 50$ (red=max, blue=min). (b) convergence of the computed solutions

Results are obtained in this configuration are promising: from $N_p = 16$ the error is less than 2% in Stokes regime, whereas $N_p = 65$ is required for the same accuracy for $\mathcal{R}e = 16$. In Dorai et al. (2014), the authors pointed out that computing a fluid flow through a packed bed cylinders requires 50% finer mesh than that of spherical particles. Compared to a cylinder (Dorai et al. (2014)), a trilobal and quadralobic need 50% finer mesh to achieve the equivalent accuracy.

5 PRESSURE DROP THROUGH PACKED BEDS OF POLY-LOBED PARTICLES

Results presented in the previous section deemed to be satisfactory enough to perform numerical simulations to predict the pressure drop through packed beds of poly-lobed particles. The objective of this section is to compute this pressure drop with trilobal and quadralobal particles based on PRS, investigate shape effects, assess uncertainty quantification and derive predictive correlations based on the Ergun's formulation (Ergun (1952)).

5.1 A quick review of single phase pressure drop in fixed beds

The theory of Kozeny (1927) describes a porous media as a collection of small channels in which a fluid is flowing in laminar regime. It reads:

$$\frac{\Delta p^*}{H^*} = 72 \frac{\eta^* (1 - \varepsilon)^2 u_{in}^*}{\varepsilon^3 d_s^{*2}} \quad (7.18)$$

From a physical view point, this formula proposes that the equivalent channel diameter is proportional to the sphere diameter d_s^* regardless of the local structure through:

$$\frac{\varepsilon d_s^*}{(1 - \varepsilon)} \quad (7.19)$$

To account for tortuosity that are present in a porous media, [Blake \(1922\)](#) corrected the coefficient 72 to 150 which led to the Blake-Kozeny equation for $\varepsilon < 0.5$ and $\mathcal{R}e_c < 10$:

$$\frac{\Delta p^*}{H^*} = 150 \frac{\eta^* (1 - \varepsilon)^2 u_{in}^*}{\varepsilon^3 d_s^{*2}} \quad (7.20)$$

[Carman \(1937\)](#) proposed $= 180$ as a correction in Stokes flow regimes ($\mathcal{R}e_c \sim 0$) in packed beds of spheres, which is more accurate than Blake's coefficient in these conditions. The equation reads:

$$\frac{\Delta p^*}{H^*} = 180 \frac{\eta^* (1 - \varepsilon)^2 u_{in}^*}{\varepsilon^3 d_s^{*2}} \quad (7.21)$$

For high Reynolds number regimes, [Burke and Plummer \(1928\)](#) considered that the pressure drop through a packed bed can be computed as an inertia term. They proposed the following equation for $\mathcal{R}e_c > 1000$:

$$\frac{\Delta p^*}{H^*} = 1.75 \frac{\rho_f^* (1 - \varepsilon) u_{in}^{*2}}{\varepsilon^3 d_s^*} \quad (7.22)$$

which is known as the Burke-Plummer equation. In this formulation the characteristic size of the channel is the same as the one proposed by Kozeny.

Combining the previous theories, [Ergun and Orning \(1949\)](#) mentioned that the pressure drop through a packed bed is directly function of ε and the constants α and β which depend on the flow regime and proposed the following correlation ([Ergun \(1952\)](#)):

$$\frac{\Delta p^*}{H^*} = \alpha \frac{\eta^* (1 - \varepsilon)^2 u_{in}^*}{\varepsilon^3 d_s^{*2}} + \beta \frac{\rho_f^* (1 - \varepsilon) u_{in}^{*2}}{\varepsilon^3 d_s^*} \quad (7.23)$$

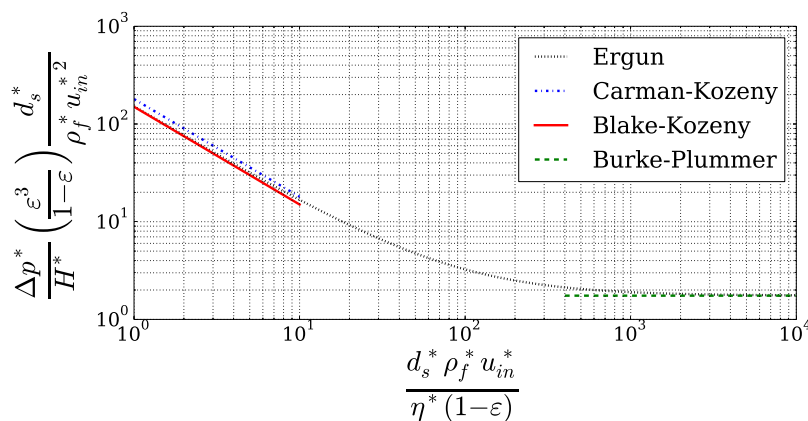


Figure 7.13 – Illustration of the correlations EQ. 7.21, EQ. 7.20, EQ. 7.22 and EQ. 7.23 .

The formulation in FIG. 7.13 has been proved to be accurate and is widely used in the chemical engineering industry. The pressure drop in EQ. 7.23 is the combination of a frictional viscous term proportional to the velocity and a quadratic term on the fluid velocity that takes into account the flow direction and change in cross-sections ([Larachi et al. \(2014\)](#)). [Ergun \(1952\)](#) proposed the constants $\alpha = 150$ and $\beta = 1.75$ to describe the pressure drop through packed beds of spheres, cylinders and crushed particles. For packed beds of complex shapes,

a definition of an universal correlation appears to be an endeavour. Many studies reveal a noticeable variation on these coefficients. For instance, [MacDonald et al. \(1991\)](#) suggested that $\alpha = 180$ and $\beta = 1.8$ as universal constants which are over estimate the Ergun's coefficients by more than 16%. It appears that any new experimental data yields a new proposition a set of coefficients. The explanations of the differences between these works are still a subject of discussion between many authors. Among others, it was measured on cylinders by [MacDonald et al. \(1991\)](#) that the value of β is dependent on the particle roughness: $\beta = 1.8$ corresponds to smooth particles, whereas $\beta = 4$ corresponds to the roughest particles.

Later on, many authors improved the correlation, among others [Nemec and Levec \(2005\)](#), to account for shape effects. The coefficients α and β are then modified to include the shape effects. An equivalent particle diameter for non-spherical particles has to be introduced and reads:

$$d_p^* = \frac{6V_p^*}{A_p^*} \quad (7.24)$$

where V_p^* and A_p^* denote respectively the volume and area of the particle.

Shape	a_r	Ψ	ε	α	β
Trilobe	4.33	0.63	0.466	295	4.71
Trilobe	4.33	0.63	0.511	263	4.99
Quadralobe	3.85	0.593	0.471	292	3.93
Quadralobe	3.85	0.593	0.502	294	4.19

Table 7.2 – Fitted Ergun constants for poly-lobed particles. Credit: [Nemec and Levec \(2005\)](#).

[Nemec and Levec \(2005\)](#) summarise the works of [Pahl \(1975\)](#), [Reichelt \(1972\)](#), [England and Gunn \(1970\)](#) in which α varies between 180 – 280 and β between 1.9 – 4.6 for cylindrical particles of aspect ratio ranging from 0.37 to 5.77. They measured the pressure drop for a large number of inlet velocities for one trilobal and one quadralobal shape. Each experiment was repeated twice (on a repacked bed), yielding only 4 additional data points (TAB. 7.2). It is interesting to note that the proposed correlation would systematically under or over predict the experimental data points. In summary, the available data for poly-lobed particles is scarce (only 2 points for TL and QL), with a large scatter.

For non-spherical particles, [Nemec and Levec \(2005\)](#) extended the correlation by introducing the sphericity Ψ :

$$\Psi = \left(\frac{36\pi V_p^{*2}}{A_p^{*3}} \right)^{\frac{1}{3}} \quad (7.25)$$

$$\frac{\Delta p^*}{H^*} = \alpha(\Psi) \frac{\eta^* (1 - \varepsilon)^2 u_{in}^*}{\varepsilon^3 d_p^{*2}} + \beta(\Psi) \frac{\rho_f^* (1 - \varepsilon) u_{in}^{*2}}{\varepsilon^3 d_p^*} \quad (7.26)$$

$$\alpha(\Psi) = \frac{150}{\Psi^a} \quad (7.27)$$

$$\beta(\Psi) = \frac{1.75}{\Psi^b} \quad (7.28)$$

Nemec and Levec (2005) proposed some values for a and b depending on the particle shapes: $(a, b) = \left(\frac{3}{2}, \frac{4}{3}\right)$ for cylinders and $(a, b) = \left(\frac{6}{5}, 2\right)$ for poly-lobed particles. The proposed correlation does not fit with all the data points. Based on numerical results in the creeping flow regime, Dorai et al. (2015) proposed $a = 5/4$ for cylinders (b was not evaluated). As matter of fact, the suggested correlation agrees fairly well with the numerical results of Dorai et al. (2015) for which the present study is a continuation. The work agrees well with the experimental data of Nemec and Levec (2005) for cylindrical particles. Other formulations have been proposed that take into account various shapes. Nevertheless, there is so far no universal method to precisely predict the Ergun's equation coefficients based only on particle shape.

From the experimental point of view, the data on poly-lobed particles is scarce and quite dispersed. The reason of this scattering is still a matter of discussion (see for example Nemec and Levec (2005)). Recently, PRS on cylinder (Dorai et al. (2015)) opened up new perspectives in "in silico" determination of the pressure drop for any particle shape, for example TL and QL. The goal of this part of this study is to suggest a correlation based on the Ergun formulation and propose coefficients α and β for trilobal and quadralobal particles.

5.2 Method

As it can be seen in *Chapter 3* that Grains3D is used as a porous media maker. The single phase fluid flowing through the packed bed is computed with PeliGRIFF using PRS. All the simulations are performed in a $Lx^* = Ly^* = 8 \text{ mm}$ wide bi-periodic container using a circumscribed diameter $d^* = 1.6 \text{ mm}$. Packed beds consist of 210 to 320 particles. The investigation is carried out with packings of TL and QL with a range of aspect ratio define as $a_r = 1.5, 2, 2.5, 3, 4$. Boundary conditions are similar to the previous convergence study on packed beds. The particles are stacked at $2.5d^*$ away from the top and $2.5d^*$ from the bottom of the domain.

The local void fraction $\langle \varepsilon \rangle_z$ is the volumetric average of void fraction on a layer of the bed of thickness Dz (Fig. 7.14b). The average void fraction $\langle \varepsilon \rangle$ is the average of all $\langle \varepsilon \rangle_z$ inside the control volume. $\langle \varepsilon \rangle_z$ is used to plot axial profiles of void fraction and obviously depends on the value of Dz . It is computed by discretizing the volume occupied by the particles. The pressure $\langle p \rangle_z$ is the average pressure on a plane located at height z . The averaging procedures are written as follows:

$$\langle \varepsilon \rangle_z = \frac{\sum_i \delta(x, y, z) v_{i,z}}{\sum_i v_{i,z}} \quad (7.29)$$

$$\text{where } \delta(x, y, z) = \begin{cases} 1, & \text{if } \mathbf{X}(x, y, z) \in \Omega_p \\ 0, & \text{otherwise} \end{cases} \quad (7.30)$$

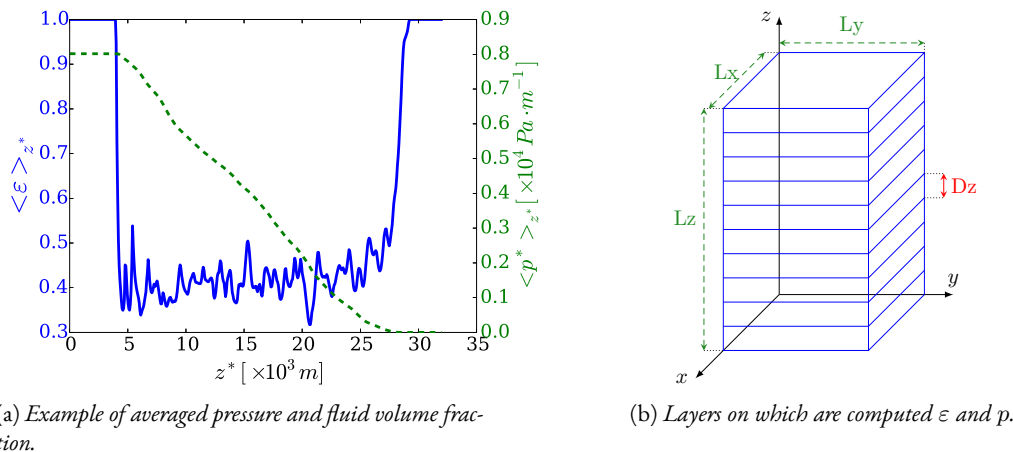
$$\langle p \rangle_z = \frac{\sum_i p_i(x, y, z)}{\sum_i v_{i,z}} \quad (7.31)$$

$\varepsilon, p_i, v_{i,z}$ denote respectively the fluid volume fraction, the pressure and the control volume of the system at the coordinate z .

The pressure drop is the difference between the pressure at planes located at $z = 3$ from the top of the packed bed and $z = 2$ from its bottom (Dorai et al. (2012; 2014; 2015)). In other

words, a layer of 3 particle diameters thick is discarded at the top of the bed, whereas a layer of 2 particle diameters thick is discarded at the bottom. The void fraction and the pressure difference are computed on the same control volume $Lx \times Ly \times Dz$.

FIG. 7.14a plots examples of values obtained from PRS of packed beds in this study. It can be seen that the pressure and the void fraction are correlated.



(a) Example of averaged pressure and fluid volume fraction.

(b) Layers on which are computed ε and p .

Figure 7.14 – Example of outputs resulting from the post-processing Eqs. 7.29 and 7.31 on a fixed bed of trilobal particles at $\mathcal{Re}_c = 0.1$ and $a_r = 1.5$.

All the PRS are performed at \mathcal{Re}_c ranging from 0.1 to 16 with the objective of capturing the onset of inertia regime ($\mathcal{Re}_c = 0.1, 0.2, 0.3, 0.4, 1, 16$). All systems are re-packed randomly several times to have different micro-structures (2 to 10 times). In particular, for both shapes, the systems of particles of aspect ratio $a_r = 2$ are repeated 10 times to quantify the effects of random packing both on the void fraction and the pressure drop simulated for $\mathcal{Re}_c = 1$. After the extraction of the pressure drop, the coefficients α and β of the Ergun's correlation are fitted according to numerical results. The fitting of β is performed only in the case of inertial flow regimes.

We observed that some pressure profiles are not fully linear arising the question of how the choice of cutting planes affect the output. A sensitivity analysis for a limited number of 7 beds based on independently changing the positions of the bottom and top cutting planes between $0.5d^*$ and $5d^*$, yields an uncertainty of 3.1% on the value of α . This trend is judged to be low enough to use always the same cutting planes positions.

FIG. 7.15 depicts a typical results of PRS for a packed bed of trilobes at $\mathcal{Re}_c = 0.1$ and $a_r = 2$.

5.3 Results

Uncertainty quantification of the packings

All packed beds are loaded randomly. For this reason, it is matter of importance to quantify the effect of repetition (re-packing) on packed bed reactors. In this section, we investigated the random packings of 10 packed beds of TL and QL of $a_r = 2$. FIG. 7.16b plots the pressure drop through successive simulations of the coupled problem (granular packing + PRS) as a function of void fraction $\langle \varepsilon \rangle$. It can be observed that void fraction may vary significantly among simulations. In this data set, the packed beds of TL have a lower void fraction $\langle \varepsilon \rangle$ compared to those of QL and induce a higher pressure drop.

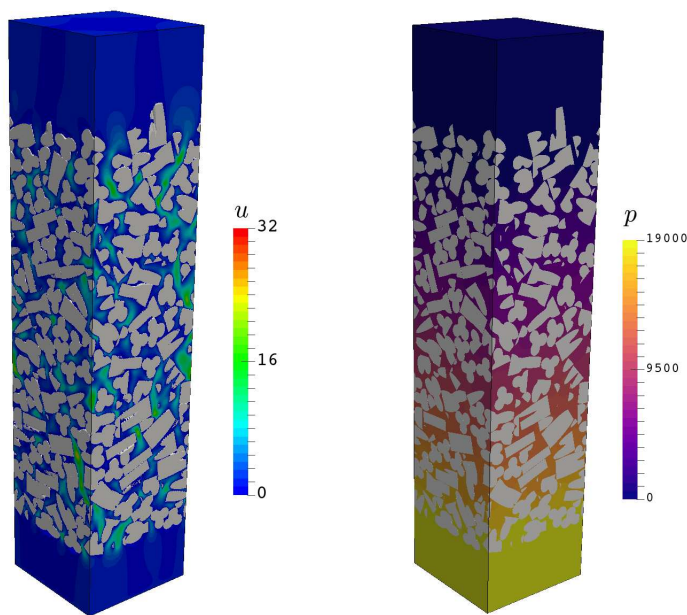


Figure 7.15 – Velocity (left) and pressure (right) fields through a packed bed of trilobal particles. $Re_c = 0.1$ and $a_r = 2$.

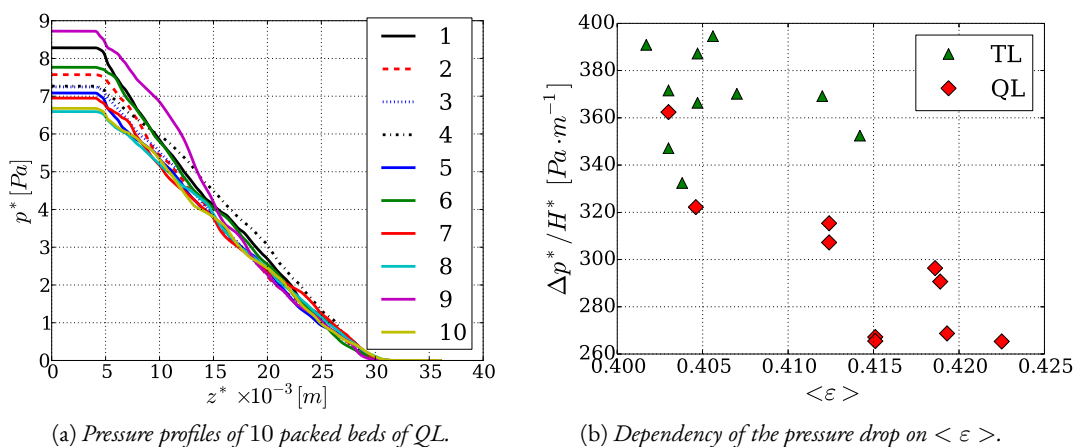


Figure 7.16 – Effects on random packing on the pressure on 10 fixed beds poly-lobed particles of aspect ratio of $a_r = 2$ at $Re_c = 1$.

TAB. 7.3 shows that despite the low standard uncertainty $I = 2\sigma \in [2, 4]\%$ on $\langle \epsilon \rangle$, the pressure drop exhibits an overall uncertainty of $I = 2\sigma \in [12, 24]\%$. The uncertainty on pressure drop partly results from the scattering on void fraction. The uncertainty of α resulting from the hydrodynamic simulations is corrected by the void fraction and is lower than $I = 2\sigma = 12\%$. This behaviour is observed for both shapes. This uncertainty, that results only from random effects during packing, is quite high. An ANOVA analysis on the data indicate that due to the large scatter, α values are statistically identical for TL and QL.

For the sake of comparison, a glance on the local pressure and the velocity field is presented in FIG. 7.17 in 4 horizontal cross-sections of the packed beds 8 (top) and 9 (bottom) at

Cases	Trilobe			Quadralobe		
	$\langle \varepsilon \rangle$	$\Delta p^*/H^*$ (PRS)	α	$\langle \varepsilon \rangle$	$\Delta p^*/H^*$ (PRS)	α
1	0.4070	370.17	212.55	0.4186	296.36	234.09
2	0.4047	366.36	205.16	0.4151	267.20	203.41
3	0.4017	390.90	211.85	0.4046	322.18	219.14
4	0.4047	387.21	216.87	0.4225	265.32	218.44
5	0.4030	371.58	204.37	0.4151	265.48	202.09
6	0.4038	332.42	184.36	0.4030	362.42	242.35
7	0.4030	347.09	190.90	0.4193	268.71	213.89
8	0.4120	369.16	223.58	0.4124	315.36	233.36
9	0.4142	352.47	218.56	0.4124	307.24	227.25
10	0.4056	394.56	223.00	0.4189	290.67	230.42
Mean	0.4060	368.19	209.12	0.4146	296.09	222.44
Std dev.	1%	5.4%	6.3%	1.8%	11.8%	6%

Table 7.3 – Repetition of random packing with identical particles. $\Delta p^*/H^*$ [$\text{Pa} \cdot \text{m}^{-1}$], $\langle \varepsilon \rangle$ [–].

$z = 4, 8, 12, 16$ made with QL of aspects ratios $a_r = 2$. As the It can be seen, despite the fact that the systems are similar in terms of particle number and domain size, the re-packing induces a noticeable difference in the local pressure and velocity magnitude. Since a zero pressure outlet is set at the top of the bed, the differences lie at the vicinity of the bed inlet. It can be noticed that at $z = 4$ the bed 8 has a lower velocity magnitude compared to the bed 9 which is translated into higher pressure compared to the bed 8. As the cross-section is moving upward, the fluid velocity magnitude and the pressure tend to be more homogeneous for both packed beds. This is a pure effect of local micro-structure.

The set of repetitions of a packed bed of QL is considered as representative to investigate the effects of the random packing on the flow dynamics. FIG. 7.16a illustrates the differences in pressure profile for each simulation of the set. It reveals that despite the fact that the system is the same in terms of number of particles and domain size, the random insertion leads to different micro-structures. This is visually confirmed in FIG. 7.17 which depicts the local structures of two packed beds (cases 8 and 9).

Values of the coefficients α and β

The values obtained for the Blake-Kozeny-Carman α and the Burke-Plummer constants β are exhibited in this section. Before presenting the values, it is important to note that the values are in the range of the experimental values, and that the uncertainty induced by the random packings on α is evaluated to be 12%.

Results for the coefficient α are presented in FIGS. 7.18a and 7.18b complemented with data set from the work of Nemeč and Levec (2005). Simulations in this work indicate that $\alpha = 200$, does not depend on particle length and does not vary between TL and QL.

Values of fitted coefficient β are plotted in FIGS. 7.19a and 7.19b as a function of aspect ratio a_r and the sphericity Ψ . The evaluation of β is performed at finite Reynolds number of $\mathcal{R}e_c = 16$, where the quadratic term accounts for approximately 30% of the total pressure drop. As explained earlier, the uncertainty on the pressure drop and α are quite high (resp. $\sim 20\%$ and $\sim 12\%$). This induces an uncertainty on the evaluation of β which approximately reaches 30%. Performing simulations at higher $\mathcal{R}e_c$ is still not possible due to computing resource limitations induced by the complexity of particle shapes. It is worth to note that at $\mathcal{R}e_c = 16$, the computations of the pressure drop through packed beds of particles of $a_r = 4$

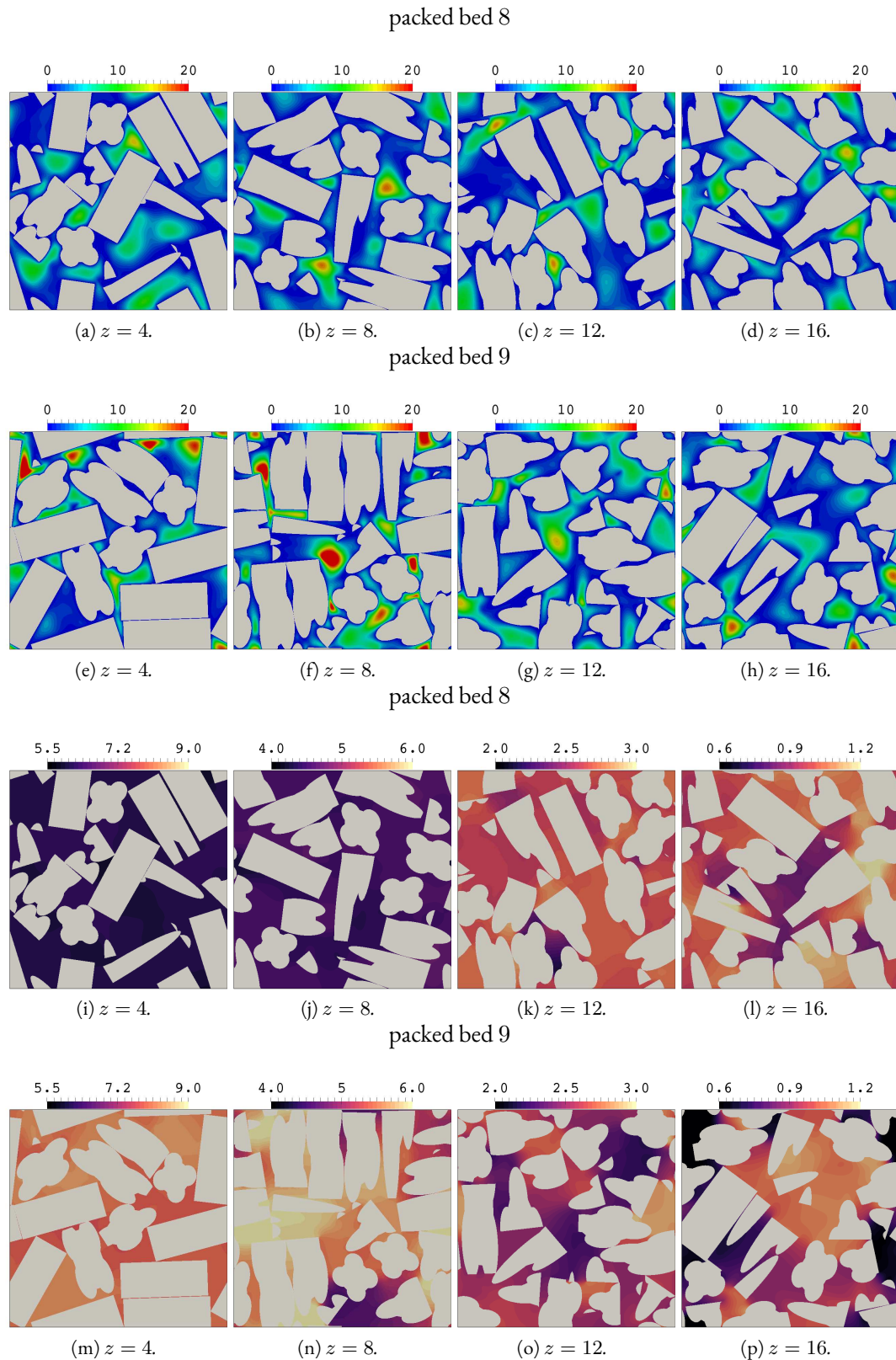


Figure 7.17 – Comparison of the horizontal cross-sectional velocity magnitude ($\|u^*\|/u_{in}^*$) and the pressure field (p^*) between two packed beds of quadralobal particles of aspect ratio of $a_r = 2$ at $Re = 1$.

need more than 3×10^8 grid cells and require more than 512 cores to resolve the problem. The fitted values of β are in the range of 2.8–4.6 which is very coherent with previous works.

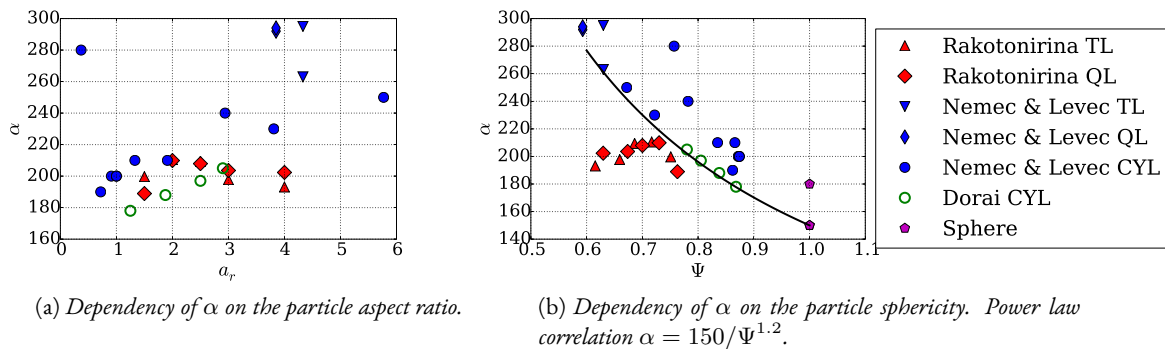


Figure 7.18 – Dependency of the fitted Blake-Kozeny-Carman constant on a_r and Ψ . Number of simulations: 128.

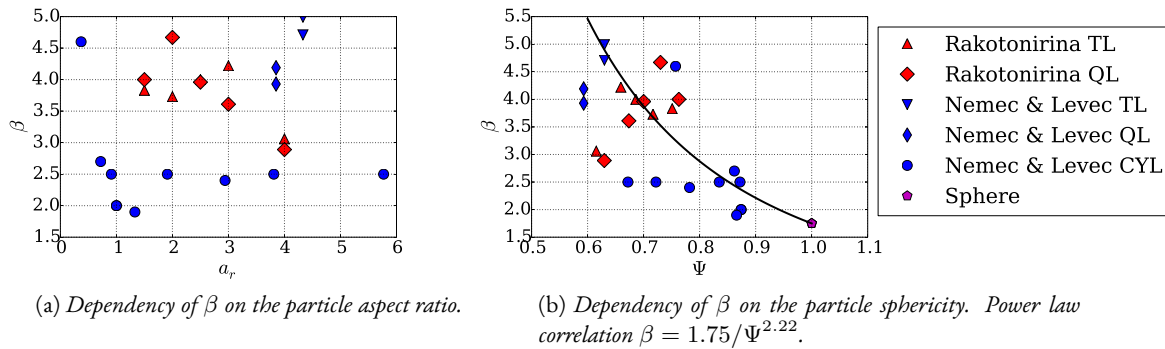


Figure 7.19 – Dependency of the fitted Burke-Plummer constant on a_r and Ψ . Number of simulations: 26.

Discussion on values of α and β

A closer look at the fitted α may indicate two trends depending on the aspect ratio a_r . When plotted as a function of a_r , two domains are identified. For $a_r \leq 2$ ($\Psi \geq 0.68$), TL and QL exhibit values of α which are in the scattered data and follow the usual trend (increasing with a_r , decreasing with Ψ). For $a_r > 2$, values of α seem to loose their dependency on the particle shape, this is most visible when plotted as a function of the sphericity.

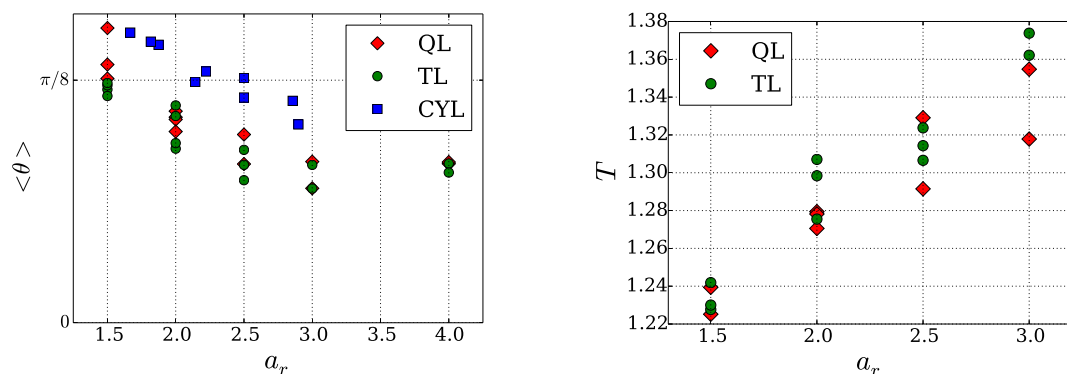
An explanation of this behaviour may be the size of the bi-periodic domain. Intuitively, if the ratio of the domain length to particle length (Lx^*/L_p^*) decreases, the results may suffer from periodicity effects. Simulations in this study were all performed with the same domain width. Therefore, when the particle length increases the ratio of the domain length to the particle length decreases. In order to clear out this risk, the following verification has been performed. Using TL of $a_r = 1.5$, various domain size of 6, 8 and 10 mm are simulated. They all give the same void fraction and pressure drop. Void fractions of particles with an aspect ratio $a_r = 4$ are in the range of 0.52 – 0.53 and in line with the data reported by Nemeč and Levec (2005) (TAB. 7.2) with similar aspect ratios. The void fraction measured by DEM is slightly higher but within the stochastic uncertainty. Last, the same DEM-PRS simulations were run while increasing the domain width from 8 to 12 mm for two cases: TL of $a_r = 2.5$ and CYL of $a_r = 2.89$ ($L_p^* = 4.62$ mm). In both cases, it was found that there are no significant differences on both void fractions (less than 0.5% variation) and pressure drop (less than 5% difference). As cylinder results follow a very regular trend even

for $a_r = 2.89$, it is concluded that the domain size has no effect for $a_r < 3$. Nevertheless, an observation on results for β indicates that the results at $a_r = 4$ can be seen as “different”. For the present time, it is safer to consider that only the results presented for $a_r < 3$ are representative of experimental data.

The verification of the results leaves the door open for an effect of a too small domain size in the simulations with the longest particles. The packing dynamics of long particles may be impacted by the size of the bi-periodic domain by very short mechanical interaction chains. To be more specific, in special conditions, a particle A can mechanically interact with another one B on one side and B’s clone on the other side: this corresponds to a B-A-B interaction chain. This type of interaction does not exist when loading large reactors and may lead to some special packing structures with an effect on pressure drop and possibly on void fraction. Longer interaction chains with 3 or more particles may be also considered but are much more likely to occur experimentally. These very short interaction chains are more likely to occur with long and horizontal particles.

Assuming a loss of representativeness for high particle aspect ratio, a few interesting facts emerge. As the numerical methods used for the simulation of the pressure drop do not depend on particle length, the loss of representativeness for high aspect ratio pressure drop must originate from the packing structure. As already discussed, the simulated void fraction is slightly higher than experimental data, which logically yield a lower pressure drop. However, the void fraction correction to compute α should have corrected for this bias and produces a higher α . The high a_r are different in some ways that are interesting to be understood as they could potentially lead to innovative packing methods that lower pressure drop at constant void fraction. Is it possible to identify this specific features ?

Using numerical data resulting from DEM simulations, it is quite straightforward to compute the angle of each particle with the horizontal plane xy and its average on all particles. As it can be seen in FIG. 7.20a, the average angle to the horizontal is a function of the particle shape and aspect ratio. For TL and QL, it decreases with a_r until an asymptote is reached for $a_r \geq 2.5$. This threshold value corresponds to a presumable transition that might impact the pressure drop. For cylindrical particles, the average angle to horizontal decreases more slowly and does not reach a plateau with the available data. Is the plateau a physical feature or the result of the limited domain size ?



(a) Dependency of the orientation angle on the particle aspect ratio a_r .

(b) Dependency of the tortuosity on the particle aspect ratio a_r .

Figure 7.20 – Dependency of T and $\langle \theta \rangle$ on the aspect ratio a_r at $Re = 0.1$.

Tortuosity is the other standard porous media descriptor, although barely used in chemical

engineering as it is very difficult to measure. This data can be measured numerically. One of the methods studied in [Duda et al. \(2011\)](#) suggests to express the tortuosity T as a ratio of the volumetric integral of the fluid flow velocity to the the volumetric integral of the velocity component of the macroscopic flow direction. It reads:

$$T = \frac{\int_{\mathcal{V}} v(\mathbf{X}) d^3\mathbf{X}}{\int_{\mathcal{V}} v_z(\mathbf{X}) d^3\mathbf{X}} = \frac{\langle v \rangle}{\langle v_z \rangle} \quad (7.32)$$

where subscript z stands for the macroscopic flow direction.

[Carman \(1937\)](#) already had this idea of computing $\langle v \rangle / \langle v_z \rangle$ for the representation of the hydraulic tortuosity but all the attempts were always restricted to simple model such as group of parallel channels which do not represent complex heterogeneous porous media. Tortuosity for TL and QL is presented in [FIG. 7.20b](#): it increases with the aspect ratio. More work is required to see how this parameter evolves for cylindrical particles but is not presented in this chapter.

6 CONCLUSION AND PERSPECTIVES

The DLM/FD method has been adapted to compute single phase flow in packed beds of polylobed particles without the need of radius calibration. A suitable set of CP location has been proposed for a trilobal and a quadrilobal particle. A perspective is to optimize distribution of the CPs so as to reduce their number without losing accuracy. Another research question is to develop some automated approach to mesh any new complex particle.

The numerical platform `Grains3D`-PeliGRIFF has then been used to simulate for the first time the pressure drop in packed beds of trilobes and quadralobes. Results have been interpreted using the Ergun formalism and agree well with the available literature for low aspect ratio. It is concluded that trilobe and quadralobe have the same pressure drop behaviour. For high aspect ratio, simulation results are not in line with the scarce experimental data available. There is no reason for the validity of the computed solutions to change with particle length, so we think that the surprising behaviour is either physical or results from the packing structures that are somehow not physical although they have a correct void fraction and no specific features. It could be that the loss of representativeness originates from a too small simulation volume that for some unknown reason impacts the granular dynamics. An open and important question for “ab silico” simulations of fixed beds is to identify a signature of “un-physical” packings. We suggest to investigate the particle orientation or the tortuosity or any other numerically accessible piece of information. A first step toward this, would be to replicate our simulations using larger domains and track how the pressure drop coefficients evolve. This effort will be limited by computing power.

RÉSUMÉ

La première partie de ce chapitre est consacrée au couplage du solveur granulaire avec le solveur des équations de Navier-Stokes pour les types de particules vus dans les précédents chapitres. Ici la méthode “Distributed Lagrange Multipliers / Fictitious Domain” est étendue aux particules de forme multi-lobée. En effet, la méthode est robuste moyennant une correcte répartition des points de colocation à la surface et à l’intérieur de la particule. A défaut de solution analytique, il est proposé une étude de convergence en espace des solutions calculées, en premier lieu sur une particule isolée dans une configuration tri-périodique, ensuite sur une collection de quelques dizaines de particules. Il a été conclu que les formes non-convexes ont besoin de plus de point de colocation que les particules convexes pour obtenir la même précision sur les solutions calculées.

La deuxième partie de ce chapitre se concentre sur l’application de la méthode sur les problèmes rencontrés dans le réacteurs à lit fixe. C’est-à-dire les effets des formes des particules sur la perte de charge dans ce genre de réacteurs. La comparaison est faite sur trois types de particules: cylindre, trilobe et quadrilobe. Effectivement, la plateforme Grains3D -plgf a été utilisée pour simuler, pour la première fois, la perte de charge au travers de lits de particules multi-lobées. Les résultats montrent une tendance qui est statistiquement identiques pour les particules multi-lobées. Cette tendance sur la perte de charge est différente de celle des particules habituellement retrouvées dans la littérature.

CONCLUSION AND PERSPECTIVES



CONCLUSION

Particulate flow modelling significantly progressed during this decade and has benefited from the growth of computing power. This opens up new opportunities to investigate the effect of particle shape in fluid-particle systems. In fact, most of existing models in the literature are only designed for spheres but in many applications particle shapes are often complex. In this thesis, a modelling of complex particle shape has been suggested. For this endeavour, a numerical multiphase flow platform (Grains3D-PeliGRIFF) dedicated to particulate flow simulations of arbitrary convex particles is extended to deal with non-convex particles.

The first part of this work is dedicated to the extension of the Discrete Element Method granular solver Grains3D to handle non-convex particle shape. To this end, the strategy is based on the decomposition of a non-convex particle into a set of convex bodies. This idea comes from the so-called “glued spheres” model widely used in the literature. The concept appears to be simple and efficient since almost any complex shape can be decomposed into a few or many arbitrary convex particles rather than spherical ones. Hence, the name of “glued convex” has been given to the new model. Due to the complexity of the shape, volume and elements of the moment of inertia is computed by discretising the shape instead of using boolean operations on the presumably overlapping elements of the “composite”. Owing to the number of elementary particles, the “composite” particle may be subjected to a multi-contact problem. In order to overcome this issue two models are tested for the resulting contact force. The first model consists in summing up all the forces while the second model is based on averaging all the forces. For both methods the resulting contact force is computed at each time step due to the probable variation of the number of contact points during an interaction. Results have been shown to be accurate when compared to analytical results but the time step decreases as a reverse function of number of contact points when we adopt the first model. The second model keeps a contact duration that is in the order of magnitude of convex particles. Based on this observation the second model is selected and implemented in the granular solver Grains3D. Using our new glued convex model, a study of the dynamics of a granular media made of non-convex particles in a rotating drum is carried out to quantify the effects of the non-convexity. Results obtained for two cross-like non-convex particles overall show that the avalanching regime is promoted at low rotation rates and that the cataracting regime is not really easy to define. These major differences are a result of the high entanglement of particles which provides a sort of cohesion to the granular media. The second application of the implemented model is the study of the packings resulting from the filling of reactors encountered in the refining industry. For this purpose, poly-lobed particles are modelled as a composite of cylinders and a polygonal prism which replicate with high fidelity the shape of catalyst particles developed at IFPEN. Due to slight micro-structural variations in packed beds, the void

fraction always differs from a bed to another bed. Packing repeatability is assessed and correlations are established for cylindrical, trilobal and quadralobal particles in cylindrical vessels and in semi-infinite domains to mimic large scale reactors. Obtained results show a clear change of void fraction between cylindrical particles and poly-lobed packed beds. Finally, the parallel performance of Grains3D was assessed on various granular flow configurations comprising both spherical and angular particles. To this end, large scale simulations of silo discharges of spherical and angular particles, dam breaks of icosahedron and fluidized beds of spherical particles were performed. All simulations showed a scalability of more than 0.75 for systems of more than 100,000 particles per core. The scalability can reach up to 0.9 for systems of non-spherical (convex) particles. In its current state, Grains3D offers unprecedented computing capabilities. Systems with up to 100,000,000 of non-spherical particles can be simulated on a few hundreds of cores.

The main goal of the second part of this thesis is to determine the effects of particle shape on the pressure drop through packed beds of trilobes and quadralobes. The first step was the extension of the capability of the fluid flow solver to handle poly-lobed particles. The granular flow solver is coupled to the micro-scale (Direct Numerical Simulation) module of PeliGRIFF in which a Distributed Lagrange Multiplier / Fictitious Domain formulation combined with a Finite Volume Staggered Grid scheme is already implemented. The extension relies on the integration of the new geometries in the formulation, i.e. designing a new construction method to homogeneously distribute the collocation points in the rigid bodies and on their surface. A space convergence study was carried out in assorted flow configurations and flow regimes such as the steady flow through a periodic array of particles and the steady flow through a packed bed of particles to assess the accuracy of computed solutions. Based on the convergence study, we found that for the same accuracy, the number of collocation points for poly-lobed particles should be higher compared to more standard particles such as spheres or cylinders. In fact, 50% more points are required to describe the cross-sectional surface of the poly-lobed particles than that of a cylindrical particle. From the previous study, the pressure drop through packed beds of poly-lobed particles have been reliably investigated. We performed around 200 particle-resolved simulations of the flow through a packed bed of trilobes or quadralobes. Based on these simulation results, we suggested a modified Ergun's correlation. The proposed correction of the Ergun's correlation is based on fitting the Blake-Kozeny-Carman (α) and the Burke-Plummer (β) constants by introducing parameters that depend on the sphericity and the particle equivalent diameter. Results have been interpreted using the Ergun formalism and agree well with the available literature for low aspect ratios. We observed that TL and QL have globally the same pressure drop behaviour. For high aspect ratios, simulation results are not in line with the scarce experimental data available. The simulated void fraction is slightly higher than experimental data, which logically yield a lower pressure drop.

PERSPECTIVES

The new extension of the multiphase flow platform Grains3D-PeliGRIFF has been successfully deployed. However, there is vast room for improvements, both on the physical modelling side and on the computational side. Since the contact resolution scales with $N_i \times N_j$ where N_i and N_j denote the number of elementary particles of the composites i and j respectively, there is an interest on implementing a convex hull or a bounding box algorithm to accelerate the contact detection. Later on, the model can be extended to take into account cohesive interactions. In addition, a dynamic load balancing would enhance the computing capabilities of Grains3D in flow configurations with high particle volume fraction heterogeneities.

On the pure parallel computing aspects, the milestone of a billion of convex particles appears attainable as suggested by the trend shown by the scaling factor of the code.

In PRS, although the accuracy of the DLM/FD formulation is satisfactory, the method does not strictly satisfy the velocity divergence-free property. In fact, our operator-splitting algorithm solves the following sequence of sub-problems at each time: (i) Navier-Stokes sub-problem and (ii) DLM/FD sub-problem. The latter enforces the rigid body motion constraint but not the velocity divergence-free constraint. Therefore, more sophisticated operator-splitting techniques as e.g. a second order Strang symmetrized algorithm, or more strongly coupled solution algorithms might further improve the computed solution accuracy. In the original version of the DLM/FD formulation, an Uzawa conjugate gradient algorithm is used to solve the saddle point sub-problem. In order to avoid the computational cost, a fast projection scheme, a variant of the Direct Forcing of the Immersed Boundary Method, can be implemented. Since the most of the computing time is spent in the DLM/FD sub-problem in dense systems, accelerating the solution of this sub-problem while keeping the same level of accuracy is highly desirable. In addition, an Adaptive Mesh Refinement strategy would be of great improvement in fixed bed simulations. Not only the AMR strategy would decrease the total number of grid cells, but it will increase the accuracy of the computed solutions where needed. A DLM/FD module to model heat and/or mass transfer with infinite diffusivity in the particles core is already available in PeliGRIFF and can be used for the simulations of flows with trilobes/quadrilobes. The extension to intra-particle diffusion would require the implementation of a Sharp Interface method to properly capture the gradient discontinuity at the particle/fluid interface. This work is currently carried out by another PhD student of the PeliGRIFF group. Numerical simulations with mass transfer would need a realistic and manageable kinetic scheme (in the sense with “not too many” equations and chemical species) and probably adapted numerical schemes to treat the different time scales involved in these chemical reactions.

Further Uncertainty Quantification of random packing would provide a better fitting of the Ergun’s coefficients for pressure drop in a packed bed of trilobes or quadrilobes. This may lead to the introduction of another parameter in the correlation such as the particle aspect ratio. Further simulations of packed beds of particles with high aspect ratio in larger domains would provide a better understanding on the low pressure drop that we measured in some of our simulations. The new “glued convex” model can be integrated in a multi-scale framework for granular flow modelling or particulate flow modelling for various industrial problems (among others geoscience, food industry, pharmaceutical industry, upstream oil & gas industry, etc ...). For instance, correlations for drag, heat flux and mass transfer for any particle shape can be derived from PRS and later integrated in a meso-scale model (of the DEM-CFD type for instance) for fluidised bed simulations.

With all these features, the numerical platform Grains₃D-PeliGRIFF can serve as a very accurate tool for virtual optimisation of processes in the chemical industry. For chemical conversion in fixed bed reactors, numerical simulations are feasible from the loading of reactors to the hydrodynamics of the flow through the bed, coupled with heat and mass transfer. This would equip chemical engineers with a predictive tool of chemical efficiency of catalysts.

RÉSUMÉ

Les écoulements fluide-particules ont connu un important progrès durant cette décennie grâce à l'avènement de l'ère du calcul haute performance. Ceci ouvre la voie à plusieurs opportunités d'investigation des effets de forme des particules dans ces systèmes. Effectivement, de nombreux modèles existant dans la littérature reposent sur des particules de forme sphériques ce qui n'est pas toujours le cas dans plusieurs applications. Au cours de cette thèse, la modélisation de systèmes comportant des particules de formes complexes est abordée en utilisant la plateforme numérique Grains3D -PeliGRIFF dédiée aux écoulements multiphasiques. Ces travaux de thèse consistent à étendre la capacité de ces outils à pouvoir prendre en compte des particules non-convexes.

La première partie de cette thèse est dédiée à l'extension du solveur granulaire (Discrete Element Method) à traiter des particules non-convexes. Elle est basée sur la décomposition d'une particule non-convexe en particules élémentaires arbitrairement convexes. Cette méthode peut être considérée comme étant une extension du modèle "glued sphere", très connu dans la littérature. Le concept paraît simple et efficace car à peu près n'importe quelle forme arbitrairement non-convexe peut être décomposée en plusieurs formes arbitrairement convexes. D'où la dénomination du nouveau modèle *glued convex*. À cause de la complexité des formes, le calcul du moment d'inertie est fait par une discrétisation spatiale du "composite" tout en considérant que les particules élémentaires peuvent se recouvrir. Cette décomposition implique aussi plusieurs points de contact dans la dynamique du composite auxquels une attention particulière a été dédiée. Ainsi, le modèle a permis, pour la première fois, d'étudier la dynamique des milieux granulaires dans un tambour tournant pour montrer l'effet de la concavité des particules en forme de croix. En effet, ces milieux granulaires montrent que le régime d'avalanche se manifeste à très faible vitesse de rotation et la transition entre régime de cascade et régime de centrifuge n'est pas évidente à définir. La seconde application du modèle consiste à simuler le remplissage de réacteurs à lit fixe avec des particules de forme multi-lobée rencontrées dans l'industrie du raffinage pour, ensuite, quantifier l'effet des formes de catalyseurs sur le taux de vide dans ces réacteurs. Finalement, la performance parallèle de Grains3D est mise en évidence sur quelques configurations d'écoulement granulaires. Ces tests ont permis de montrer que des systèmes de plus de 100,000,000 de particules non-sphériques peuvent être simulés sur quelques centaines de processeurs et que désormais des simulations numériques de systèmes atteignant le milliard de particules sphériques peuvent être envisageables.

La deuxième partie de ce travail est consacrée au couplage entre le nouveau modèle de particule non-convexe implémenté dans le solveur Grains3D et le solveur des équations de Navier-Stokes PeliGRIFF en utilisant le module de simulation numérique directe de ce dernier. Cette résolution directe repose sur la méthode "Distributed Lagrange Multipliers / Fictitious Domain". Elle consiste à imposer une condition de corps rigide au sein de la particule et à la surface de celle-ci en imposant une condition d'égalité des vitesses fluide et solide à l'aide de multiplicateurs de Lagrange. Dans le cas d'un lit fixe, cette vitesse est nulle dans la particule et sur sa surface. À défaut de solutions analytiques, une étude de convergence spatiale des solutions calculées est menée dans le cas d'une particule isolée, puis sur un lit fixe de quelques dizaines de particules multi-lobées. Après la comparaison avec des particules cylindriques, cette étude a conduit à conclure que 50% de point de colocation supplémentaires sont indispensables pour décrire la surface issue de la coupe transversale des particules multi-lobées. À partir de cette étude, une campagne de simulations numériques a été menée dans le but de quantifier l'effet des formes des particules sur la perte de charge au travers d'un lit fixe en utilisant le for-

malisme d'Ergun. Les résultats illustrent que les trilobes et les quadrilobes ont statistiquement le même effet sur la perte de charge.

BIBLIOGRAPHY

- M. Abbaspour-Fard. Theoretical validation of a multi-sphere, discrete element model suitable for biomaterials handling simulation. *Biosystems Engineering*, 88(2):153 – 161, 2004. ISSN 1537-5110. (Cited in page 27.)
- S. Afandizadeh and E. Foumeny. Design of packed bed reactors: guides to catalyst shape, size, and loading selection. *Applied thermal engineering*, 21(6):669–682, 2001. (Cited in page 56.)
- E. Aharonov and D. Sparks. Rigidity phase transition in granular packings. *Phys. Rev. E*, 60: 6890–6896, Dec 1999. (Cited in page 14.)
- A. S. Almgren, J. B. Bell, P. Colella, L. H. Howell, and M. L. Welcome. A conservative adaptive projection method for the variable density incompressible navier–stokes equations. *Journal of computational Physics*, 142(1):1–46, 1998. (Cited in page 106.)
- F. Alonso-Marroquín and Y. Wang. An efficient algorithm for granular dynamics simulations with complex-shaped objects. *Granular Matter*, 11(5):317–329, 2009. (Cited in pages 21, 27, and 30.)
- C. Ancey, R. M. Iverson, M. Rentschler, and R. P. Denlinger. An exact solution for ideal dam-break floods on steep slopes. *Water Resources Research*, 44(1). ISSN 1944-7973. (Cited in page 85.)
- T. B. Anderson and R. Jackson. Fluid mechanical description of fluidized beds. equations of motion. *Industrial & Engineering Chemistry Fundamentals*, 6(4):527–539, 1967. (Cited in pages 91 and 92.)
- B. Andreotti and S. Douady. Selection of velocity profile and flow depth in granular flows. *Phys. Rev. E*, 63:031305, Feb 2001. (Cited in page 14.)
- R. Aris. On shape factors for irregular particles – I: The steady state problem. *Chemical Engineering Science*, 6(6):262–268, 1957. (Cited in pages 7, 8, 9, and 56.)
- A. Attou, C. Boyer, and G. Ferschneider. Modelling of the hydrodynamics of the cocurrent gas–liquid trickle flow through a trickle-bed reactor. *Chemical Engineering Science*, 54(6): 785–802, 1999. (Cited in page 56.)
- E. Azéma, F. Radjai, R. Peyroux, and G. Saussine. Force transmission in a packing of pentagonal particles. *Physical Review E*, 76(1):011301, 2007. (Cited in page 16.)
- M. Babic, H. H. Shen, and H. T. Shen. The stress tensor in granular shear flows of uniform, deformable disks at high solids concentrations. *Journal of Fluid Mechanics*, 219:81–118, 10 1990. (Cited in page 14.)
- N. J. Balmforth and R. R. Kerswell. Granular collapse in two dimensions. *Journal of Fluid Mechanics*, 538:399–428, 9 2005. (Cited in pages 85, 89, and 90.)

- G. Barker. Computer simulations of granular materials. In A. Mehta, editor, *Granular Matter*, pages 35–83. Springer New York, 1994. (Cited in page 17.)
- A. H. Barr. Superquadrics and angle-preserving transformations. *IEEE Computer Graphics and Applications*, 1(1):11–23, 1981. (Cited in page 19.)
- R. Beetstra, M. Van der Hoef, and J. Kuipers. Drag force of intermediate reynolds number flow past mono-and bidisperse arrays of spheres. *AIChE Journal*, 53(2):489–501, 2007a. (Cited in pages 93 and 102.)
- R. Beetstra, M. Van der Hoef, and J. Kuipers. Numerical study of segregation using a new drag force correlation for polydisperse systems derived from lattice-boltzmann simulations. *Chemical Engineering Science*, 62(1):246–255, 2007b. (Cited in pages 93 and 102.)
- H. Bekker and J. B. Roerdink. An efficient algorithm to calculate the minkowski sum of convex 3d polyhedra. In *Computational Science–ICCS 2001*, pages 619–628. Springer, 2001. (Cited in page 27.)
- T. Belytschko, J. M. Kennedy, and D. Schoeberle. Quasi-eulerian finite element formulation for fluid-structure interaction. *Journal of Pressure Vessel Technology*, 102(1):62–69, 1980. (Cited in page 103.)
- G. v. d. Bergen. A fast and robust GJK implementation for collision detection of convex objects. *Journal of Graphics Tools*, 4(2):7–25, 1999. (Cited in page 27.)
- M. J. Berger and P. Colella. Local adaptive mesh refinement for shock hydrodynamics. *Journal of computational Physics*, 82(1):64–84, 1989. (Cited in page 106.)
- M. J. Berger and J. Olinger. Adaptive mesh refinement for hyperbolic partial differential equations. *Journal of computational Physics*, 53(3):484–512, 1984. (Cited in page 106.)
- R. Berger, C. Kloss, A. Kohlmeyer, and S. Pirker. Hybrid parallelization of the LIGGGHTS open-source DEM code. *Powder Technology*, 278:234 – 247, 2015. ISSN 0032-5910. (Cited in page 98.)
- M. Bernard. *Multi-scale approach for particulate flows*. PhD thesis, Institut National Polytechnique de Toulouse, 2014. (Cited in page 93.)
- M. Bernard, A. Wachs, and E. Climent. Euler/Lagrange numerical modeling of the dynamics of bubbling and spouted fluidized beds. *submitted to Computers and Chemical Engineering*, 2016. (Cited in pages 93 and 97.)
- F. Blake. The resistance of packing to fluid flow. *Transactions of the American Institute of Chemical Engineers*, 14(415-421):3, 1922. (Cited in page 125.)
- R. I. Borja and J. R. Wren. Micromechanics of granular media Part I: Generation of overall constitutive equation for assemblies of circular disks. *Computer Methods in Applied Mechanics and Engineering*, 127(1–4):13–36, 1995. (Cited in page 17.)
- W. Breugem. A second-order accurate immersed boundary method for fully resolved simulations of particle-laden flows. *Journal of Computational Physics*, 231(13):4469–4498, 2012. (Cited in page 113.)
- R. L. Brown and J. C. Richards. *Principles of Powder Mechanics: essays on the packing of powders and bulk solids*. Oxford: Pergamon Press, 1970. (Cited in page 2.)

- K. Buist, L. Seelen, N. Deen, J. Padding, and J. Kuipers. On an efficient hybrid soft and hard sphere collision integration scheme for dem. *Chemical Engineering Science*, 153:363–373, 2016. (Cited in page 16.)
- S. Burke and W. Plummer. Gas flow through packed columns. *Industrial & Engineering Chemistry*, 20(11):1196–1200, 1928. (Cited in page 125.)
- F. Camborde, C. Mariotti, and F. Donzé. Numerical study of rock and concrete behaviour by discrete element modelling. *Computers and geotechnics*, 27(4):225–247, 2000. (Cited in page 26.)
- C. S. Campbell. Rapid granular flows. *Annual Review of Fluid Mechanics*, 22(1):57–90, 1990. (Cited in page 16.)
- J. Capecelatro and O. Desjardins. An Euler–Lagrange strategy for simulating particle-laden flows. *Journal of Computational Physics*, 238:1–31, 2013. (Cited in page 92.)
- P. C. Carman. Fluid flow through granular beds. *Transactions-Institution of Chemical Engineers*, 15:150–166, 1937. (Cited in pages 57, 125, and 134.)
- I. Christie, D. F. Griffiths, A. R. Mitchell, and O. C. Zienkiewicz. Finite element methods for second order differential equations with significant first derivatives. *International Journal for Numerical Methods in Engineering*, 10(6):1389–1396, 1976. (Cited in page 103.)
- P. Cleary. Industrial particle flow modelling using discrete element method. *Engineering Computations*, 26(6):698–743, 2009. (Cited in page 79.)
- P. Cleary. DEM prediction of industrial and geophysical particle flows. *Particuology*, 8(2): 106–118, 2010. (Cited in pages 18 and 79.)
- P. Cleary and M. Sawley. DEM modelling of industrial granular flows: 3D case studies and the effect of particle shape on hopper discharge. *Applied Mathematical Modelling*, 26(2): 89–111, 2002. (Cited in page 79.)
- B. H. Cooper, B. B. L. Donnis, and B. Moyses. Hydroprocessing conditions affect catalyst shape selection. *Oil Gas J. (United States)*, 84(49), 1986. (Cited in pages 6, 7, 9, and 56.)
- P. A. Cundall. Formulation of a three-dimensional distinct element model—Part I. A scheme to detect and represent contacts in a system composed of many polyhedral blocks. *International Journal of Rock Mechanics and Mining Sciences & Geomechanics Abstracts*, 25(3): 107–116, 1988. (Cited in pages 20, 26, 57, and 70.)
- P. A. Cundall and O. D. Strack. A discrete numerical model for granular assemblies. *Geotechnique*, 29(1):47–65, 1979. (Cited in pages 15, 57, and 70.)
- G. D’Avino and M. Hulsen. A comparison between a collocation and weak implementation of the rigid-body motion constraint on a particle surface. *International Journal for Numerical Methods in Fluids*, 64(9):1014–1040, 2010. (Cited in page 121.)
- N. Deen and J. Kuipers. Direct Numerical Simulation of Fluid Flow and Mass Transfer in Dense Fluid–Particle Systems. *Industrial & Engineering Chemistry Research*, 52(33):11266–11274, 2013. (Cited in page 102.)
- N. Deen, M. van Sint Annaland, and J. Kuipers. Multi-scale modeling of dispersed gas–liquid two-phase flow. *Chemical Engineering Science*, 59(8):1853–1861, 2004. (Cited in page 102.)

- N. Deen, S. Kriebitzsch, M. van der Hoef, and J. Kuipers. Direct numerical simulation of flow and heat transfer in dense fluid-particle systems. *Chemical Engineering Science*, 81:329–344, 2012. (Cited in page 113.)
- C. Denniston and H. Li. Dynamics and stress in gravity-driven granular flow. *Phys. Rev. E*, 59:3289–3292, Mar 1999. (Cited in page 14.)
- J. Derksen and S. Sundaresan. Direct numerical simulations of dense suspensions: wave instabilities in liquid-fluidized beds. *Journal of Fluid Mechanics*, 587:303–336, 2007. (Cited in page 104.)
- R. Descartes. *Oeuvres philosophiques de Descartes*. Panthéon littéraire, 1852. (Cited in pages 1 and 2.)
- A. G. Dixon and M. Nijemeisland. CFD as a design tool for fixed-bed reactors. *Industrial & Engineering Chemistry Research*, 40(23):5246–5254, 2001. (Cited in page 102.)
- R. Doe. *CGAL, Computational Geometry Algorithms Library*, jun 2009. URL <http://www.cgal.org>. (Cited in page 30.)
- F. Dorai, M. Rolland, A. Wachs, M. Marcoux, and E. Climent. Packing fixed bed reactors with cylinders: influence of particle length distribution. *Procedia Engineering*, 42:1335–1345, 2012. (Cited in pages 59 and 127.)
- F. Dorai, L. Briquet, A. Hammouti, M. Rolland, and A. Wachs. Multi-scale simulation of reactive flow through a fixed bed of catalyst particles. In *ASME 2014 4th Joint US-European Fluids Engineering Division Summer Meeting collocated with the ASME 2014 12th International Conference on Nanochannels, Microchannels, and Minichannels*. American Society of Mechanical Engineers, 2014. (Cited in pages 67, 118, 123, 124, and 127.)
- F. Dorai, C. M. Teixeira, M. Rolland, E. Climent, M. Marcoux, and A. Wachs. Fully resolved simulations of the flow through a packed bed of cylinders: Effect of size distribution. *Chemical Engineering Science*, 129:180–192, 2015. (Cited in pages 57, 67, 102, 106, 115, 118, 123, and 127.)
- A. Drescher. On the criteria for mass flow in hoppers. *Powder Technology*, 73(3):251 – 260, 1992. (Cited in page 16.)
- A. Duda, Z. Koza, and M. Matyka. Hydraulic tortuosity in arbitrary porous media flow. *Physical Review E*, 84(3):036319, 2011. (Cited in page 134.)
- J. Duran. *Sables, poudres et grains: Introduction à la physique des milieux granulaires*. Eyrolles sciences, 1999. (Cited in page 2.)
- A. Džugys and B. Peters. An approach to simulate the motion of spherical and non-spherical fuel particles in combustion chambers. *Granular matter*, 3(4):231–266, 2001. (Cited in pages 16, 17, 18, 30, and 32.)
- R. England and D. Gunn. Dispersion, pressure drop, and chemical reaction in packed beds of cylindrical particles. *TRANSACTIONS OF THE INSTITUTION OF CHEMICAL ENGINEERS AND THE CHEMICAL ENGINEER*, 48(7-10):T265, 1970. (Cited in page 126.)

- S. Ergun. Fluid flow through packed columns. *Chem. Eng. Prog.*, 48:89–94, 1952. (Cited in pages 8, 56, 124, and 125.)
- S. Ergun and A. A. Orning. Fluid flow through randomly packed columns and fluidized beds. *Industrial & Engineering Chemistry*, 41(6):1179–1184, 1949. (Cited in pages 8 and 125.)
- R. Escudié, N. Epstein, J. Grace, and H. Bi. Effect of particle shape on liquid-fluidized beds of binary (*and ternary*) solids mixtures: segregation vs. mixing. *Chemical engineering science*, 61(5):1528–1539, 2006. (Cited in page 16.)
- A. Esteghamatian, M. Bernard, A. Wachs, M. Lance, and A. Hammouti. Micro/meso simulation of a fluidized bed in a homogeneous bubbling regime. *Submitted to International Journal of Multiphase Flow*, 2016. (Cited in pages 93 and 102.)
- J. Favier, M. Abbaspour-Fard, M. Kremmer, and A. Raji. Shape representation of axis-symmetrical, non-spherical particles in discrete element simulation using multi-element model particles. *Engineering Computations*, 16(4):467–480, 1999. (Cited in pages 5 and 22.)
- J. Feng, H. Hu, and D. Joseph. Direct simulation of initial value problems for the motion of solid bodies in a Newtonian fluid. Part 1. Sedimentation. *Journal of Fluid Mechanics*, 261: 95–134, 1994a. (Cited in page 103.)
- J. Feng, H. Hu, and D. Joseph. Direct simulation of initial value problems for the motion of solid bodies in a Newtonian fluid. Part 2. Couette and Poiseuille flows. *Journal of Fluid Mechanics*, 277(271):271–301, 1994b. (Cited in page 103.)
- Y. Feng and D. Owen. A 2D polygon/polygon contact model: algorithmic aspects. *Engineering Computations*, 21(2/3/4):265–277, 2004. (Cited in pages 17 and 26.)
- Z. Feng and E. Michaelides. The immersed boundary-lattice Boltzmann method for solving fluid-particles interaction problems. *Journal of Computational Physics*, 195(2):602–628, 2004. (Cited in page 104.)
- Z. Feng and E. Michaelides. Robust treatment of no-slip boundary condition and velocity updating for the lattice-Boltzmann simulation of particulate flows. *Computers & Fluids*, 38(2):370–381, 2009. (Cited in page 113.)
- R. L. Flemmer, J. Pickett, and N. N. Clark. An experimental study on the effect of particle shape on fluidization behavior. *Powder technology*, 77(2):123–133, 1993. (Cited in page 16.)
- F. Y. Fraige, P. A. Langston, and G. Z. Chen. Distinct element modelling of cubic particle packing and flow. *Powder Technology*, 186(3):224–240, 2008. (Cited in pages 18 and 26.)
- H. Freund, J. Bauer, T. Zeiser, and G. Emig. Detailed simulation of transport processes in fixed-beds. *Industrial & engineering chemistry research*, 44(16):6423–6434, 2005. (Cited in page 102.)
- E. G. Nezami, Y. M. A. Hashash, D. Zhao, and J. Ghaboussi. Shortest link method for contact detection in discrete element method. *International Journal for Numerical and Analytical Methods in Geomechanics*, 30(8):783–801, 2006. (Cited in page 20.)
- E. G. Gilbert and C. Foo. Computing the distance between general convex objects in three-dimensional space. *Robotics and Automation, IEEE Transactions on*, 6(1):53–61, 1990. (Cited in pages 17, 28, 31, and 58.)

- E. G. Gilbert, D. W. Johnson, and S. S. Keerthi. A fast procedure for computing the distance between complex objects in three-dimensional space. *Robotics and Automation, IEEE Journal of*, 4(2):193–203, 1988. (Cited in pages 17, 27, 28, 31, and 58.)
- L. Girolami, V. Hergault, G. Vinay, and A. Wachs. A three-dimensional discrete-grain model for the simulation of dam-break rectangular collapses: comparison between numerical results and experiments. *Granular Matter*, 14(3):381–392, 2012. (Cited in page 85.)
- R. Glowinski, T. Pan, T. Hesla, and D. Joseph. A distributed Lagrange multiplier/fictitious domain method for particulate flows. *International Journal of Multiphase Flow*, 25(5):755–794, 1999. ISSN 0301-9322. (Cited in pages 105 and 113.)
- R. Glowinski, T. Pan, T. Hesla, D. Joseph, and J. Periaux. A fictitious domain approach to the direct numerical simulation of incompressible viscous flow past moving rigid bodies: application to particulate flow. *Journal of Computational Physics*, 169(2):363–426, 2001. ISSN 0021-9991. (Cited in pages 105 and 113.)
- C. González-Montellano, A. Ramirez, E. Gallego, and F. Ayuga. Validation and experimental calibration of 3d discrete element models for the simulation of the discharge flow in silos. *Chemical Engineering Science*, 66(21):5116–5126, 2011. (Cited in pages 77, 78, 79, and 80.)
- N. Govender, D. Wilke, and S. K. Collision detection of convex polyhedra on the NVIDIA GPU architecture for the discrete element method. *Applied Mathematics and Computation*, 267:810–829, 2015. (Cited in page 70.)
- G. S. Grest, B. Dünweg, and K. Kremer. Vectorized link cell Fortran code for molecular dynamics simulations for a large number of particles. *Computer Physics Communications*, 55(3):269–285, 1989. (Cited in page 31.)
- W. Gropp, E. Lusk, and A. Skjellum. *Using MPI (2Nd Ed.): Portable Parallel Programming with the Message-passing Interface*. MIT Press, Cambridge, MA, USA, 1999. ISBN 0-262-57132-3. (Cited in page 70.)
- P. R. Gunjal, V. V. Ranade, and R. V. Chaudhari. Computational study of a single-phase flow in packed beds of spheres. *AIChE Journal*, 51(2):365–378, 2005. (Cited in page 102.)
- F. Günther, F. Janoschek, S. Frijters, and J. Harting. Lattice boltzmann simulations of anisotropic particles at liquid interfaces. *Computers & Fluids*, 80:184–189, 2013. (Cited in page 105.)
- D. M. Hanes and O. R. Walton. Simulations and physical measurements of glass spheres flowing down a bumpy incline. *Powder Technology*, 109(1-3):133 – 144, 2000. (Cited in page 14.)
- R. Hart, P. Cundall, and J. Lemos. Formulation of a three-dimensional distinct element model—Part II. Mechanical calculations for motion and interaction of a system composed of many polyhedral blocks. In *International Journal of Rock Mechanics and Mining Sciences & Geomechanics Abstracts*, volume 25, pages 117–125. Elsevier, 1988. (Cited in pages 20 and 26.)
- S. Hentz, L. Daudeville, and F. V. Donzé. Identification and validation of a discrete element model for concrete. *Journal of engineering mechanics*, 130(6):709–719, 2004. (Cited in page 26.)

- H. Herrmann and S. Luding. Modeling granular media on the computer. *Continuum Mechanics and Thermodynamics*, 10(4):189–231, 1998. (Cited in page 15.)
- R. Hill, D. Koch, and A. Ladd. Moderate-Reynolds-number flows in ordered and random arrays of spheres. *Journal of Fluid Mechanics*, 448(2):243–278, 2001a. (Cited in pages 104 and 105.)
- R. Hill, D. Koch, and A. Ladd. The first effects of fluid inertia on flows in ordered and random arrays of spheres. *Journal of Fluid Mechanics*, 448(2):213–241, 2001b. (Cited in pages 104 and 105.)
- K. Höfler and S. Schwarzer. Navier-Stokes simulation with constraint forces: Finite-difference method for particle-laden flows and complex geometries. *Physical Review E*, 61:7146–7160, Jun 2000. (Cited in page 116.)
- D. Höhner, S. Wirtz, H. Kruggel-Emden, and V. Scherer. Comparison of the multi-sphere and polyhedral approach to simulate non-spherical particles within the discrete element method: Influence on temporal force evolution for multiple contacts. *Powder Technology*, 208(3):643 – 656, 2011. (Cited in pages 27, 34, 35, and 36.)
- D. Höhner, S. Wirtz, and V. Scherer. Experimental and numerical investigation on the influence of particle shape and shape approximation on hopper discharge using the discrete element method. *Powder technology*, 235:614–627, 2013. (Cited in page 5.)
- D. Höhner, S. Wirtz, and V. Scherer. A study on the influence of particle shape and shape approximation on particle mechanics in a rotating drum using the discrete element method. *Powder Technology*, 253:256–265, 2014. (Cited in page 5.)
- A. Hölzer and M. Sommerfeld. Lattice boltzmann simulations to determine drag, lift and torque acting on non-spherical particles. *Computers & Fluids*, 38(3):572–589, 2009. (Cited in page 105.)
- H. Hu. Direct simulation of flows of solid-liquid mixtures. *International Journal of Multiphase Flow*, 22(2):335–352, 1996. (Cited in page 103.)
- H. Hu, N. Patankar, and M. Zhu. Direct numerical simulations of fluid–solid systems using the arbitrary Lagrangian–Eulerian technique. *Journal of Computational Physics*, 169(2): 427–462, 2001. (Cited in page 103.)
- K. Iglberger and U. Rüde. Massively parallel rigid body dynamics simulations. *Computer Science-Research and Development*, 23(3-4):159–167, 2009. (Cited in pages 70, 71, 73, and 76.)
- K. Iglberger and U. Rüde. Large-scale rigid body simulations. *Multibody System Dynamics*, 25(1):81–95, 2011. (Cited in pages 70, 71, 73, and 76.)
- T. Iwai, C.-W. Hong, and P. Greil. Fast particle pair detection algorithms for particle simulations. *International Journal of Modern Physics C*, 10(05):823–837, 1999. (Cited in page 17.)
- F. Janoschek, J. Harting, and F. Toschi. Accurate lubrication corrections for spherical and non-spherical particles in discretized fluid simulations. *arXiv preprint arXiv:1308.6482*, 2013. (Cited in page 105.)
- M. Jean. Frictional contact in collections of rigid or deformable bodies: numerical simulation of geomaterial motions. *Studies in Applied Mechanics*, 42:463–486, 1995. (Cited in page 16.)

- M. Jean. The non-smooth contact dynamics method. *Computer methods in applied mechanics and engineering*, 177(3):235–257, 1999. (Cited in page 16.)
- M. Jean and E. Pratt. A system of rigid bodies with dry friction. *International journal of engineering science*, 23(5):497–513, 1985. (Cited in page 16.)
- A. Jenike. A theory of flow of particulate solids in converging and diverging channels based on a conical yield function. *Powder Technology*, 50(3):229 – 236, 1987. (Cited in page 16.)
- F. Jin, H. Xin, C. Zhang, and Q. Sun. Probability-based contact algorithm for non-spherical particles in DEM. *Powder Technology*, 212(1):134–144, 2011. (Cited in page 27.)
- L. Jing. Formulation of discontinuous deformation analysis (dda)—an implicit discrete element model for block systems. *Engineering Geology*, 49(3):371–381, 1998. (Cited in page 26.)
- A. Johnson and T. Tezduyar. Simulation of multiple spheres falling in a liquid-filled tube. *Computer Methods in Applied Mechanics and Engineering*, 134(3):351–373, 1996. (Cited in pages 103 and 104.)
- A. Johnson and T. Tezduyar. 3D simulation of fluid-particle interactions with the number of particles reaching 100. *Computer Methods in Applied Mechanics and Engineering*, 145(3):301–321, 1997. (Cited in page 104.)
- A. Johnson and T. Tezduyar. Advanced mesh generation and update methods for 3D flow simulations. *Computational Mechanics*, 23(2):130–143, 1999. (Cited in page 104.)
- R. Jullien and P. Meakin. Simple three-dimensional models for ballistic deposition with restructuring. *EPL (Europhysics Letters)*, 4(12):1385, 1987. (Cited in page 17.)
- Y. Kanarska, I. Lomov, and T. Antoun. Mesoscale simulations of particulate flows with parallel distributed lagrange multiplier technique. *Computers & Fluids*, 48:16–29, 2011. (Cited in pages 106, 107, and 118.)
- T. Kawaguchi, T. Tanaka, and Y. Tsuji. Numerical simulation of two-dimensional fluidized beds using the discrete element method (comparison between the two-and three-dimensional models). *Powder Technology*, 96(2):129–138, 1998. (Cited in pages 91, 92, and 93.)
- D. V. Khakhar, A. V. Orpe, P. Andrésén, and J. M. Ottino. Surface flow of granular materials: model and experiments in heap formation. *Journal of Fluid Mechanics*, 441:255–264, 8 2001. (Cited in page 14.)
- D. Kim and H. Choi. Immersed boundary method for flow around an arbitrarily moving body. *Journal of Computational Physics*, 212(2):662–680, 2006. (Cited in page 105.)
- C. Y. King. *Collision Detection for Ellipsoids and Other Quadrics*. PhD thesis, University of Hong Kong, 2008. (Cited in page 17.)
- J. B. Knight, C. G. Fandrich, C. N. Lau, H. M. Jaeger, and S. R. Nagel. Density relaxation in a vibrated granular material. *Phys. Rev. E*, 51:3957–3963, May 1995. (Cited in page 87.)
- M. Kodam, R. Bharadwaj, J. Curtis, B. Hancock, and C. Wassgren. Cylindrical object contact detection for use in discrete element method simulations. part I—Contact detection algorithms. *Chemical Engineering Science*, 65(22):5852–5862, 2010a. (Cited in page 18.)

- M. Kodam, R. Bharadwaj, J. Curtis, B. Hancock, and C. Wassgren. Cylindrical object contact detection for use in discrete element method simulations. part II—Experimental validation. *Chemical Engineering Science*, 65(22):5863–5871, 2010b. (Cited in pages 36, 37, 40, and 52.)
- J. Kozeny. *Über kapillare Leitung des Wassers im Boden:(Aufstieg, Versickerung und Anwendung auf die Bewässerung)*. Hölder-Pichler-Tempsky, 1927. (Cited in page 124.)
- H. Kruggel-Emden, S. Rickelt, S. Wirtz, and V. Scherer. A study on the validity of the multi-sphere discrete element method. *Powder Technology*, 188(2):153 – 165, 2008. (Cited in pages 21, 22, 27, 34, and 35.)
- J. Kuipers and W. Van Swaij. Computational fluid dynamics applied to chemical reaction engineering. *Advances in chemical engineering*, 24:227–328, 1998. (Cited in page 102.)
- A. Ladd. Numerical simulations of particulate suspensions via a discretized Boltzmann equation. Part 2. Numerical results. *Journal of Fluid Mechanics*, 271(1):311–339, 1994. (Cited in page 104.)
- A. Ladd. Sedimentation of homogeneous suspensions of non-Brownian spheres. *Physics of Fluids*, 9:491–499, 1997. (Cited in page 104.)
- A. Ladd and R. Verberg. Lattice-Boltzmann simulations of particle-fluid suspensions. *Journal of Statistical Physics*, 104(5):1191–1251, 2001. (Cited in page 104.)
- E. Lajeunesse, J. B. Monnier, and G. M. Homsy. Granular slumping on a horizontal surface. *Physics of Fluids*, 17(10), 2005. (Cited in pages 85 and 89.)
- P. Langston, U. Tüzün, and D. Heyes. Continuous potential discrete particle simulations of stress and velocity fields in hoppers: transition from fluid to granular flow. *Chemical Engineering Science*, 49(8):1259–1275, 1994. (Cited in page 31.)
- P. Langston, U. Tüzün, and D. Heyes. Discrete element simulation of granular flow in 2d and 3d hoppers: Dependence of discharge rate and wall stress on particle interactions. *Chemical Engineering Science*, 50(6):967–987, 1995. (Cited in page 31.)
- F. Larachi, R. Hannaoui, P. Horgue, F. Augier, Y. Haroun, S. Youssef, E. Rosenberg, M. Prat, and M. Quintard. X-ray micro-tomography and pore network modeling of single-phase fixed-bed reactors. *Chemical Engineering Journal*, 240:290–306, 2014. (Cited in pages 56 and 125.)
- Y. Lee, C. Fang, Y.-R. Tsou, L.-S. Lu, and C.-T. Yang. A packing algorithm for three-dimensional convex particles. *Granular Matter*, 11(5):307–315, 2009. (Cited in pages 20 and 26.)
- M. Leva and M. Grummer. Pressure drop through packed tubes. 3. prediction of voids in packed tubes. *Chemical Engineering Progress*, 43(12):713–718, 1947. (Cited in page 64.)
- J. Li, P. A. Langston, C. Webb, and T. Dyakowski. Flow of sphero-disc particles in rectangular hoppers—a DEM and experimental comparison in 3D. *Chemical Engineering Science*, 59(24):5917–5929, 2004. (Cited in page 26.)
- W. K. Liu, C. Herman, C. Jiun-Shyan, and B. Ted. Arbitrary lagrangian-eulerian petrov-galerkin finite elements for nonlinear continua. *Computer methods in applied mechanics and engineering*, 68(3):259–310, 1988. (Cited in page 103.)

- S. A. Logtenberg and A. G. Dixon. Computational fluid dynamics studies of fixed bed heat transfer. *Chemical Engineering and Processing: Process Intensification*, 37(1):7 – 21, 1998. ISSN 0255-2701. (Cited in page 102.)
- G. Lu, J. R. Third, and C. R. Müller. Effect of wall rougheners on cross-sectional flow characteristics for non-spherical particles in a horizontal rotating cylinder. *Particuology*, 12:44–53, Feb. 2014. (Cited in page 5.)
- G. Lu, J. Third, and C. Müller. Discrete element models for non-spherical particle systems: From theoretical developments to applications. *Chemical Engineering Science*, 127:425–465, 2015. (Cited in pages 19, 20, and 21.)
- G. Lube, H. E. Huppert, R. S. J. Sparks, and A. Freundt. Collapses of two-dimensional granular columns. *Phys. Rev. E*, 72:041301, Oct 2005. (Cited in pages 85, 87, and 89.)
- V. Luchnikov, N. Medvedev, L. Oger, and J.-P. Troadec. Voronoi-delaunay analysis of voids in systems of nonspherical particles. *Phys. Rev. E*, 59:7205–7212, Jun 1999. (Cited in page 42.)
- M. J. MacDonald, C.-F. Chu, P. P. Guilloit, and K. M. Ng. A generalized blake-kozeny equation for multisized spherical particles. *AIChE Journal*, 37(10):1583–1588, 1991. (Cited in page 126.)
- N. J. Mariani, C. Mocciaro, S. D. Keegan, O. M. Martínez, and G. F. Barreto. Evaluating the effectiveness factor from a 1d approximation fitted at high thiele modulus: Spanning commercial pellet shapes with linear kinetics. *Chemical Engineering Science*, 64(11):2762–2766, 2009. (Cited in page 56.)
- S. McNamara and H. Herrmann. Measurement of indeterminacy in packings of perfectly rigid disks. *Physical Review E*, 70(6):061303, 2004. (Cited in page 16.)
- J. Mellmann. The transverse motion of solids in rotating cylinders—forms of motion and transition behavior. *Powder Technology*, 118(3):251 – 270, 2001. (Cited in pages 5 and 47.)
- N. Midoux, M. Favier, and J.-C. Charpentier. Flow pattern, pressure loss and liquid holdup data in gas-liquid downflow packed beds with foaming and nonfoaming hydrocarbons. *Journal of Chemical Engineering of Japan*, 9(5):350–356, 1976. (Cited in page 8.)
- B. Miller, C. O’Hern, and R. P. Behringer. Stress fluctuations for continuously sheared granular materials. *Phys. Rev. Lett.*, 77:3110–3113, Oct 1996. (Cited in page 14.)
- J. S. Mohammadzadeh and A. Zamaniyan. Catalyst shape as a design parameter—optimum shape for methane-steam reforming catalyst. *Chemical Engineering Research and Design*, 80(4):383–391, 2002. (Cited in page 56.)
- J. J. Moreau. Evolution problem associated with a moving convex set in a hilbert space. *Journal of differential equations*, 26(3):347–374, 1977. (Cited in page 16.)
- J. J. Moreau. Some numerical methods in multibody dynamics: application to granular materials. *European journal of mechanics. A. Solids*, 13:93–114, 1994. (Cited in page 16.)
- B. Moysé. Raschig ring hds catalysts reduce pressure drop. *Oil Gas J.:(United States)*, 82(53), 1984. (Cited in page 56.)

- A. Munjiza, J. F. Peters, M. A. Hopkins, R. Kala, and R. E. Wahl. A poly-ellipsoid particle for non-spherical discrete element method. *Engineering Computations*, 26(6):645–657, 2009. (Cited in page 26.)
- R. Nedderman and C. Laohakul. The thickness of the shear zone of flowing granular materials. *Powder Technology*, 25(1):91 – 100, 1980. (Cited in page 14.)
- D. Nemeč and J. Levec. Flow through packed bed reactors: 1. single-phase flow. *Chemical Engineering Science*, 60(24):6947–6957, 2005. (Cited in pages 9, 57, 126, 127, 130, and 132.)
- I. Newton. *Sir Isaac Newton's mathematical principles of natural philosophy and his system of the world*. Univ of California Press, 1687. (Cited in pages 17 and 28.)
- E. G. Nezami, Y. M. Hashash, D. Zhao, and J. Ghaboussi. A fast contact detection algorithm for 3-d discrete element method. *Computers and Geotechnics*, 31(7):575 – 587, 2004. (Cited in page 21.)
- G. Nolan and P. Kavanagh. Random packing of nonspherical particles. *Powder technology*, 84(3):199–205, 1995. (Cited in pages 21, 26, 28, and 58.)
- C. Nouguièr-Lehon, B. Cambou, and E. Vincens. Influence of particle shape and angularity on the behaviour of granular materials: a numerical analysis. *International Journal for Numerical and Analytical Methods in Geomechanics*, 27(14):1207–1226, 2003. (Cited in page 16.)
- H. Ouadfel and L. Rothenburg. An algorithm for detecting inter-ellipsoid contacts. *Computers and Geotechnics*, 24(4):245 – 263, 1999. (Cited in page 19.)
- M. H. Pahl. *Über die Kennzeichnung diskret disperser Systeme und die systematische Variation der Einflußgrößen zur Ermittlung eines allgemeingültigeren Widerstandsgesetzes der Porenströmung*. na, 1975. (Cited in page 126.)
- I. J. Palmer and R. L. Grimsdale. Collision detection for animation using sphere-trees. In *Computer Graphics Forum*, volume 14, pages 105–116. Wiley Online Library, 1995. (Cited in page 17.)
- J. Park. *Modeling the dynamics of fabric in a rotating horizontal drum*. PhD thesis, Purdue University, 2003. (Cited in pages 36 and 37.)
- N. Patankar, P. Singh, D. Joseph, R. Glowinski, and T. Pan. A new formulation of the distributed Lagrange multiplier/fictitious domain method for particulate flows. *International Journal of Multiphase Flow*, 26(9):1509–1524, 2000. ISSN 0301-9322. (Cited in page 105.)
- P. Pepiot and O. Desjardins. Numerical analysis of the dynamics of two-and three-dimensional fluidized bed reactors using an Euler-Lagrange approach. *Powder Technology*, 220:104–121, 2011. (Cited in pages 91, 92, 93, and 95.)
- C. Peskin. Numerical analysis of blood flow in the heart. *Journal of Computational Physics*, 25(3):220–252, 1977. (Cited in page 105.)
- C. Peskin. The immersed boundary method. *Acta Numerica*, 11(1):479–517, 2002. (Cited in page 105.)
- D. Petit, F. Pradel, G. Ferrer, and Y. Meimon. Shape effect of grain in a granular flow. *Powders and grains*, page 425, 2001. (Cited in page 27.)

- H. Polderman, J. Boom, E. D. Hilster, and A. Scott. Solids flow velocity profiles in mass flow hoppers. *Chemical Engineering Science*, 42(4):737 – 744, 1987. (Cited in page 16.)
- O. Pouliquen and F. Chevoir. Dense flows of dry granular material. *Comptes Rendus Physique*, 3(2):163 – 175, 2002. (Cited in page 14.)
- L. Pournin and T. Liebling. A generalization of Distinct Element Method to tridimensional particles with complex shapes. In *Powders and Grains*, volume 5805, pages 1375–1378. R. García-Rojo, H J Herrmann, and S McNamara, 2005. (Cited in pages 21 and 27.)
- C. Radeke, B. Glasser, and J. Khinast. Large-scale mixer simulations using massively parallel GPU architectures. *Chemical Engineering Science*, 65:6435–6442, 2010. (Cited in page 70.)
- F. Radjai and V. Richefeu. Contact dynamics as a nonsmooth discrete element method. *Mechanics of Materials*, 41(6):715–728, 2009. (Cited in page 16.)
- F. Radjai and S. Roux. Turbulentlike fluctuations in quasistatic flow of granular media. *Physical Review Letters*, 89(6):064302, 2002. (Cited in page 16.)
- F. Radjai, M. Jean, J.-J. Moreau, and S. Roux. Force distributions in dense two-dimensional granular systems. *Physical review letters*, 77(2):274, 1996. (Cited in page 16.)
- F. Radjai, D. E. Wolf, M. Jean, and J.-J. Moreau. Bimodal character of stress transmission in granular packings. *Physical review letters*, 80(1):61, 1998. (Cited in page 16.)
- M. Rahmani and A. Wachs. Free falling and rising of spherical and angular particles. *Physics of Fluids*, 26:083301, 2014. (Cited in pages 102, 106, 107, and 112.)
- W. Reichelt. Zur berechnung des druckverlustes einphasig durchströmter kugel-und zylinderschüttungen. *Chemie Ingenieur Technik*, 44(18):1068–1071, 1972. (Cited in page 126.)
- L. F. Richardson. The approximate arithmetical solution by finite differences of physical problems involving differential equations, with an application to the stresses in a masonry dam. *Philosophical Transactions of the Royal Society of London A: Mathematical, Physical and Engineering Sciences*, 210(459-470):307–357, 1911. ISSN 0264-3952. (Cited in page 118.)
- G. Ristow. Dynamics of granular materials in a rotating drum. *EPL (Europhysics Letters)*, 34(4):263, 1996. (Cited in page 33.)
- A. Ritter. Die fortpflanzung de wasserwellen. *Zeitschrift Verein Deutscher Ingenieure*, 36(33): 947–954, 1892. (Cited in page 85.)
- A. M. Roma, C. S. Peskin, and M. J. Berger. An adaptive version of the immersed boundary method. *Journal of computational physics*, 153(2):509–534, 1999. (Cited in page 106.)
- S. Romkes, F. Dautzenberg, C. Van den Bleek, and H. Calis. CFD modelling and experimental validation of particle-to-fluid mass and heat transfer in a packed bed at very low channel to particle diameter ratio. *Chemical Engineering Journal*, 96(1):3–13, 2003. (Cited in page 102.)
- L. Rothenburg and R. J. Bathurst. Numerical simulation of idealized granular assemblies with plane elliptical particles. *Computers and Geotechnics*, 11(4):315 – 329, 1991. (Cited in page 19.)
- S. Schöllmann. Simulation of a two-dimensional shear cell. *Phys. Rev. E*, 59:889–899, Jan 1999. (Cited in page 14.)

- Q. Segers, J. Kuipers, and N. Deen. Immersed boundary method applied to single phase flow past crossing cylinders. *Chemical Engineering Science*, 100:33–38, 2013. (Cited in page 106.)
- L. E. Silbert, D. Ertas, G. S. Grest, T. C. Halsey, D. Levine, and S. J. Plimpton. Granular flow down an inclined plane: Bagnold scaling and rheology. *Phys. Rev. E*, 64:051302, Oct 2001. (Cited in page 14.)
- Y. Song, R. Turton, and F. Kayihan. Contact detection algorithms for DEM simulations of tablet-shaped particles. *Powder Technology*, 161(1):32–40, 2006. (Cited in page 26.)
- M. Sussman, A. S. Almgren, J. B. Bell, P. Colella, L. H. Howell, and M. L. Welcome. An adaptive level set approach for incompressible two-phase flows. *Journal of Computational Physics*, 148(1):81–124, 1999. (Cited in page 106.)
- V. S. Sutkar, N. G. Deen, B. Mohan, V. Salikov, S. Antonyuk, S. Heinrich, and J. Kuipers. Numerical investigations of a pseudo-2d spout fluidized bed with draft plates using a scaled discrete particle model. *Chemical Engineering Science*, 104:790–807, 2013. (Cited in page 102.)
- K. Szarf, G. Combe, and P. Villard. Influence of the grains shape on the mechanical behavior of granular materials. *AIP Conference Proceedings*, 1145(1):357–360, 2009. (Cited in page 16.)
- H. Tavassoli, E. Peters, and J. Kuipers. Direct numerical simulation of fluid–particle heat transfer in fixed random arrays of non-spherical particles. *Chemical Engineering Science*, 129:42–48, 2015. (Cited in pages 106 and 113.)
- T. Tezduyar, J. Liou, and M. Behr. A new strategy for finite element computations involving moving boundaries and interfaces- the deforming-spatial-domain/space-time procedure: I. The concept and the preliminary numerical tests. *Computer Methods in Applied Mechanics and Engineering*, 94(3):339–351, 1992. (Cited in page 103.)
- E. W. Thiele. Relation between catalytic activity and size of particle. *Industrial & Engineering Chemistry*, 31(7):916–920, 1939. (Cited in page 7.)
- J. R. Third, Y. Chen, and C. R. Müller. Comparison between finite volume and lattice-boltzmann method simulations of gas-fluidised beds: bed expansion and particle–fluid interaction force. *Computational Particle Mechanics*, 3(3):373–381, 2016. ISSN 2196-4386. (Cited in pages 104 and 105.)
- T. Tsuji, K. Yabumoto, and T. Tanaka. Spontaneous structures in three-dimensional bubbling gas-fluidized bed by parallel DEM-CFD coupling simulation. *Powder Technology*, 184(2):132–140, 2008. (Cited in pages 91, 92, and 93.)
- Y. Tsuji, T. Kawaguchi, and T. Tanaka. Discrete particle simulation of two-dimensional fluidized bed. *Powder technology*, 77(1):79–87, 1993. (Cited in page 16.)
- U. Tüzün, G. Housby, R. Nedderman, and S. Savage. The flow of granular materials – ii : Velocity distributions in slow flow. *Chemical Engineering Science*, 37(12):1691 – 1709, 1982. (Cited in page 16.)
- M. Uhlmann. An immersed boundary method with direct forcing for the simulation of particulate flows. *Journal of Computational Physics*, 209(2):448–476, 2005. ISSN 0021-9991. (Cited in pages 105 and 113.)

- P. Umbanhowar. Patterns in the sand. *Nature*, 389:541–542, October 1997. (Cited in pages 15 and 17.)
- M. S. van Buijtenen, N. G. Deen, S. Heinrich, S. Antonyuk, and J. A. Kuipers. Discrete particle simulation study on the influence of the restitution coefficient on spout fluidized-bed dynamics. *Chemical engineering & technology*, 32(3):454–462, 2009. (Cited in page 102.)
- M. Van der Hoef, R. Beetstra, and J. Kuipers. Lattice-Boltzmann simulations of low-Reynolds-number flow past mono-and bidisperse arrays of spheres: results for the permeability and drag force. *Journal of Fluid Mechanics*, 528:233–254, 2005. (Cited in page 104.)
- M. Van der Hoef, M. van Sint Annaland, N. Deen, and J. Kuipers. Numerical simulation of dense gas-solid fluidized beds: A multiscale modeling strategy. *Annual Review of Fluid Mechanics*, 40:47–70, 2008. (Cited in page 102.)
- R. Van Loon, P. D. Anderson, J. De Hart, and F. P. Baaijens. A combined fictitious domain/adaptive meshing method for fluid–structure interaction in heart valves. *International Journal for Numerical Methods in Fluids*, 46(5):533–544, 2004. (Cited in page 106.)
- M. Vanella, A. Posa, and E. Balaras. Adaptive mesh refinement for immersed boundary methods. *Journal of Fluids Engineering*, 136(4):040909, 2014. (Cited in pages 105, 106, and 107.)
- A. Wachs. A DEM-DLM/FD method for direct numerical simulation of particulate flows: Sedimentation of polygonal isometric particles in a Newtonian fluid with collisions. *Computers & Fluids*, 38(8):1608–1628, 2009. (Cited in pages 93, 106, 114, and 116.)
- A. Wachs. PeliGRIFF, a parallel DEM-DLM/FD direct numerical simulation tool for 3D particulate flows. *Journal of Engineering Mathematics*, 71(1):131–155, 2011. (Cited in pages 16, 50, 106, 112, 114, and 116.)
- A. Wachs, G. Vinay, and A. Hammouti. PeliGRIFF Home Page. <http://www.peligriff.com>, 2007-2016. (Cited in pages 93 and 114.)
- A. Wachs, L. Girolami, G. Vinay, and G. Ferrer. Grains3D, a flexible DEM approach for particles of arbitrary convex shape—Part I: Numerical model and validations. *Powder Technology*, 224:374–389, 2012. (Cited in pages 26, 27, 28, 31, 32, 34, 42, 44, 45, 46, 47, 51, 52, 57, 58, 70, 71, 72, 77, 78, 79, 84, and 112.)
- A. Wachs, A. Hammouti, G. Vinay, and M. Rahmani. Accuracy of finite volume/staggered grid distributed lagrange multiplier/fictitious domain simulations of particulate flows. *Computers & Fluids*, 115:154 – 172, 2015. (Cited in pages 102, 106, 112, 113, 114, 115, 116, 121, and 123.)
- J. H. Walther and I. F. Sbalzarini. Large-scale parallel discrete element simulations of granular flow. *Engineering Computations*, 26(6):688–697, 2009. (Cited in pages 15, 70, and 71.)
- D. Wan and S. Turek. Fictitious boundary and moving mesh methods for the numerical simulation of rigid particulate flows. *Journal of Computational Physics*, 222(1):28–56, 2007. (Cited in pages 103 and 104.)
- J. R. Williams and R. O’Connor. A linear complexity intersection algorithm for discrete element simulation of arbitrary geometries. *Engineering computations*, 12(2):185–201, 1995. (Cited in page 27.)

- J. R. Williams and A. P. Pentland. Superquadrics and modal dynamics for discrete elements in interactive design. *Engineering Computations*, 9(2):115–127, 1992. (Cited in pages 19 and 27.)
- B. H. Xu and A. B. Yu. Numerical simulation of the gas-solid flow in a fluidized bed by combining discrete particle method with computational fluid dynamics. *Chemical Engineering Science*, 52(16):2785–2809, 1997. (Cited in page 92.)
- R. Yang, R. Zou, and A. Yu. Microdynamic analysis of particle flow in a horizontal rotating drum. *Powder Technology*, 130(1-3):138–146, 2003. (Cited in page 45.)
- R. Yang, A. Yu, L. McElroy, and J. Bao. Numerical simulation of particle dynamics in different flow regimes in a rotating drum. *Powder Technology*, 188(2):170–177, 2008. (Cited in page 45.)
- Z. Yu and X. Shao. A direct-forcing fictitious domain method for particulate flows. *Journal of Computational Physics*, 227(1):292–314, 2007. (Cited in page 105.)
- Z. Yu, N. Phan-Thien, Y. Fan, and R. Tanner. Viscoelastic mobility problem of a system of particles. *Journal of Non-Newtonian Fluid Mechanics*, 104(2-3):87–124, 2002. (Cited in page 105.)
- M. Zastawny, G. Mallouppas, F. Zhao, and B. Van Wachem. Derivation of drag and lift force and torque coefficients for non-spherical particles in flows. *International Journal of Multiphase Flow*, 39:227–239, 2012. (Cited in pages 105, 106, and 113.)
- A. Zick and G. Homsy. Stokes flow through periodic arrays of spheres. *Journal of Fluid Mechanics*, 115(1):13–26, 1982. (Cited in page 119.)